Development of Tunable and Miniature Microwave Filters for Modern Wireless Communications

by

JIA NI

A dissertation submitted in partial fulfillment of the

requirements for the degree of Doctor of Philosophy

(Electrical Engineering)

in Heriot-Watt University

March 2014

Abstract

Due to the increasing demand for new wireless services and applications, the high level of integration and the coexistence of multi-standard (MS) or multi-band operations into a single device are becoming defining trends in designing microwave filters. This has driven considerable technological advances in reconfigurable/tunable and miniaturized filters. More specifically, reconfigurable/tunable filters that tune to different frequency bands instead of classical filter banks have great potential to significantly reduce the system size and complexity; while reducing the filter size becomes essential to achieve the highest degree of integration density in compact and portable wireless devices.

In the light of this scenario, the objective of this dissertation is to develop the new design technologies, concepts and filtering configurations for tunable microstrip filters and compact passive microwave filters. To this aim, this dissertation is divided into two main parts.

The first part (Part I) focuses on the designs of novel varactor-tuned microstrip filters with advanced performances. In this aspect, new topologies for realizing tunable lowpass and highpass filters are firstly developed. State-of-the-art performances, including wide tuning range, high selectivity with multiple transmission zeros, low insertion loss and compact size for all the tuning states are obtained in both of these filters. Secondly, two novel classes of tunable bandpass filters are presented. One of them is designed based on varactor-loaded parallel-coupled microstrip lines (PCML) and short-circuited stubs, which allows the lower passband edge together with two transmission zeros located around the lower passband skirt to be reconfigured separately. While the other tunable bandpass filter is

constructed by the combination of tunable bandpass and lowpass filters, featuring both centre frequency and bandwidth tunabilities, as well as high selectivity with abundant transmission zeros. Furthermore, a new concept of tunable lossy filter is demonstrated, which attempts to achieve an equivalent high-*Q* tunable performance by using low-*Q* resonators. This concept makes the presented tunable combline filter interesting for some frequency-agile applications in which the low in-band loss variation and high selectivity are much desired while the absolute insertion loss can be a tradeoff.

The second part (Part II) is devoted to the design of miniaturized passive microwave filters with improved characteristics. For this, the concept of artificial right-handed and left-handed transmission lines are applied to the signal interference filtering topology, which results in a compact circuit size and good out-of-band performance. In particular, for a further size reduction, such filter is implemented in the forms of multilayered structure by using liquid crystal polymer (LCP) technology. Additionally, another two types of miniaturized bandpass filters using stepped impedance resonators are demonstrated, which are implemented based on different fabrication processes (i.e. LCP bonded multilayer PCB technology and a standard planar PCB technology). Among their main features, the compact size, wide passband, broad stopband with multiple transmission zeros and circuit simplicity are highlighted.

For all the proposed design techniques and filtering structures, exhaustive theoretical analyses are done, and design equations and guide rules are provided. Furthermore, all the proposed schemes and/or ideas have been experimentally validated through the design, implementation and measurement of different filters. The fabrication processes of multilayer technology utilized: liquid crystal polymer (LCP) technology and liquid crystal polymer (LCP) bonded multilayer printed circuit board (PCB) technology, are also demonstrated for reference. All of the results achieved in this dissertation make the proposed filters very attractive for their use in modern wireless communication systems.

Dedication

To my grandparents and maternal grandparents

Acknowledgment

First and foremost, I would like to thank and express my heartfelt gratitude to my advisor Prof. Jiasheng Hong for his invaluable guidance, encouragement and support throughout my doctoral program. During the years of working with him, I learned a great deal both about the technical issues and professional sprit. He always focused on the principles and asked us to think about them in a physical fashion and asked ourselves “Does it make sense?” He always encouraged us to deeply analyze every failed experiment and learn from our mistakes. He always said “this is the reason why we do the research” when we were encountered with difficulties on the way. There is a lot to say about Prof. Hong as a great advisor. Overall, his unique care and attention toward student benefited me immensely, which gave me a solid standing ground in my research. His trust and support which let me work and learn in my own way and yet I am increasingly independent on my research.

I also sincerely thank Prof. Dagang Fang, Nanjing University of Science and Technology, China, for his generous gift of friendship and inspiration in the past years. He could not even realize without his encouragement and support when I was undergraduate student, probably I couldn’t devote to research on microwave engineering after finishing the bachelor degree. His unyielding enthusiasm for research and great devotion deeply touched me and set a good example for my life.

I would like to thank all my colleagues (past and present) and friends for their generous sharing and giving me a lot of support, which made my stay abroad a more pleasant experience. My thanks go to all of the Microwave engineering group and MISEC group including Dr. Zhangchen Hao, Dr. Wenxing Tang, Dr. Alex Miller, Shilong Qian, Francisco Cervera, J. Ross Aitken, Maria Lorente, Dr. Mazher-Iqbal Mohammed, Dr. Yevs Lacrotte, Dr Stefan Wilhelm, David Watson, Elizabeth

McKeever, Xin Jiang and Tomas Jones. Particularly, I am grateful to Dr. Wenxing Tang for his friendship and help in my research and my daily life, to Francisco Cervera and J. Ross Aitken for their valuable helps on my dissertation writing. The overseas supports from Dr. Jianpeng Wang and my best friend Lili Song are also highly appreciated.

I would like to thank MultiWaves Project (PIRSES-GA-2010-247532) of the Seventh Framework Programme (FP7) of the European Commission, for funding me to visit St. Petersburg Electrotechnical University and Cape Town University several times during my doctoral program. Those were wonderful and valuable experiences both in technically and socially. Thanks Prof. Irina Vendik (Russia), Prof. Dmitry Kholodnyak (Russia) and Prof. Riana Geschke (South Africa) for welcoming me in their groups and providing big helps on my research. It is a great pleasure to make a lot of friends during my visit, including Mike Odit, Irina Munina, Shamim Omar and Leokadia Nepaya and so on.

I am grateful to Prof. Marc Desmulliez for his unselfishly sharing of his laser lab and other facilities. Also, the entire technicians in the electrical engineering department workshop were important contributors to helping my research.

Finally, my deepest appreciations go to my parents for their unconditional love and ever-lasting support. Since I was a child, my Dad and Mom always told me “You are unique in the world.” I strongly believe such words that have been the greatest motivation for me to keep progressing during these years. I am still committing myself to develop and exploit those talents into my unique, special area of expertise.

Contents

Part I: Development of Tunable Filters

Part II: Development of Miniature Filters

List of Figures

List of Tables

Glossary of Terms

HSDPA	High-speed Downlink Packet Access
CR	Cognitive Radio
SAW	Surface-acoustic-wave
PA	Power Amplifier
LNA	Low Noise Amplifier
BOM	Bill of Material
BST	Barium Strontium Titanate
YIG	Yttrium-iron-garnet
MEMS	Micro-Electro-Mechanical System
E.S.M	Electronic Support Measure systems
LCP	Liquid Crystal Polymer
PCB	Printed Circuit Board
IIP3	Input Third-order Intercept Point
PCL	Parallel-coupled Line
PCML	Parallel-coupled Microstrip Lines
IMUX	Input Multiplexer
LTCC	Low Temperature Co-fired Ceramic
HTCC	High Temperature Co-fired Ceramic
SIR	Stepped Impedance Resonator
SoP	System-on-package

List of Publications by the Candidate

Journal Papers

1. **Jia Ni** and Jiasheng Hong, "Compact Continuously Tunable Microstrip Low-Pass Filter," *IEEE Transactions on Microwave Theory and Techniques*, vol. 61, no. 5, pp. 1793-1800, May. 2013.

2. **Jia Ni** and Jiasheng Hong, "Compact Varactor-Tuned Microstrip High-Pass Filter with a Quasi-Elliptic Function Response," *IEEE Transactions on Microwave Theory and Techniques*, vol. 61, no. 11, pp. 3853-3859, Nov. 2013.

3. **Jia Ni**, Irina Vendik, Dmitry Kholodnyak and Jiasheng Hong, "A Compact Bandpass Filter Based on Right- and Left-Handed Transmission Line Sections," *IEEE Microwave and Wireless Components Letters*, vol. 23, no. 6, pp. 279-281, Jun. 2013.

4. **Jia Ni** and Jiasheng Hong, "Varactor-Tuned Microstrip Bandpass Filters with Different Passband Characteristics," *Microwaves, Antennas & Propagation, IET*, vol. 8, no.6, pp. 415-422, Apr. 2014.

5. **Jia Ni**, Wenxing Tang, Jiasheng Hong and Riana H. Geschke, "Design of Microstrip Lossy Filter Using an Extended Doublet Topology," *IEEE Microwave and Wireless Components Letters*, (in press)

Conference Papers

6. **Jia Ni** and Jiasheng Hong, "An Investigation of Performance Enhancement for Tunable Microstrip Filter," *Proceedings of the 41st European Microwave Conference*, Oct. 2011.

7. **Jia Ni** and Jiasheng Hong, "Compact Wideband Combline Filter Using LCP bonded Multilayer PCB Technology," *Proceedings of the 42st European Microwave Conference*, Oct. 2012.

8. W. Tang, **Jia Ni** and J.-S. Hong, "Parallel Feed Microstrip Quasi-Elliptic Function Bandpass Filter," *Proceedings of the 41st European Microwave Conference*, Oct. 2011.

CHAPTER 1

Introduction to Tunable Filter

1.1 Motivation

In today crowded RF environments, tunable microwave filters are attracting more attention for research and development because of their increasing importance in improving the capability of current and future wireless systems [1]. Common applications for tunable filters include multi-band transceivers, cognitive radio (CR) systems, next generation cell phones, wide-band radars and satellite payloads. Generally speaking, such applications put high requirements on the performance of the wireless systems, demanding for more functionality, higher efficiency and flexibility in frequency spectrum usage, smaller size, longer battery life and lower cost. Moreover, the integration and coexistence of multi-standard (MS) or multiband operations in a single device is becoming a major trend. Indeed, these requirements have been manifested in the roadmap for RF section development in cellular phones, as depicted in Fig. 1.1.

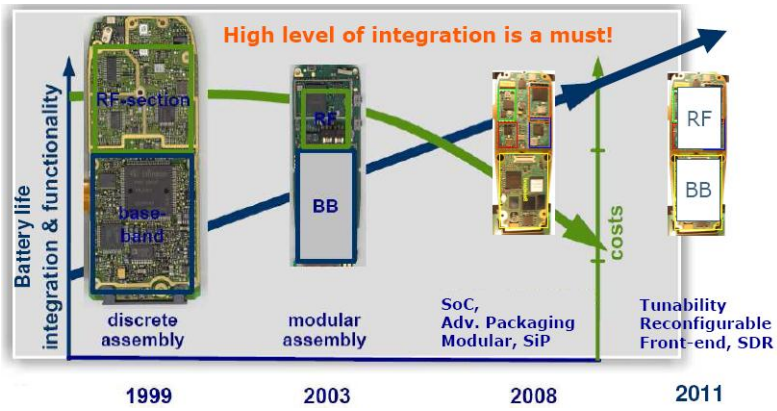

Figure 1.1: Roadmap for RF section in cellular phones [2].

Although the industry has made progresses over the past few years in packaging technology, a higher level of integration is still challenging for today's wireless communication systems. This is because traditionally designers who seek to support

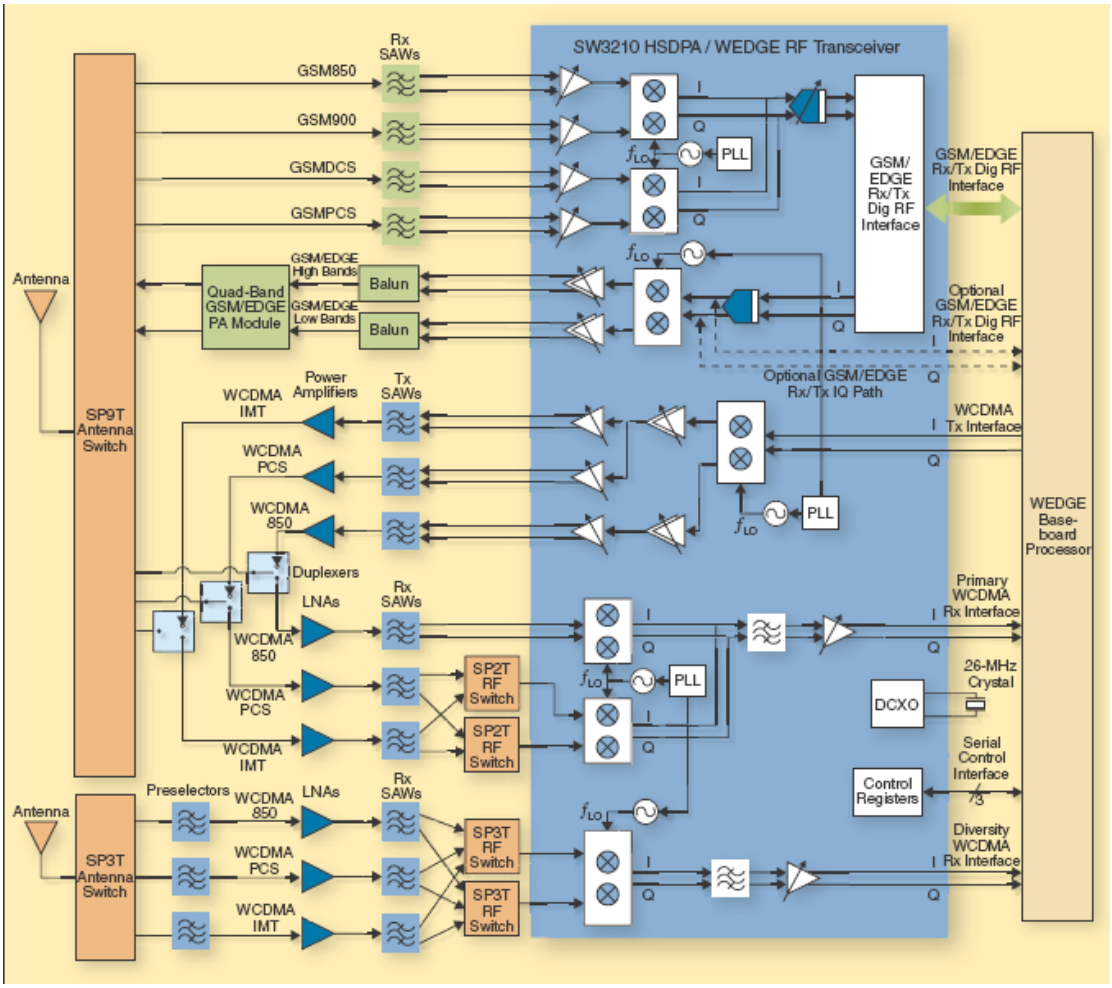

Figure 1.2: System architecture for a multiband HSDPA/WEDGE diversity radio subsystem [3].

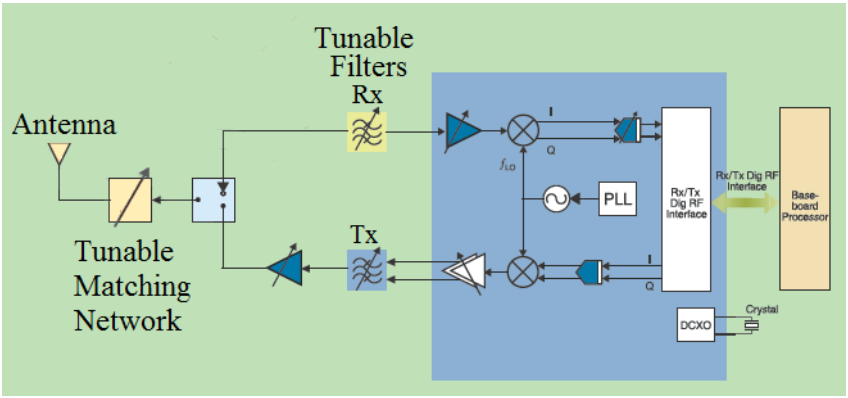

Figure 1.3: A concept illustration of a tunable RF front-end [4].

multiple operation standards in the same device have resorted to stacked radio architectures with separate radio transceiver for different standards. As a typical example, a multiband HSDPA/WEDGE diversity radio block diagram is shown in Fig. 1.2, where it is noted that currently 3 power amplifiers (PAs), 19 fixed surface-acoustic-wave (SAW) filters, 3 duplexers, 6 low noise amplifiers (LNAs) and a large nine-throw switch are required to realize a cell phone front-end, covering a frequency range from 850 MHz to 2400 MHz. Apparently, the passive part (such as filters and switches) in this system occupies a large board area to hinder higher integration achieved. However, considering the alternative architecture of a fully reconfigurable RF front-end proposed in Fig. 1.3, the overall size and complexity of the system can be significantly reduced by using tunable components such as tunable matching network and tunable filters. Moreover, the total Bill of Material (BOM) costs for a system can be driven down accordingly.

A newly emerged reconfigurable system is cognitive radio. It is well known that the ultimate objective of cognitive radio is to obtain the best available spectrum efficiently through cognitive capability and reconfigurability [5]. In order to enable the cognitive radio to adapt easily to dynamic radio environment, the network requires several parameters such as the operating frequency, modulation, transmission power and communication technology, can be reconfigured without any modification on the hardware components. To this aim, it is certain that tunable filters can ease these challenging requirements.

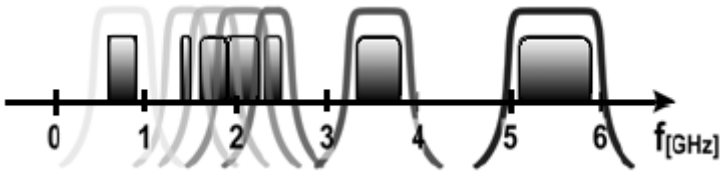

Figure 1.4: A strategy to realize a wideband receiver by using narrow band tunable filters [6].

Wide band receivers are also currently an active area of application that can benefit greatly from the use of tunable filters. As an illustrative strategy shown in Fig.

1.4, in order to cover the wide frequency range from 1 to 6 GHz, a wide band receiver is used together with narrow band tunable filters to split the whole spectrum of interest into smaller sub-bands, thus performing RF selectivity of narrow band system. Further, the linearity specifications of LNA in the communication systems can be relaxed, since the interfering signal is attenuated enough that any signals produced by the LNA do not have enough power to interfere with the desired receive signal.

Overall, the general advantages of using tunable filter can be concluded as:

- Efficiency and flexibility in spectrum usage are enhanced,
- RF component count is reduced,
- System complexity is reduced
- System size and cost are reduced,
- Capacity is increased,
- Software control can be applied,
- System performance is optimized,
- The specifications of other devices in the system can be relaxed.

1.2 Tunable Filter Technology

In the open literature, microwave tunable filters can be realized by different types of technologies. Filter topologies presenting a discrete tuning generally use PIN diodes or MEMS switches. While in order to obtain a continuous tuning ability, varactor diodes, MEMS capacitors, mechanical tuning elements (piezoelectric transducers/actuators), ferroelectric materials or ferromagnetic materials are frequently used.

Mechanically tunable filters are the earliest type of tunable filters. Generally speaking, the tuning mechanism is physically moving a material or tuning screws to affect the resonant frequency of a coaxial, cavity or waveguide resonator. As illustrative tuning methods presented in [7]-[9], by using piezoelectric transducers/actuators, a dielectric slab which can either be moved in the vertical direction above a microwave filter, or be utilized to deform a conductive film to tune dielectric resonator filters or evanescent-mode cavity filters. Usually this type of

filters offers high-*Q* and high-power-handling capabilities. However, their bulky size and low tuning speed limit their applications in certain areas.

YIG filters utilizing yttrium-iron-garnet (YIG) spheres have been proved the most popular type among the magnetically tunable filters [10]-[11]. The tunable nature arises from applying an external dc magnetic field to change the effective permeability of the ferromagnetic material. These filters feature good advantages of a multi-octave tuning range, low insertion loss and high power handling capability. While the main drawbacks are a complex bias circuit to tune the device with high power consumption, a low tuning speed (ms) and a large physical size, limiting their use in modern communication systems.

Barium Strontium Titanate (BST) is most intensively studied ferroelectric material in tunable applications at room temperature [12]-[14]. Used in the paraelectric phase, BST thin film typically exhibits a large dielectric constant (ε_r=300-800) that can be changed by an applied dc electric filed. The high dielectric constant of BST film results in compact BST thin film varactors that are widely used to implement tunable filter, tunable matching networks and delay lines. BST tunable filters can be tuned at nanosecond speeds, and can be fabricated on a variety of substrates using standard semiconductor manufacturing process with ease of integrating microwave devices compatible with planar circuits. However, the relatively high loss of room temperature BST tunable filters has been a significant drawback limiting their microwave applications. A continuous effort is carried out to improve the quality factors of BST varactors. But this is still challenging today.

RF MEMS (Micro-Electro-Mechanical System) reconfigurable devices such as MEMS switches or MEMS varactors, are quite popularly used in filter topologies with discrete and continuous tuning [15]-[17]. RF MEMS devices mostly utilize micrometer level movement to obtain a switching function or an adjustable capacitance with the applied dc voltage. In general, they can offer small size and good integration capabilities with microwave electronics. They also have the merit of low loss (about 0.05-0.2 dB from 1-100 GHz for switches [18]), high linearity with low signal distortion, low power consumption, high isolation (for switches) and high

Table 1.1: Comparison of Typical Tunable Technologies [a]

Tuning Technology	Mech.	YIG	PIN diode	Vacator diode	BST	RF MEMS
Unload *Q*	> 1000	> 500	R_s=1- 4Ω	30-50[b]	30-150[b]	50-400
Tuning Speed	> 10μs	ns	ns	ns	ns	μs
Bias	> 100V	N/A	10-40mA	< 30V	< 30V	20-100V
Linearity (IIP3: dBm)	high	< 30	> 33	10-35	10-35	> 60
Power handling	high	2W	~ mW	~ mW	~ mW	1-2W
Power Consumption	high	high	medium	low	negligible	negligible
Size	large	large	small	small	small	small
Cost	high	high	low	low	low	medium
Integration	difficult	difficult	good	good	good	good

[a] From reference [18] and [20] [b] at 10GHz

power-handling capability. However, the requirements of hermetic packaging and high voltage drive circuits (20-100 V) besides the reliability issues have prevented RF MEMS from being widely used in industry.

Another promising candidate for tunable filters is varactor diode whose capacitance varies as a function of the reverse voltage applied across its p-n junction. Generally, the operation of a varactor diode is based on altering the width of the junction depletion region under a reverse voltage, thus similarly changing the distance between the two plates of a capacitor to vary the capacitance. And this variable capacitance is inversely proportional to the square root of applied voltage [19]. Although the varactor diodes have low quality factor and suffer from poor linearity, they still have been the state of art for building tunable filters and have been widely used in Electronic Support Measure (E.S.M) systems, mainly resulting from the advantages of fast tuning speed, high tunability, compact size, low cost and proven reliability. In this dissertation, varactor diodes are used as the tuning elements

considerably to explore different novel tunable filter topologies, including tunable lowpass filter, tunable highpass filter and tunable bandpass filter. Additionally, investigations of performance enhancements for varactor diode based tunable bandpass filters are demonstrated, which attempts to overcome the performance degradation arising from the low *Q* of varactor-tuned resonators.

Table 1.1 presents the performance comparison among the different tunable technologies reviewed in this section. Apparently, none of them is perfect and choosing strongly depends upon the particular system specifications. There are always some trade-offs involved for consideration, such as the tunable performance, the filter size and cost, circuit complexity, ease of integration, reliability, and repeatability.

1.3 Varactor-Diode-Based Tunable Filter

1.3.1 Basic concepts of varactor diode

For many modern communication systems, it is desireable to have filters with high tuning speeds in excess of 1 GHz/μs [21]. To achieve this requirement, varactor tuning techniques are quite popular for some microwave applications. As demonstrated in Fig. 1.5, varactor diodes essentially consist of p-n juction operated in a reverse-biased state and this gives rise to three regions. At either end of the diode are the P and N regions where the current can be conducted. However, around the junction is the depletion region where no current flow. As a result, current can be carried in the P and N regions, but the depletion region is an insulator. Indeed, this is exactly the same construction as the parallel plate capacitor that has conductive plates separeted by an insulating dielectric. In general, if the reverse voltage is increased, the depletion region of the diode will increase accordingly, thus resulting in a decreased capactiance and vice versa. This property can be further observed based on the *C*-V curvers illustrated in Fig. 1.6.

The most commonly used forms of tuning varactor diodes are abrupt and hyperabrupt junction varactors that are constructed based on silicion or Gallium Aresenide (GaAs) material. Generally, silicon varactor diodes suffer from low *Q* factors so that they are only used at low microwave frequencies-up to a few GHz at

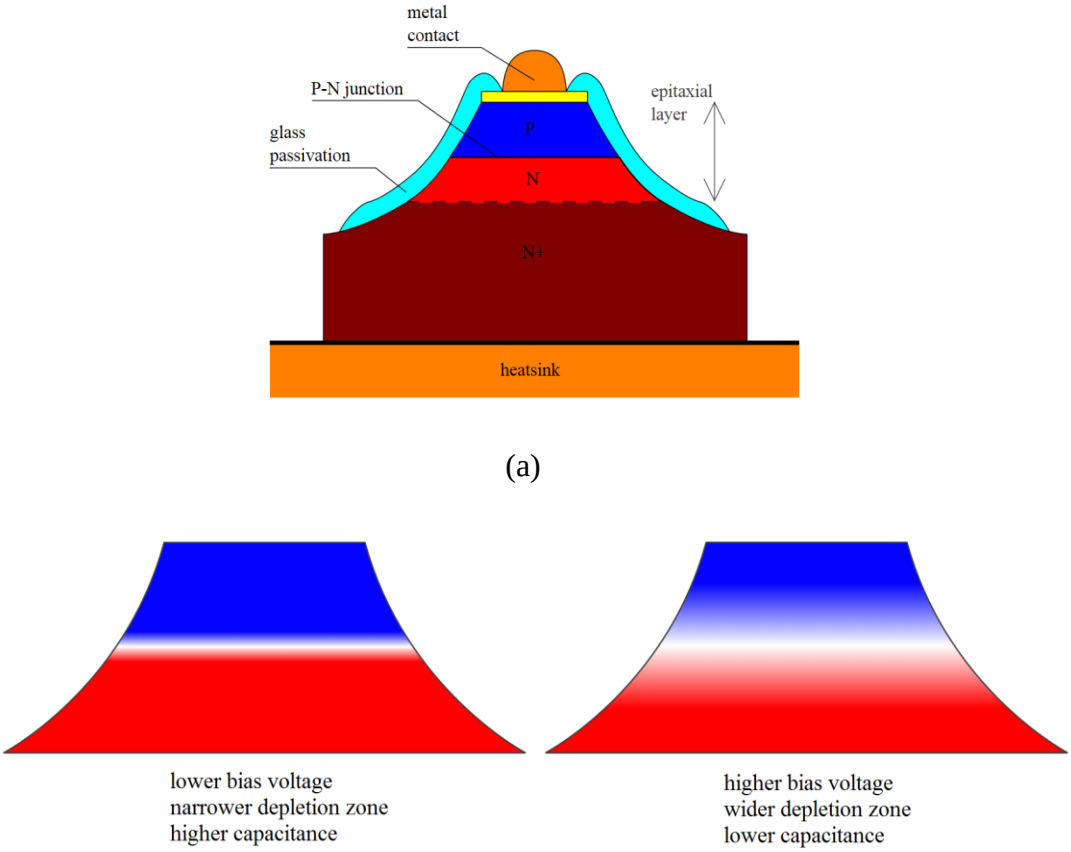

Figure 1.5: (a). Internal structure of a varactor diode. (b).Operation of a varactor diode [22].

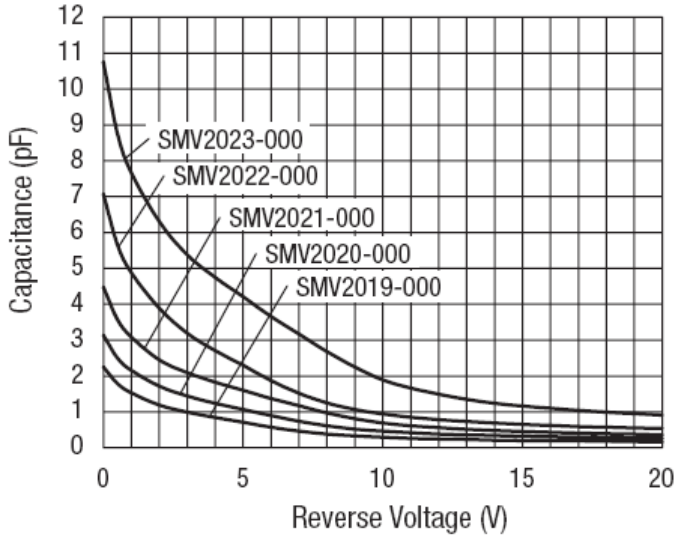

Figure 1.6: Typical capacitance-voltage curves of varactor diodes from Skyworks Ltd. [23].

most. While GaAs varactors has lower parasitic resistance and higher *Q* than the silicon counterparts, hence they are more favourable in high radio frequencies. For instance, GaAs tuning varactors MA46580 series from MA-COM [24] and DMK2308 series from Skyworks [25] are useful at frequencies as high as 40 GHz and 100 GHz, respectively. Furthermore, with the advance of new package technologies, such as surface mount and flip-chip technologies, varactor diodes have more compact footprint, resulting in an increasing demand in mordern wireless communication systems.

When choosing a varactor diode, usually there are a lot of different electrical parameters available in the datasheet for users' consideration, such as reverse voltage, operating temperautre, power dissipation and so on. Among them, the key specifications guidling the selection and useage are:

- *Reverse breakdown voltage*; The breakdown voltage defines the operating limit for the revers bias across the diode. A rule of thumb is to choose a varactor diode that has a good margin between its maximum operating reverse dc voltage and its reverse breakdown voltage. Otherwise, it is likely to cause an avalanche of conductors through the diode.
- *Capacitance value and capacitance-voltage change behavior;* The absolute capacitance of the varactor diode is very important for determining the operating frequency of the circuit. While the capacitance-voltage variation property mostly governs the change of frequency or the phase of the signal. Hence, it is necessary to consult the curvers for the particular diode to ensure that it will give the required capacitance change over the voltages that will be applied.
- *Maximum frequency operation;* The available maximum frequency of varactor diode is mostly used to determine the frequency limits in the practical applications. Normally there are a lot of items that limit this frequency of operation, such as the minimum capacitance of the diode and the parastic effects arising from the device package [26]. By taking into account these considerations, it is necessary to choose a varactor with the maximum frequency operation that is most suitable for the desired application. For some of varactor diode products, the maximum operating frequencies

have been directly stated in data sheets.

- *Quality factor of varactor diode;* Another important characteristic of varactor diode is quality factor *Q*, since it determines the frequency limit applicability for the diode. The higher *Q* factor of the varactor diode, the lower energy dissipation and higher the operating frequency limit of the *LC* circuit in which it is used. For most of varactor diode products, it is notable that their *Q* factors are only claimed at 50MHz in the datasheets. Obviously, this available *Q* is not enough for a varactor to be fully considered in a design, since the *Q* is heavily dependent on the operating frequency. Therefore, in order to get more accurate design, it is quite necessary to extract the *Q* of varactors at different frequency. In this aspect, the associated methods will be introduced in the next section.

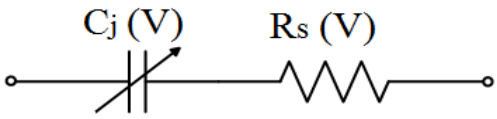

Figure 1.7: Simple circuit model of a varactor diode under the assumption that the diode is unpackaged.

1.3.2 The methods to extract the Q of a varactor diode

The *Q* factor, also known as the figure of merit and the quality factor, is classically defined as:

$$Q = \frac{\text{Energy Stored}}{\text{Energy Dissipated}} \qquad (1.1)$$

For the simple circuit model of a varactor diode shown in Fig. 1.7, the related *Q* factor is given by:

$$Q = \frac{1}{2\pi f \mathrm{C_j(V)R_s(V)}} \qquad (1.2)$$

where *f* is the operating frequency, C_j is the junction capactiance, and R_s is the series resistance of the diode that mainly arising from the resistance of undepleted region of the epilayer. From the above equation it follows that *Q* is a sensitive function of the

applied reverse bias. Genearlly as the bias is increased, both of the capacitance C_j and resistance R_s will be reduced, resulting in an incresased Q.

Regarding the approaches to extract the varactor Q at the desired tunable frequencies, probably the most straightforward one is to employ some specific instruments to measure the series resistance R_s of the varactor diode. For instance, with the help of Agilent E4491A impedance analyzer, Park et al. [33] measured the series resistance R_s of the varactor MA46H202 (from MA-COM) at frequencies from 600 to 1600 MHz. Alternatively, the following methods can be used.

A. Extraction Based on the Equation

Although the tuning varactor business develops the hait of specifying Q at 50 MHz, the users may extrapolate Q to a different frequency simply by using the reciprocal relationship given in (1.3) [27]. Nevertheless, the Q value calculated in this way couldn't be used for a precise EM simulation due to the inaccuracies of this equation.

$$Q(f_1) = Q(f_2)\frac{f_2}{f_1} \qquad (1.3)$$

B. Extraction Based on the SPICE Model

In order to achieve more accurate quality factor Q, a more detailed equivalent circuit model of varactor diode is needed, such as SPICE model that generally can be obtained from the associated manufactures or online resource. The technique used should be based on the varactor model extraction procedure from *S*-parameter data. Taking the varactor diode SMV2019-040LF [28] as an example, the SPICE model with the dc bias circuit is provided in Fig. 1.8. Obviously, the SPICE model uses more parameters than the counterpart of Fig. 1.7 to describe the electrical characterstics of the varacotr diode, as well as its package effects. The related *Q*-extraction process can start with achieving the *S*-parameters (i.e s2p files) of the diode at different voltages by using microwave office or another circuit simulator, and then apply the obtained *S*-parameters to define a varactor diode in the final EM simulations.

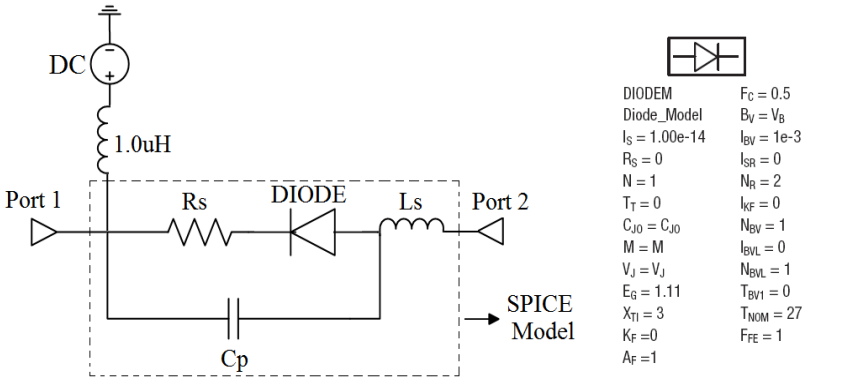

CJO (pF)	VJ (V)	M	CP (pF)	RS (Ω)	LS (nH)
2.05	3.3	1.42	0.075	4.8	0.45

Figure 1.8: SPICE model of varactor diode SMV2019-040LF with a dc bias circuit.

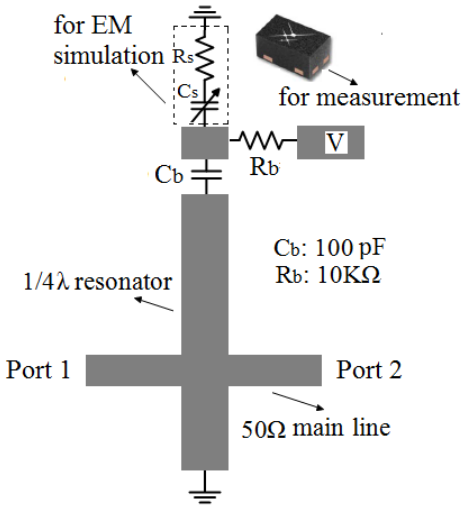

Figure 1.9: Test circuit for measuring the equivalent circuit parameters of a varactor.

C. Extraction Based on Measurements.

Another approach for *Q* extraction is using a simple varactor-loaded resontor, as shown in Fig. 1.9, to meausre the associated series resistance R_s of the varactor used. Specifically, there are three steps required. Firstly, we should set up a proper EM test model such as the one given in Fig. 1.9, enabling to cover the desired operating frequencies. Secondly, do the expertiment using the chosen pratical diode and get the measured results. Finally, adjust the values of C_s and R_s during the EM simulating in turn, to make the simulated responses approximate to the measured ones. In this manner, the simulated and measured responses of varactor SMV2019-040LF

operating at a bias voltage of 6V are illustrated in Fig. 1.10, where the results obtained by the SPICE model is also given for comparision. The extracted values of C_s and R_s are obtained as 0.54 pF and 2.4 Ω, respectively. As can be seen, the extracted value of C_s is very close to 0.51 pF as indicated in the datasheet [28]. Furthermore, it is found that the responses using the SPICE model almost agree well with the measurements except a slight difference, which results from inaccuracy of the SPICE model.

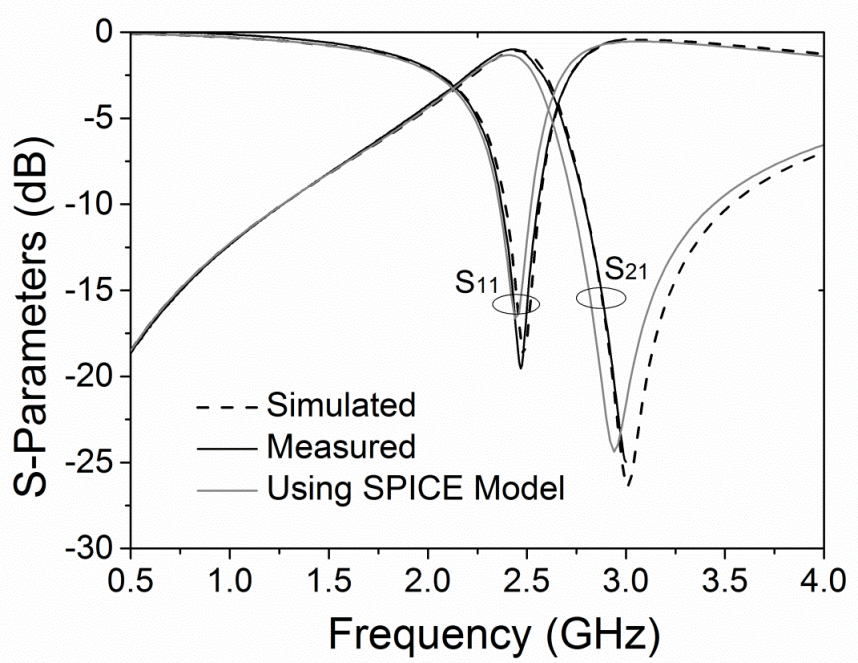

Figure 1.10: Illustrative responses of varactor diode SMV2019-040LF operating at voltage of 6V for comparison.

1.3.3 Literautre Survey of varactor-tuned microwave filters

In past decades, extensive research has been done on the design of varactor-tuned microwave filters and includes the work presented in [29]-[53], where various degrees of tunability have been quotaed for various structures. It is notable that most of these works have concentrated on the developments of varactor-tuned bandpass filters [29]-[45] and bandstop filters [46]-[51], particularly on the former. While only a few varactor-tuned microwave lowpass filter and highpass filter designs have been reported thus far [52]-[53]. An obvious reason for this is the lack of viable monolithic tunable inductor solution that increases the difficulity in realizing a good tunable performance.

In general, research in tunable bandpass/banstop filters has been mainly focused on the realizaiton of frequency tuning as well as bandwidth controlling. Among the different physical structures, varactor-loaded $\lambda/4$ and $\lambda/2$ resontors as well as dual-mode resonators, such as the ones shown in Fig. 1.11, are broadly used due to their compactness and simple tuning schemes. For instance, based on $\lambda/4$ resonator, Hunter and Rhodes [29] reported a varactor-tuned two-pole stripline combline filter at 3500-4600 MHz with a 3-5 dB insertion loss. In order to obtain constant absolute bandwidth, the resontor having 53° electrical length at the mid-band frequency is required. This method can also be used in varactor-tuned comline filter using stepped-impedance microstrip lines [30]. Sanchez et al. [31] proposed a tunable combline filter operating at 450-850 MHz. By inserting variable coupling reducers between resonators to control the coupling, the bandwidth tuning is accomplished. Wang et al. [32] proposed a varactor-tuned microstrip combline bandpass filter that is loaded with lumped series resonators instead of the short-circuited end of combline. Based on this concept, the slope parameter of the proposed resontor can be controlled to result in a constant absolute bandwidth achieved over a wide tuning range. Park et al. [33] demonstrated varactor-diode two-pole tunable filters with three different predefined bandwidth characteristics (i.e. constant fractional bandwidth, constant absolute bandwidth and decreasing fractional bandwidth) at 850-1400 MHz by utilizing an independent electric and magnetic coupling filter topology. On the other hand, based on $\lambda/2$ resontor, Zhang et al. proposed varactor-tuned two-pole bandpass and bandstop filter in [34] and [48], respectively. Both of them obtain constant absolute bandwidth by using a mixed electric and magnetic coupling scheme. Similarly, the mixed coupling in corrugated coupled lines is also utilized to design a two-pole varactor-tuned filter with a frequency coverage of 1.32-1.89 GHz [35]. Furthermore, as recently presented works in [36]-[38], different types of varactor-tuned dual-mode resonators, such as dual-mode open loop resontor [36], dual-mode ring resonator [37] and dual-mode triangular-patch resonator [38], are also popular to realize flexible adjustments of centre frequency and bandwidth. This is because such dual-mode resonators have uncoupled degenerate modes that leads to

the tuning elements can be positioned in a way to affect each mode individually. Besides the above-referred distributed filters, varactor-tuned lumped bandpass/bandstop filters are studied in [39], [46]. The main advantage of these tunable lumped *LC* filters is offering the smallest size compared to other alternative implementations in the VHF or UHF range.

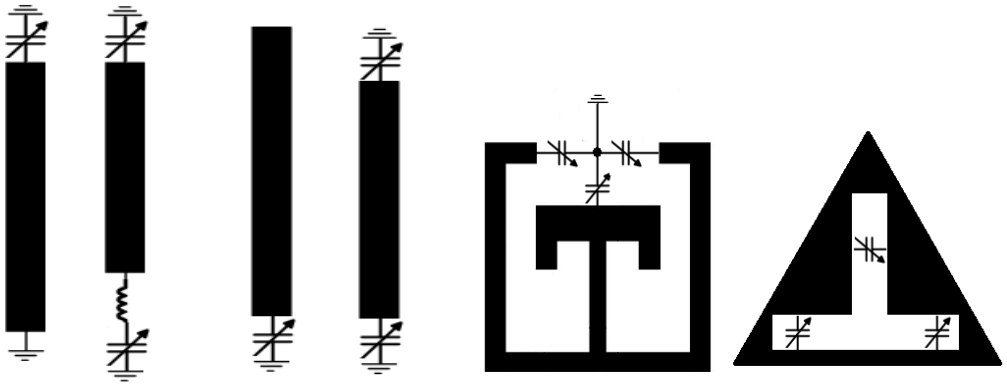

(a) (b) (c)

Figure 1.11: Some of resonators commonly used in tunable filters. (a) Varactor-loaded $\lambda/4$ resontors [32]. (b) Varactor-loaded $\lambda/2$ resontors [34]. (c) Varactor-loaded dual-mode resontors [36][38].

More recently, tunable filter selectivity and linearity have also become points of interest. This is because from a system–level prospective, the selectivity and nonlinear characteristics of tunable filters have a severe impact on the RF front-end performance since the tunable filter is placed between the antenna and the low-noise amplifier (LNA). Genearlly speaking, in order to achieve high selectivity tunable designs, most solutions have been proposed by either increasing the order of the filter or introduce the transmission zeros at stopbands. For instance, Chiou et.al [40][41] presented two types of three-pole varactor-tuned combline filter with an extra tranmission zero created at lower stopband. In [40], the present tunable filter mainly inserted an external close-loop circuit to produce a tunable zero at low band. In [41], the enhanced roll-off reponse of the tunable filter was realized by adding extra diodes between non-adjacent resonators. Different from these designs, Chiou et al. recently

reported another four-pole elliptic tunable combline filter with two controllable transmission zeros [42]. These zeros mostly results from the fourth order employed and adequate cross-coupling achieved in the circuit. Regarding the linearity characteristics, fundamentally, for a given input power, the amount of distortion generated from a varactor diode is proportional to RF signal voltage across it [43]-[45]. In this context, back-to-back varactor diode is frequently used in tunable filters to improve linearity. Like the varactor-tuned second-order filter presented in [44], by using back-to-back configuration wit a high-value biasing resistor, the measured third-order intermodulation intercept point (IIP3) was improved to 22-41 dBm that is 13-15 dB better than the single-diode design. In addition, Athukorala et al. [45] proposed compact second-order varactor-tuned dual-mode filters with high lineariy IIP3>43 dBm by using different approach, which introduce a fixed capactiance and make it be in series with the varactor diode. In this manner, the series conection of two capacitances effectively acts as a capacitive potential divider to reduce overall RF lotage across the varactor diode thus gives better linearity for the same input power.

1.4 Objectives and Organisation

Following the motivation and literature survery demonstrated above, the primary objective of this dissertatation is to introduce a power efficient tunable solution for modern wireless communication systems. This task is divided into four research topics as given below. Accordingly, the tunable part (Part I) of this dissertation is organized into four chapters.

- *Topic 1: Developing a new topology for tunable lowpass filter design with high performance of compact size, high selectivity and wide tuning range.*

In Chapter 2, a compact continously varactor-tuned lowpass filter using microstrip stepped-impedance hairpin resonators is presented. A detailed theoretical analysis for the performance tuning mechanism is illustrated by using equivalent circuit model. The experiment results are provided to validate the proposed filter. From the measured results, it is found that five varactor diodes with two applied bias

voltages used in the proposed design work well as a flexible tuning network, which not only provide a wide frequency tuning range of 46% from 1.60 to 2.94 GHz, but also offer an ability of selectivity controlling by using different applied voltages. Furthermore, the proposed filter using multiple cascaded hairpin resonators provides a very sharp cutoff frequency response with low insertion loss in each state, together with a wide and deep stopband with a rejection level greater than 20 dB. The measured IIP3 of 27-33 dBm shows a high linearity is also achieved in this proposed design.

- *Topic 2: Developing a new topology for tunable highpass filter design with high performance of compact size, high selectivity and wide tuning range.*

Chapter 3 presents a novel circuit topology of a tunable highpass filter with a quasi-elliptic function response. A detailed theoretical analysis for the performance operating mechanism is demonstrated. With the assistance of mutually inductive coupling creation, a pair of tunable transmission zeros is synthesized at the lower passband edges and significantly improves the filter selectivity. Experiments are carried out by using liquid crystal polymer (LCP) bonded multilayer printed circuit board (PCB) technology to validate the design. It is found that the implemented filter achieves a wide continuous tuning range covering from 1030-2150 MHz with low insertion loss, and which indeed are limited by the varactor diodes used. Also, it is illustrated that two measured transmission zeros are properly controlled at each tuning stage, which not only offers a sharp cutoff frequency response with a rejection level greater than 22 dB, but also provides an approximately unchanged response shape.

- *Topic 3: Developing a new topology for tunable bandpass filter design with high performance of high selectivity and great tunability on centre frequency and bandwidth.*

In Chapter 4, two novel types of tunable bandpass filter with different passband characterstics are presented. The first type is composed of varactor-loaded parallel-coupled lines and short-circuited stubs, which allows for the lower passband edge and two transmission zeros around the lower passband skirt to be reconfigured

separately within the tuning range from 1160 to 2019 MHz, while the corresponding upper ones maintain fixed. The second type of tunable bandpass filter is built by cascading the first type of tunable bandpass and another tunable lowpass filter, which results in a great flexibility to tune both centre frequency and passband bandwidth simultaneously and simply. The designed prototype tunable filters are implemented using LCP bonded multilayer PCB technology. The measured results demonstrate very promising performance in terms of wide tunability and high selectivity achieved in both of designs.

- *Topic 4: Investigating a solution to overcome the performance degradation arising from the low Q of varactor-tuned narrowband bandpass filter, leading to improvements on passband flatness and selectivity.*

Chapter 5 mainly demonstrates a novel three-pole tunable microstrip combline filter with improved performance, namely passband flatness and selectivity, at the expense of other filter parameters (such as absolute insertion loss in the passband) that might not be critical in some applications. In order to achieve a flatter passband and higher selectivity, the proposed approach mainly utilizes the concept of detuning the resonators by loading lumped elements, together with a nonuniform *Q* distribution considered in the filter. A detailed theoretical analysis for the performance enhancement mechanism is illustrated by using an equivalent circuit model, and the design procedure is introduced in this chapter. In addition, a general selectivity is defined to evaluate the selectivity enhancement of the proposed tunable filter. Finally, the proposed tunable combine filter have been designed, fabricated and tested to demonstrate different levels of performance improvements over the entire tuning range.

Reference

[1] J.-S. Hong, "Reconfigurable planar filters", *IEEE Microwave Mag.*, pp. 73-83, Oct. 2009.

[2] H. Tilmans, "RF-MEMS: An enabling technology or reconfigurable radio front-ends", *NanoWal-Microsystems-Event*, Mar. 2009.

[3] K. Konanur, "CMOS RF transceiver chip tackles multiband 3.5G radio system," *RF Design*, pp. 22-30, Apr. 2006.

[4] X. G. Liu, "High-Q MEMS tunable resonators and filters for reconfigurable radio frequency front-ends," Doctor of Philosophy thesis, The Purdue University, 2010.

[5] Ian F. Akyidiz, W.-Y. Lee, M. C. Vuran and S. Mohanty "NeXt generation/dynamic spectrum access/cognitive radio wireless networks: A survey," *Computers Networks*, vol. 50, no. 13, pp. 2127-2159, May. 2006.

[6] F. Svelto, M. B. Vahidfar and M. Brandolini, "Reconfigurable Si RF Receiver Front-Ends for Multistandard Radios," *Proc. 1st Euro. Wireless Tech. Conf., Amsterdam, the Netherlands*, pp. 33-36, Oct 2008.

[7] T.-Y. Yun and K. Chang, "Piezoelectric-Transducer-Controlled Tunable Microwave Circuits," *IEEE Trans. Microwave Theory Tech.*, Vol. 50, No. 5, pp. 1303-1310, 2002.

[8] F. Huang and R.R. Mansour, "Tunable Compact Dielectric Resonator Filters," *Proceedings of the 42st European Microwave Conference*, pp 559-562, Oct. 2009.

[9] E. J. Naglich, J. Lee, D. Peroulis and W. J. Chappell., "Extended passband bandstop filter cascade with continuous 0.856.6-GHz coverage," *IEEE Trans. Microw. Theory Techn.*, vol. 60, no. 1, pp. 21–30, Jan. 2012.

[10] R. F. Fjerstad, "Some design considerations and realizations of iris-coupled YIG-tuned filters in the 12-40 ghz region," *IEEE Trans. Microwave Theory Tech.*, vol. 18, pp. 205-212, Apr. 1970.

[11] C. S. Tsai and G. Qiu, "Wideband microwave filters using ferromagnetic resonance tuning in flip-chip YIG-GaAs layer structures," *IEEE Trans. Magn.*, vol. 45, no. 2, pp. 656–660, Feb. 2009.

[12] A. Tombak, J. P. Maria, F. T. Ayguavives, J. Zhang, G. T. Stauf, A. Kingon and A. Mortazawi., "Voltage-controlled RF filters employing thin-film bariumstrontium- titanate tunable capacitors," *IEEE Trans. Microwave Theory & Tech.*, vol. 51, no. 2, pp. 462–467, Feb. 2003.

[13] Y.-H. Chun, J. S. Hong, P. Bao, T. J. Jackson and M. J. Lancaster., "BST-Varactor Tunable Dual-Mode Filter Using Variable ZC Transmission Line," *IEEE Microw. Wireless Compon. Lett*., vol. 18, no. 3, pp.167-169, Sep. 2008.

[14] J. Nath, D. Ghosh, J. P. Maria, A.I. Kingon, W. Fathelbab, P. D. Franzon, and M. B. Steer, "An electronically tunable microstrip bandpass filter using thin-film barium-strontium-titanate (BST) varactors," *IEEE Trans. Microw. Theory Tech*., vol. 53, no. 9, pp. 2707–2712, Sep. 2005.

[15] A. Abbaspour-Tamijani, L. Dussopt, and G. M. Rebeiz, "Miniature and tunable filters using MEMS capacitors", *IEEE Transactions on Microwave Theory and Techniques,* vol. 51, no. 7, pp. 1878-1885, July. 2003.

[16] L. Dussopt and G.M. Rebeiz, "Intermodulation distortion and power handling in RF MEMS switches, varators, and tunable filters," *IEEE Trans. Microwave Theory & Tech*., vol. 51, no. 4, pp. 1247–1256, Apr. 2003.

[17] S. Park, M. A. El-Tanani, I. Reines, and G. M. Rebeiz, "Low-loss 4-6 GHz tunable filter with 3-bit high-Q orthogonal bias RF-MEMS capacitance network," *IEEE Trans. Microwave Theory & Tech*., vol. 56, no. 10, pp. 2348–2388, Oct. 2008.

[18] M. El-Tanani, "High Linearity 1.5-2.5 GHz RF-MEMS and Varactor Diod Based Tunable Filters for Wireless Applications," Doctor of Philosophy thesis, The University of California, San Diego, 2009.

[19] Varactor / varicap diode, www.radio-electronics.com.

[20] J.-S. Hong, "Microstrip Filters for RF/Microwave Application," *Second Edition*, *Wiley*, 2010.

[21] P. W. Wong and I. C. Hunter, "Electronically tunable filters," *IEEE Microw. Mag*., vol. 10, no. 6, pp. 46–54, Oct. 2009.

[22] Varactor / varicap diode, http://en.wikipedia.org/wiki/Varicap.

[23] "Skyworks: SMV2019—SMV2023: Silicon Hyperabrupt Junction Varactors, Packaged and Bondable Planar Chips data sheet," Skyworks Solutions, Sunnyvale, CA, 2008.

[24] "M/A-COM: MA46580 & MA46585, data sheet," M/A-COM Lowell, 2006.

[25] "Skyworks: DMK2790 Series and DMK2308 Series GaAs Flip-Chip Schottky Diodes: Singles and Antiparallel Pairs, data sheet," Skyworks Solutions, Sunnyvale, CA, 2013.

[26] Varactor diode specifications, www.radio-electronics.com.

[27]"Skyworks: Varactor Diodes Application Note," Skyworks Solutions, Sunnyvale, CA, 2008.

[28]"Skyworks: SMV2019-040LF: Surface Mount, 0402 Silicon Hyperabrupt Tuning Varactor Diode data sheet," Skyworks Solutions, Sunnyvale, CA, 2008.

[29]I. C. Hunter and J. D. Rhodes, "Electronically tunable microwave bandpass filters," *IEEE Trans. Microwave Theory & Tech*., vol. 30, no. 9, pp. 1354–1360, Sep. 1982.

[30]B. W. Kim and S. W. Yun, "Varactor-tuned combline bandpass filter using step-impedance microstrip lines," *IEEE Trans. Microw. Theory Tech*., vol. 52, no. 4, pp. 1279–1283, Apr. 2004.

[31]M. Sanchez-Rendo, R. Gomez-Garcia, J. I. Alonso, and C. Briso-Rodriguez, "Tunable combline filter with continuous control of center frequency and bandwidth," *IEEE Trans. Microw. Theory Tech*., vol. 53, no. 1, pp. 191–199, Jan. 2005.

[32]X. G. Wang, Y. H. Cho, and S. W. Yun, "A tunable combline bandpass filter loaded with series resonator," *IEEE Trans. Microw. Theory Tech*., vol. 60, no. 6, pp. 1569–1576, Jun. 2012.

[33]S. Park and G. M. Rebeiz, "Low-loss two-pole tunable filters with three different predefined bandwidth characteristics," *IEEE Trans. Microwave Theory & Tech*., vol. 56, no. 5, pp. 1137–1148, May 2008.

[34]X. Y. Zhang, Q. Xue, C.H. Chan, and B.-J. Hu, "Low-Loss Frequency-Agile Bandpass Filters With Controllable Bandwidth and Suppressed Second Harmonic," *IEEE Trans. Microw. Theory Tech.*, vol. 58, no. 6, pp. 1557–1564, Jun. 2010.

[35]M. A. El-Tanani and G. M. Rebeiz, "Corrugated microstrip coupled lines for constant absolute bandwidth tunable filters," *IEEE Trans. Microw. Theory Tech*., vol. 58, no. 4, pp. 956–963, Apr. 2010.

[36]W. Tang and J.-S. Hong, "Varactor-tuned dual-mode bandpass filters," *IEEE Trans. Microw. Theory Tech*., vol. 58, no. 8, pp. 2213-2219, Aug. 2010.

[37]H.-J. Tsai, N.-W. Chen and S.-K. Jeng, "Center frequency and bandwidth controllable microstrip bandpass filter design using loop-shaped dual-mode resontor," *IEEE Trans. Microw. Theory Tech*., vol. 61, no.10, pp. 3590-3600, Oct. 2013.

[38]A. L. C. Serrano, F. S. Correra, T.-P. Vuong, and P. Ferrari, "Synthesis methodology applied to a tunable patch filter with independent frequency and bandwidth control," *IEEE Trans. Microw. Theory Tech*., vol. 60, no.3, pp. 484-493,

Mar. 2012.

[39] Q. Y. Xiang, Q. Y. Feng, X. G. Huang, and D. H. Jia, "Electrical tunable microstrip LC bandpass filters with constant bandwidth," *IEEE Trans. Microw. Theory Tech.*, vol. 61, no. 3, pp. 1124–1130, Mar. 2013.

[40] Y.-C. Chiou and G. M. Reibez, "A tunable three-pole 1.5-2.2-GHz bandpass filter with bandwidth and transmission zero control," *IEEE Trans. Micro. Theory Tech.*, vol. 59, no. 11, pp. 2872-2878, Nov. 2011.

[41] Y.-C. Chiou and G. M. Rebeiz, "A quasi elliptic function 1.75–2.25 GHz 3-pole bandpass filter with bandwidth control," *IEEE Trans. Microw. Theory Tech.*, vol. 60, no. 2, pp. 244–249, Feb. 2012.

[42] Yi-Chyun Chiou and Gabriel M. Rebeiz," Tunable 1.55–2.1 GHz 4-Pole Elliptic Bandpass Filter with Bandwidth Control and >50 dB Rejection for Wireless Systems," *IEEE Trans. Microw. Theory Tech.*, vol. 61, no. 1, pp. 117-124, Jan. 2013.

[43] B. E. Carey-Smith and P. A.Warr, "Distortion mechanisms in varactor diode-tuned microwave filters," *IEEE Trans. Microw. Theory Tech.*, vol. 54, no. 9, pp. 3492–3500, Sep. 2006.

[44] M. Tanani and G. M. Rebeiz, "A two-pole two-zero tunable filter with improved linearity," *IEEE Trans. Microw. Theory Tech.*, vol. 57, no. 4, pp. 830–839, Apr. 2009.

[45] L. Athukorola and D. Budimir, "Compact second-order highly linear varactor-tuned dual-mode filters with constant bandwidth," *IEEE Trans. Microw. Theory Tech.*, vol. 59, no. 9, pp. 2214–2220, Sep. 2011.

[46] Yu-Chin Ou and Gabriel M. Rebeiz, "Lumped-Element Fully Tunable Bandstop Filter for Cognitive Radio Application," *IEEE Trans. Microw. Theory Tech.*, vol.59, no.10, pp. 2461–2468, Oct. 2011.

[47] I. C. Hunter and J. D. Rhodes, "Electronically tunable microwave bandstop filters," *IEEE Trans. Microw. Theory Tech.*, vol. MTT-30, no. 9, pp. 1361-1367, Sep. 1982.

[48] X. Y. Zhang, C. H. Chan, Q. Xue, and B.-J. Hu, "RF tunable bandstop filters with constant bandwidth on a doublet configuration," *IEEE Trans. Ind. Electron.*, vol. 59, no. 2, pp. 1257–1265, Feb. 2012.

[49] X. H. Wang, B.-Z. Wang, H. L. Zhang and K. J. Chen, "A tunable bandstop resonator based on a compact slotted ground structure," *IEEE Trans. Microw. Theory Tech.*, vol. 55, no. 9, pp. 1912-1918, Sep. 2007.

[50] Z. P. Wang, J. Kelly and P. S. Hall, “Reconfigurable bandstop filter with wide tuning range,” *Electron. Letters*, vol. 46, no. 11, pp. 1188-1195, May. 2010.

[51] A. C. Guyette, “Design of fixed- and varactor-tuned bandstop filters with spurious suppression,” *in Eur. Microw. Conf.*, 2010, pp. 288–291.

[52] C.-C. Huang, N.-W. Chen, H.-J. Tsai and J.-Y. Chen, “A Coplanar Waveguide Bandwidth-Tunable Lowpass Filter with Broadband Rejection,” *IEEE Trans. Microw. Wireless Compon*. vol. 23, no.3, pp. 134-136, Mar. 2013.

[53] A. Abbosh, "Compact tunable low-pass filter using variable mode impedance of coupled structure," *Microwaves, Antennas & Propagation, IET*, vol. 6, pp. 1306-1310, 2012.

[54] B. E. Carey-Smith and P. A. Warr, “Distortion mechanisms in varactor diode-tuned microwave filters,” *IEEE Trans. Microw. Theory Tech*., vol. 54, no. 9, pp. 3492–3500, Sep. 2006.

CHAPTER 2

Compact Continuously Tunable Microstrip Lowpass Filter

2.1 Introduction

A lowpass filter, located in the communication system or between the transceiver and the baseband, is widely used to remove undesired harmonics or spurious of mixing products in the nonlinear portion of RF front-end and baseband circuits [1]-[5]. As one of the key components for emerging reconfigurable RF front-end architectures, tunable lowpass filters having wide tuning range and good stopband performance are in increasing demand to suppress the unwanted mixed frequency elements and leakages of RF. Furthermore, tunable lowpass filters can offer a possibility to obtain tunable bandpass/bandstop performance when cascading tunable highpass or bandpass/bandstop filters, which would be very attractive in centre frequency tuning as well as bandwidth controlling. However, in the open literature, there are very few works on tunable lowpass filters [6]-[14], particularly on varactor-based tunable lowpass filters.

In this chapter, a new technique for designing a continuously tunable microstrip lowpass filter with merits of compact size, wide tuning range, high selectivity and broad stopband is fully presented. Specifically, the chapter is arranged as follows: in Section 2.2, different types of tunable lowpass filter topologies from unit cell to multiple cells are proposed and thoroughly analyzed. Design equations, curves and guidelines are provided to reveal the performance controlling mechanisms. Subsequently, Section 2.3 mainly presents a microstrip implementation of varactor-tuned lowpass filter by using multiple cascaded stepped-impedance hairpin resonators. Additionally, the approach to synthesize the associated physical dimensions is described. In Section 2.4, experimental results are demonstrated to verify the proposed concept. Moreover, one method to further extend stopband bandwidth of the proposed filter for some stringent applications is described in Section 2.5. Finally, this chapter is summarized in Section 2.6 with performance comparison between this work and the other reported works.

2.2 Different Tunable Lowpass Filter Topologies

2.2.1 Tuning mechanisms of the proposed unit-cell models

It is well known that for an ideal tunable filter design, it would require not only variable capacitors, i.e. varactors, but also variable inductors for good matching within the tuning range. However, tunable filter designs have often relied on the varactor as the sole tuning element due to the lack of viable monolithic tunable inductor solution, which severely limits their tuning ranges and tunable performance.

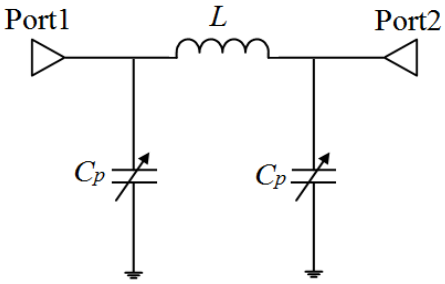

(a)

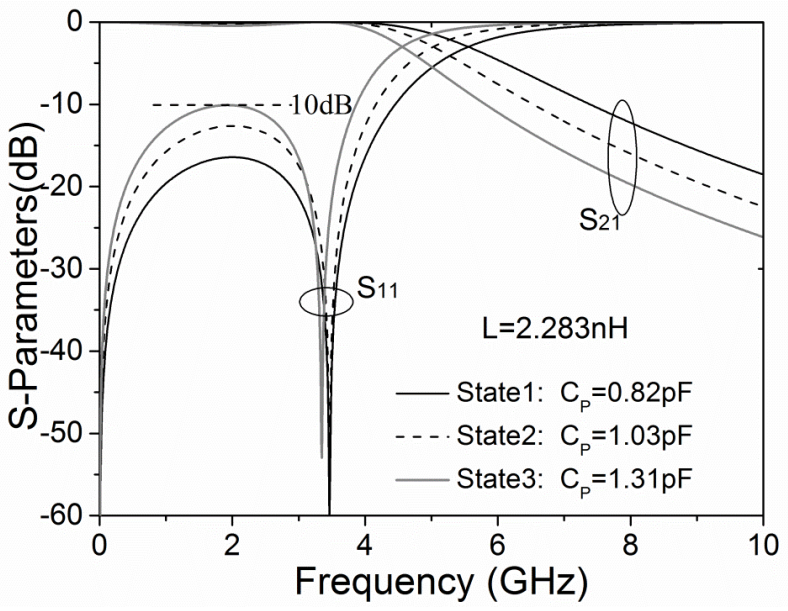

(b)

Figure 2.1: (a). The conventional Chebyshev tunable topology used in [11]. (b). Tunable responses obtained by only tuning capacitance C_p.

As illustrated in Fig. 2.1, for a conventional Chebyshev tunable LPF circuit model

adopted in [11], without tuning the value of inductance L, the 3 dB cutoff frequency would only be tuned from 5.56 GHz down to 4.56 GHz (under the requirement $S_{11} \leq -10\text{dB}$) by increasing the capacitances C_p. Additionally, such filter suffers from a poor selectivity within the tuning range that will limit its use in modern communication systems.

In order to improve tunable performance, Fig. 2.2 proposed two novel types of tunable lowpass filter topologies, namely proposed Unit I and proposed Unit II. Unlike the conventional Chebyshev filter discussed above, the proposed Unit I of Fig. 2.2 (a) not only can generate a finite-frequency transmission zero with a better selectivity, but also can achieve a wider tuning range when tuning two capacitances, i.e. C_p and C_g. These promising features are demonstrated with the results in Fig. 2.3. Fig. 2.3 shows the responses achieved by individually tuning the elements C_p and C_g, as compared with the initial state with C_p = 0.75 pF and C_g = 0.1 pF for the 3 dB cutoff frequency of 5.35 GHz. As can be seen, when the capacitance C_g is tuned from original 0.1 pF to 0.36 pF while keeping C_p unchanged (i.e. 0.75 pF), the cutoff frequency and the transmission zero are shifted down, which leads to a better selectivity at the cost of the rejection level. Note that in this case, the tuning does not degrade the return loss. In contrast to the case of tuning C_g, tuning the capacitance C_p, for example from 0.75 to 1.53 pF with a constant C_g of 0.1 pF to shift the 3 dB cutoff frequency to the same location, as shown in Fig. 2.3, the out-of-band rejection is better but the in-band return loss becomes poorer. However, if we allow adjusting the capacitances C_p and C_g jointly, they can compensate the shortcomings of each other to achieve a wider matching range, which will be later illustrated by some detailed comparisons. In fact, herein this tuning mechanism can be explained as follows. For the proposed model Unit I, the equivalent inductance of parallel section can be expressed as:

$$L_{eq} = \frac{L}{1 - \omega^2 C_g L} \qquad (2.1)$$

thus in a certain frequency range, tuning the capactiance C_g will vary the equivalent inductance L_{eq}, which avoids the mismatching occurred in the conventional tuning

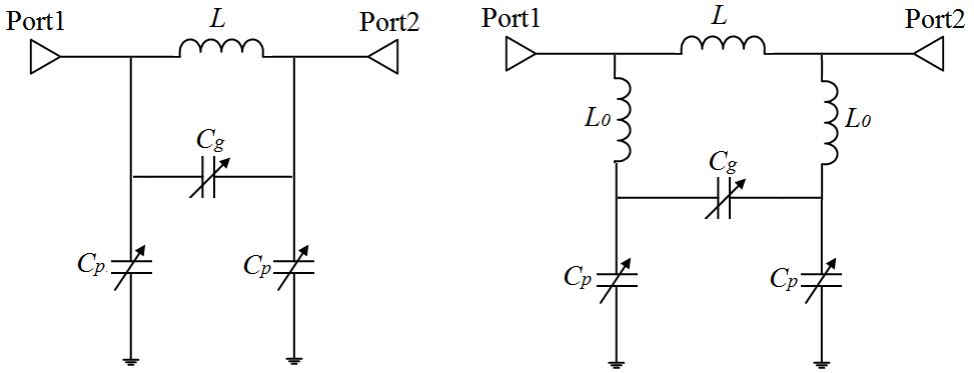

(a) (b)

Figure 2.2: Two types of proposed tunable LPF unit cells. (a) Proposed Unit I. (b) Proposed Unit II.

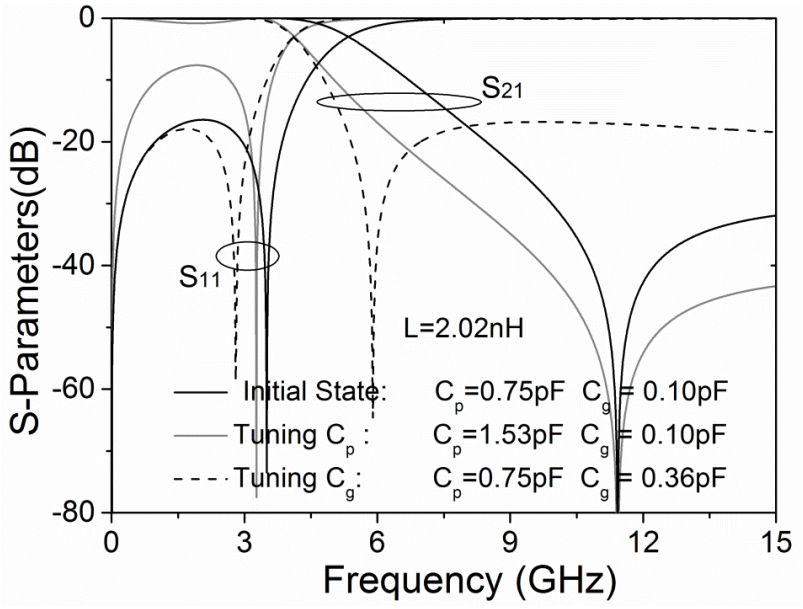

Figure 2.3: Tunable responses obtained by individually tuning the elements C_p and C_g in the proposed Unit I.

topology (Fig. 2.1(a)). For instance, Fig. 2.4 shows the extracted equivalent inductance L_{eq} versus capactiances C_g at the different tunable cutoff frequencies. It is obvious that by increasing the capactiance C_g, the equivalent inductance L_{eq} is increased while the cutoff frequency decreases, which is a desired characteristic for tunable filter design. Indeed, the similar filter properties can also be achieved in the circuit of proposed Unit II, which is comfirmed by the results indicated in Fig. 2.5. In addition, it is apparent to see the proposed Unit II has two transmission zeros

generated in the stopband. The first zero is close to the passband leading to improved selectivity, whereas the second one benefits the LPF in the upper stopband for wide- and deep-stopband rejection. The locations of these zeros will be further discussed in the next section.

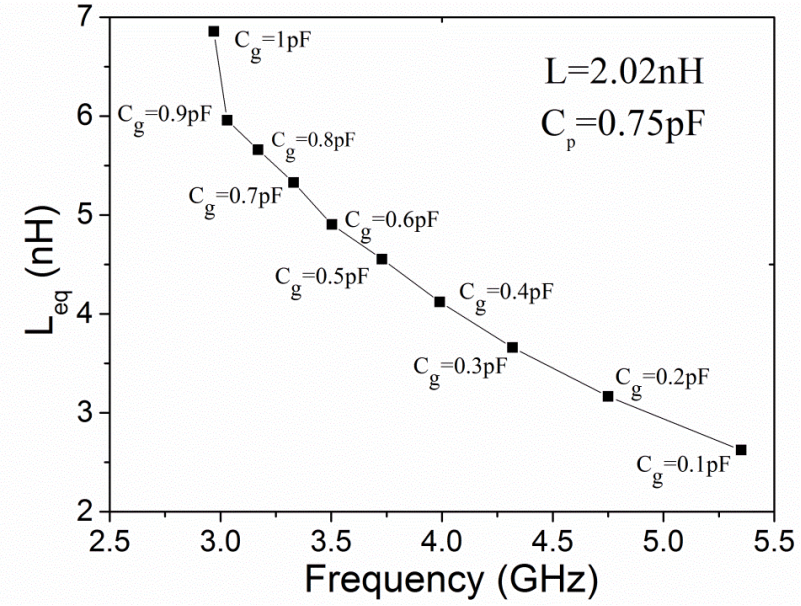

Figure 2.4: Extracted equivalent inductance L_{eq} versus capactiances C_g at the different tunable cutoff frequencies.

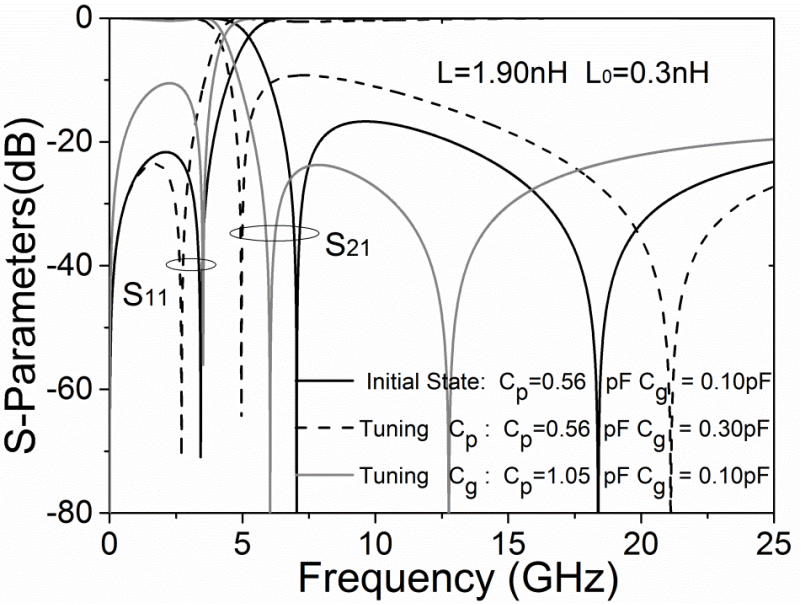

Figure 2.5: Tunable responses obtained by individually tuning the elements C_p and C_g in the proposed Unit II.

2.2.2 Analytical design equations for proposed unit-cell models

A. Synthesised L-C Element Values of Proposed Unit I

The proposed Unit I in Fig. 2.2 (a) is a typical elliptic-function lowpass prototype filter [15]. Hence, the corresponding *L*-*C* elements values can be easily calculated as:

$$L = \left(\frac{Z_0 \Omega_c g_2}{2\pi f_c}\right) \qquad (2.1)$$

$$C_g = \left(\frac{g_2{}'}{Z_0}\frac{\Omega_c}{2\pi f_c}\right) \qquad (2.2)$$

$$C_p = \left(\frac{g_1}{Z_0}\frac{\Omega_c}{2\pi f_c}\right) \qquad (2.3)$$

where $\Omega_c = 1.0\, rad/s$, $Z_0 = 50\Omega$, and g_i is the element value for elliptic-function lowpass prototype. Herein, it should be highlighted that f_c is the equal-ripple cutoff frequency, while in order to obtain a desired 3 dB cutoff frequency, the value of f_c should be chosen smaller than the specification.

Regarding the finite-frequency transmission zero produced in proposed Unit I, it comes from the series branch of parallel-resonant circuit *L* and C_g, and the location is actually prescribed to be at certain frequency as:

$$f_z = \frac{1}{2\pi\sqrt{LC_g}} \qquad (2.4)$$

As an example, let us consider a design with desired 3dB cutoff frequency of 5.35 GHz (i.e. the initial state illustrated in Fig. 2.3). According to the principle demonstrated above, f_c is chosen as 4 GHz (smaller than 5.35 GHz) for the calculation. With given $g_0 = g_4 = 1$, $g_1 = g_3 = 0.947$, $g_2 = 1.0173$ and $g_2{}' = 0.1205$, the calculated values of lumped elements are demonstrated in Table 2.1 as: *L*=2.023 nH, C_g=0.096 pF and C_p =0.753 pF.

B. Synthesised L-C Element Values of Proposed Unit II

The synthesis of the proposed Unit II is carried out by an optimization process since it is not a traditional lowpass prototype filter. However, the starting values of lumped elements can be determined by

$$L = \left(\frac{Z_0 \Omega_c g_1}{2\pi f_c}\right) \qquad (2.5)$$

$$L_0 = \left(\frac{Z_0 \Omega_c g_2{}'}{2\pi f_c}\right) \qquad (2.6)$$

$$C_p = \left(\frac{g_2}{Z_0}\frac{\Omega_c}{2\pi f_c}\right) \qquad (2.7)$$

where C_g is not considered initially, g_i is the element value of the elliptic filter prototype, f_c is the cutoff frequency, $Z_0 = 50\,\Omega$ and Ω_c=1. For this example, the proposed Unit II is designed to have a 3 dB cutoff frequency of 5.26 GHz at the initial tuning state. By using above equations, the preliminary components values are calculated as: L=1.88 nH, L_0=0.24 nH, C_p=0.80 pF and C_g=0 pF. The corresponding simulated frequency response is plotted in Fig. 2.6. It can be noted that this initial filter design has a 3 dB cutoff frequency around 5.5 GHz that approximates to the desired one of 5.26 GHz. Then the optimization is employed after including C_g in the circuit. As a rule of thumb, it is suggested to mainly adjust the capactiances of C_p and C_g rather than the inductances of L and L_0 to reproduce satisfactory response. Specifically, how to make adjustments can be referred to the impacts of tuning elements C_p and C_g on the filter response, as indicated in Fig. 2.5. In this manner, a set of optimal component values and the associated frequency response are finally given in Table 2.1 and Fig. 2.6, respectively. As can be seen, the main function of C_g is to obtain two split transmission zeros (Tzs). The first one at the near end improves filter skirt selectivity, and the other one at far end helps to extend the stopband to a large extent. These two Tzs can be determined by using odd-even mode analysis as:

$$f_{z1,z2} = \frac{1}{2\pi}\sqrt{\frac{Q_2 \pm \sqrt{{Q_2}^2 - 8Q_1}}{2Q_1}} \qquad (2.8)$$

where

$$Q_1 = 4{L_0}^2 C_p C_g + 2{L_0}^2 {C_p}^2 \qquad (2.9)$$

$$Q_2 = 4L_0 C_p + 4L_0 C_g + 2LC_g \qquad (2.10)$$

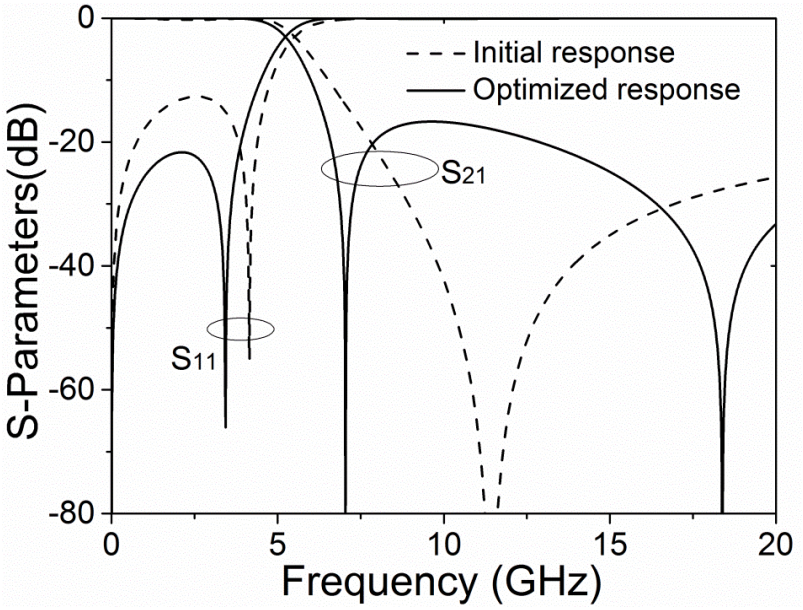

Figure 2.6: Simulated frequency responses of the proposed Unit II with calculated and optimized *L*-*C* elements values.

Table 2.1: Performance Comparison among the Proposed and the Conventional Unit-cell Models

Filter Type	State 1 (Highest-frequency state)						State 2 (Lowest-frequency state)						Tuning range
	L (nH)	L_0 (nH)	C_p (pF)	C_g (pF)	3dB f_c (GHz)	Roll-off rate ξ (dB/GHz)	L (nH)	L_0 (nH)	C_p (pF)	C_g (pF)	3dB f_c (GHz)	Roll-off rate ξ (dB/GHz)	
Conventional	2.28	n/a	0.82	n/a	5.56	2.792	2.28	n/a	1.31	n/a	4.56	3.88	18%
Proposed Unit I	2.02	n/a	0.75	0.1	5.35	5.90	2.02	n/a	1.56	2.2	2.05	74.59	62%
Proposed Unit II	1.90	0.3	0.56	0.1	5.26	16.28	1.90	0.3	1.29	0.96	2.52	80.11	52%

2.2.3 Tunable performance comparison

For comparision, Fig. 2.7 and Table 2.1 summarize the detailed tunable performances of the proposed unit-cell models as well as the conventional one discussed above, where the roll-off rate ξ and the tuning range are defined as:

$$\xi = \frac{\alpha_{\max} - \alpha_{\min}}{f_s - f_c} \ (\mathrm{dB/GHz}) \qquad (2.11)$$

$$\text{Tuning range} = \frac{f_H - f_L}{f_H} \times 100\% \qquad (2.12)$$

where $\alpha_{\max}$ is the 30 dB attenuation point; $\alpha_{\min}$ is the 3 dB attenuation point; f_s is the 30 dB stop-band frequency; f_c is the 3 dB cutoff frequency, as for the definition in (2.12), f_H is the highest cutoff frequency among all the tuning states and f_L is the lowest one.

As can be seen in Fig. 2.7 and Table 2.1, it is clear that within the tuning range, the roll-off rates of the proposed circuits (i.e. Unit I and Unit II) are significantly sharper than the conventional one, which result from the variable capacitances C_g introduced in both circuits. But with the help of an extra inductance L_0, the proposed Unit II can achieve an even sharper cutoff frequency response and one more transmission zero than the circuit Unit I, as illustrated in Fig. 2.7 (a). Furthermore, from the comparision in Table 2.1, it is understood that the roll-off rates of the proposed Unit I and Unit II are getting sharper against the cutoff frequencies decrease, which are mainly controlled by the capacitances C_g. This provides a possibility of selectivity controlling and will be demonstrated in the Section 2.3.

Additionally, observing the Fig. 2.7 and Table 2.1, both the tuning ranges of proposed circuits are significantly improved over the conventional one of 18%. However, due to the added inductance L_0, the proposed Unit II obtains a bit narrower tuning range than Unit I. Nevertheless, the tuning rates of the proposed Unit II is higher than Unit I, which means that the proposed Unit II would only need a smaller capacitances variation for a desirable frequency shifting range.

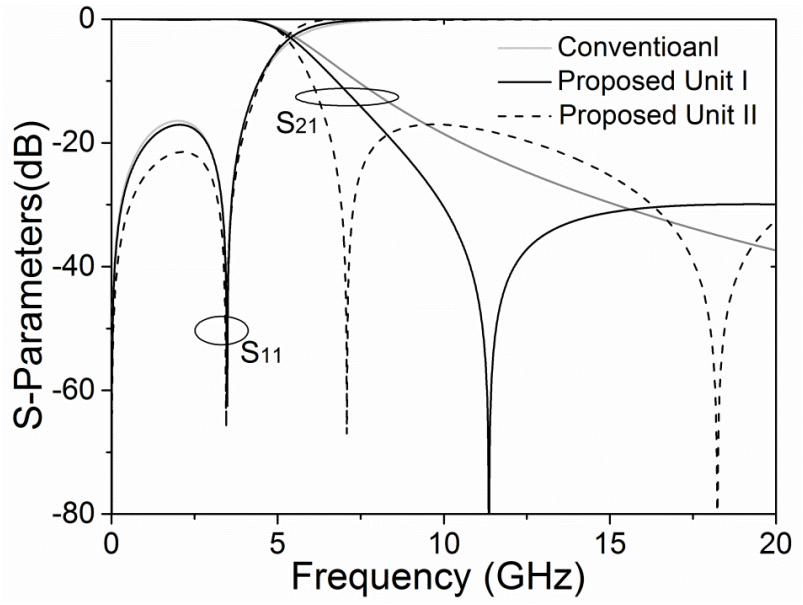

(a)

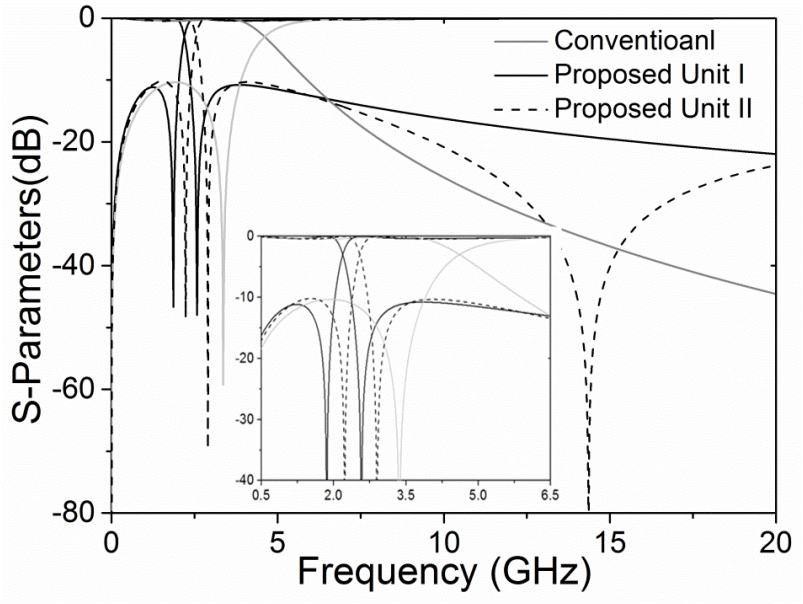

(b)

Figure 2.7: Tunable responses obtained using the proposed and conventional circuit models. (a). Highest-frequency state. (b). Lowest-frequency state.

2.2.4 Cascading cells for higher order filter

Although the above proposed unit-cell LPFs (i.e. Unit I and Unit II) have advantages of wide tuning range and good selectivity with one/two transmission zeros, the rejection depth and the skirt selectivity may not satisfy some applications if deeper rejection or sharper roll-off is required. To this end, a simple and general approach is to cascade the unit-cell LPF topology for a high-order LPF, which can further improve the rejection level and stopband skirt selectivity at the cost of additional insertion loss and circuit size. As a rule of thumb, for the cell cascading, if deep stopband rejection but narrow bandwidth and good skirt selectivity are demanded, it is better to design the different unit cells with the same component parameters to make the stopband bandwidth similar to that of the unit cells while the rejection level and skirt selectivity are enhanced. If the wide stopband is required, it is better to designedly make the different cells with different element values to allocate transmission zeros in a wide stopband frequency range.

For our demonstration, a tunable lowpass filter is designed to meet the following specifications:

3 dB cutoff frequency tuning range: 1.5 to 3.3 GHz

Passband insertion loss: <1.5 dB

Return loss in the passband: >10 dB

Rejection: >20 dB within 50MHz

To this aim, a tunable high order LPF topology as shown in Fig. 2.8 is employed. As can be seen, this topology is constructed with both types of proposed unit cells, that results in the high order LPF can achieve the advantages of each unit cell simultaneously, such as the wider tuning range of proposed Unit I and the higher selectivity of proposed Unit II. For this design, the optimized components values for the highest frequency state f_c=3.3 GHz are given as: L=2.50 nH, L_0=0.50 nH, C_0=0.40 pF, C_p=1.13 pF, C_{g1}=0.37 pF and C_{g2}=0.59 pF. These lumped elements values will be referred for microstrip implementation in the following discussion.

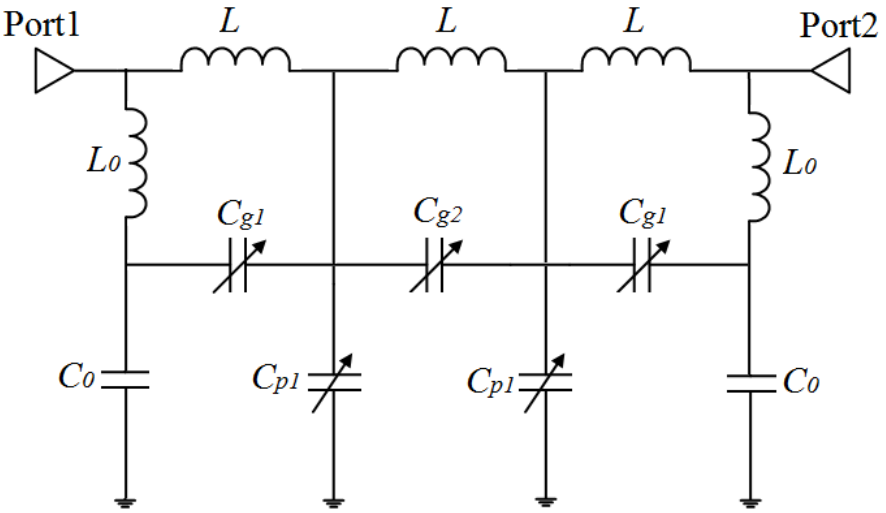

Figure 2.8: Proposed tunable high order LPF topology.

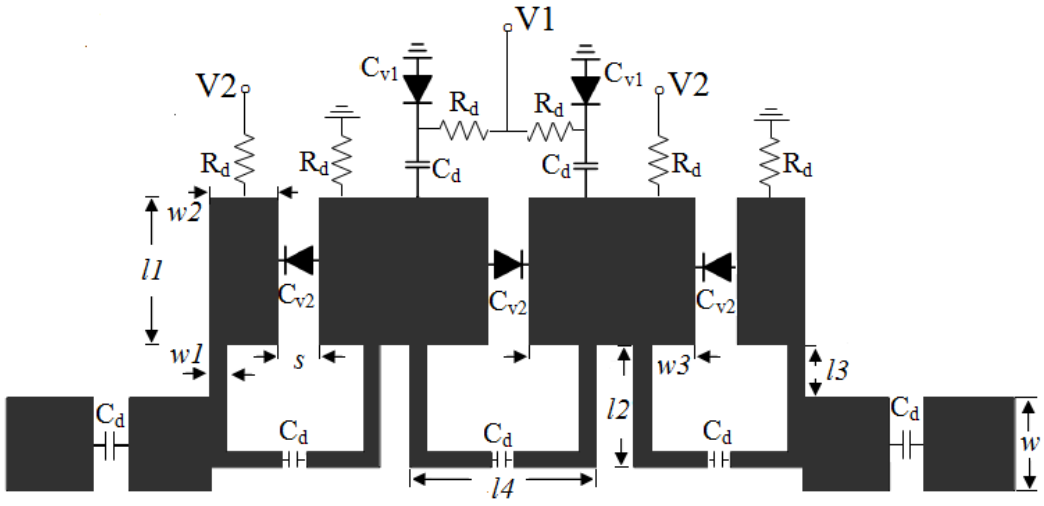

Figure 2.9: The proposed compact varactor-diode-based tunable microstrip lowpass filter.

2.3 Tunable Microstrip Lowpass Filter Implementation and Analysis

Having obtained a suitable lumped-element filter design, the next step is to convert the lumped element circuit to a physically implementable structure and this is a main discussion in this section. For our demonstration, the substrate RT/Duriod 6010 with a dielectric constant $\varepsilon_{\mathrm{r}} = 10.2$ and a thickness $h = 1.27\mathrm{mm}$ is used for the filter design. All the EM simulations are performed using a commercially available tool Sonnet [16].

2.3.1 Physical structure of tunable microstrip lowpass filter

Based on the circuit model demonstrated in Fig. 2.8, Fig. 2.9 presents a mircostrip tunable LPF configuration with biasing scheme, which consists of three multiple cascaded stepped-impedance hairpin resonators with five varactor diodes to provide a wide band matching. A pair of diodes, C_{v1}, is attached at the ends of microstrip rectangular patches, resulting in cutoff frequency tuning. The other three diodes, C_{v2}, located between two adjacent resonators are used for cutoff frequency tuning and for selectivity control. In addition, C_d is the bypass or dc block capacitor. R_d is the dc bias resistor.

Inspecting this structure and the associated circuit model, it can be understood that the inductance L corresponds to the equivalent inductance of the main transmission line. C_0 is mostly associated with the equivalent capacitance of the smaller microstrip rectangular patch. L_0 is related to the short transmission line with the length "*l3*" (see in Fig. 2.9) [1]. The variable capacitances C_{g1}, C_{g2} and C_{p1} are realized by the combined effects of the varactor diodes (C_{v2}, C_{v1}) and the distributed microstrip capacitances.

2.3.2 Synthesis of physical dimensions of microstrip structure

For the layout design of tunable microstrip lowpass filter, initially it is required to choose one tuning state for transforming the lumped element values to the physical structure's dimensions. In this filter, we select the highest cutoff frequency state for parameters conversion, where all the varactor capacitances are assumed to be the minimum. In addition, it has been mentioned that the variable capacitances C_{g1}, C_{g2}

and C_{p1} in the circuit model are the sum of capacitances of varactor diodes (C_{v2}, C_{v1}) and the distributed microstrip capacitances. As a result, during the process of physical dimensions synthesis, the values of diodes C_{v2}, C_{v1} should be deducted from the total capacitances of C_{g1}, C_{g2} and C_{p1}. Referring to the circuit design illustrated in the Section 2.2.4, under the assumption of C_{v2} = C_{v1} = 0.23 pF (the minimum value of varactor diode SMV2019-040LF [18] used in the fabrication) at the highest frequency state, the real component values used for the synthesis are given as: L=2.50 nH, L_0=0.50 nH, C_0=0.40 pF, C_p=0.90 pF, C_{g1}=0.14 pF and C_{g2}=0.36 pF.

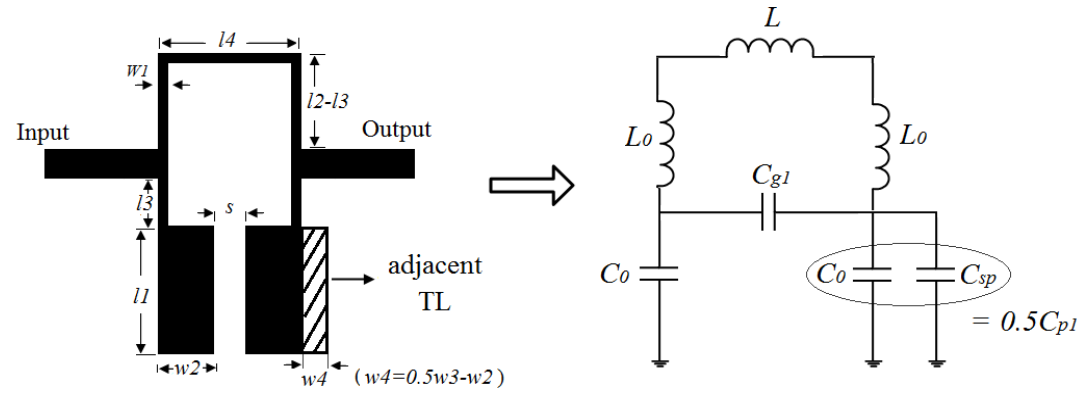

(a)

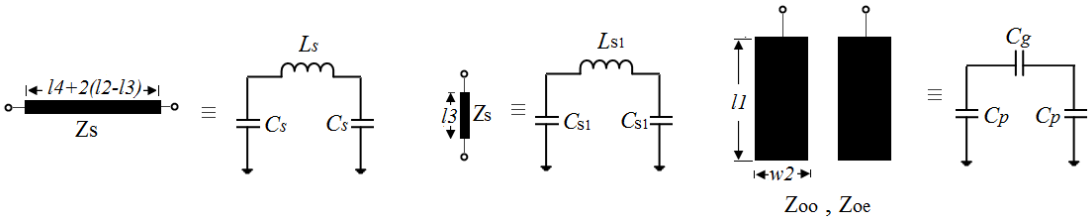

(b)

Figure 2.10: Equivalent circuit of: (a) One stepped-impedance hairpin resonator. (b) Individual segments of one hairpin resonator.

Moreover, noted that the proposed microstrip structure (see in Fig. 2.9) is composed of three identical hairpin resonators linked by an adjacent transmission line, thus, it only requires to synthesis the physical dimensions of one hairpin resonator to save time. Fig. 2.10 indicates such hairpin resonator unit as well as its detailed equivalent circuits. Neglecting the discontinuity effects, the element-value relationship between the whole circuit (Fig. 2.10 (a)) and the individual segments (Fig.

2.10 (b)) can be concluded as:

$$L = L_s \qquad (2.13)$$

$$L_0 = L_{s1} \qquad (2.14)$$

$$C_0 = C_P + C_S + C_{s1} \qquad (2.15)$$

$$C_{g1} = C_g \qquad (2.16)$$

Further, the physical dimensions of the structure can be determined by using *ABCD* matrix analysis, as described in Appendix A. Normally, once the characteristic impedances (i.e. Z_s and Z_{oo}, Z_{oe}) of the high-impedance and coupled lines are chosen, the parameters of *w*, *w1*, *w2* and *s* in the structure can be obtained by employing transmission line calculator TXline [17], while the associated physical lengths can be approximately found by:

$$l_1 = \frac{\tan^{-1}(2\omega_c C_{g1} Z_{oe} Z_{oo}/(Z_{oe} - Z_{oo}))}{\beta} \text{ (unit: mm)} \qquad (2.17)$$

$$l_3 = \frac{\sin^{-1}(\omega_c L_0/Z_s)}{\beta} \text{ (unit: mm)} \qquad (2.18)$$

$$l_4 + 2(l_2 - l_3) = \frac{\sin^{-1}\left(\frac{\omega_c L}{Z_s}\right)}{\beta} \text{ (unit: mm)} \qquad (2.19)$$

where the ω_c is the 3-dB cutoff angular frequency, and β is the phase constant. Additionally, the width of adjacent transmission line can be determined as:

$$w4 = \frac{h * \left(0.5C_{p1} - C_0\right)}{\varepsilon_0 \varepsilon_r * l_1 * 10^{-3}} \text{ (unit: mm)} \qquad (2.20)$$

where *h* is the substrate thickness, $l_1$is the physical length achieved in (2.17).

Based on the above equations, the calculated and optimized physical dimensions of the proposed microstrip structure in Fig. 2.9 are summarized in Table 2.2. As can be seen, these two sets of parameters are close to each other. This means the demonstrated analytical formulas are efficient and useful for the layout design. Fig.

2.11 shows the simulated frequency response of the optimized physical design in comparison to that of the circuit model at highest-frequency state, where good agreement between each other can be observed. As desired, the present results meet all design requirements at the highest frequency state, including the 3 dB cutoff frequency of 3.3 GHz as well as good selectivity.

Table 2.2: Calculated and Optimized Dimensions for the Proposed Tunable Microstrip LPF (in millimeters)

Z_s=96 Ohm Z_{oe}=64 Ohm Z_{oo}=30 Ohm									
	l1	*l2*	*l4*	*l3*	*w*	*w1*	*w2*	*w4/w3*	*s*
Calculated	1.82	*l2*+*l4*=3.27		0.62	1.2	0.2	1.0	0.18/2.36	0.3
Optimized	1.9	1.6	2	0.7	1.2	0.2	1.0	0.2/2.4	0.3

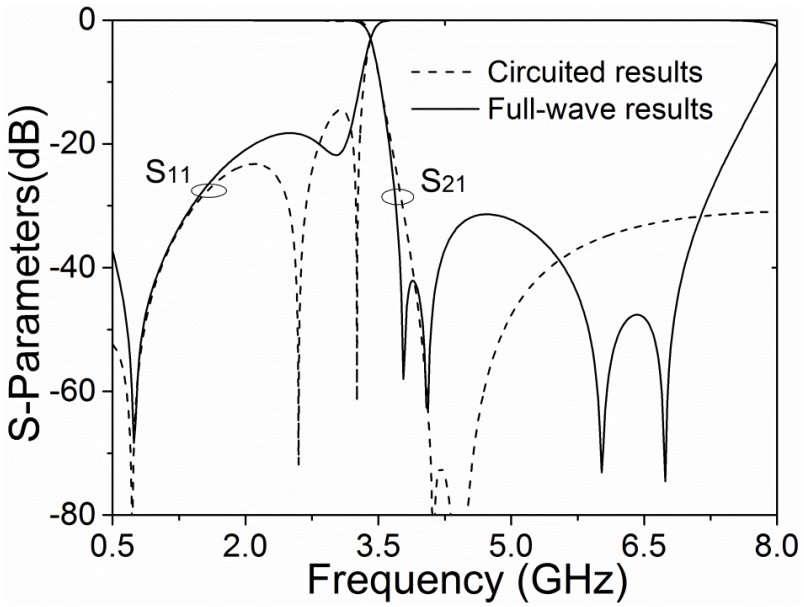

Figure 2.11: Simulated frequency responses obtained at highest frequency tuning state by using microstrip structure and circuit model.

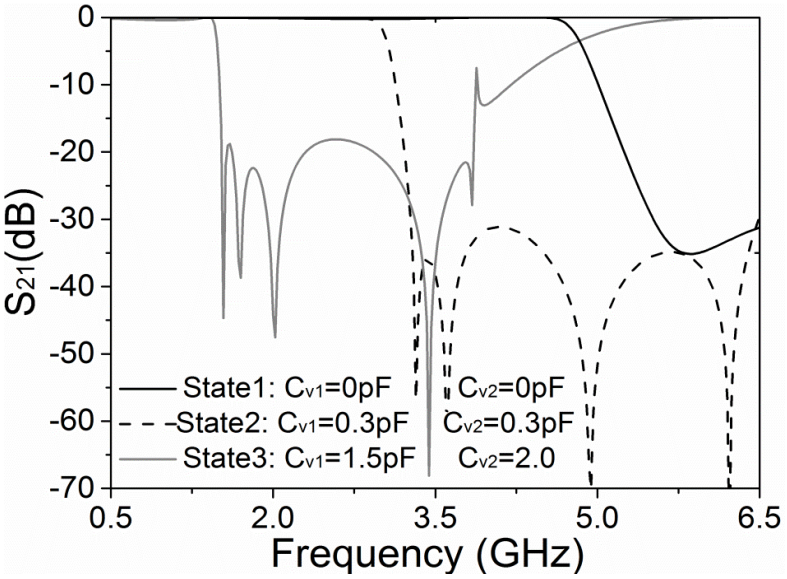

(a)

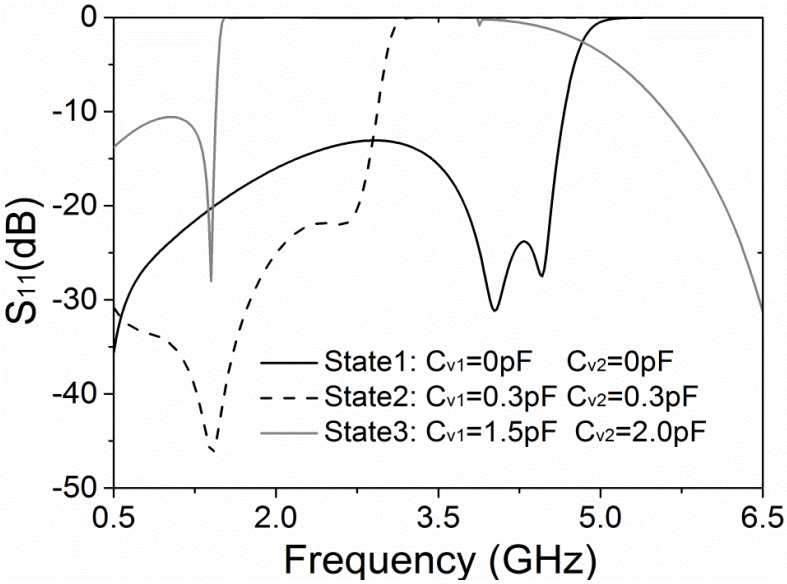

(b)

Figure 2.12: Tunable responses of the proposed tunable LPF obtained using ideal variable capacitors. (a). Insertion loss S_{21}. (b). Return loss S_{11}.

2.3.3 Performance analysis

A. Ideal Tuning Range of the Proposed Tunable Microstrip LPF

Based on the physical structure given in last section, some lossless tunable cases are considered here to demonstrate the potential tuning ability of the proposed structure. This is somehow ideal as the responses obtained did not take into account the loss and limited variable capacitance range of varactor used. Fig. 2.12 plots three

typical simulated tunable LPF responses versus C_{v1}, C_{v2} for 3 dB cutoff frequency f_c= 4.82, 3.05 and 1.47 GHz, whose tuning range is as wide as 69.5%. Also at each state, the filter has a sharp cutoff frequency response, whose roll-off rate ξ (α_{max}=30dB in the definition) is 38.6, 122.7 and 450, respectively. The increased selectivity is mostly associated with the increased coupling capacitances C_{v2} in the tuning process. Moreover, it can be seen the filter provides abundant transmission zeros to achieve a wide stopband performance. The characteristics of a sharp cutoff frequency response and a wide stopband would be very promising in cascading with a HPF/BPF in application.

B. Selectivity Control

As discussed in Section 2.2, it is found that both of the capacitances C_g and C_p in the equivalent circuit have an effect on cutoff frequency tuning, and C_g is mostly associated with the sharp cutoff frequency response. In other words, in the EM simulation, to achieve the same cutoff frequency, different combinations C_{v1} and C_{v2} can be used, but the selectivity can be well controlled by the variable capacitance C_{v2}. As shown in Fig.2.13, two illustrative cases roughly operate at the same 3 dB cutoff frequency, while due to a larger capacitance C_{v2} used, the case II realizes a shaper selectivity. In fact, this filter property is very promising, since the response would be very flexible and controllable to meet different requirements in each state.

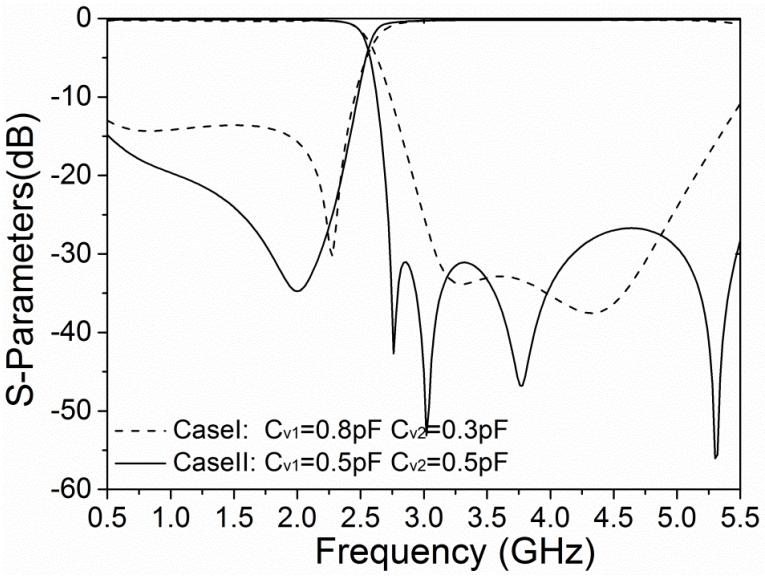

Figure 2.13: Illustrative simulated tunable response for selectivity control.

C. Effect of Q on Filter Response

Fig. 2.14 (a) indicates a simple lossy varactor diode model for simulation, where the series resistors R_{v1} and R_{v2} represent the dissipation losses of varactor diodes C_{v1}, C_{v2} respectively. From the responses of an illustrative tuning state C_{v1}=0.8 pF and C_{v2}=0.8 pF shown in Fig. 2.14 (b), both of limited low Q factors of varactor diodes C_{v1}, C_{v2} round off the passband edge leading to a poorer selectivity, but which become more pronounced in the response using lower Q of varactor C_{v2} than the counterpart. Also the dissipation losses of varactors C_{v2} have much more effect on the attenuation characteristic of stopband, especially for the null rejection levels than the varactors C_{v1}. The same tendencies occur in the other tuning states.

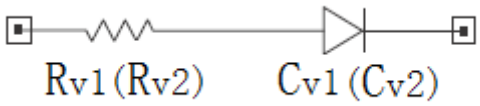

(a)

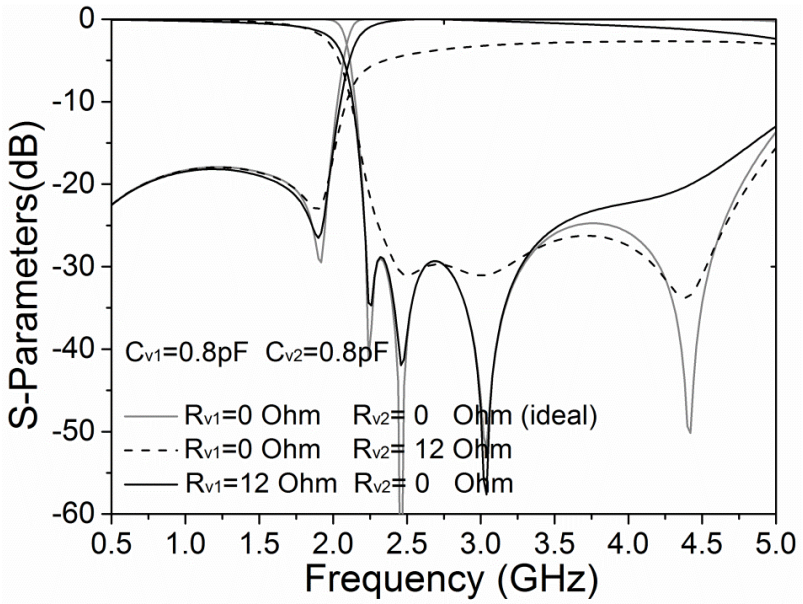

(b)

Figure 2.14: (a). Dissipative varactor diode model. (b) Dispassion effect on LPF response.

2.4 Filter Fabrication and Measurement

2.4.1 Fabrication and S-parameter measurement

The proposed compact tunable LPF was fabricated on the RT/Duriod 6010 with 1.27 mm thickness ($\tan\delta = 0.0023$) for experimental demonstration. A detailed photograph of the filter with the biasing scheme is shown in Fig. 2.15. Excluding the input/output lines and bias circuits, the size of the filter is 7.7 mm × 3.5 mm ($0.11\lambda_g \times 0.05\lambda_g$ at lowest f_c). Silicon abrupt junction diodes SMV2019-040LF are used for tunable capacitors C_{v1} and C_{v2} (see Fig. 2.9), with Q = 500 for V_R = 4 V at f =50 MHz. Murata 0402 GRM 100 pF capacitors are used for bypass capacitors. Also Panasonic resistors 100 kΩ are utilized to reduce the RF signal leakage in the bias network.

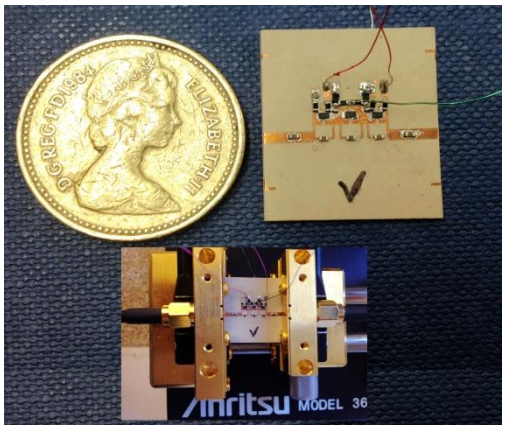

Figure 2.15: Fabricated varactor-tuned lowpass filter.

In the final EM simulation, the SPICE model of the varactor diode provided in [18] is analyzed and considered by using the method discussed in Chapter 1. The measured several typical tunable frequency responses are obtained using HP8510 network analyzer and Anritsu Test Fixture, which are compared with the simulated ones, as shown in Fig. 2.16. The reverse voltage V1, V2 applied on the varactors ranges from 3V to 20V, 1V to 20V respectively, resulting in the 3 dB cutoff frequency changing from 1.60 to 2.94 GHz with a tuning range up to 45.6%. Over the entire tuning range, the proposed tunable LPF provides a sharp, continuously tunable cutoff frequency response with a wide stopband of rejection level greater than 20 dB. For instance, the measured roll-off rates at state I and state IV are 64.7 and 77.2 respectively, where α_{max} is assumed as 25 dB attenuation point in the definition (2.11). The measured

return loss is also better than 10 dB for all states, with the insertion loss varying from 0.3 to 0.8 dB. In general, good agreement between the measured and simulated *S*-parameters is observed in Fig. 2.16, except cutoff frequencies slightly shift in some states due to the accuracy of the diode SPICE model and manufacturing tolerances. Also compared with the desired specification stated previously and the ideal tuning range achieved in the Section 2.3.3, the measured one is slightly narrower, which is constrained by capacitance ratio provided by the varactor diodes used here.

Fig. 2.17 presents two illustrative measured states operating at roughly the same cutoff frequency with different selectivity, which further proves the proposed tunable LPF has a flexible selectivity control by combining different applied voltages experimentally. As a guideline, lower voltage for varactor C_{v2} lead to a higher selectivity realized.

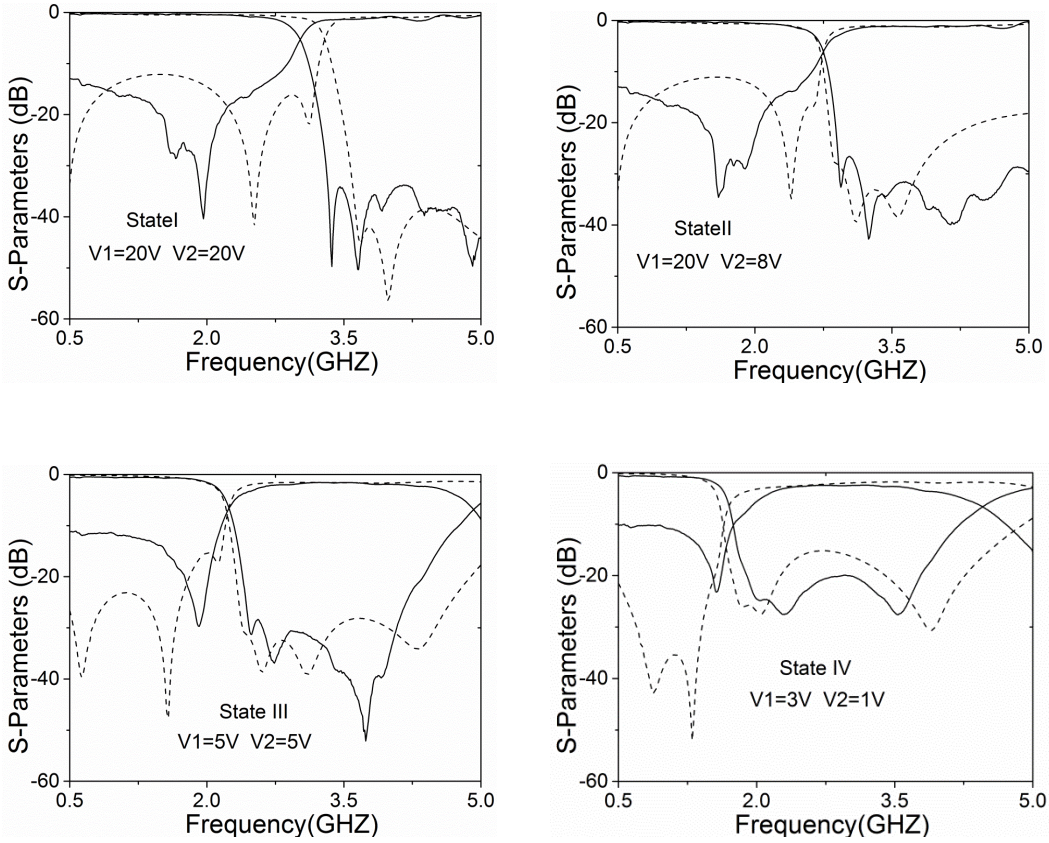

Figure 2.16: Measured (solid line) and simulated (dash line) *S*-parameters of the proposed tunable LPF.

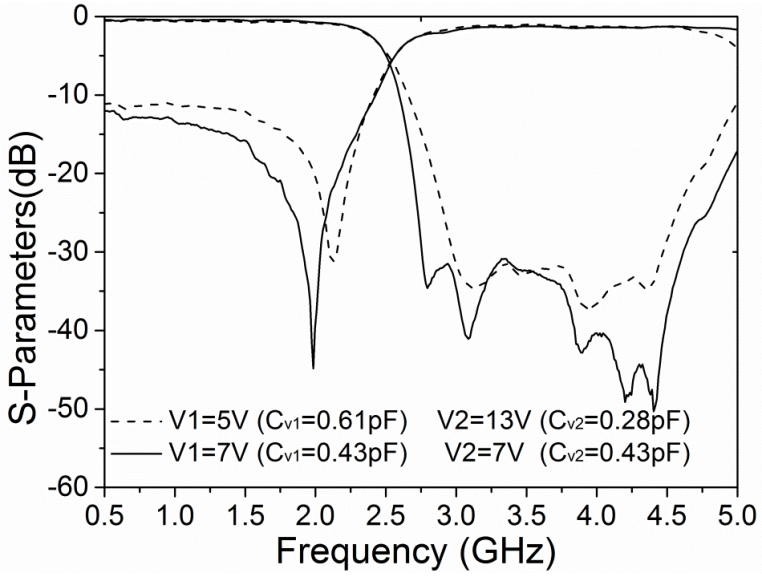

Figure 2.17: Illustrative measured tunable response for selectivity control.

2.4.2 Nonlinear measurement

The nonlinear behaviour of the proposed tunable filter is mainly due to the varactor diodes used and the large voltage swing across them. Fig. 2.19 presents the nonlinear characterizations of the proposed tunable LPF, which is performed by the experimental setup shown in Fig. 2.18

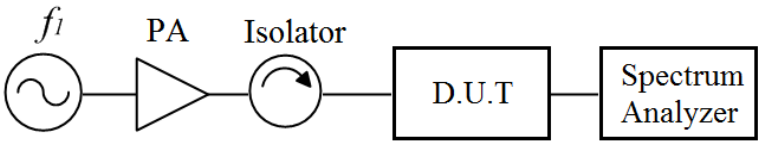

(a)

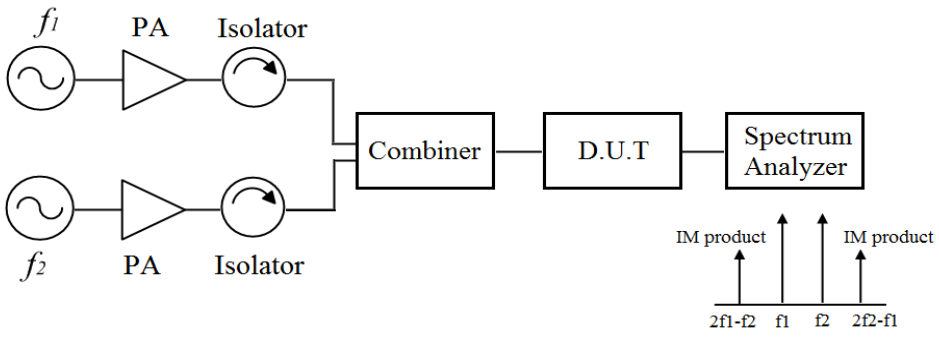

(b)

Figure 2.18: Experimental setup for: (a) 1-dB compression point measurement. (b) third-order intermodulation intercept point (IIP3) measurement.

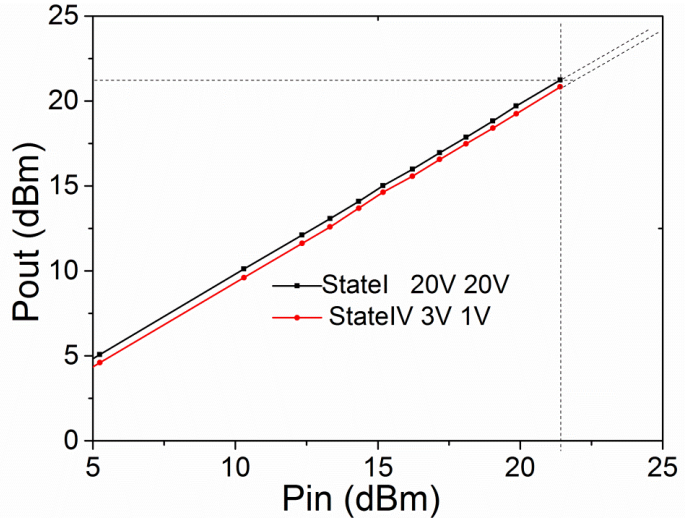

(a)

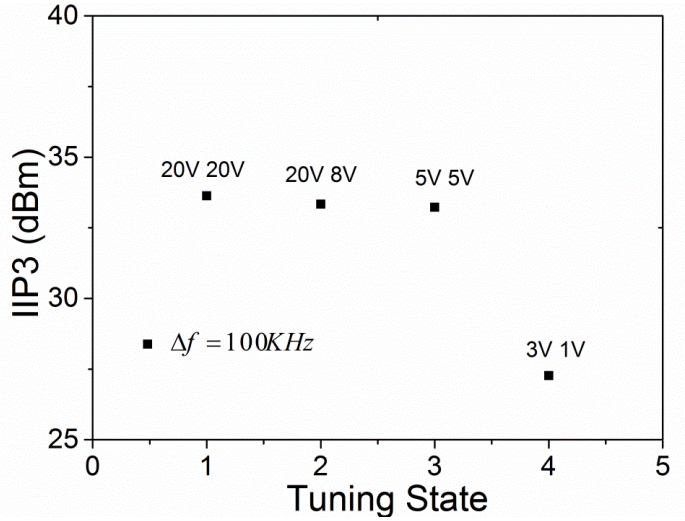

(b)

Figure 2.19: Nonlinear characterizations. (a) 1-dB compression point and (b) IIP3.

The 1-dB compression points of the filter are measured at the highest- and lowest-frequency tuning states to examine the power-handling capacity. The results can be seen in Fig. 2.19 (a). The maximum available input power for the testing is 21 dBm and the filter does not show any 1 dB compression up to this power level.

The input third-order intercept point (IIP3) measurements are carried out at *f*=1.4 GHz in the passband with two tone spacing of 100 kHz. As shown in Fig. 2.19 (b), the IIP3 value ranges from 27.3 to 33.6 dBm over the entire tuning states. It can be observed that the linearity is the best at state I with largest applied voltages resulting from the widest bandwidth at this state. The IIP3 is lowest at state 4 with the narrowest passband when the applied voltages are small.

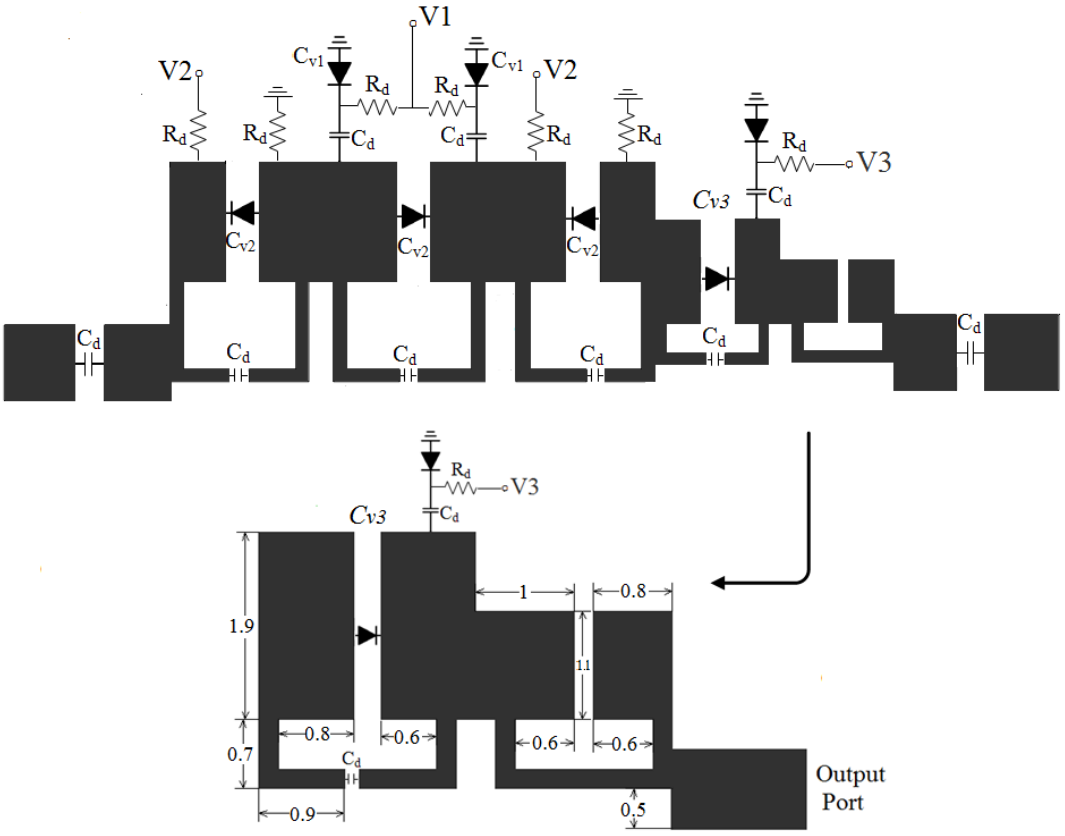

Figure 2.20: Layout of the tunable microstrip LPF design with extended stopband bandwidth.

2.5 Further Discussion on Extending Stopband Bandwidth

Observing the measured frequency responses of the tunable lowpass filter shown in Fig. 2.16, although the second harmonic is suppressed at each tuning state, the stopband bandwidth is still a bit narrow for some stringent applications. In order to obtain a broader stopband bandwidth, as discussed previously, it is better to purposely design the different cells with different parameters to make the zeros be allocated at harmonics for suppression. Operating in this manner, Fig. 2.20 proposed an improved design based on the original structure demonstrated in Fig. 2.9. As can be seen, the improved structure is mainly added two additional hairpin resonators, but only one of them is controllable by using two identical varactor diodes C_{v3}. This consideration is mostly to avoid increasing the circuit complexity and the filter insertion loss arising from the extra varactor diodes. The detailed dimensions of the additional resonators

can be found in Fig. 2.20. Fig. 2.21 plots two sets of comparative results between the improved and the original designs at highest- and lowest-frequency tuning states. It is obvious to see the improved design achieves a significantly wider stopband bandwidth with attenuation better than 10 dB roughly from 3.6 to 14.5 GHz, 1.8 to 11.2 GHz at state I and state IV, respectively.

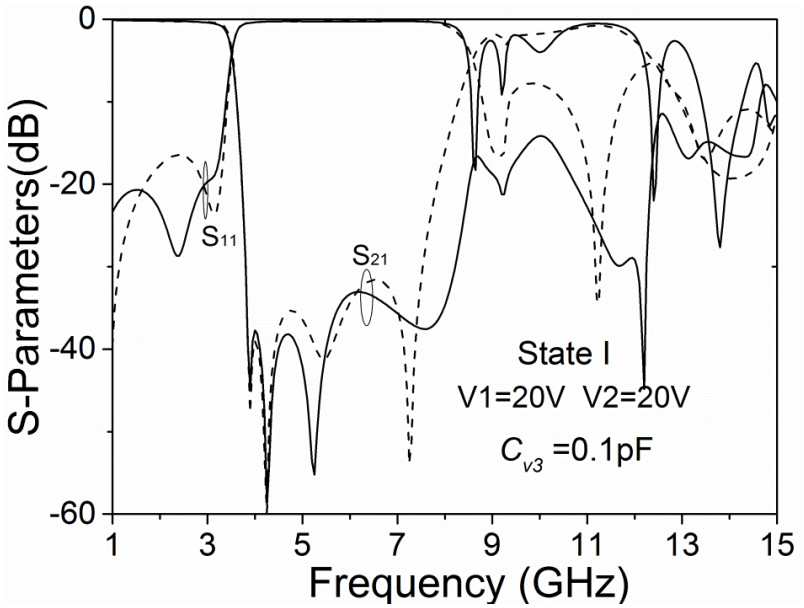

(a)

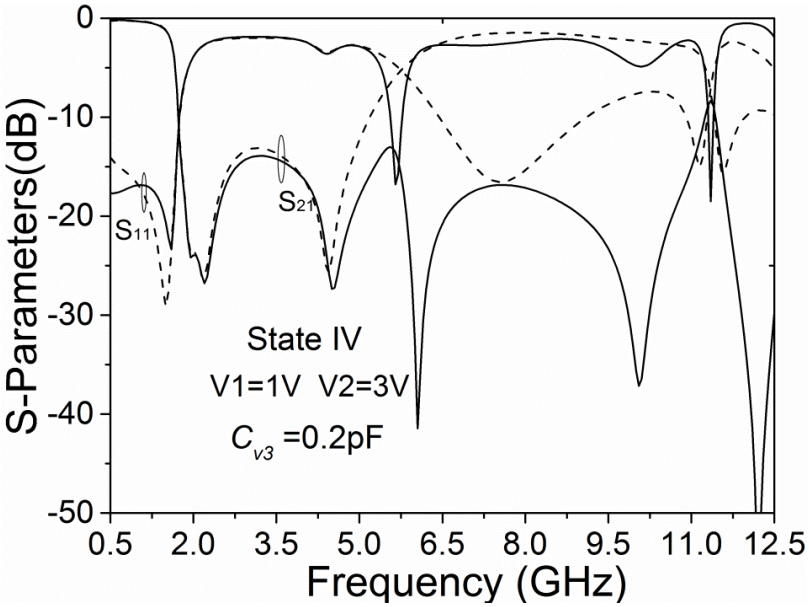

(b)

Figure 2.21: Comparative frequency responses between the improved design (solid line) and original design (dash line) at highest- and lowest-frequency states.

2.6 Summary

In this chapter, three different types of tunable lowpass filter topologies with unit cell and multiple cells have been proposed and investigated. Design equations, curves and rules have been provided for revealing the performance controlling mechanisms of all the suggested topologies and also guiding the associated microstrip realization. As an illustrative design example, a compact varactor-diode-based tunable lowpass filter using multiple cascaded stepped-impedance hairpin resonators has been designed, fabricated and tested. It is promising to see the proposed tunable microstrip lowpass filter addressed diverse aspects of filter high performance, such as a wide continuous tuning range covering from 1600 to 2940 MHz (up to 46%), sharp cutoff frequency response, a broad stopband bandwidth (second harmonic suppression) and low insertion loss. Performance comparison with related works in the literature is summarized in the Table 2.3. In addition, an alternative approach to further extend the stopband bandwidth of the proposed tunable filter has been provided for some certain applications with wider stopband bandwidth requirement. Overall, in light of theoretical analysis and experimental results, the proposed tunable lowpass topologies seem to be valuable candidates for emerging reconfigurable communication systems.

Table 2.3: Performance Comparison among Tunable/Reconfigurable LPFs

Reported Tunable LPF	Tuning Technique	Tuning State	3dB f_c Tuning Range		Insertion loss Variation
Ref. [6]	MEMS Switch	Discrete (2 states)	28/67GHz	58%	0.27/0.32 dB
Ref. [7]	MEMS Switch	Discrete (2 states)	20/53GHz	62%	n/a
Ref. [9]	MEMS Switch	Discrete (2 states)	10/30GHz	67%	0.8/1.1 dB
Ref. [10]	PIN Diode	Discrete (3 states)	2.0/3.0/4.0 GHz	50%	n/a
Ref. [11]	BST	Continuous	120-170 MHz	30%	0.8dB
Ref. [13]	Varactor	Continuous	1.29-2.13 GHz	39%	0.7dB
This work	**Varactor**	**Continuous**	**1.6-2.94 GHz**	**46%**	**0.3-0.8 dB**

Reference

[1] Lung-Hwa Hsieh and Kai Chang, "Compact Elliptic-Function Low-Pass Filters Using Microstrip Stepped-Impedance Hairpin Resonators," *IEEE Trans. Microw. Theory Tech.*, vol. 51, no. 1, pp. 193-199, Jan. 2003.

[2] M.H. Yang and J. Xu, "Design of compact, broad-stopband lowpass filter using modified stepped impedance hairpin resonators," *Electron. Lett.*, vol. 44, no. 20, pp. 1198-1199, Jan. 2008.

[3] Vamsi Krishna Velidi and Subrata Sanyal, "Sharp Roll-off Lowpass Filter With Wide Stopband Using Stub-Loaded Coupled-Line Hairpin Unit," *IEEE Microw. Wireless Compon. Lett.*, vol. 21, no. 6, pp.301-303, Jun. 2011.

[4] J.-L. LI, S.-W. Qu and Q. Xue, "Compact microstrip lopwass filter with sharp roll-off and wide stop-band," *Electron. Lett.*, vol. 45, no. 2, pp. 110-111, Jan. 2009.

[5] D. Kaddour, E. Pistono, J.-M. Duchamp, J.-D. Arnould, H. Eusebe, P. Ferrari and R. G. Harrison, "A Compact and Selective Low-Pass Filter With Reduced Spurious Responses, Based on CPW Tapered Periodic Structures," *IEEE Trans. Microw. Theory Tech.*, vol.54, no.6, pp. 2367–2375, Jun. 2006.

[6] S. Lee, J. H. Park, J. M. Kim, H. T. Kim, Y. K. Kim, and Y. Kwon, "A Compact Low-Loss Reconfigurable Monolithic Low-Pass Filter Using Multiple-Contact MEMS Switches," *IEEE Microw. Wireless Compon. Lett.*, vol. 14, no. 1, pp. 37–39, Jan. 2004.

[7] S. Lee, J.-M. Kim, J.-M. Kim, Y.-K. Kim, and Y. Kwon, "Millimeter-Wave MEMS Tunable Low Pass Filter With Reconfigurable Series Inductors and Capacitive Shunt Switches," *IEEE Microw. Wireless Compon. Lett.*, vol. 15, no. 10, pp. 691 – 693, Oct. 2005.

[8] R. Zhang and P.R. Mansour, "Novel Tunable Lowpass Filter Using Folded Slots Etched in the Ground Plane," in *IEEE MTT-S Int. Microw. Symp. Dig.*, 2005, pp. 775-778.

[9] D. Peroulis, S. Pacheco, K. Sarabandi, and L. P. B. Katehi, "Tunable Lumped Components With Applications to Reconfigurable MEMS Filters," in *IEEE MTT-S Int. Microw. Symp. Dig.*, 2001, pp. 341–344.

[10] Miguel A. Sanchez-Soriano and Jia-Sheng Hong, "Reconfigurable Lowpass Filter Based on Signal Interference," in *IEEE MTT-S Int. Microw. Symp. Dig.*, 2011, pp. 1-4.

[11] Ali Tombak, Jon-Paul Maria Francisco T. Ayguavives, Zhang Jin, Gregory T. Stauf, Angus I. Kingon and Amir Mortazawi, “Voltage-Controlled RF Filters Employing Thin-Film Barium-Strontium-Titanate Tunable Cpacitors,” *IEEE Trans. Microw. Theory Tech*., vol. 51, no. 2, pp. 462-467, Feb. 2003.

[12] E. Pistono, J.-M. Fournier, L. Duvillaret, J. M. Duchamp, A. Volcot, and P. Ferrari,“A MMIC 4.3-GHz tunable low-pass filter,” *Microwave Opt. Technol. Lett.*, vol. 50, no. 10, pp. 2566–2568, Oct. 2008.

[13] C.-C. Huang, N.-W. Chen, H.-J. Tsai and J.-Y. Chen, “A Coplanar Waveguide Bandwidth-Tunable Lowpass Filter with Broadband Rejection,” *IEEE Trans. Microw. Wireless Compon.* 2013.

[14] A. Abbosh, "Compact tunable low-pass filter using variable mode impedance of coupled structure," *Microwaves, Antennas & Propagation, IET*, vol. 6, pp. 1306-1310, 2012.

[15] J.-S. Hong, Microstrip filter for RF/Microwave applications, 2nd Edtion, New York: John Wiley & Sons, 2011.

[16] Sonnet *em*, Version 13.54, Sonnet Software Inc., New York, 2011.

[17] “AWR Microwave Office/Analog Office 9.06,” Appl. Wave Res. Inc., El Segundo, CA, 2010

[18] “Skyworks SMV2019—040LF data sheet,” Skyworks Solutions, Sunnyvale, CA, 2011.

CHAPTER 3

Compact Tunable Microstrip Highpass Filter with a Quasi-Elliptic Function Response

3.1 Introduction

In the open literature, there are a few reports on tunable highpass filters. An obvious reason for this is due to the lack of viable monolithic tunable inductor solution for matching to realize a wide tuning range. In [1] [2], left-handed tunable transmission line (LH TL) of highpass nature were studied to realize tunable bandpass (BPF) and bandstop (BSF) filters, whose cutoff frequencies were controlled by the voltages of varactor diodes for roughly obtaining 33% and 15% tunability, respectively. Olsak et al. [3] proposed an electronically high-order tunable highpass filter by employing operational transconductance amplifier (OTA) as active tuning elements, which was continuously controlled by an external voltage or current source. In [4], a tunable highpass filter-type response was provided by employing an especially designed epitaxial, metal-oxide-semiconductor (MOS) transistor.

The objective of this chapter is to present a novel and simple circuit topology of quasi-elliptic tunable highpass filter having a wide continuous tuning range, with two applications in mind: the first application is to block the dc current or eliminate the unwanted noise signals in different types of networks; the second one is to be used in conjunction with a tunable LPF such as the one discussed in Chapter 2 to create a tunable BPF or BSF with more independent passband edge and selectivity control [5].

In general, this chapter is organized as follows: Section 3.1 is introductory. Section 3.2 proposes a tunable highpass filter topology with a quasi-elliptic function response. The associate performance tuning mechanism and lumped-element synthesis procedure are thoroughly discussed. Section 3.3 tells how to convert the proposed tunable circuit topology into a microstrip physical structure by using

parameter-extraction method. In Section 3.4, the proposed filtering configuration is experimentally validated by using liquid crystal polymer (LCP) bonded multilayer printed circuit board (PCB) technology. Finally, Section 3.5 concludes this chapter.

3.2 Tunable Highpass Filter Topology and Characteristics

Fig. 3.1 presents the proposed quasi-elliptic tunable highpass filter topology that has a symmetrical structure. Three variable capacitors C_{v1} and C_{v2} are used to provide a wide cutoff frequency tuning range. The mutual inductive coupling k between two inductors L_0 is introduced to generate two split transmission zeros close to the passband skirt of highpass filter to improve the selectivity and these two transmission zeros can be tuned together with cutoff frequency by varying the capacitors C_{v1} and C_{v2}.

For our later discussions, let us define:

$$\text{Cutoff Frequency } f_c \textbf{ at } S_{11}|_{f=f_c} = -10 \text{ (dB)} \qquad (3.1)$$

$$\text{Roll off Rate } \xi = \frac{\alpha_{max} - \alpha_{min}}{f_c - f_s} \left(\frac{\text{dB}}{\text{GHz}}\right) \qquad (3.2)$$

$$\text{Tuning range } = \frac{f_H - f_L}{f_H} \times 100\% \qquad (3.3)$$

In (3.2), α_{max} is the nominal attenuation point, say 30 dB, at the stopband frequency f_s; α_{min} is the attenuation point at the cutoff frequency f_c. In (3.3), f_H is the highest cutoff frequency among all the tuning states and f_L is the lowest one.

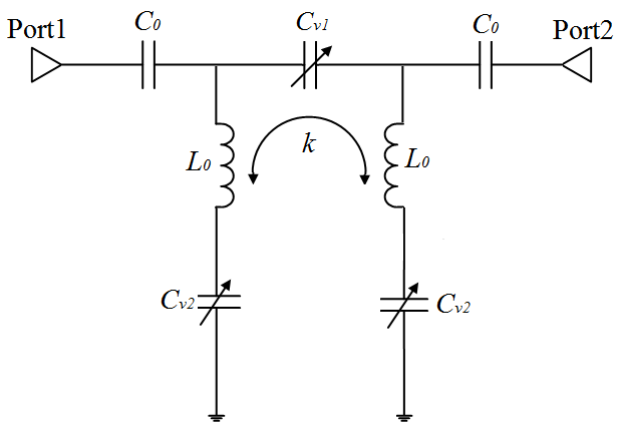

Figure 3.1: Proposed tunable highpass filter circuit topology.

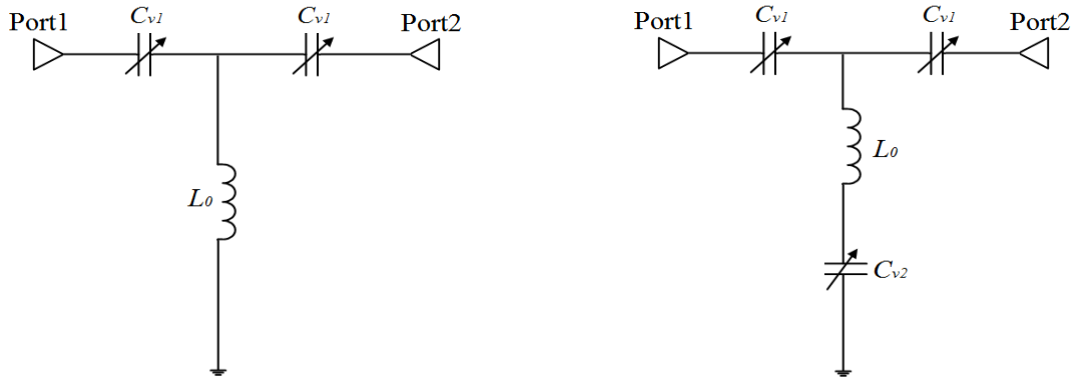

(a) (b)

Figure 3.2: (a) The conventional Chebyshev topology used in [1] and [2]. (b) Basic unit of the proposed tunable HPF.

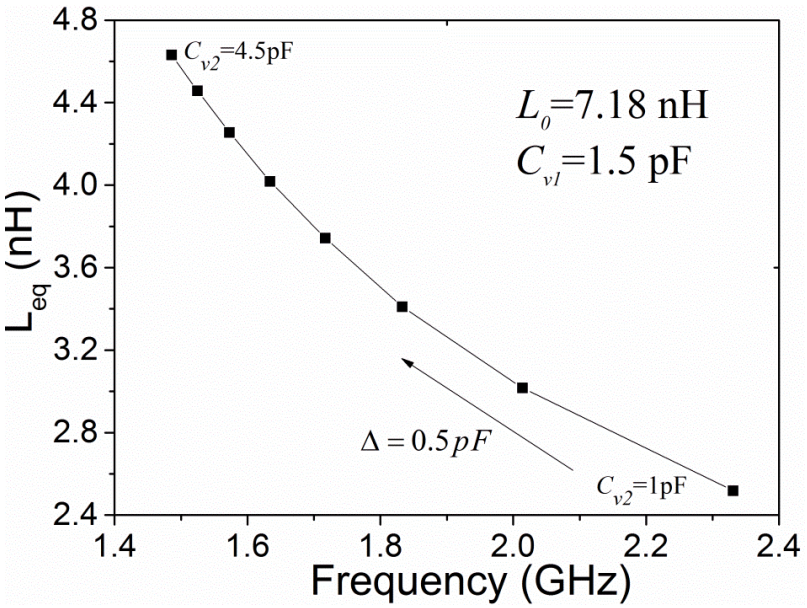

Figure 3.3: Extracted equivalent inductance L_{eq} versus capactiances C_{v2} at the different tunable cutoff frequencies.

3.2.1 Mechanism of wide-range cutoff frequency tuning

As aforementioned in Chapter 2, due to the lack of viable monolithic tunable inductor solution for good matching within the tuning range, the obtainable tunability of tunable lowpass filter is somewhat limited. Actually, this issue also exist in the tunable highpass filter designs. Such as the tuning designs presented in [1]-[2], by solely tuning capacitors in the conventional Chebyshev high-pass filter topology (see Fig. 3.2 (a)), their controllable cutoff frequencies only shifted from 480 to 721 MHz (tuning range: 33.4%) and 840 to 925 MHz (tuning range: 14.7%), respectively. In order to alleviate the mismatching resulting from invariable inductors, the proposed topology shown in Fig. 3.1 mostly introduces variable capacitors C_{v2} in shunt branches, with connecting inductors L_0 in series. Accordingly, the equivalent inductance of each series section can be easily expressed as:

$$L_{eq} = L_0 - \frac{1}{\omega^2 C_{v2}} \qquad (3.4)$$

thus in a certain frequency tuning range, changing the capacitance C_{v2} can produce a variable equivalent inductance L_{eq} to maintain a good matching. For convenience, a basic unit of the proposed topology as shown in Fig. 3.2 (b) is utilized to verify this theory. Fig. 3.3 gives the extracted equivalent inductance L_{eq} versus capacitance C_{v2} at different tunable cutoff frequencies. It is desired to see by increasing the capacitance C_{v2}, the equivalent inductance L_{eq} is increased while the cutoff frequency decreases. To further illustrate the tuning mechanism, Fig. 3.4 shows a set of comparative responses achieved by individually tuning the elements C_{v1} and C_{v2}, to examine the impacts of these two varactors on the filter performance. As can be seen, when the capacitance C_{v1} is tuned from original 1.5 to 3.0 pF while keeping C_{v2} unchanged (i.e. 1.0 pF), the cutoff frequency is just slightly changed as well as the transmission zero. Also note that in this case, such tuning leads to a better return loss but degrades the rejection level in the stopband. In contrast to the case of tuning C_{v1}, varying the capacitance C_{v2}, for example from 1.0 to 5.0 pF with a constant C_{v1} of 1.5 pF, results in the cutoff frequency more significantly shifts downwards so does the transmission zero. Additionally, the out-of-band rejection is better but the in-band return loss becomes poorer. However, if we allow adjusting the capacitance C_{v1} and C_{v2} jointly in

the circuit, they can compensate the drawbacks of each other to obtain a wider matching range. Apparently, this filter operating mechanism is quite similar to that of tunable lowpass filter presented in Chapter 2. In brief, both of tunable LPF and HPF obtain a wider tuning range by mainly introducing extra variable capacitors with connecting inductors in the series or shunt branches.

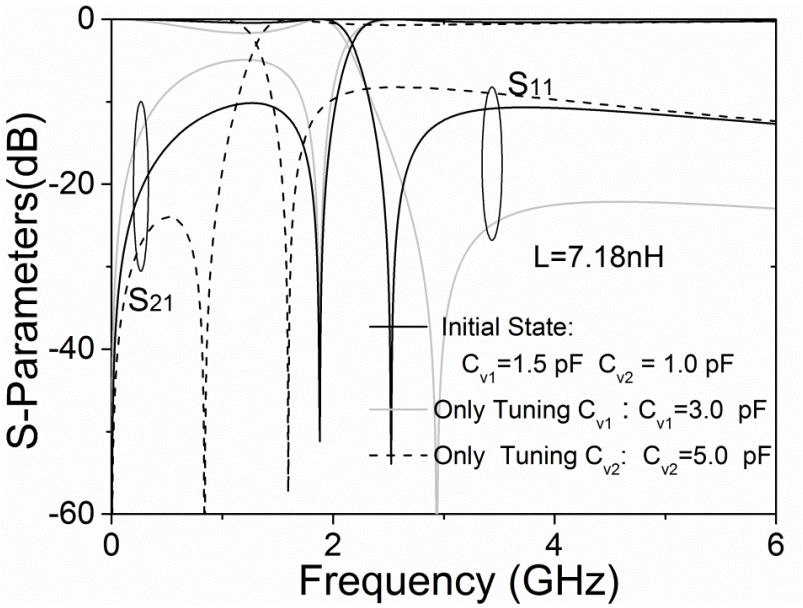

Figure 3.4: Tunable responses obtained by individually tuning the elements C_{v1} and C_{v2} in the basic unit given in Figure. 3.2 (b).

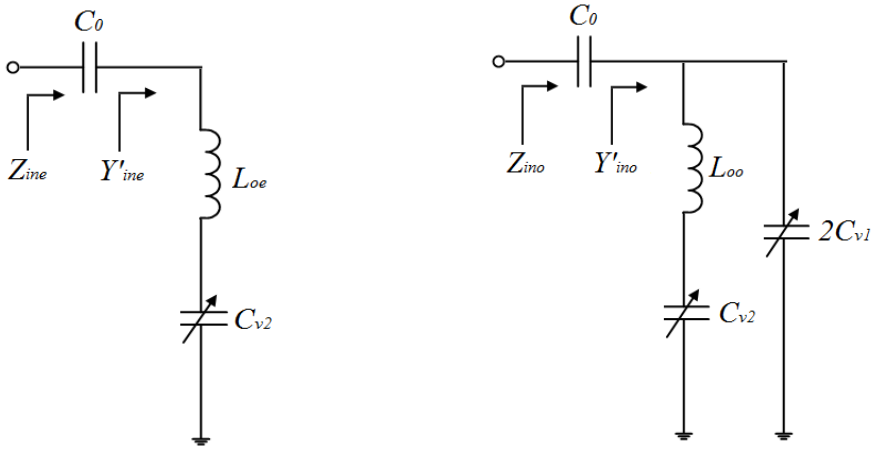

(a) (b)

Figure 3.5: (a) Even-mode circuit of the proposed topology. (b) Odd-mode circuit of the proposed topology.

3.2.2 Transmission zeros creation

Due to the symmetry, the proposed topology shown in Fig. 3.1 can be analyzed based on the even-and odd-mode circuits, as shown in Fig. 3.5 (a) and Fig. 3.5 (b), where

$$L_{oe} = L_0(1+k) \tag{3.5}$$

$$L_{oo} = L_0(1-k) \tag{3.6}$$

as referring to [6]. The corresponding input impedance Z_{ine} and Z_{ino} can be respectively solved by (3.7)-(3.10)

$$Z_{ine} = \frac{1}{j\omega C_0} + \frac{1}{Y'_{ine}} \tag{3.7}$$

$$Z_{ino} = \frac{1}{j\omega C_0} + \frac{1}{Y'_{ino}} \tag{3.8}$$

$$Y'_{ine} = \frac{j\omega C_{v2}}{1-\omega^2 L_o C_{v2}} \tag{3.9}$$

$$Y'_{ino} = 2j\omega C_{v1} + \frac{j\omega C_{v2}}{1-\omega^2 L_{oo} C_{v2}} \tag{3.10}$$

S_{21} can then be written as

$$S_{21} = \frac{Z_o(Z_{ine} - Z_{ino})}{(Z_o + Z_{ine})(Z_o + Z_{ino})} \tag{3.11}$$

where Z_0 is normalized terminal impedance. Enforcing $S_{21}=0$, the frequency of two transmission zeros can be given by

$$f_{z1,z2} = \frac{1}{2\pi}\sqrt{\frac{Q_2 \pm \sqrt{{Q_2}^2 - 8Q_1 C_{v1}}}{2Q_1}} \quad (0 \le k < 1) \tag{3.12}$$

where

$$Q_1 = 2{C_{v2}}^2 C_{v1} L_{oe} L_{oo} \tag{3.13}$$

$$Q_2 = 2C_{v1}C_{v2}L_{oo} + 2C_{v1}C_{v2}L_{oe} + {C_{v2}}^2 L_{oe} - {C_{v2}}^2 L_{oo} \tag{3.14}$$

From the formulas (3.12)-(3.14), it is noteworthy that the locations of two transmission zeros have no relationship with capacitance C_0, but they are well controlled by the capacitances C_{v1} and C_{v2}. This means the transmission zeros can be properly tuned together with the cutoff frequency by only varying the capacitances C_{v1} and C_{v2}. By using the above analytic equations, Fig. 3.6 shows the locations of the two transmission zeros (TZ_1 and TZ_2) versus C_{v1}, C_{v2}, and k, respectively. In Fig. 3.6 (a), one can clearly observe that when the capacitance C_{v1} is tuned from 1.0 pF to 3.0 pF with keeping C_{v2} unchanged (i.e. 0.6 pF), the TZ_1 and TZ_2 are slightly shifted from 2.30 to 2.34 GHz, 2.49 to 2.45 GHz, individually. Increasing the capacitance C_{v2} from 0.6 to 5.0 pF makes TZ_1 and TZ_2 decrease proportionally with an approximately constant separation (Fig. 3.6 (b)), which offers a possibility to keep a filter response shape unchanged versus frequency tuning. Overall, the TZs control is more dependent on the capacitance C_{v2}.

Basically, the desired locations of the transmission zeros can also be adjusted by properly selecting the value of the mutually inductive k. As implied in Fig. 3.6 (c), only one transmission zero ($f_{z1,z2} = 2.392$ GHz) is generated without mutually inductive coupling introduced (k=0). While by increasing the coupling k, it is observed that the original transmission zero is split into two new symmetrical ones, and a larger mutual coupling k results in a wider TZs separation at expense of rejection level (the peak between two TZs). This will be a trade-off in the design. However, under the specific rejection requirement (e.g. 20 dB), a wider stopband bandwidth can be realized by increasing the mutual coupling k.

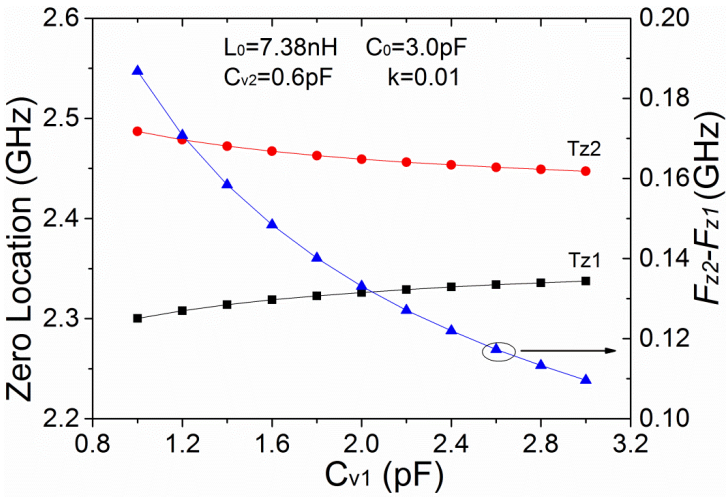

(a)

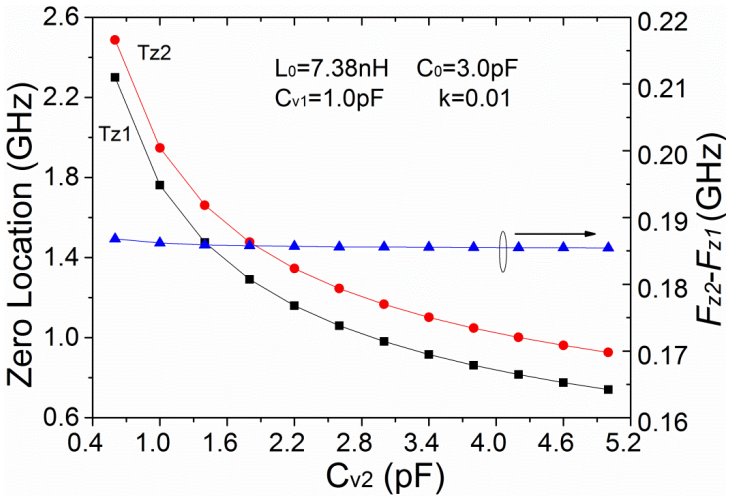

(b)

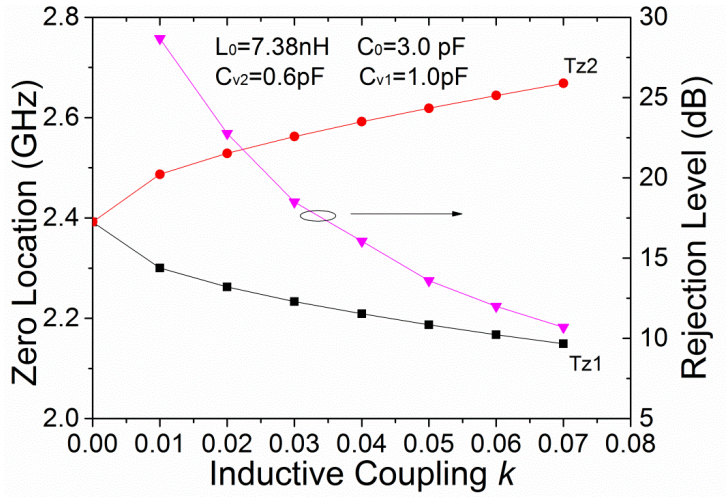

(c)

Figure 3.6: (a) Transmission zeros (TZs) locations and separation versus C_{v1}. (b) TZs locations and separation versus C_{v2}. (c) TZs locations and rejection level versus k.

3.2.3 L-C elements synthesis and optimization

Since the proposed tunable filter circuit of Fig. 3.1 is different from a traditional elliptic or Chebyshev filter design, a synthesis procedure based on optimization is adopted. The procedure starts with a standard five-pole Chebyshev lowpass prototype and the mutual inductive coupling k=0 is assumed initially.

Step 1: *Determine the initial L-C element values from the available Chebyshev lowpass prototype tables* [6]. The lowpass prototype values (g_1, g_2, g_3, g_4, g_5, g_6) of the five-order Chebyshev filter used here are 1.1468, 1.3712, 1.9750, 1.3712, 1.1468 and 1.0000, respectively. Consequently, the initial values of C_0 and C_{v1} shown in Fig. 1 (a) can be derived as:

$$C_0 = \left(\frac{1}{Z_0 g_1}\frac{1}{2\pi f_c \Omega_c}\right); \qquad C_{v1} = \left(\frac{1}{Z_0 g_3}\frac{1}{2\pi f_c \Omega_c}\right) \qquad (3.15)$$

where f_c is the cutoff frequency of the highpass filter at initial state with the highest cutoff frequency response, Z_0=50 ohm and Ω_c=1. On the other hand, the variable capactiance C_{v2} can be set by the minimum values of the varactor diodes adopted in the practical implementation. In order to achieve the desired cutoff frequency, the inductance L_0 can be expressed as:

$$L_0 = \left(\frac{Z_0}{g_2}\frac{1}{2\pi f_c \Omega_c} + \frac{1}{4\pi^2 {f_c}^2 C_{v2}}\right) \qquad (3.16)$$

As an example, 2.5 GHz is chosen for the desired highest cutoff frequency (f_H) of the proposed tunable filter at state I. With the assistance of the equations (3.15)-(3.16), the corresponding components C_0, C_{v1}, L_0 and C_{v2} are then obtained as 1.1 pF, 0.65 pF, 7.38 nH and 0.8 pF as given in Table 3.1, where the available minimum capacitance for C_{v2} is assumed to be 0.8 pF. As a result, the initial frequency response is plotted in Fig. 3.7 (a) (black curves), showing a cutoff around 2.5 GHz but rather a poor return loss in the passband.

Step 2: *Increase the capacitances C_0 and C_{v1} to achieve a better return loss.* Based on the initial response achieved in Step 1, optimization is then carried out by increasing the capacitances C_0 *and* C_{v1} while keeping the other elements L_0 and C_{v2}

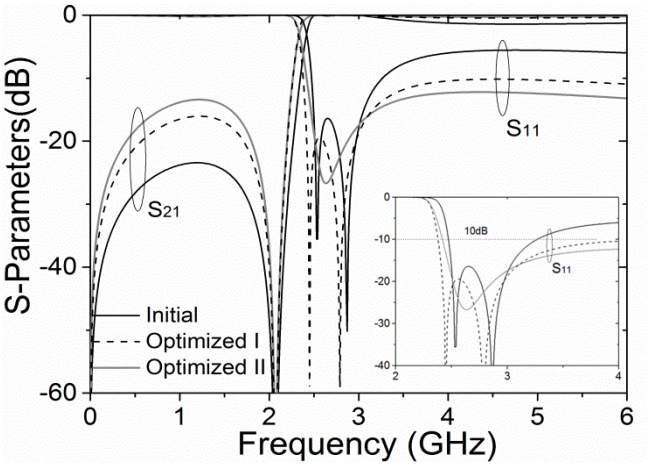

(a)

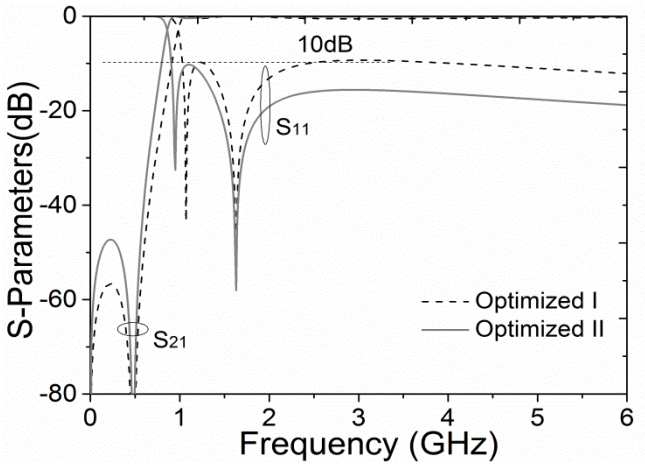

(b)

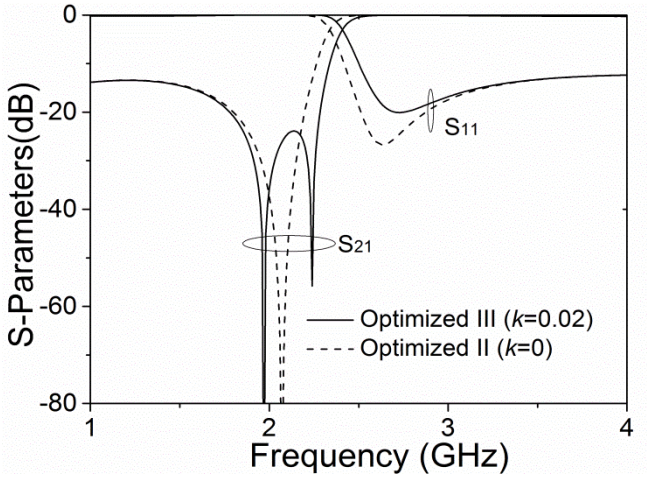

(c)

Figure 3.7: Simulated frequency responses of the proposed highpass filter with calculated and optimized *L*-*C* element values in Figure. 3.1. (a) State I with highest cutoff frequency. (b) Sate II with lowest cutoff frequency. (c) Sate I of the optimized responses for $k > 0$ (Optimized III) and $k = 0$ (Optimized II).

unchanged initially. In this manner, two illustrative optimized responses, i.e. optimized I and optimized II, are obtained in Fig. 3.7. As can be seen in Fig. 3.7 (a) and Table 3.1, for the optimized I, when the capacitances C_0 and C_{v1} become 2.0 and 1.0 pF, respectively, the filter keeps the similar cutoff frequency at about 2.5 GHz, but with a better return loss at the expense of the out-of-band rejection level. This means the variations of capacitances C_0 and C_{v1} have more significant effect on the in-band and out-of-band performance adjustment than the cutoff frequency shifting. This filter property can be further proved by the response of optimized II, which is obtained by further increasing C_0 from 2 to 3 pF.

Fig. 3.7 (b) plots the frequency responses for state II of this tunable filter with the lowest cutoff frequency (f_L). The obtained f_H (State I) and f_L (Stare II) are listed in Table 3.1. It is noteworthy that the optimized II obviously achieves a larger tuning range up to 62.8% than the optimized I of 56.9%. This is mainly associated with a larger capacitance C_0 of the optimized II that provides a wider matching range for tuning the capacitances C_{v1} and C_{v2}. However, compared with response of the optimized I, the larger C_0 of the optimized II also leads to poorer rejections in the stopband. So there is a trade-off between the tuning range and stopband performance.

Step 3: *Choose a proper mutual coupling k to accomplish the desired stopband performance.* Actually to some extent, the minimum rejection level in the stopband is determined by the values of C_0 and C_{v1} chosen during the optimization in the Step 2 (see in Fig. 3.7 (a)) owning to their limitation on out-of-band performance adjustment. However, according to the discussion in Fig. 3.6 (c), mutual coupling k is introduced and optimized here to achieve a better stopband performance (i.e. sharper cutoff frequency response and wider stopband width) by allocating two TZs. For instance, Fig. 3.7 (c) shows a further improved response (i.e. optimized III) with considering a mutual coupling of k=0.02 based on the response of optimized II at state I, where C_0, C_{v1}, and C_{v2} are kept the same except L_0 is decreased slightly to achieve the desired cutoff frequency (2.5GHz) (Table 3.1). As can be seen, if taking 20 dB rejections in the stopband as the design requirement, the optimized III can accomplish a wider stopband next to the cutoff frequency with shaper skirt selectivity than optimized II.

Table 3.1: *L*-*C* Element Values of the Proposed Filter in Figure. 3.1

		L_0 (nH)	C_0 (pF)	C_{V1} (pF)	C_{V2} (pF)	f_c (GHz)
Calculated		7.38	1.11	0.65	0.8	2.47
Optimized I	State I	7.38	2.0	1.0	0.8	2.38
	State II	7.38	2.0	1.36	15.0	1.025
Optimized II	State I	7.38	3.0	1.0	0.8	2.42
	State II	7.38	3.0	2.06	15.0	0.90
Optimized III	k=0.02	7.18	3.0	1.0	0.8	2.50

To go through the above synthesis procedure, two final optimized tunable states responses are illustrated as dash line in Fig. 3.11. The values of corresponding components k, L_0, $C_{0,}$ in Fig. 3.1 are then obtained as 0.02, 7.18 nH and 3.0 pF; while the tunable capacitances C_{v1} *and* C_{v2} are 1.0 pF and 0.8 pF for state I, and 2.1pF and 15pF for state II, respectively. Fig. 3.11 clearly shows the circuitry filter has a large frequency tuning range covering 0.92 to 2.50 GHz (up to 63.2%) as well as two controllable transmission zeros. Actually, this tuning range is kind of limited by the available minimum variable capacitance of C_{v2} in practice, otherwise it could be wider (e.g. when C_{v2}=0.6 pF, f_c=2.76 GHz, tuning rage = 66.7%). Besides, it can be seen at each state, the circuited simulated filter has a sharp cutoff frequency response, whose roll-off rate ξ, defined by (3.2), is 117 and 121 respectively. The physical implementation of this tunable highpass filter prototype topology will be demonstrated in subsequent section.

Overall, through the above analysis and illustrative design example it is found that the proposed topology has a simple and efficient operating mechanism to realize a wide tuning range with two adjustable TZs by using only two controller sources for three varactor diodes. While this advantage would be difficult to achieve by using a traditional elliptic topology (T-network) of the same five-order that results from its

asymmetrical characteristic as well as invariable inductors limitation. Also, compared with the same order Chebyshev prototype, the proposed one of Fig. 3.1 apparently has great advantages of sharper skirt selectivity with two controllable TZs and wider tuning range. In addition, based on the impact of C_0 on filter response discussed above, it is easily concluded that the tunable performance of the proposed topology, such as tuning range, can be further improved if capacitor C_0 is being adjusted as well. However in this manner, the complexity of dc bias circuits as well as the filter insertion loss will be increased accordingly. Hence, there is a trade-off between the tunable performances and circuit complexity.

3.3 Microstrip Implementation of Tunable Highpass Filter

3.3.1 Physical structure of tunable highpass filter

Fig. 3.8 shows the configuration of the proposed tunable highpass filter with biasing scheme. In this physical layout, neglecting the microstrip discontinuities, broadside-coupled patches located on two layers mainly contribute to the series capacitors C_0 in Fig. 3.1. Although C_0 may also be realized with chip capacitors for a smaller size, the trade-off would be the loss and spurious response. High-impedance microstrip meander lines are adopted to implement design inductors L_0. Varactor diodes attached here, C_{v1} and C_{v2}, correspond to the variable capacitors C_{v1} and C_{v2} in Fig. 3.1, respectively. As illustrated in Fig. 3.8 (c), the proposed filter is implemented by using a LCP bonded PCB multilayer technology, which consists of three metal layers including a solid ground plane at the bottom. LCP core film with a thickness of 25 μm ($\varepsilon_r = 3.0$ and $\tan\delta = 0.0025$) are double-side etched to support the metal circuits, and which is bonded directly on to a high dielectric constant PCB substrate ($\varepsilon_r = 10.2$, $h = 1.27$ mm and $\tan\delta = 0.0023$) with a 25-μm-thick LCP bonding film without any adhesive. As referred in [7], this multilayer technology best uses the available high dielectric constant of the PCB to realize compact size and to obtain the same features of LCP, such as 3D design flexibility and low cost, which is very promising in a simple multilayer circuit (e.g. three- metal layer circuit) realization. The fabrication process of LCP bonded multilayer PCB technology will be introduced in Chapter 8.

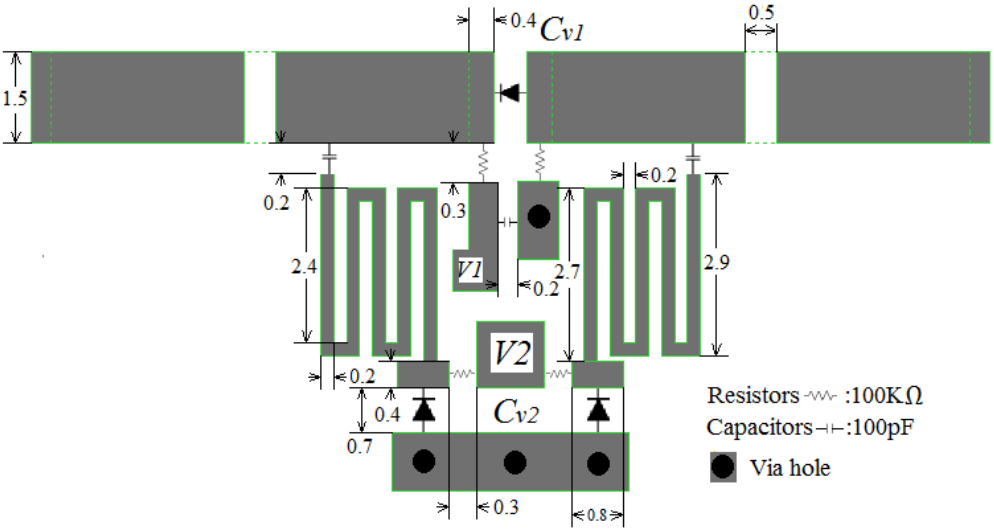

(a)

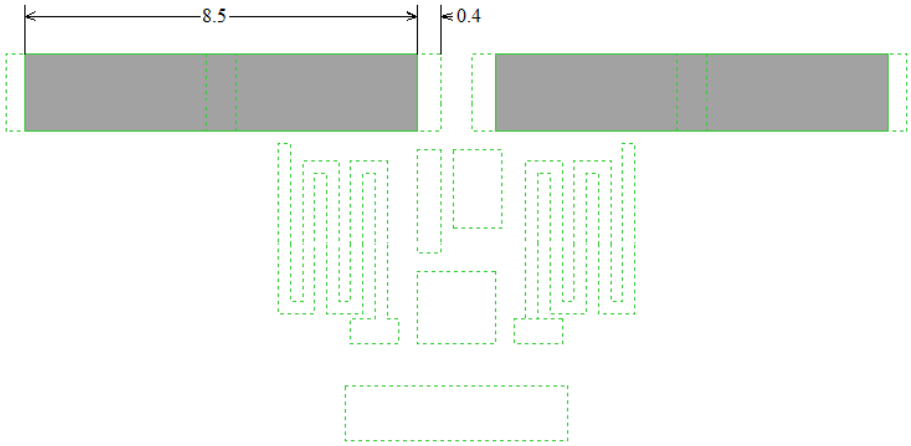

(b)

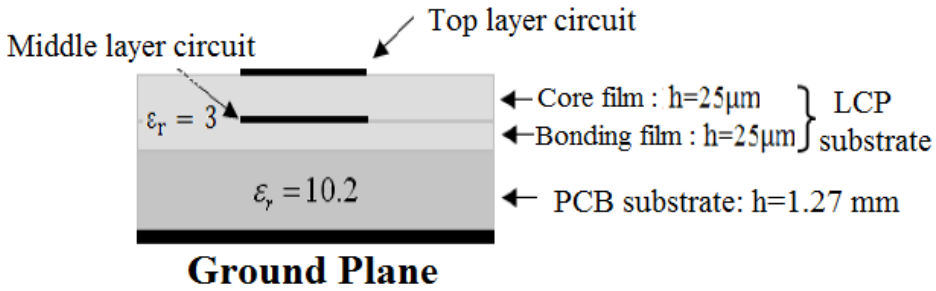

(c)

Figure 3.8: Physical layout of the proposed tunable HPF filter with dimensions. (a) Top layer layout. (b) Middle layer layout. (c) Views of the multilayer technology.

3.3.2 A parameter-extraction method for physical implementation

Although there are many classical formulas available in [6] and [8] to relate the lumped circuit elements to physical dimensions, for the proposed tunable highpass filter, these formulas are no longer valid since the design is built on inhomogeneous medium with two different substrates of LCP and PCB. Hence, a parameter-extraction method with a flowchart illustrated in Fig. 3.9 is employed in this work to determine the physical dimensions. Particularly, this procedure is composed of the following three steps:

Step 1: *Choose a proper physical implementation for each basic lumped element circuit*. The key building blocks of lumped-element circuits are inductors and capacitors, which can be designed in various physical layouts. For instance, in this work, the forms of MIM capacitor (see in Fig. 3.10 (a)) and high-impedance meander-line inductor (see in Fig. 3.10 (b)) are employed to realize a series capacitor C_0 and a shunt inductor L_0 in the proposed circuit model of Fig. 3.1. Basically, the use of one or any other layout mostly depends on the electrical performances that must be obtained as well as the ease of the realization.

Step 2: *Simulate the S-parameters of each microwave lumped component and utilize the obtainable 3 dB cutoff frequency to extract the associated element value.* Theoretically, microwave functional lumped components, including the ones adopted in this design (see in Fig. 3.10 (a) and Fig. 3.10 (b)), should exhibit the same transmission coefficient S_{21} as that of their ideal equivalent circuits (Fig. 3.10 (c) and Fig. 3.10 (d)) at 3 dB cutoff frequency, as expressed as:

$$S_{21}|_{\omega=\omega_c} = \left|\frac{2j\omega_c C_0 Z_0}{2j\omega_c C_0 Z_0 + 1}\right| = \frac{\sqrt{2}}{2} \qquad (3.17)$$

$$S_{21}|_{\omega=\omega_c} = \left|\frac{2j\omega L_0}{2j\omega_c L_0 + Z_0}\right| = \frac{\sqrt{2}}{2} \qquad (3.18)$$

where $Z_0 = 50\Omega$ is terminated impedance and ω_c is the obtainable 3 dB cutoff angular frequency in the EM simulation. As a result, the extracted C_0 and L_0 can be solved as:

$$C_0 = \frac{1}{2\omega_c Z_0} \qquad (3.19)$$

$$L_0 = \frac{Z_0}{2\omega_c} \qquad (3.20)$$

Step 3: *Make a comparison between the extracted and the desired element values*. If all the extract values approximate to the desired ones, we can accomplish the final design by stacking up all these components and then carry out fine-tuning of the whole design. Otherwise, modify the dimensions of related components until satisfying the requirements.

Apparently, the above-mentioned parameter-extraction method is a generalized technique that would be suitable for all the lumped-element designs built on homogeneous or inhomogeneous medium. However, the extracted element values obtained in (3.19)-(3.20) are not highly accurate, which result from the simple equivalent circuit models used in Fig. 3.10 (c) and (d) without considering the parasitic effects.

Based on this present method, the final designed tunable highpass filter (see in Fig. 3.8) is determined by comparison with the circuited ones at two stages as implied in Fig. 3.11. Additionally, herein it should be emphasized that the distance between two high-impedance sections in the physical layout is crucial for the two transmission zeros generation, resulting in an expected mutual inductive coupling *k*. The simulations are done using commercially available tool Sonnet [9] and Microwave Office [10]. Note that the simulated and theoretical insertion loss S_{21} and return loss S_{11} are almost identical over a very wide frequency tuning range except a little inconsistent.

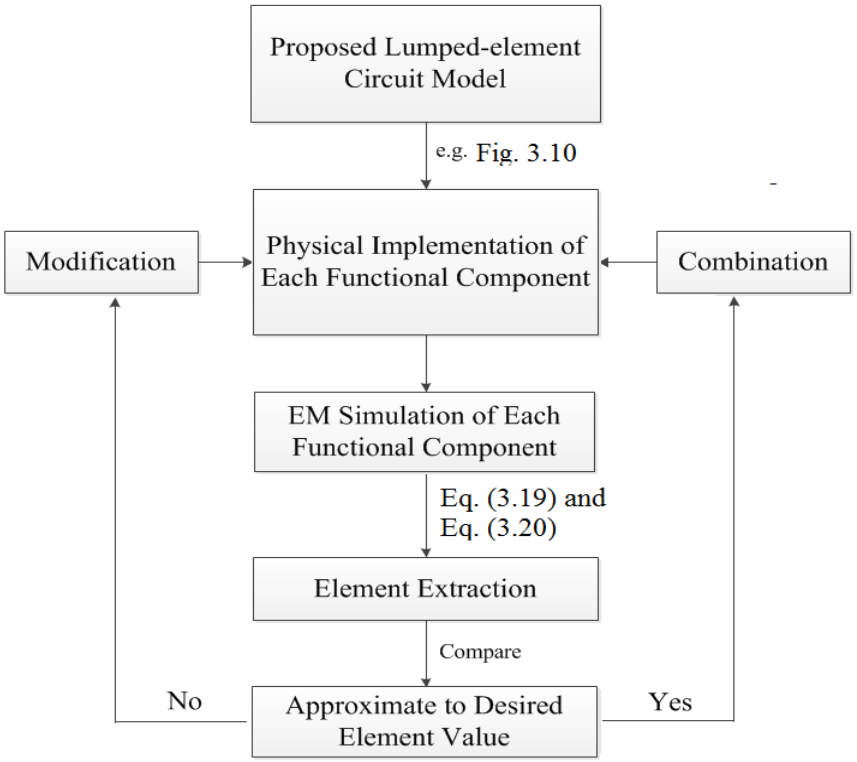

Figure 3.9: A general flowchart for the parameter-extraction procedure.

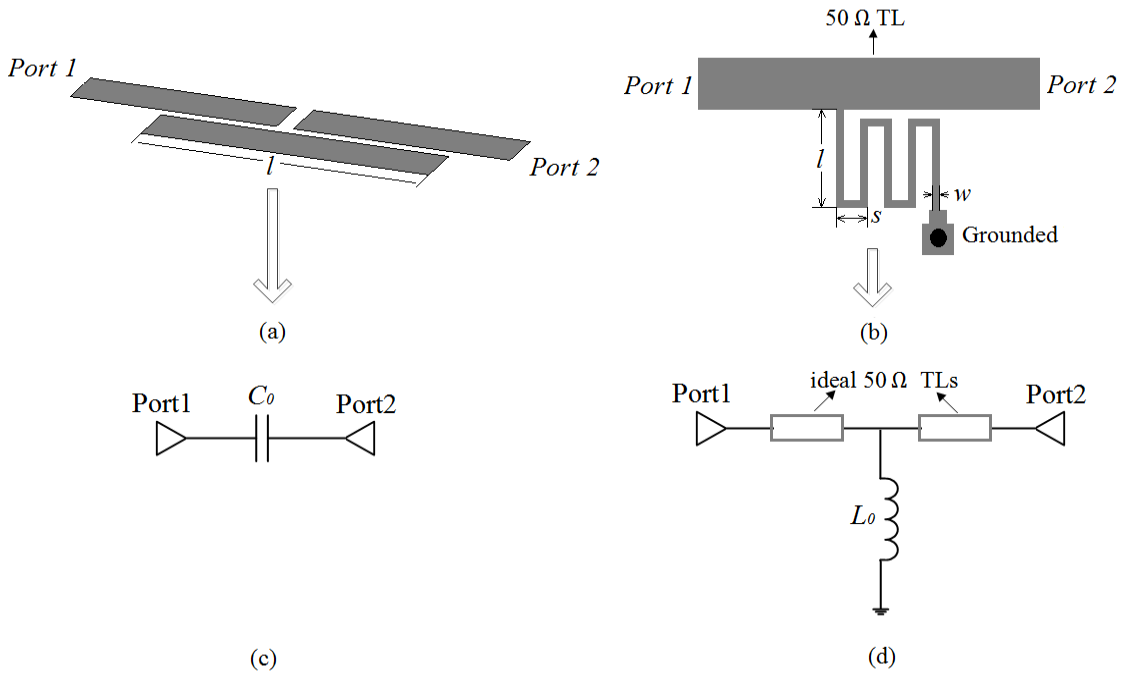

Figure 3.10: (a) and (c) Microwave lumped capacitor used in the proposed work and its ideal circuit model. (b) and (d): Microwave lumped inductor used in the proposed work and its ideal circuit model.

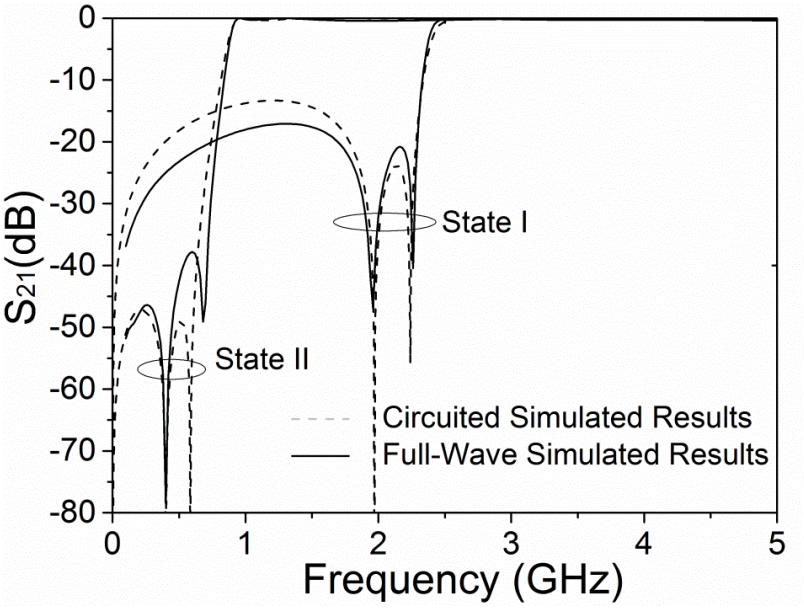

(a)

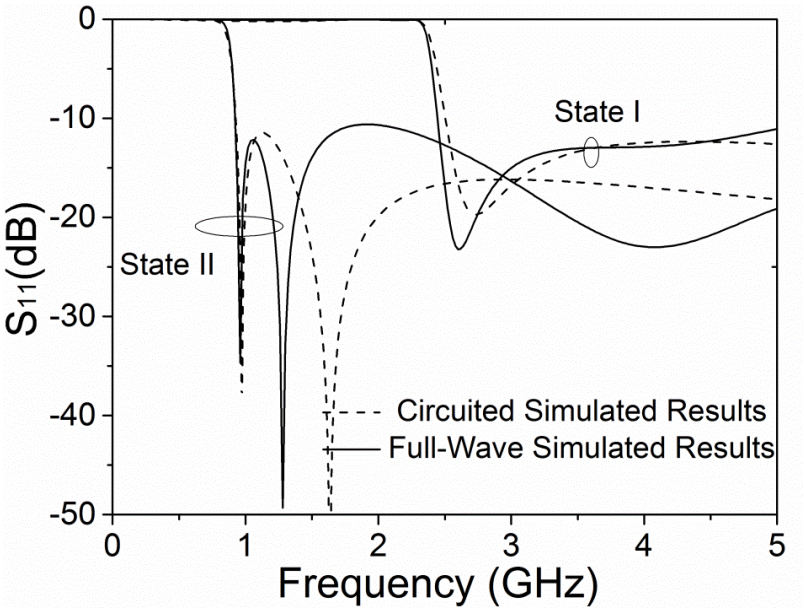

(b)

Figure 3.11: Full-wave simulation results and circuit responses of the proposed tunable HPF with two-stages. (a) S_{21}. (b) S_{11}.

3.3.3 Effect of Q on filter response

The effect of different varactor diode (i.e. C_{v1} *and* C_{v2}) unloaded Q on filter response is examined individually at state I (Fig. 3.11), as indicated in Fig. 3.12. As expected, both of limited low Q factors of varactor diodes C_{v1}, C_{v2} round off the passband edge leading to a poorer selectivity, but which become more pronounced in the response using lower Q of C_{v2} than the counterpart. Also it is seen that the dissipation loss of varactor C_{v2} has a greater effect on the null rejection than the case of C_{v1}. This verifies the lossy-component influence on the passband and stopband performance [6]. However, the zeros are well defined even with Q=25, showing the robustness of this design.

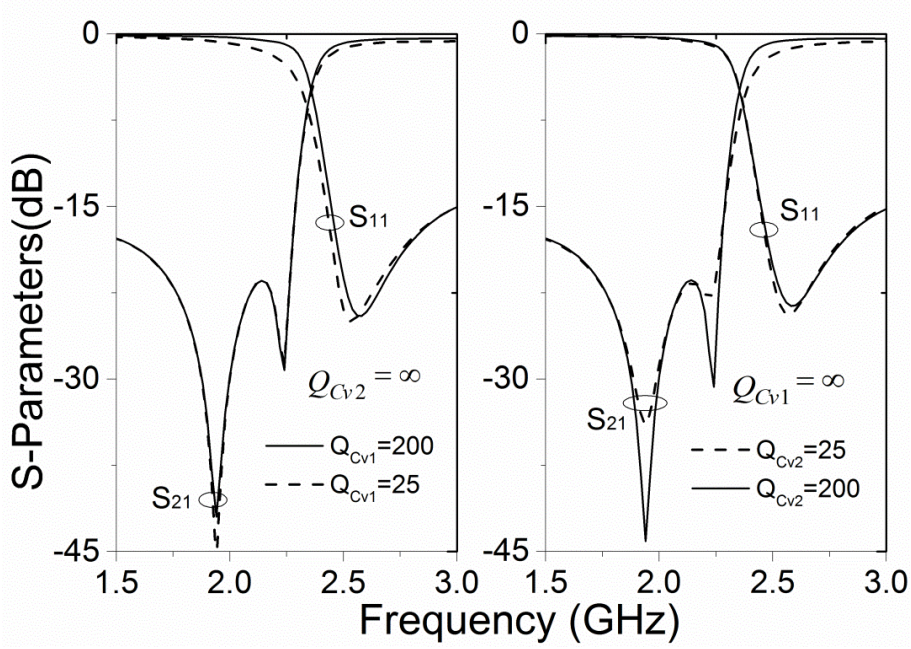

Figure 3.12: Simulated response of the proposed HPF versus different Q of C_{v1} and different Q of C_{v2}.

3.4 Fabrication and Measurement

A photograph of the fabricated tunable highpass prototype is shown in Fig. 3.13, where a compact circuit size of 18.3mm × 6.7mm ($0.15\lambda_g \times 0.05\lambda_g$, where λ_g is the guided wavelength at lowest f_c=1.03GHz) is achieved, excluding the input/output feed lines. Low-Q silicon abrupt junction diodes SMV2020-079LF (0.35-3.20 pF, and Q=500 for V_R=4 V at f=50 MHz) and SMV1800-079LF (0.84-15.78 pF, and R_s=3Ω for V_R=1.5 V at f=470 MHz) are adopted for tunable capacitors C_{v1} and C_{v2},

respectively. Murata 0402 GRM 100 pF capacitors are used for bypass capacitor, and Panasonic resistors 100 kΩ are utilized to reduce the RF-signal leakage in the bias network.

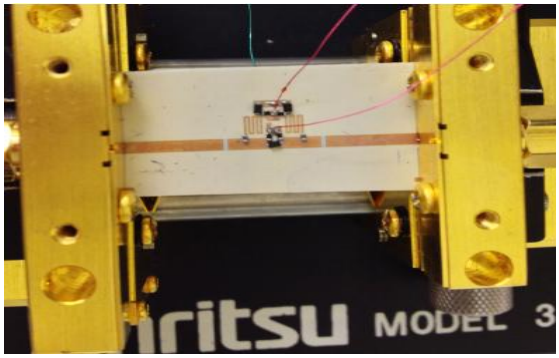

Figure 3.13: Photograph of the proposed tunable HPF with two transmission zeros.

In the final EM simulation, the SPICE models of the varactor diodes provided in [11]-[12] are analyzed and considered. The measured several typical tunable frequency responses are obtained using HP8510 network analyzer and Anritsu Test Fixture with reference planes defined at the I/O ports, which are compared with the simulated ones, as shown in Fig. 3.14. The reverse voltages V1, V2 applied on the varactors range from 1.5V to 7V, 2V to 30V, respectively, resulting in the cutoff frequency changing from 1.03 to 2.15 GHz with a tuning range up to 52.1%. The measured return loss is greater than 10 dB for all states, with the minimum insertion loss roughly varying from 0.6 to 1.0 dB. Furthermore, Fig. 3.15 presents the measured location of the first (f_{TZ1}), second (f_{TZ2}) transmission zeros and the cutoff frequency (f_c). One can see that both zeros tune together with the cutoff frequency with an approximately constant frequency separation. This means the filter response shape remains almost unchanged over the entire tuning range. Also as can be seen in Fig. 3.14, the implemented filter provides a sharp cutoff frequency response at each stage with stopband rejection level greater than 20 dB. The measured roll-off rates at sate I and state IV are 116 and 133 respectively, where α_{max} is assumend as 22 dB attenuation point in the definition (3.2). In general, good agreement between the measured and simulated *S*-parameters is observed in the experiment. While compared with the wide tuning range achieved in the ideal circuit prototype (section 3.2), the measured one is a bit smaller, which is constrainded by varactor diodes used here.

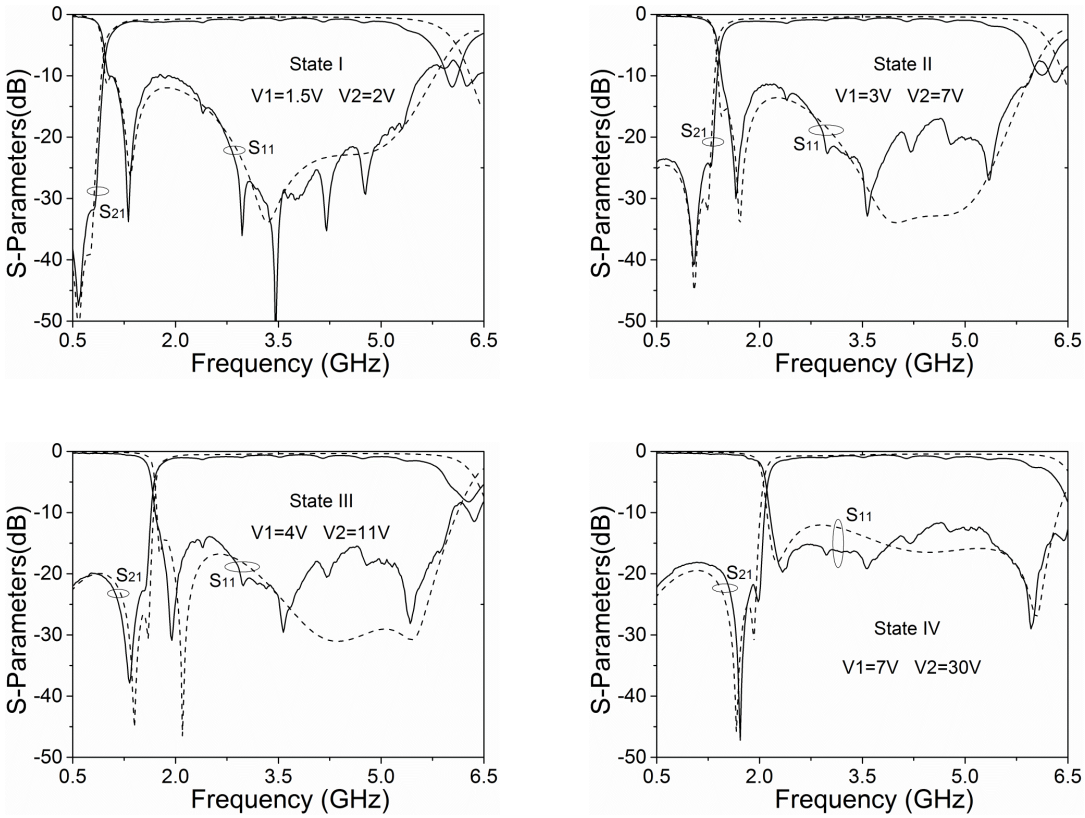

Figure 3.14: Measured (solid line) and simulated (dash line) *S*-parameters of the proposed tunable HPF.

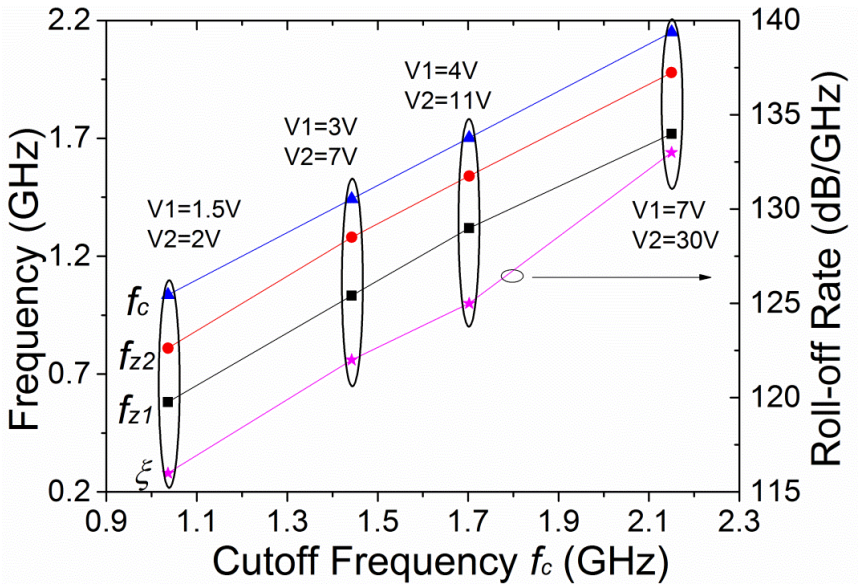

Figure 3.15: Measured the locations of TZs versus the cutoff frequency tuning and the corresponding measured roll-off rates.

3.5 Summary

In this chapter, a compact continuously tunable highpass filter with quasi-elliptic function response has been presented and discussed. Through the analysis on the tunable circuit model, the mechanisms of cutoff frequency tuning as well as transmission zeros controlling have been revealed. Analytical equations, design curves and lumped-element values synthesis procedure have been provided for easy reference. Further, a generalized parameter-extraction method for physical implementation has been demonstrated, which allowed extracting the values of microwave lumped structures built on inhomogeneous medium. To verify the proposed tunable topology and design procedure, a varactor-based tuned microstrip highpass filter has been implemented and characterized by using the LCP bonded multilayer PCB technology. It is shown that the implemented tunable highpass filter employed three varactor diodes but with only two common DC bias voltages to achieve a frequency tuning range covering 1030-2150 MHz. And over the entire tuning range, the proposed filter almost kept unchanged response shape with sharp skirt selectivity. To the author's knowledge, a varactor-tuned microstrip highpass filter with such wide continuous tuning range, compact size and sharp cutoff frequency response has not previously been reported.

Reference

[1] H. Kim, S.-J. Ho, M.-K. Choi, A.B. Kozyrev and D.W. van der Weide, "Combined Left- and Right-Handed Tunable Transmission Lines with Tunable Passband and 0° Phase Shift," *IEEE Trans. Microw. Theory Tech.*, vol. 54, no. 12, pp. 4178-4184, Dec. 2006.

[2] E.-K. Kim, G.-J. Sung, Y. Kim and Y.-C. Y., "Tunable Band-Stop Filter with Combined Right/Left-Handed Transmission Line," in *Proc. Asia-Pacific Micro. Conf.*, Singapore, Dec. 2009, pp. 1372-1375.

[3] M. Olsak, L. Matejicek, K. Vrba and Z. Smekal., "Realization of Nth-order electronically tunable highpass filter employing only N OTAs," in *Telecommunication, 10th International Conference.,* Mar.2003, vol. 1, pp. 671-676.

[4] V.G.K. Reddi, "Tunable High-Pass Filter Characteristics of a Special MOS Transistor," *IEEE Trans. Electron. Device.*, vol. 12, no. 11, pp. 581-589, Nov.1965.

[5] R.V. Snyder., "A Wide-Band Tunable Filter Technique Based on Double-diplexing and Low-Q Tuning Elements," in *IEEE MTT-S Int. Microw. Symp. Dig.*, vol. 3. Jun. 2000, pp. 1759-1763.

[6] J.-S. Hong, Microstrip filter for RF/Microwave applications, 2nd Edition, New York: John Wiley & Sons, 2011.

[7] J. Ni and J.-S. Hong," Compact Wideband Combline Filter Using LCP bonded Multilayer PCB Technology," *Proceedings of the 42st European Microwave Conference*, Oct. 2012.

[8] Inder Bahl, Lumped Element for RF and Microwave Circuits. Boston: Artech House, 2003.

[9] Sonnet *em*, Version 13.54, Sonnet Software Inc., New York, 2011.

[10]"AWR Microwave Office/Analog Office 9.06," Appl. Wave Res. Inc., El Segundo, CA, 2010

[11]"Skyworks SMV2020—079LF data sheet," Skyworks Solutions, Sunnyvale, CA, 2011.

[12]"Skyworks SMV1800—079LF data sheet," Skyworks Solutions, Sunnyvale, CA, 2011.

CHAPTER 4

Varactor-Tuned Microstrip Bandpass Filters with Different Passband Characteristics

4.1 Introduction

Previously, we discussed the designs of tunable lowpass and highpass filter based on various lumped-element filter topologies which solve the specific challenges in RF frond-end design. In this chapter, we put focus on the realizations of high performance tunable bandpass filters, since they are in an increasing demand in current and emerging multifunctional communication and radar systems and attracting a lot of attention for research.

An ideal tunable bandpass filter design generally requires a filter topology that can provide a wide tuning frequency range and bandwidth-controlling capability, as well as skirt selectivity and high linearity. In this context, coupled-resonators filters such as tunable combline filters are the most popular due to their compactness and wide stopband bandwidth characteristics [1]-[7]. However, when designing such tunable filters, owning to the frequency-dependence of the filter's constituent parts (couplings, electrical lengths, etc), it is difficult to maintain a good filter response over the entire tuning range without suitable coupling controlling networks for the compensation [2]-[5]. Also note that most of filters are designed in second-order coupled resonator configurations and do not possess a sharp roll-off filter response. Consequently, some solutions to this issue have been proposed recently by either increasing the order of the filter or employing extra variable capacitors to introduce transmission zeros at the expense of increasing the circuit size and complexity [6] [7]. Recent techniques, including dual-mode loop resonators [8] [9] and dual-mode patch resonator [10] [31], were exploited for centre-frequency and/or bandwidth tunabilities. Although there were high design freedoms on the control of non-coupled degenerate

modes, i.e. even- and odd-mode in these filters, the external couplings were still obstacles for achieving good matching and then which limited the tuning capabilities. In addition, a different class of reconfigurable bandpass filter based on parallel-coupled switched delay line approach was present in [11], which allowed centre frequency and passband bandwidth to be reconfigured, but consumed a relatively large circuit area. In [12], a tunable bandpass filter was constructed by the combination of a tunable high/lowpass filter, but the demonstrated BPF did not feature good tunability due to the limitations on the performance of LPF and HPF modules used. Tunable X-band bandpass filter employing BPF cascading BPF was also reported in [13], which was implemented by using YIG/GGG layers on RT/Duroid substrates.

In this chapter, two different, but related realizations of tunable bandpass filter with various passband characteristics are proposed, analyzed theoretically and demonstrated experimentally. The corresponding organization is as follows: initially, Section 4.2 presents a brief review on the fundamentals of traditional parallel-coupled line (PCL) bandpass filter design, which serves as the underlying theory for the following reported tunable bandpass filters. In Section 4.3, the first type of tunable bandpass filter that consists of varactor-loaded parallel-coupled microstrip lines (PCML) and short-circuited stubs is introduced and thoroughly analyzed. The benefit of this type of filter is that the lower passband edge and two transmission zeros positioned around the lower passband skirt can be reconfigured separately while the corresponding upper ones remain fixed. After that, Section 4.4 presents another type of tunable bandpass filter design that is based on cascading the first type of tunable bandpass filter and the tunable lowpass filter illustrated in Chapter 2. Plenty of experimental results are provided that demonstrate the operating principles of the proposed filter and address the promising filter characteristics of both centre frequency and passband bandwidth can be flexibly and simultaneously reconfigured within a wide tuning range, as well as multiple transmission zeros leading to high selectivity.

4.2 Fundamental Theory of Parallel-coupled Line Filter

Parallel-coupled transmission-line filters have found wide applications in microwave systems because of their compact size and easy fabrication [14]-[17]. Usually their parallel strips can provide a large coupling for a small spacing between the resonators, enabling the filter can achieve a wide bandwidth.

Fig. 4.1 illustrates a typically simple structure of PCL bandpass filter along with the equivalent circuit. As can be seen, the coupled-line section behaves simultaneously as two quarter-wavelength resonators and one admittance (*J*) inverter in between them, similar to a traditional parallel-coupled half-wavelength resonator filter. The difference is that the traditional parallel-coupled line filter utilizes half-wavelength resonators, while this filter is designed using quarter-wavelength resonators, thus the filter size can be reduced by half. Additionally, the two resonators are coupled with external ports by using the stepped impedance couplings that can be equivalent to *K*-inverters.

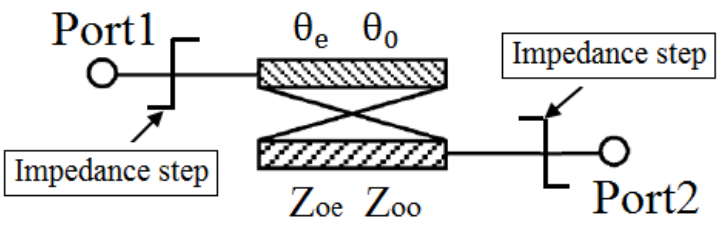

(a)

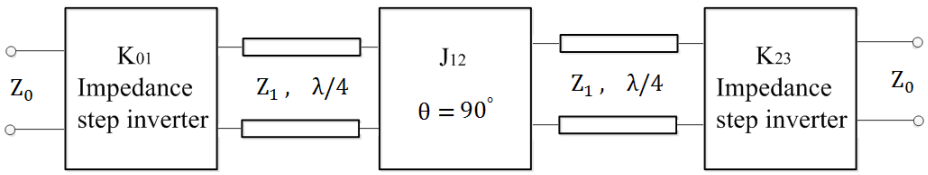

(b)

Figure 4.1: (a) Typical parallel coupled-line bandpass filter using $\lambda/4$ resonators. (b) Equivalent circuit.

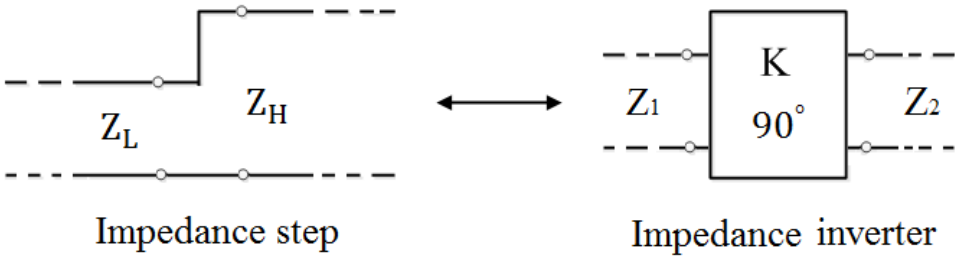

Figure 4.2: Equivalence between an impedance step and an impedance inverter [17].

For our investigation, Fig. 4.2 demonstrates a realization of transmission-line discontinuities by impedance step, which can be equivalent to an ideal impedance *K*-inverter. The main difference between each type is the impedance step can be physically realized over a wide band of frequencies, while the ideal 90° impedance inverter is only valid over a limited bandwidth. In theory, these two circuits are related by junction VSWR, where they exhibit the same coupling level at the transition junction [18]. In other word, the junction VSWR for both circuits should be equal, as expressed as:

$$\frac{Z_H}{Z_L} = \left(\frac{K^2}{Z_1 Z_2}\right)^{\pm 1} > 1 \qquad (4.1)$$

where Z_H/Z_L is defined as impedance ratio, Z_1 and Z_2 correspond to the characteristic impedances of the connecting transmission lines, and choose +1 when $K^2 > Z_1 Z_2$ and choose -1 when $K^2 < Z_1 Z_2$, ensuring the VSWR is always larger than one. For a practical filter design, it is suggested to use a full-wave simulator to select the step impedance for the same insertion loss as the original inverter circuit, where the coupling coefficient is inversely proportional to the impedance ratio [17]. Compared with other kinds of external couplings, using impedance step can produce a very strong coupling, since the transmission level can be very high, having a value around 1.9 dB for an impedance ratio of 2:1. As a result, this characteristic is often utilized in filters for realizing a wide bandwidth, even an ultra-wide bandwidth.

Furthermore, as stated previously, the filter illustrated Fig. 4.1 is similar to a traditional parallel-coupled half-wavelength resonator filter, so that the design equations can be given by [18]:

$$K_{01} = \sqrt{\frac{Z_0 \xi_1 FBW}{g_0 g_1}} \qquad (4.2)$$

$$J_{12} = FBW \sqrt{\frac{Z_0 \zeta_1 \zeta_2}{g_0 g_1}} \qquad (4.3)$$

$$K_{23} = \sqrt{\frac{Z_0 \xi_2 FBW}{g_2 g_3}} \qquad (4.4)$$

where $g_0,\ g_1,\ g_2,\ g_3$ are the element values of the lowpass prototype, *FBW* is the fraction bandwidth defined by $\Delta f / f_0$, and, since the two resonators are quarter-wavelength, we have the susceptance slope parameters $\zeta_1 = \zeta_2 = \pi/4Z_1$ and reactance slope parameters $\xi_1 = \xi_2 = \pi Z_1/4$. Substituing (4.1) into (4.2) and (4.4), the characteristic impedances of high-impedance sections (i.e Z_1 in Fig. 4.1) are achieved; the normalized *J*-inverter admittance is obtained directly from (4.3). Further, the even- and odd-mode impedances of coupled-lines can be determined by [11]:

$$Z_{oe} = Z_1[1 + Z_1 J + (Z_1 J)^2] \qquad (4.5)$$

$$Z_{oo} = Z_1[1 - Z_1 J + (Z_1 J)^2] \qquad (4.6)$$

However, for a practical design, a difficulty arises because it is generally not possible to realize arbitrary Z_{oe} and Z_{oo} with a fixed-line width. For this reason, a coupling coefficient *k* is defined as (4.7) to achieve more flexible coupling matching to the desired Z_{oe} and Z_{oo} [19].

$$k = \frac{Z_{oe} - Z_{oo}}{Z_{oe} + Z_{oo}} \qquad (4.7)$$

As an example, a parallel-coupled microstrip line bandpass filter is designed to have a fractional bandwidth of 86% at centre frequency $f_0 = 2$ GHz. A two-order Butterworth lowpass filter prototype is chosen, with the element values are $g_0 = g_3 = 1$ and $g_1 = g_2 = 1.4142$. By using the above equations (4.1)-(4.7), Z_1 Z_{oe} and Z_{oo} are calculated as: 104 Ω, 178 Ω and 78 Ω, respectively; the coupling coefficient k is obtained around 0.39. Fig. 4.3 indicates the circuit-simulated

S-parameters of an ideal circuit (see in Fig. 4.1) and those by full-wave simulating a microstrip realization that is built on a substrate with a dielectric constant of 10.2 and thickness of 1.27 mm, as inserted in Fig. 4.3. Regarding the physical dimensions of such a microstrip structure, the physical length *l* corresponds to an electrical length of $\lambda/4$ at the desired center frequency, and the gap *s* is mostly determined by the obtainable coupling coefficient *k*. As shown in Fig. 4.3, it is noted that two sets of responses generally agree well with each other in the passband, except the maximum attenuation of the ideal circuit model appears at $2f_0$ (4 GHz), while that of the microstrip structure is larger than $2f_0$. This is because unlike the case of $\theta_{\mathrm{e}} = \theta_{\mathrm{o}} = \pi/2$ assumed in the ideal model (homogeneous medium), microstrip is inhomogeneous medium, the even- and odd-mode propagation velocities for a coupled pair of microstrip lines are not equal that leads to $\theta_o < \theta_e$ [20].

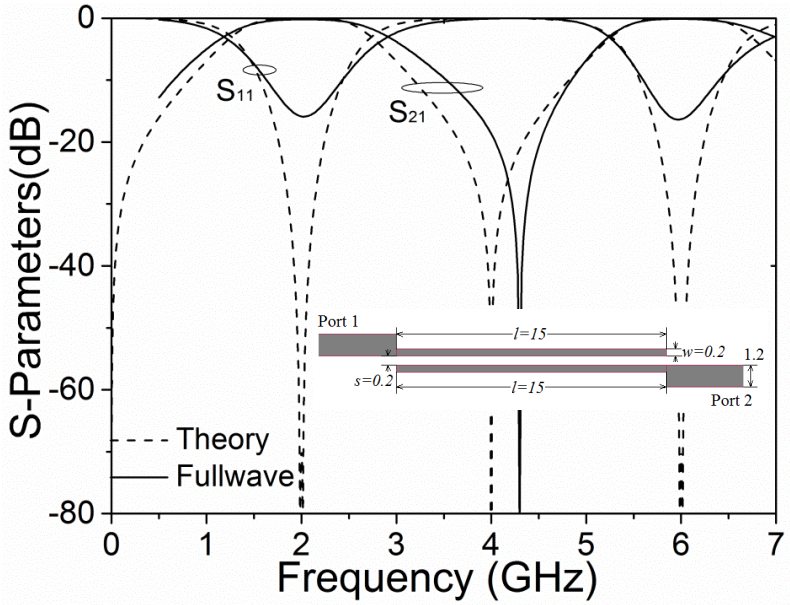

Figure 4.3: Simulated results of the illustrative parallel-coupled line bandpass filter by both circuited simulator and full-wave simulations.

4.3 Tunable Bandpass Filter with Reconfigurable Lower Passband Edge

4.3.1 Physical layout of tunable bandpass filter

A varactor-tuned bandpass filter based on PCML with biasing scheme is proposed in Fig. 4.4, which is designed by using LCP bonded multilayer PCB technology.

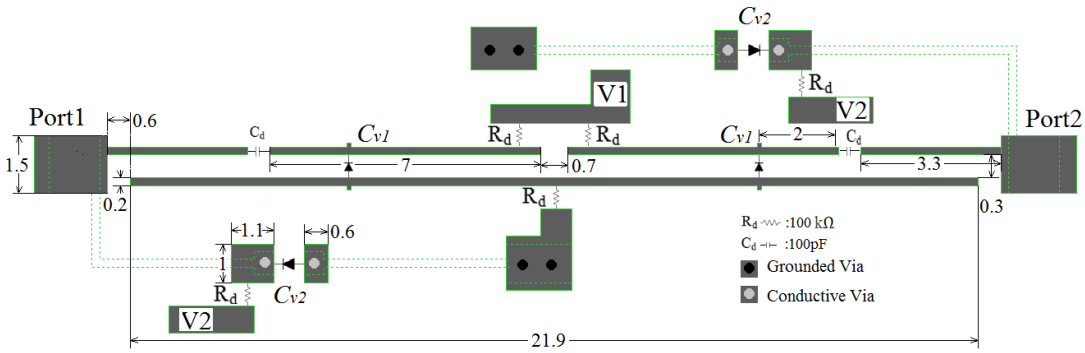

(a)

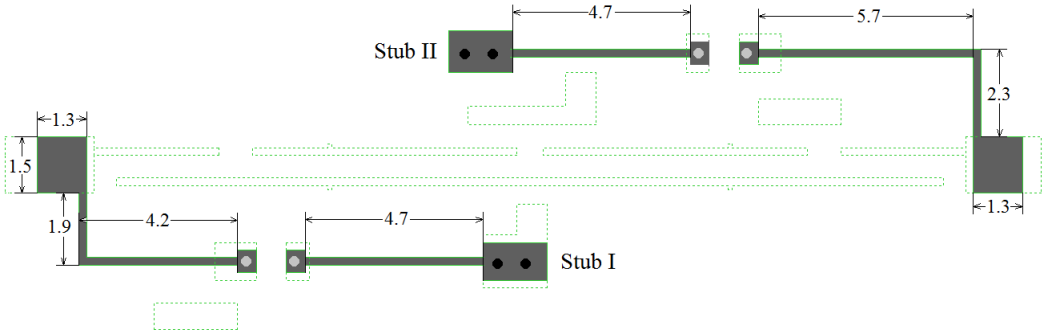

(b)

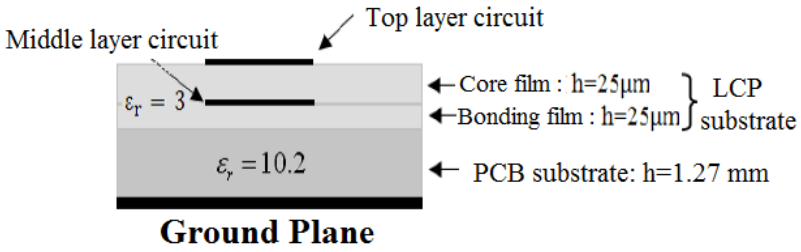

(c)

Figure 4.4: Proposed tunable bandpass filter with reconfigurable lower passband edge. (a) Top layer layout. (b) Middle layer layout. (c) View of the multilayer technology (All dimensions are in millimeters).

Shown in Fig. 4.4 (a) is the main body of the proposed bandpass filtering structure on the top layer with excitation ports, where two varactor diodes C_{v1} are centrally attached between each pair of parallel-coupled lines, resulting in the lower passband edge tuning while keeping the upper one constant. The other two varactor diodes C_{v2} are connected, through conductive vias, to two different short-circuited stubs (i.e. Stub I and Stub II) placed in the middle layer (Fig. 4.4 (b)), which are mostly used to generate two controllable transmission zeros close to the lower passband skirt to improve the selectivity for the tunable lower passband edge. It should be highlighted that these two stubs coupled to input/output ports can also contribute to increasing the slope of upper stopband by introducing another two fixed transmission zeros. The associated analyses will be elaborate later. As demonstrated in Fig. 4.4 (c), LCP core film with a thickness of 25μm ($\varepsilon_r = 3.0$ and $\tan\delta = 0.0025$) is double-side etched to support the metal circuits, which is then bonded directly on to a high dielectric constant PCB substrate ($\varepsilon_r = 10.2$, $h = 1.27$mm and $\tan\delta = 0.0023$) with a 25-μm-thick LCP bonding film without any adhesive.

4.3.2 Characteristics of varactor-loaded parallel coupled-line filter

As one part of the proposed design, the parallel-coupled line structure with varactor diodes loaded is studied firstly, which can be divided into two identical subsections, as shown in Fig. 4.5. For simplicity, the equivalent circuit of one subsection is given in Fig. 4.6 (a) to investigate the properties of the proposed tunable filter. Herein it is assumed that the even- and odd-mode electrical lengths are equal.

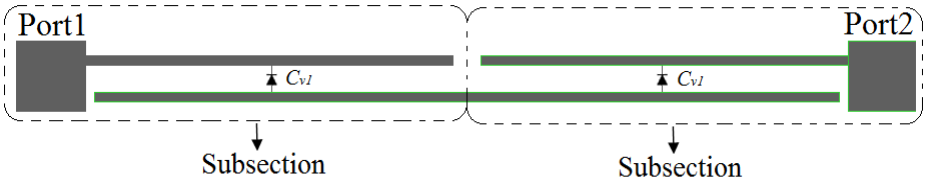

Figure 4.5: Symmetrical varactor- tuned parallel-coupled line structure with two subsections.

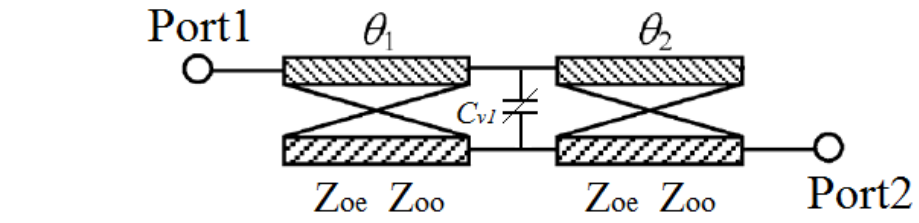

(a)

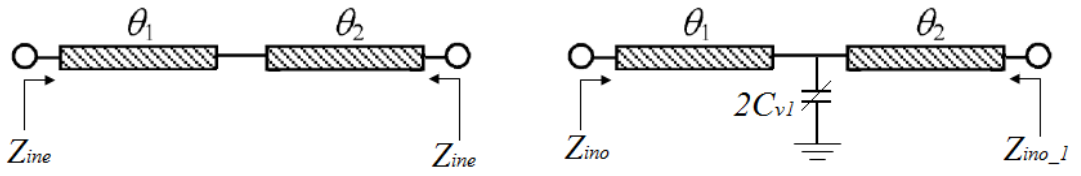

(b) (c)

Figure 4.6: (a) Equivalent circuit of one subsection demonstrated in Figure. 4.5. (b) Even-mode circuit. (c) Odd-mode circuit.

In order to obtain the electrical characterization of varactor-loaded PCL filter shown in Fig. 4.6 (a), the impedance matrix is derived in Appendix B. Generally, using the even-odd mode analysis for a symmetrical four-port coupled line network [21] and by imposing open circuits at two of the four ports as shown in Fig. 4.6 (a), the corresponding impedance parameters are obtained as:

$$Z_{11} = \frac{1}{2}(Z_{ine}+Z_{ino}) \qquad (4.8)$$

$$Z_{22} = \frac{1}{2}(Z_{ine}+Z_{ino\_1}) \qquad (4.9)$$

$$Z_{12} = Z_{21} = \frac{1}{2}\left(\frac{Z_{ine}}{A_e} - \frac{Z_{ino\_1}}{A_o}\right) \qquad (4.10)$$

where Z_{ine} is the even-mode input impedance seen at left or right port of Fig. 4.6 (b) when the other port is open-circuited. Similarly, Z_{ino} / Z_{ino_1} represents the odd-mode input impedance obtained from left/right port of Fig. 4.6 (c) when the other port is open-circuited. While A_e and A_o can be derived from the *ABCD* matrices for even- and odd-mode circuits of Fig. 4.6 (b) and (c) respectively. It can be shown that

$$Z_{ine} = -jZ_{oe}\cot(\theta_1 + \theta_2) \tag{4.11}$$

$$Z_{ino} = -j\frac{Z_{oo} - Z_{oo}\tan\theta_1(2Z_{oo}\omega C_{v1} + \tan\theta_2)}{2Z_{oo}\omega C_{v1} + \tan\theta_1 + \tan\theta_2} \tag{4.12}$$

$$Z_{ino\_1} = -j\frac{Z_{oo} - Z_{oo}\tan\theta_2(2Z_{oo}\omega C_{v1} + \tan\theta_1)}{2Z_{oo}\omega C_{v1} + \tan\theta_1 + \tan\theta_2} \tag{4.13}$$

$$A_e = cos(\theta_1 + \theta_2) \tag{4.14}$$

$$A_o = \cos(\theta_1 + \theta_2) - 2Z_{oo}\omega C_{v1}\cos\theta_1\sin\theta_2 \tag{4.15}$$

Consequently, the scattering parameters can be found by

$$S_{11} = \frac{(Z_{11} - Z_0)(Z_{22} + Z_0) - Z_{12}Z_{21}}{(Z_{11} + Z_0)(Z_{22} + Z_0) - Z_{12}Z_{21}} \tag{4.16}$$

$$S_{22} = \frac{(Z_{11} + Z_0)(Z_{22} - Z_0) - Z_{12}Z_{21}}{(Z_{11} + Z_0)(Z_{22} + Z_0) - Z_{12}Z_{21}} \tag{4.17}$$

$$S_{12} = S_{21} = \frac{2Z_{21}Z_0}{(Z_{11} + Z_0)(Z_{11} + Z_0) - Z_{12}Z_{21}} \tag{4.18}$$

where Z_0 is the 50-Ω terminal characteristic impedance.

To examine the resonant frequency of the PCL structure as shown in Fig. 4.6 (a), a loose coupling mechanism, which does not greatly load the circuit to yield influence on the resonant frequency, is required for external excitation. According to the discussions in Section 4.2, the external coupling level is proportional to the inverse of the impedance ratio, thus the terminal impedance Z_0 is set to 0.1 Ω in order to obtain a weak coupling (ideal case: Z_0 = 0 with an infinite impedance ratio). First of all, without varactor loading or C_{v1} = 0, by utilizing the above equations (4.8)-(4.18), Fig. 4.7 illustrates the resonant responses versus different Z_{oe} and Z_{oo} at f_0=2 GHz. As can be seen, there are two frequency peaks obtained and they are shifted synchronously by changing Z_{oe} and Z_{oo}, individually. Normally, larger coupling results in a broader separation of the two resonant peaks. For clarity of description, let

us define such two resonant peaks as the characteristic frequencies f_e and f_m based on the general theory of couplings stated in [19]. In this way, the frequencies f_e and f_m are associated with the odd-mode (electrical wall) and even-mode (magnetic wall) circuits of the structure, respectively. Additionally, since there is a larger potential difference along the coupled lines, a strong capacitive coupling (electrical coupling) is dominated, resulting in $f_e < f_m$ observed.

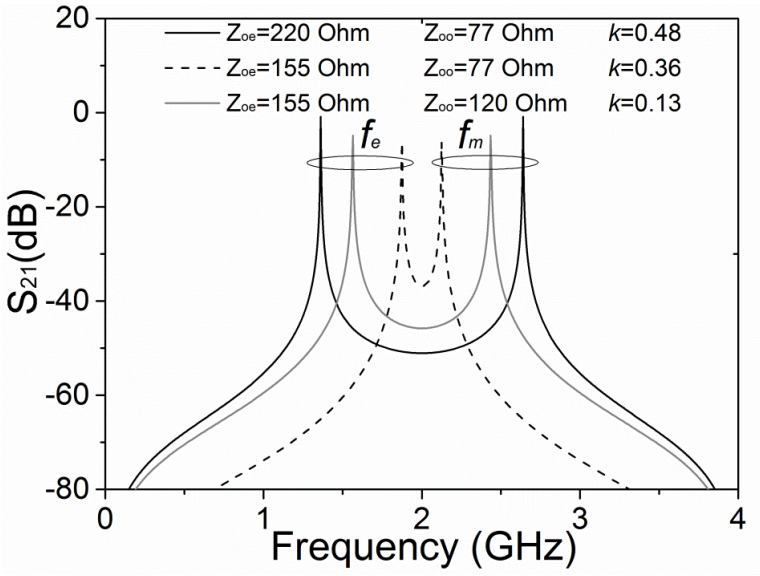

Figure 4.7: Resonant frequency responses of the parallel coupled-line structure shown in Figure. 4.6 (a) versus different Z_{oe} and Z_{oo} under a weak external coupling.

With varactor loading, Fig. 4.8 illustrates the effect of variable capacitor C_{v1} on the resonant frequency responses, with selected values of $Z_{oe} = 155\ \Omega, Z_{oo} = 77\ \Omega$ and f_0=2 GHz. In Fig. 4.8 (a), it is remarkable that for the case of symmetrically loading varactor diode (i.e. θ_1/θ_2 =1), by solely increasing the capacitance C_{v1} from 0 pF to 2.0 pF, the resonant frequency of f_e is dramatically tuned down, while the frequency of f_m remains stationary. This is because from the even-odd mode analysis stated above, it is noteworthy the loaded capacitor C_{v1} only has effect on odd-mode input impedance rather than even-mode one. Technically, the relationship between the capacitance C_{v1} and frequency f_e can be analytically expressed by solving the equations (4.8)-(4.18). But due to the solution being too complex, a discussion will only be given here.

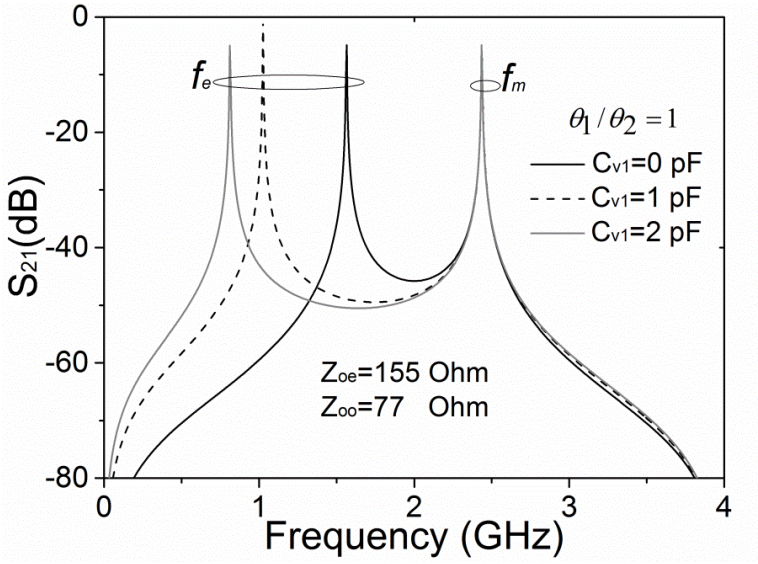

(a)

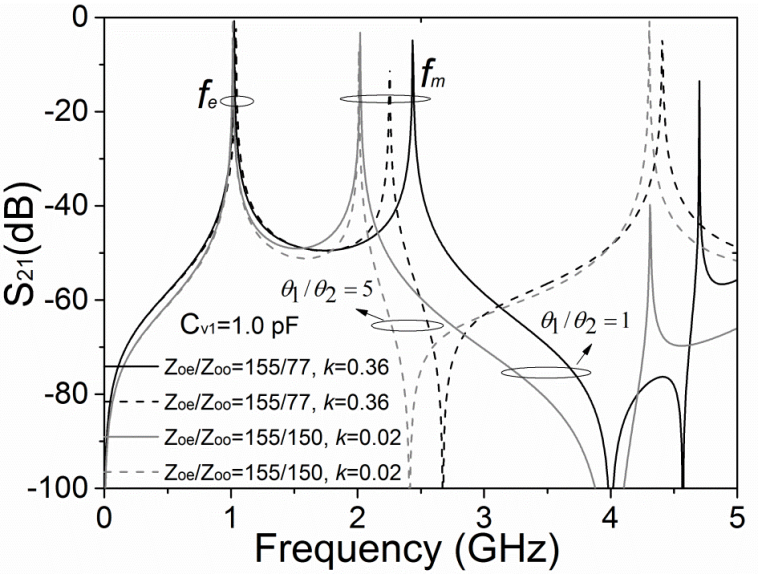

(b)

Figure 4.8: Under the weak external coupling, resonant responses of the varactor-loaded parallel-coupled line structure of Figure. 4.6 (a) obtained by varying: (a) Capacitances of varactor diode C_{v1}. (b) Loading location of $C_{v1.}$

Fig. 4.8 (b) mainly discusses the resonant responses dependence on the loading location θ_1/θ_2. Note that with C_{v1} =1.0 pF, only the symmetrical cases ($\theta_1/\theta_2 = 1$) will produce a constant transmission zero at $2f_0$. This is because, at $2f_0$, the symmetrical cases can provide a virtual short circuit at the loading location of capacitor to eliminate the effect of C_{v1}. While for the asymmetrical cases (e.g. $\theta_1/\theta_2 = 5$), the transmission zeros are usually placed at frequencies smaller than $2f_0$. Additionally, as shown in Fig. 4.8 (b), it is interesting to see that varying the loading location of C_{v1}, the frequency f_e is always kept fixed. This is because, for the odd-mode circuit of parallel coupled lines, only the values of C_{v1} contributes to the total coupling capacitance between the lines rather than its location [22]. While regarding the frequency f_m, it seems to be related with the coupling coefficient. In theory, it shouldn't be changed since C_{v1} has no effect on the even-mode, as illustrated the weak-coupling cases of $Z_{oe} = 155\ \Omega$ and $Z_{oo} = 150\ \Omega$ with different loading locations. However, under a strong coupling (e.g. $Z_{oe} = 155\ \Omega$ and $Z_{oo} = 77\ \Omega$), it seems that the transmission zeros' shifting enforce frequency peak f_m to be somehow changed accordingly.

Based on the discussions in Fig. 4.8, Fig. 4.9 illustrates the corresponding filter responses with strong external couplings (Z_0 =50 Ω) considered. As expected, by adjusting the capacitance C_{v1} from 0 to 2 pF, the lower passband edge (3 dB bandedge) can be significantly tuned from 1.38 to 1.48 GHz, with the left transmission pole dramatically tuned as well, while the upper passband edge remains almost stationary around 2.7 GHz (see in Fig. 4.9 (a)). On the other hand, as shown in Fig. 4.9 (b), with a fixed element value of C_{v1} (e.g. C_{v1} =1 pF), by varying its loading location, both the upper passband edge and the transmission zero are adjusted accordingly, resulting in a narrower bandwidth obtained than the symmetrical one. As a rule, the bandwidth becomes smaller as the loading location of C_{v1} is closer to the open end. Moreover, we can observe that two transmission poles in the passband almost maintain constant when changing the loading location of C_{v1}, which further proves the conclusion obtained in Fig. 4.8 (b).

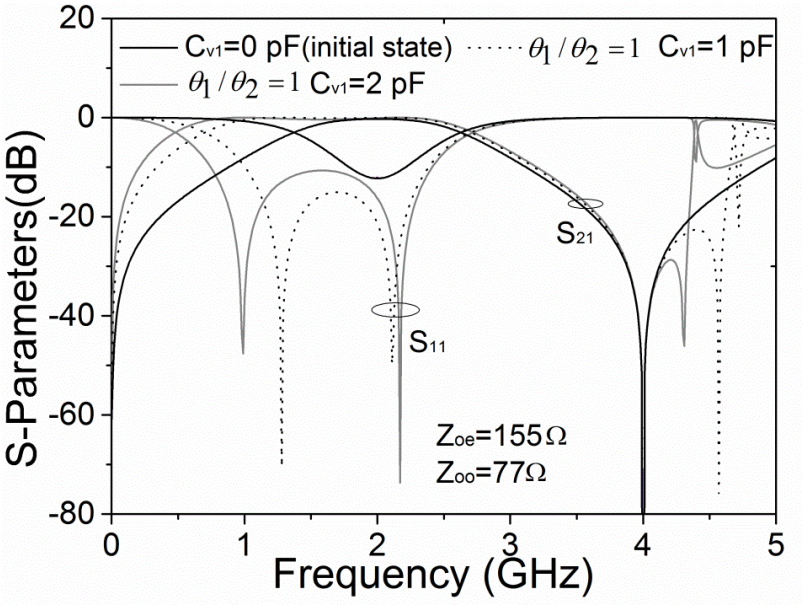

(a)

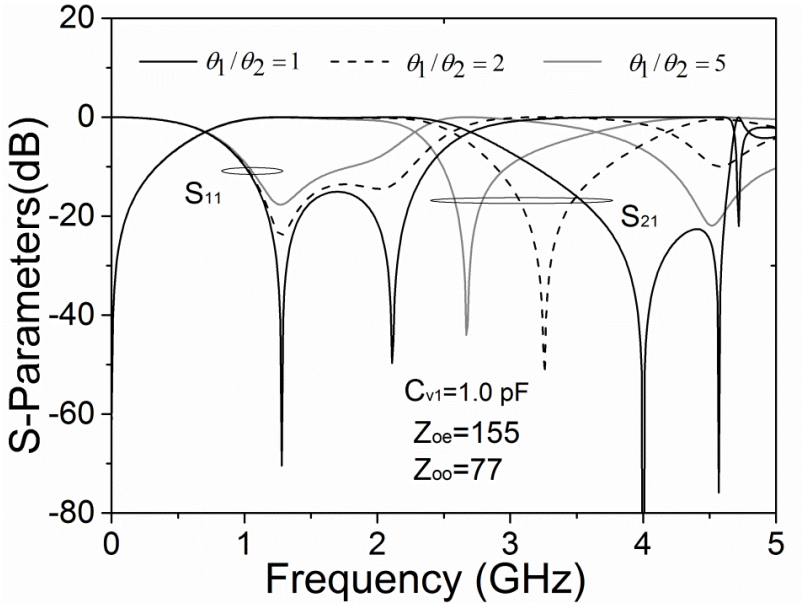

(b)

Figure 4.9: Under the strong external coupling, filter responses of the varactor-loaded parallel-coupled line structure of Figure. 4.6 (a) obtained by varying: (a) Capacitances of varactor diode C_{v1}. (b) Loading location of $C_{v1.}$

In light of the above discussions, *S*-parameters of the whole structure of Fig. 4.5 versus C_{v1} for $\theta_1/\theta_2 = 1$ are calculated in Fig. 4.10 by utilizing the following formulas [23]:

$$S_{11}{}^{\text{whole}} = S_{11} + \frac{S_{21}{}^2 S_{11}}{1 - S_{22}S_{11}} \qquad (4.19)$$

$$S_{12}{}^{\text{whole}} = S_{21}{}^{\text{whole}} = \frac{S_{21}{}^2}{1 - S_{22}S_{11}} \qquad (4.20)$$

$$S_{22}{}^{\text{whole}} = S_{22} + \frac{S_{21}{}^2 S_{22}}{1 - S_{22}S_{11}} \qquad (4.21)$$

where S_{11}, S_{22} and S_{21} are given by (4.16)-(4.18). From Fig. 4.10, it is clear that the whole structure has similar tunable characteristics as one subsection discussed above, which has controllable lower passband edge by properly tuning the value of C_{v1} while almost keeping the same filter shape at the upper band. Obviously, due to the higher order, the stopband performance of the whole structure, especially the selectivity in the lower stopband, is improved than that of one subsection.

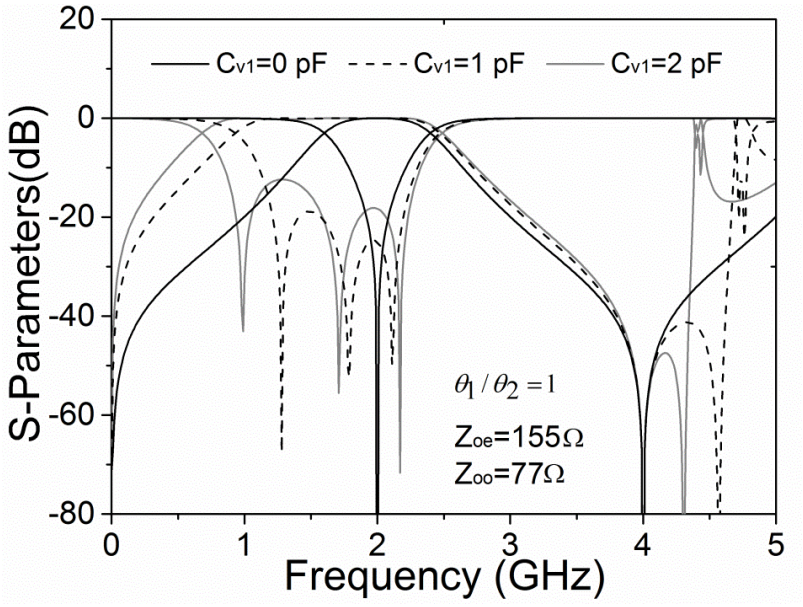

Figure 4.10: Frequency responses of Figure. 4.5 obtained by tuning varactor diode C_{v1}.

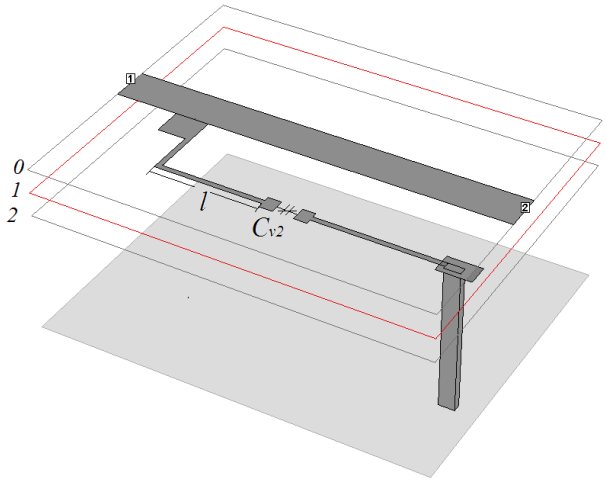

Figure 4.11: Simplified structure for demonstrating transmission zeros creation.

4.3.3 Creation of additional transmission zeros

In order to improve the selectivity, additional transmission zeros are introduced in the proposed tunable filter design of Fig. 4.4. The mechanism of creating these transmission zeros is elaborated by using a simplified structure of a short-circuited stub coupling to a 50 Ω transmission line, as implied in Fig. 4.11. Herein the stub is assumed to have a fixed total length as the Stub I in Fig. 4.4 (b) except with adjustable loading location (marked as '*l*') of varactor diode C_{v2}. Initially, for *l*=4.2mm in Fig. 4.11, Fig. 4.12 (a) indicates there are two sharp narrow notch bands originated from this stub. While by changing the capacitance of C_{v2} from 0.5 to 5.0 pF, it is very interesting to see the first notch band is successfully tuned rather than the second one. This is attributed to the lumped nature of the stub when operating at the first notch band. Technically, it can be equivalent to a lumped element model of C_0, L and C_{v2} connecting in series as indicated by the small insert in Fig. 4.12 (a), where C_0 represents the coupling between the stub and main transmission line; L is the equivalent inductance of this shunt stub. To this end, the first notch frequency can be expressed as:

$$\omega_{z1} = 1/\sqrt{LC_s} \qquad (4.22)$$

$$C_s = C_0 C_{v2}/(C_0 + C_{v2}) \qquad (4.23)$$

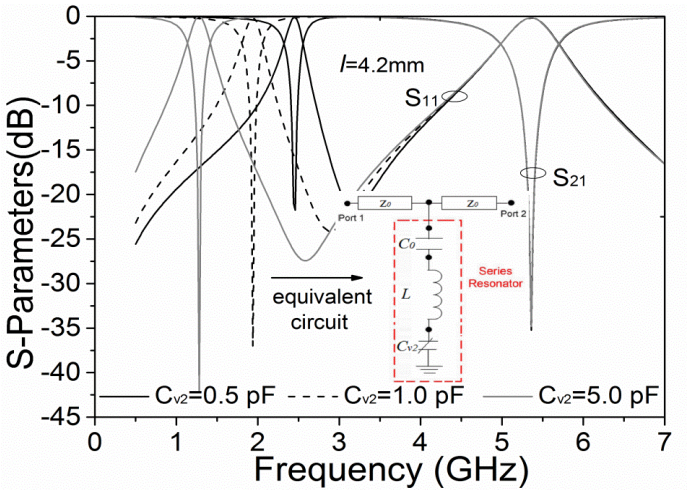

(a)

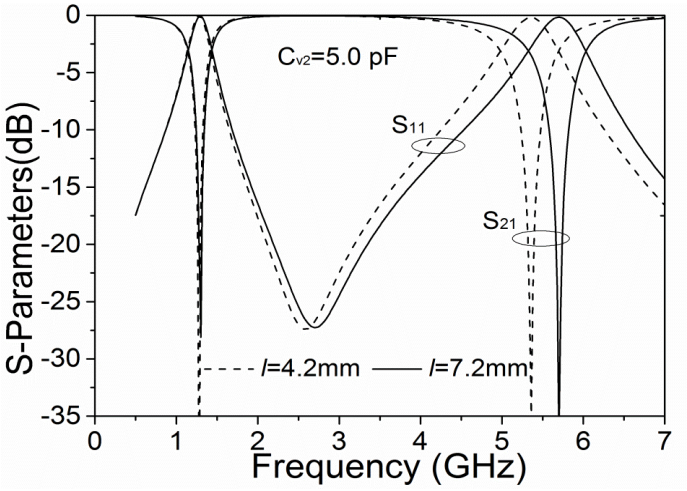

(b)

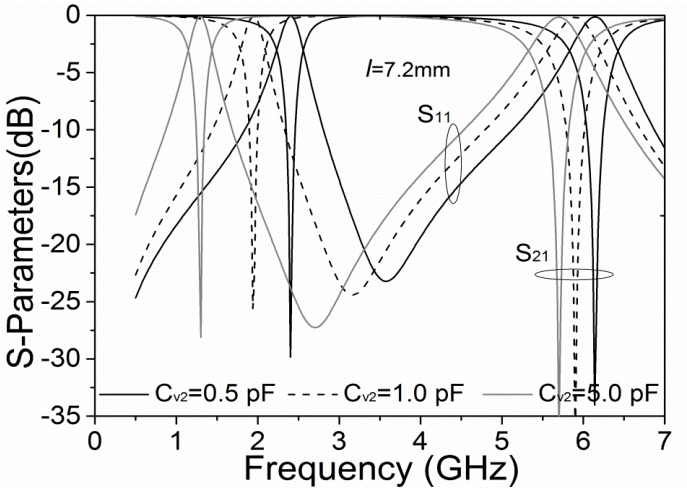

(c)

Figure 4.12: Notch band frequencies versus (a) Capacitances of C_{v2} with l=4.2mm. (b) Loading location l with C_{v2}=5.0 pF. (c) Capacitances of C_{v2} with l=7.2mm.

In this equivalent model, the capacitor C_0 also somehow reduces the effect of tunable C_{v2} capacitance so as to increase the frequency tuning resolution. Actually, this lumped property can be further proved by the responses given in Fig. 4.12 (b), where varying the loading location l of C_{v2} has little effect on the first notch band. In contrast, it is found that the second notch band is more dependent on the location l. This is because at the second notch band, the short-circuited stub acts more like as a distributed resonator electromagnetically coupled to the main transmission line to form a transmission zero. In this case, theoretically, only when the magnitude of electrical field along the capacitor C_{v2} is very weak that approximates to zero, the effect of capacitances C_{v2} on the frequency of second notch band can be eliminated. Otherwise, as illustrative example of l=7.2mm given in Fig. 4.12 (c), varying the capacitance C_{v2} also leads to the second notch band a bit tuning together with the first one. Overall, the dimension of the stub can be determined by the first desired transmission zero, while the loading location of C_{v2} needs to be optimized according to the design specification of the second transmission zero. In this proposed design, as illustrated in Fig. 4.4 (b), two different short-circuited stubs loaded by one pair of varactor diodes C_{v2} are employed to introduce four transmission zeros around the lower and upper passband skirt to improve the selectivity.

4.3.4 Design procedure

To better demonstrate the design procedure, Fig. 4.13 presents a general flowchart for determining the physical dimensions and capacitances of varactors. Generally, this design procedure can be divided into two independent parts, i.e. passband design and stopband design, since the lower passband edge and transmission zeros are controlled separately by employing different varactors.

Regarding the passband design, it starts from a conventional parallel coupled-line filter design with an assumption of C_{v1}=0. In this step, the desired requirements of f_{1H} and f_2 can be roughly treated as the specifications for the highest-frequency tuning state, except the frequency of lower passband edge need to be chosen a bit larger than f_{1H}. This consideration arises from the lower passband edge will be slightly shifted

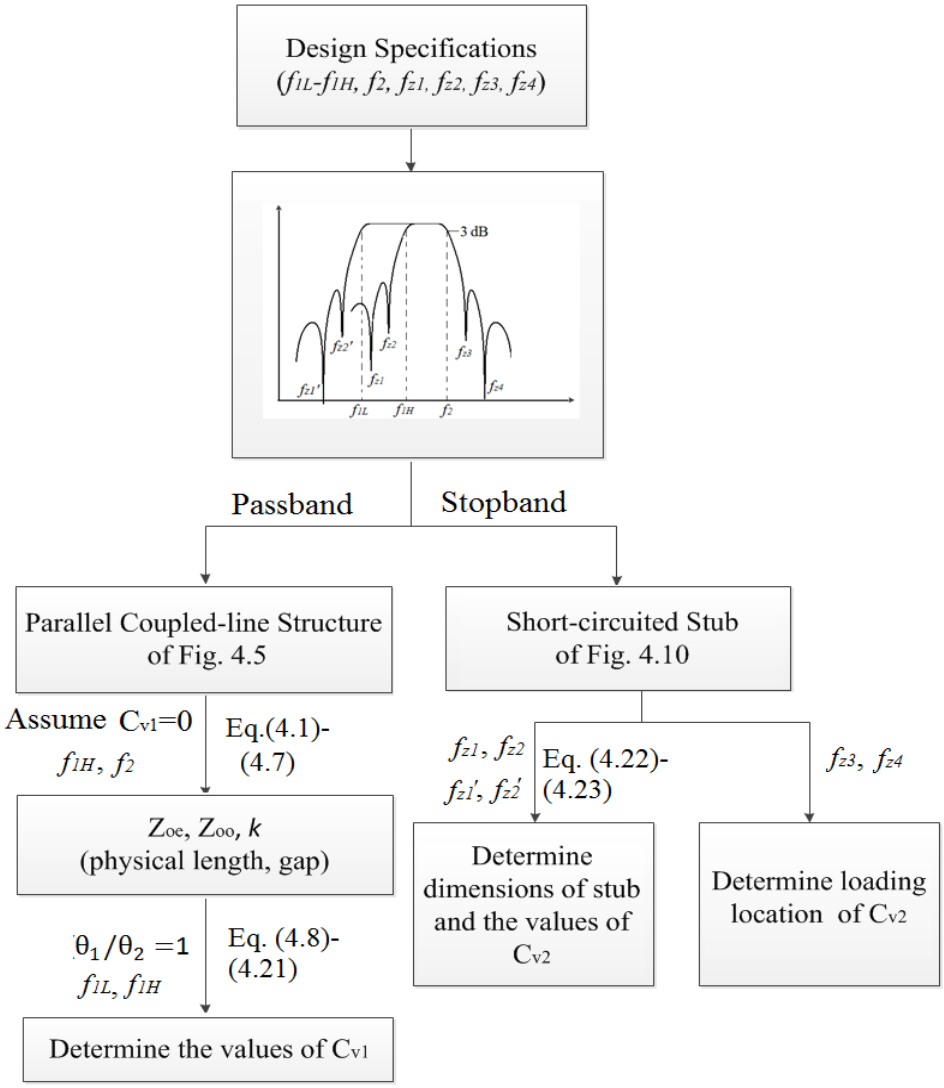

Figure 4.13: Design procedure of the proposed tunable bandpass filter with reconfigurable lower passband edge.

after loading a small capacitance C_{v1} at the highest-frequency state. By applying the fundamental theory stated in Section 4.2, the Z_{oe} and Z_{oo} of the parallel-coupled lines and the associated coupling coefficient k can be easily obtained. Consequently, the physical lengths of the coupled lines and gaps between them can be determined. After that, with centrally-loaded varactor C_{v1} involved, based on the desired tuning range from f_{1L} to f_{1H} , we can determine the values range of C_{v1} by using equations (4.8)-(4.21).

With respect to the stopband design, as mentioned in Section 4.3.3, the transmission zeros located in the lower stopband are mainly determined by the lumped effects of short-circuited stubs, so the determination of the associated dimensions and the values of C_{v2} can be referred to the equations (4.22)- (4.23), and then, the loading location of varactors C_{v2} can be optimized according to the desired frequencies of transmission zeros placed at the upper stopband.

To go through the design procedure, one design example is given with experimental results in the following section.

4.3.5 Fabrication and measurement

The final designed tunable bandpass filter is fabricated and measured by using LCP bonded multilayer PCB technology. The detailed layout dimensions and multilayer technology information has been provided in Fig. 4.4. Throughout the fabrication process, CO_2 laser is used to drill conductive via holes for varactor diodes C_{v2} connecting to the stubs in the middle layer. A photograph of the fabricated tunable bandpass filter is shown in Fig. 4.14, where a compact circuit size of 26.1 mm × 6.1 mm is achieved, excluding the input/output feed lines. GaAs diode MA46H120 (0.17-0.9 pF, and Q=3000 for V_R=4 V at f=50 MHz) and silicon abrupt junction diode SMV1800-079LF (0.84-15.78 pF, and R_s=3 Ω for V_R=1.5 V at f=470 MHz) are adopted for tunable capacitors C_{v1} and C_{v2}, respectively, which are controlled by only two dc voltage sources V1 and V2, individually. Also, Murata 0402 GRM 100 pF capacitors are used for bypass capacitor, and Panasonic resistors 100 kΩ are utilized to reduce the RF-signal leakage in the bias network.

In the final EM simulation, a full-wave electromagnetic simulator Sonnet [24] is employed. The SPICE models of the varactor diodes provided in [25]-[26] are

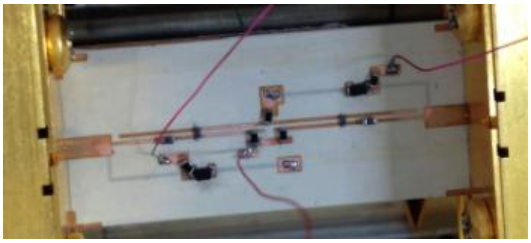

Figure 4.14: Fabricated varactor-tuned bandpass filter.

analyzed and considered in the EM simulations. Several typical measured tunable frequency responses are obtained using HP8510 network analyzer and Anritsu Test Fixture with reference planes defined at the I/O ports, which are compared with the simulated ones, as shown in Fig. 4.15 (a). The reverse bias voltages V1, V2 applied on the varactors ranges from 0V to 10V, 0V to 30V respectively, resulting in the lower passband edge changing from 1.16 to 2.09 GHz with a tuning range up to 44.5%. Accordingly, two transmission zeros located at the lower stopband f_{Lz1}/ f_{Lz2} are also shifted from 1.02/0.95 GHz (State I) to 1.99/1.85 GHz (State IV) to result in a sharp selectivity at each state. Moreover, as indicated by the theoretical analysis, the measured upper passband edge and transmission zeros remains fixed with increased voltages, which correspond to 3.78, 3.96 and 4.53 GHz, individually (clearly seen in Fig. 4.15 (b)). The measured return loss over the entire tuning range is better than 10 dB. The minimum passband insertion losses measured at State I and State IV are around 0.5 and 0.6 dB, respectively. Such low insertion losses are related with wide bandwidth obtained at each state. In addition, it is well known that when the parallel-coupled line is fabricated with the microstrip structure, unequal even-and odd-mode phase velocities usually results in unwanted harmonic at $2f_0$. However, from the measured results shown in Fig. 4.15 (a), it is noteworthy that due to capacitively compensated parallel-coupled microstrip lines employed [27]-[28], the second passband of the proposed design operates around 6.2 GHz that are well above twice the centre frequency to accomplish a wider stopband. In general, good agreement between the measured and simulated *S*-parameters is observed in the experiment, except that the frequency responses in the higher frequencies are sort of inconsistent. This is likely due to some fabrication tolerances, which would have more effects at higher frequencies. Furthermore, performance comparison with related work in the literature is summarized in Table 4.1, indicating that this presented filter has merits of tuning range and stopband performance.

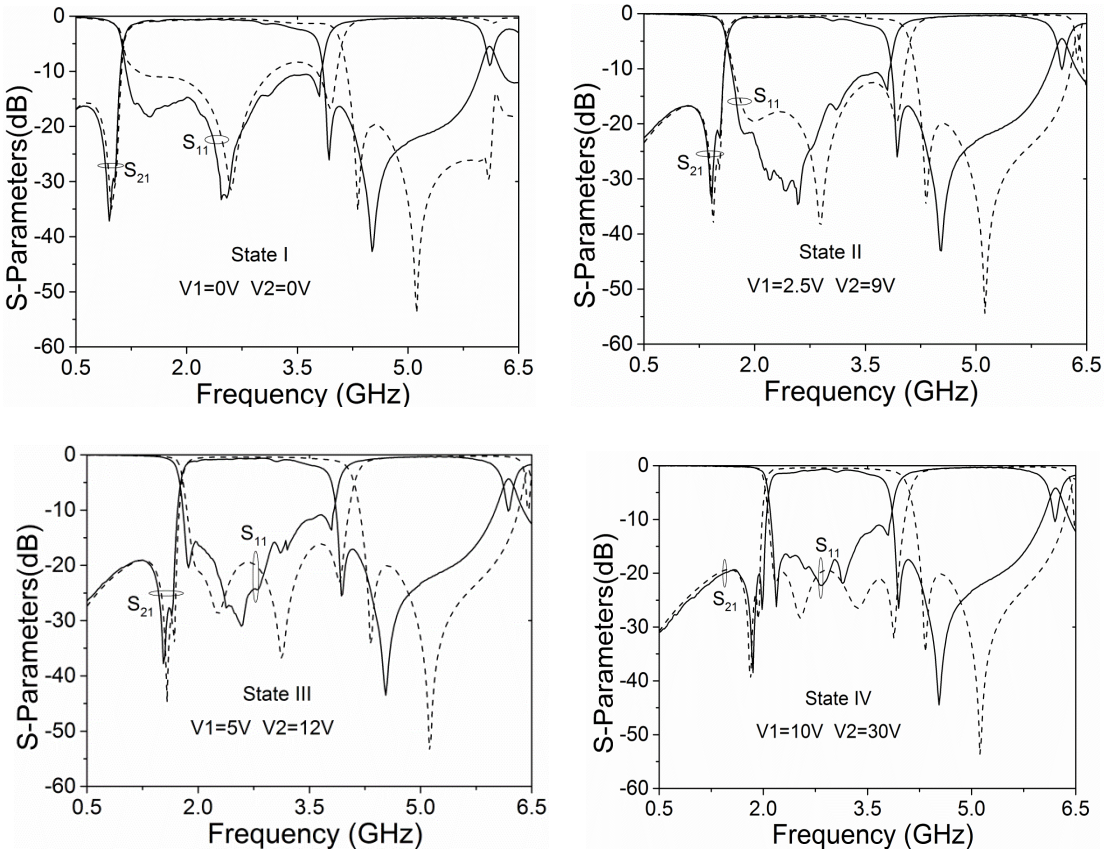

(a)

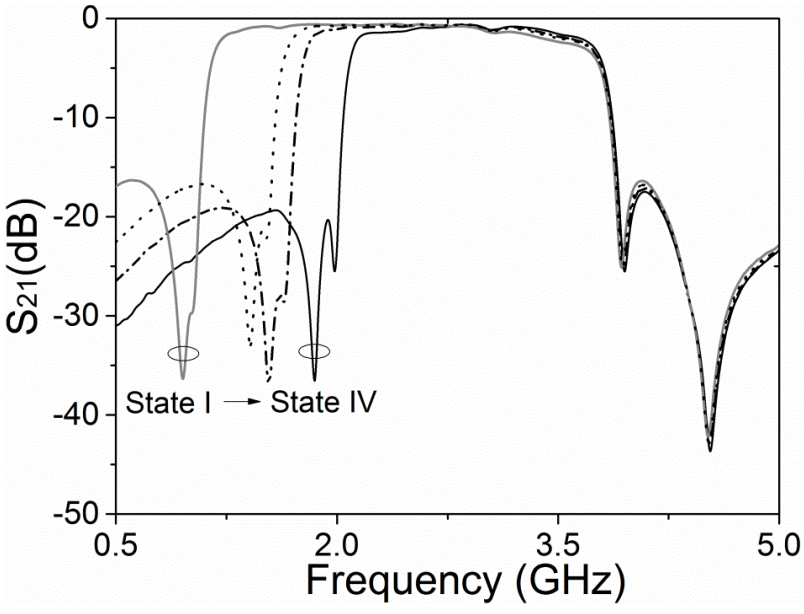

(b)

Figure 4.15: (a) Measured (solid line) and simulated (dashed line) *S*-parameters of the proposed design. (b) Measured S_{21} of the proposed filter with lower passband edge controlling from 1.16 to 2.09 GHz.

Table 4.1: Performance Comparison with Other Related Works

Ref.	Tuning Technique	Lower passband edge Tuning Range		*SR (dB)	*TZ (LS/HS)
[29]	Varactor	1.1-1.3GHz	15.4%	≥15	1/1
[30]	Varactor	1.51-1.73GHz	12.7%	≥15	1/1
[31]	Varactor	3.1-3.4GHz	8.8%	≥13	1/1
[32]	Varactor	1.5-2.3 GHz	34.8%	≥14	1/1
This	**Varactor**	**1.16-2.09 GHz**	**44.5%**	**≥16**	**2/2**
***SR: Sideband rejection *TZ (LS/HS): number of transmission zeros in lower/higher stopband**					

4.4 Tunable Bandpass Filter with Control of Centre Frequency and Bandwidth

The development of efficient methods for tuning both the centre frequency and bandwidth of the filter response is one of the main goals in tunable bandpass filter research field and it is always challenging. Generally, the centre-frequency tunability maintaining the general shape of the filter response is easily accomplished by adjusting the effective electrical lengths of the filter resonators. While the tunability of bandwidth controlling is relatively difficult for reason the lack of adequate methods to vary the inter-resonator couplings as desired in a coupled-resonator filter topology. Thus, the main objective of this section is to present a novel realization of bandpass filter with continuous control of centre frequency and bandwidth by using cascaded bandpass and lowpass filters.

4.4.1 Filter configuration and working principle

Following the design introduced above and the tunable lowpass filter presented in Chapter 2, a novel concept of tunable bandpass filter realization is proposed in Fig. 4.16 (a), which is constructed by the combination of a tunable BPF and LPF module in cascaded. As seen in Fig. 4.16 (a), it reveals variable centre frequency and bandwidth can be flexibly achieved by controlling the tunable BPF or LPF module individually or jointly. Specifically, tunable BPF and LPF modules are mostly associated with the filter shape at the lower and the upper band, respectively.

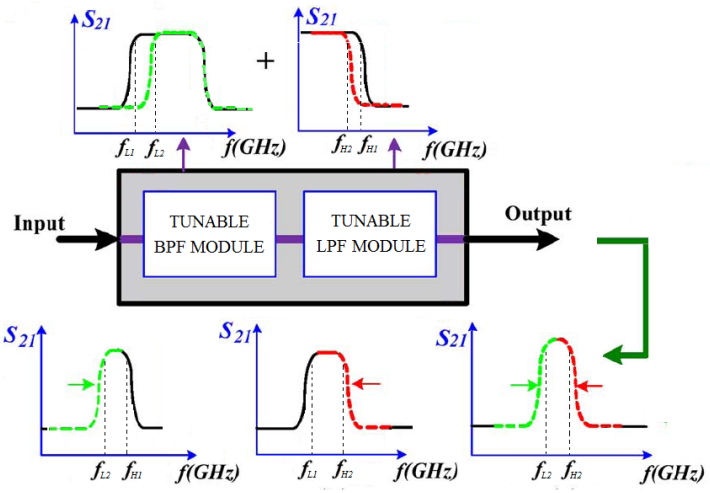

(a)

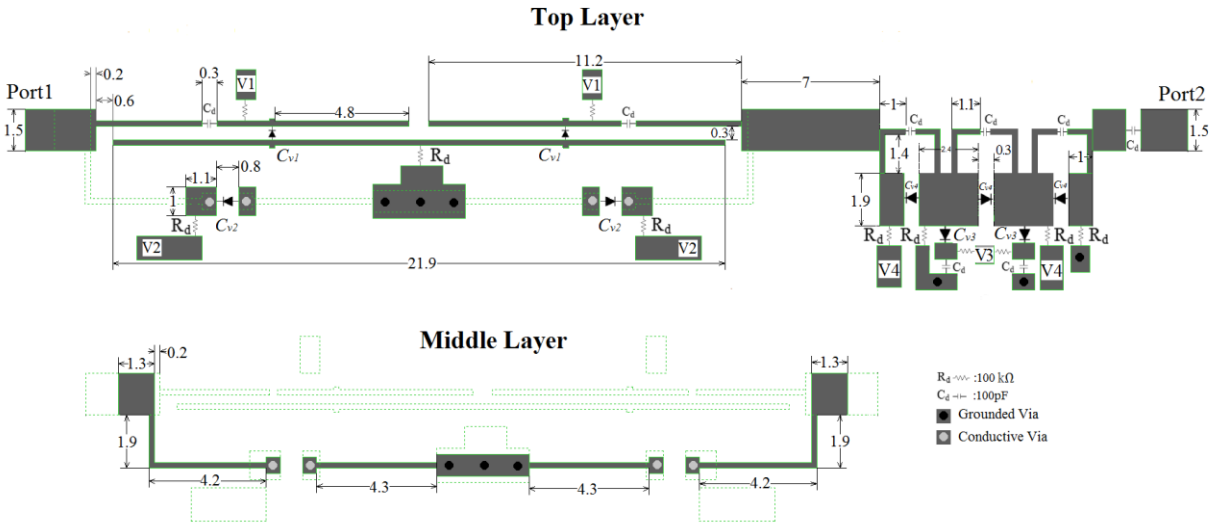

(b)

Figure 4.16: (a) Novel topology of tunable bandpass filter realization. (b) Layout of the proposed tunable bandpass filter (All dimensions are in millimeters).

Consequently, the tunable performance of each module adopted in the topology is very critical to get a good final response. Particularly, for the narrow bandwidth realization during the tuning process, it requires each module providing a very sharp bandedge frequency response to obtain a good matching within the passband.

Fig. 4.16 (b) shows the layout of the final filter design, which is also implemented by using LCP bonded multilayer PCB technology as demonstrated in Fig. 4.4 (c). Note that the tunable BPF module adopted here is slightly different from the design presented in Section 4.3, which employs two same short short-circuited stubs that coupled through a shunt inductor *L0* by common metal vias to the ground. The corresponding equivalent circuit is inserted in Fig. 4.17. Such modifications not only accomplish a symmetrical structure with reduced circuit size, but also result in asymmetrical response with better selectivity at the desired tunable lower band edge. The simulated tunable responses are plotted in Fig. 4.17, showing a controllable lower passband edge in association with two tunable lower stopband transmission zeros. It is clear to see, within a wide tuning range, the module maintains a steep slope at the lower passband skirt, which provides a possibility to realize a narrow bandwidth during the tuning process in connection with the tunable LPF module addressed in Chapter 2, which is demonstrated below.

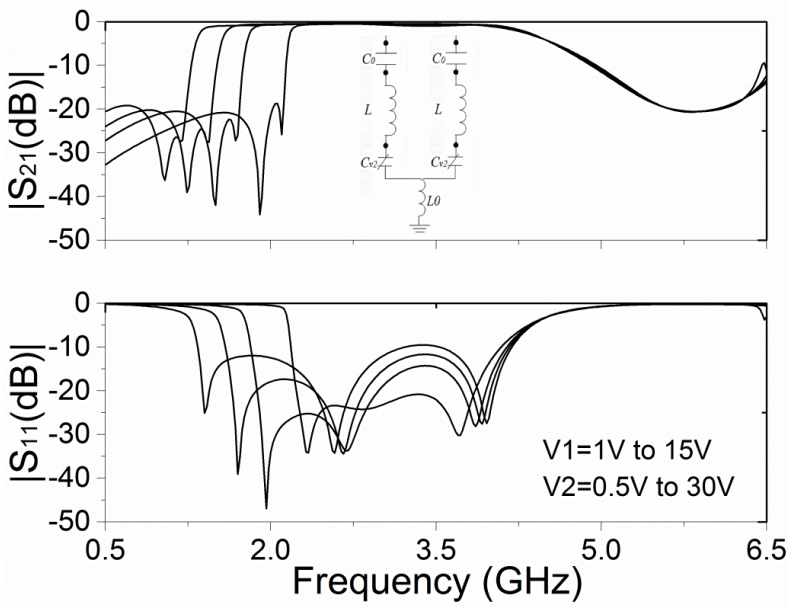

Figure 4.17: Simulated responses of tunable BPF module adopted in Figure. 4.16 (b).

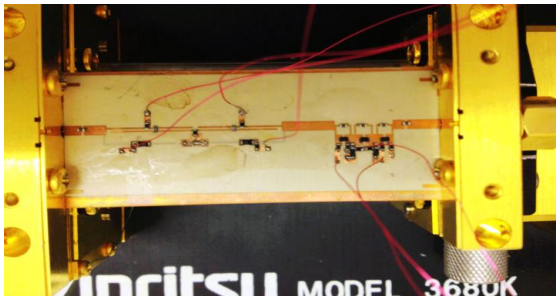

Figure 4.18: Fabricated tunable bandpass filter by using a cascaded topology.

4.4.2 Experimental results on the performance tuning

Fig. 4.18 shows the photo of the fabricated tunable bandpass filter. Four dc biases are required for this tunable bandpass filter, namely V1 and V2 for the BPF module on the left and V3 and V4 for the LPF module on the right. Regarding the measured responses, Fig. 4.19 illustrates several typical tuning performance of the developed tunable BPF filter, corresponding to the working principles demonstrated in Fig. 4.16 (a). For instance, in Fig. 4.19 (a), when keeping the applied voltages V3 and V4 fixed at 5V, increasing the voltages V1, V2 of BPF module from 0V, 0V to 10V, 15V results in the lower passband edge is tuned upwardly toward the high end frequency from 1.17 to 2.01 GHz, with measured minimum insertion loss varying from 1.6 to 3.3 dB. Similarly, by only adjusting the voltages V3, V4 from 5V, 5V to 20V, 20V, while keeping V1 and V2 fixed at 10 and 15 V respectively, as indicated in Fig. 4.19 (b), the upper passband edge can be shifted from 2.22 to 3.17 GHz, with measured minimum insertion loss changing from 3.3 to 1.2 dB. Furthermore, when four applied voltages are controlled simultaneously, it is clear from the results of Fig. 4.19 (c) that both of passband edges are moved toward to the centre frequency (around 2GHz), which results in the corresponding 3 dB bandwidth changing from 1.78 to 0.26 GHz with a minimum measured insertion loss of 1.1 and 4.9 dB, respectively. The bandwidth tuning ratio is up to 6.85:1. In fact, this bandwidth controlling capability can be further improved at the expense of higher insertion loss suffered in the narrow passband. Hence, there is a tradeoff between the insertion loss and bandwidth tunability. Technically, the filter can provide a bandwidth variance from wideband to narrowband at any operating frequency with both high selectivity and good matching.

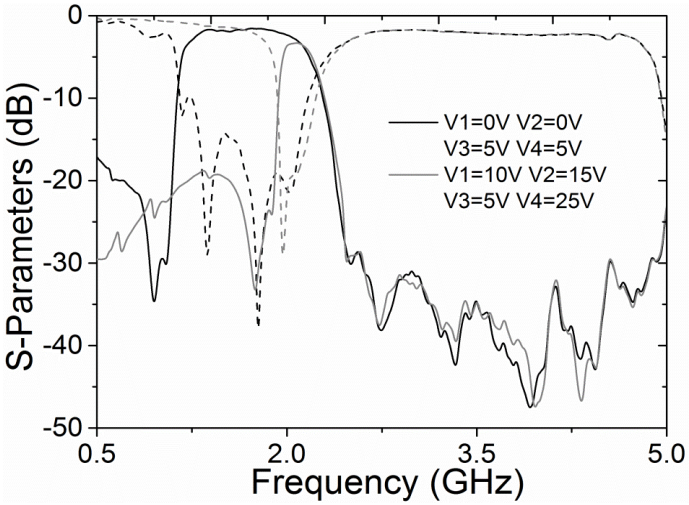

(a)

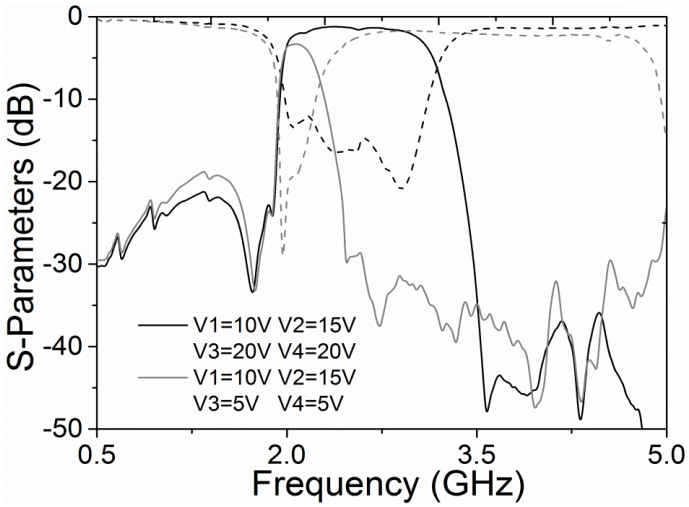

(b)

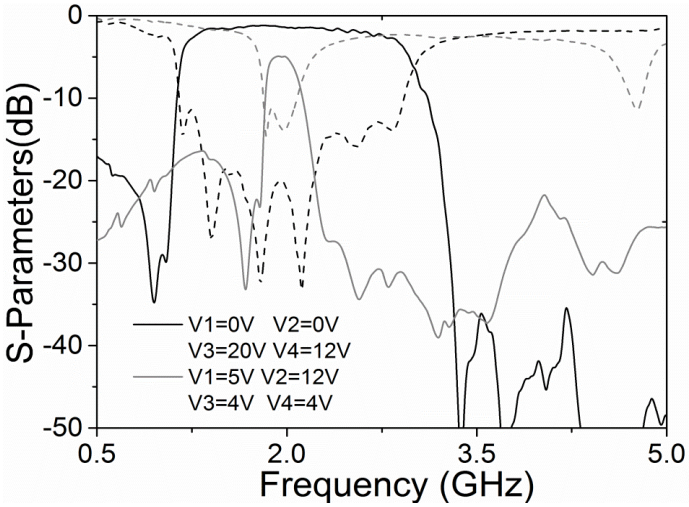

(c)

Figure 4.19: Illustrative responses of the proposed tunable bandpass filter obtained by controlling (a) Sole BPF module. (b) Sole LPF module. (c) Both modules.

4.5 Summary

In this chapter, two classes of tunable bandpass filter with different tunabilities have been design, fabricated and tested based on LCP bonded multilayer PCB technology. The measured results demonstrated that the first design exhibited a reconfigurable lower passband edge with a tuning range from 1160 to 2019 MHz. Particularly, two controllable transmission zeros placed on the lower side of passband greatly enhanced the filter selectivity at each tuning state. Also it is interesting to see the second harmonic of this proposed design is successfully suppressed due to capacitive compensation from varactor diodes loaded between the parallel-coupled microstrip lines. Furthermore, another type of tunable bandpass filter utilizing cascaded bandpass and lowpass filters was presented with elaborated operating principles, which addressed its flexibility on centre frequency and bandwidth controlling. The measured bandwidth tuning of 685% is obtained at centre frequency around 2 GHz. The achieved features are very promising for systems with different reconfigurable requirements.

Reference

[1] M. A. El-Tanani and G. M. Rebeiz, “High performance 1.5–2.5 GHz RF MEMS tunable filters for wireless applications,” *IEEE Trans. Microw.Theory Tech.*, vol. 58, no. 6, pp. 1629–1637, Jun. 2010

[2] I. C. Hunter and J. D. Rhodes, “Electronically tunable microwave bandpass filters,” *IEEE Trans. Microw. Theory Tech.*, vol. MTT-30, no. 9, pp. 1354–1360, Sep. 1982.

[3] Sang-June Park and Gabriel M. Rebeiz, “Low-Loss Two-Pole Tunable Filters With Three Different Predefined Bandwidth Characteristics,” *IEEE Trans. Microw. Theory Tech.*, vol. 56, no. 5, pp. 1137–1148, May. 2008.

[4] X. Y. Zhang, Q. Xue, C.H. Chan, and B.-J. Hu, “Low-Loss Frequency-Agile Bandpass Filters With Controllable Bandwidth and Suppressed Second Harmonic,” *IEEE Trans. Microw. Theory Tech.*, vol. 58, no. 6, pp. 1557–1564, Jun. 2010.

[5] M. Sanchez-Renedo, R. Gomez-Garcia, J. I. Alonso, and C. Briso-Rodriguez, “Tunable combline filter with continuous control of center frequency and bandwidth,” *IEEE Trans. Microw. Theory Tech.*, vol. 53, no. 1, pp. 191–199, Jan. 2005

[6] Yi-Chyun Chiou and Gabriel M. Rebeiz,” Tunable 1.55–2.1 GHz 4-Pole Elliptic Bandpass Filter with Bandwidth Control and >50 dB Rejection for Wireless Systems,*” IEEE Trans. Microw. Theory Tech.*, vol. 61, no. 1, pp. 117-124, Jan. 2013.

[7] Y.-C. Chiou and G. M. Rebeiz, “A quasi elliptic function 1.75–2.25 GHz 3-pole bandpass filter with bandwidth control,” *IEEE Trans. Microw. Theory Tech.*, vol. 60, no. 2, pp. 244–249, Feb. 2012.

[8] W. Tang and J.-S. Hong, “Varactor-tuned dual-mode bandpass filters,” *IEEE Trans. Microw. Theory Tech.*, vol. 58, no. 8, pp. 2213-2219, Aug. 2010.

[9] H.-J. Tsai, N.-W. Chen and S.-K. Jeng, “Center frequency and bandwidth controllable microstrip bandpass filter design using loop-shaped dual-mode resontor,” *IEEE Trans. Microw. Theory Tech.*, vol. 61, no.10, pp. 3590-3600, Oct. 2013.

[10] A. L. C. Serrano, F. S. Correra, T.-P. Vuong, and P. Ferrari, “Analysis of Reconfigurable Bandpass Circular Patch Filter,” *IEEE Trans. Microw. Theory Tech.*, vol. 58, no.12, pp. 484-493, Dec. 2010.

[11] W. Peng Wen and I. C. Hunter, “Electronically reconfigurable microwave bandpass filter,” *IEEE Trans. Microw. Theory Tech.*, vol. 57, no. 12, pp.

3070-3079, Dec. 2009.

[12] R. V. Snyder, “A wideband tunable filter technique based on double-diplexing and low-Q tuning elements,” in *Proc*. IEEE *Int. Microw. Symp. Digest,* 2000, vol. 3, pp. 1759–1762.

[13] Y. Zhu, G. Qiu, K. H. Chi, B. T. Wang, and C. S. Tsai, “A Compact X-band tunable band-pass filter module using a pair of microstrip composite bandpass filters in cascade,” *IEEE Trans. Magn.*, vol. 46, no. 6, pp. 1424–1427, Jun.2010.

[14] M. Makimoto and S. Yamashita, “Bandpass filters using parallel coupled stripline stepped impedance resonators,” *IEEE Trans. Microw. Theory Tech.*, vol. MTT-28, no. 12, pp. 1413–1417, Dec. 1980.

[15] A. M. Abbosh, “Design method for ultra-wideband bandpassfilter with wide stopband using parallel-coupled microstrip lines,” *IEEE Trans. Microw. Theory Tech.*, vol. 60, no. 1, pp. 31–38, Jan. 2012.

[16] C. W. Tang, C.T. Tseng and S. H. Chiu, “Design of wide passband/stopband microstrip bandpass filters with the stepped coupled line,” *IEEE Trans. Microw. Theory Techn.*, vol. 61, no. 3, pp. 1095–1102, Mar. 2013.

[17] N. Yang, C. Caloz, K. Wu, and Z.-N. Chen*, “Broadband and compact coupled coplanar stripline filters with impedance steps,” IEEE Trans. Microw. Theory Tech., vol. 55, no. 12, pp. 2874–2886, Dec. 2007.*

[18] G. Matthaei, L. Young, and E. M. T. Jones, *Microwave Filters, Impedance-Matching Networks, and Coupling Structures*. Boston, MA: Artech House, 1985.

[19] J.-S. Hong, Microstrip filter for RF/Microwave applications, 2nd Edtion, New York: John Wiley & Sons, 2011.

[20] G. I. Zysman and A. K. Johnson, “Coupled transmission line networks in an inhomogeneous dielectric medium,” *IEEE Trans. Microw. Theory Tech.*, vol. MTT-17, no. 10, pp. 753–759, Oct. 1969

[21] D. Pozar, *Microwave Engineering*, 3rd ed. New York: Wiley, 2005.

[22] R. K. Mongia, I. J. Bahl, P. Bhartia and J. Hong, RF and microwave coupled-lines, 2nd Edition, MA: Artech House, 2007.

[23] R. J. Cameron, C. M. Kudsia, and R. R. Mansour, *Microwave Filters for Communication Systems: Fundamentals, Design and Applications*. New York, NY, USA: Wiley, 2007.

[24] Sonnet *em*, Version 13.54, Sonnet Software Inc., New York, 2011.

[25] M/A-COM MA46H120 data sheet," M/A-COM Lowell, 2006.

[26] "Skyworks SMV1800—079LF data sheet," Skyworks Solutions, Sunnyvale, CA, 2011.

[27] I. J. Bahl, "Capacitively compensated high performance parallel coupled microstrip filters," in *IEEE MTT-S Symp. Dig*., 1989, pp. 679–682.

[28] M. Dydyk, "Microstrip directional couplers with ideal performance via single-element compensation," *IEEE Trans. Microw. Theory Techn.,* vol. 47, no. 6, pp. 956–964, Jun. 1999.

[29] H.-J. Tsai, N.-W. Chen and S.-K. Jeng, "Reconfigurable Bandpass Filter with Separately Relocatable Passband Edge," *IEEE Trans. Microw. Wireless Compon. Lett.*, vol. 22, no. 11, pp. 559-561, Nov. 2012.

[30] X.-G. Huang, Q.-Y. Feng and Q.-Y. Xiang, "Bandpass filter with tunable bandwidth using quadruple-mode stub-loaded resonator," *IEEE Trans. Microw. Wireless Compon. Lett*., vol. 22, no. 4, pp. 76-178, Apr. 2012.

[31] A. L. C. Serrano, F. S. Correra, T.-P. Vuong and P. Ferrari "Synthesis methodology applied to a tunable patch filter with independent frequency and bandwidth control," *IEEE Trans. Microw. Theory Techn.,* vol. 60, no. 3, pp. 481-493, Mar. 2012.

[32] J.-Y. Chen, H.-J. Tsai and N.-W. Chen, "Bandwidth Reconfigurable Microwave Bandpass Filter," in *IEEE MTT-S Int. Microw. Symp. Dig*., Jun. 2011, pp.1-4.

CHAPTER 5

Enhancements of Passband Flatness and Selectivity for Microstrip Lossy Filters Including Tunable Design

5.1 Introduction

High-performance microwave and RF filters are in a huge demand for modern wireless communication systems such as wireless base stations and communications satellites. Generally, high-performance filter is required to provide the most efficient use of the frequency spectrum, a low-loss filter passband and a steep transition into the rejection band, while issues of circuit size, cost and mass are also critical [1].

Conventionally, synthesis techniques for microwave filters assume that the filter is composed of lossless components. However, in a practical filter, power dissipation is always present, and as a result the actual response function of the filter will deviate somewhat from the theoretical response of the ideal prototype [1]-[3]. Particularly for the microstrip tunable filters, due to the effects of limited low Q factors of tuning elements and other dissipation loss associated in the circuits, the performance deviation including an increased in-band insertion loss and a rounding of the passband edge leading to a poorer selectivity can be observed, which become more pronounced in narrow band filters. Like recently, the 1.5-2.2 GHz three-pole tunable combline filters published in [4], [5] suffered from degraded insertion loss and rounded passband responses owning to the finite unloaded Q (40-90) of varactor diodes. In this context, how to enhance the performance of tunable microstrip filters or at least maintain similar performance by using low Q resonators is challenging. To the author's knowledge, so far there has been no literature reported on this issue.

Hence, the main objective of this chapter is to investigate the solutions to overcome the aforementioned filter performance degradation arising from low Q resonators, leading to improvements on passband flatness and selectivity. In other

words, we aim to find ways to use low *Q* resonators and make them behave like high *Q* resonators in microstrip filter design, particularly in the tunable microstrip filters. In general, this chapter is organized as follows: Section 5.2 is a brief review of lossy filter synthesis techniques, which helps designers to understand the needs for lossy filters and where compromises can be made in designs. After that, a novel design of third order narrowband lossy filter utilizing an extended doublet configuration is discussed in Section 5.3. Compared with the other lossy filters reported in the literature, the presented work mainly attempts to realize a high-*Q* performance using pure microstrip technology with easier fabrication, i.e. without any requirement for resistive coupling and tiny resistor. Section 5.4 puts focus on investigating a design technique that can be applicable to the tunable combline filter, leading to an improved in-band loss variation and out-of-band selectivity. A straightforward design process by using the equivalent circuit model is illustrated, thoroughly analyzing the operating mechanisms of performance enhancement. To demonstrate the validity of the proposed concept, design guidelines and experimental results are provided. Finally, the main conclusions of this chapter are reported in Section 5.5.

5.2 Overview of Microwave Lossy Filters

Classical filter synthesis techniques require the use of high quality factor (*Q*) resonators to realize a filter response with high selectivity and flat passband. Usually this might be unfeasible or impractical in wireless systems that have stringent weight and volume restrictions. While the development of synthesis techniques that take into account the finite *Q* of the filter resonators allows to optimize the filter selectivity and passband flatness, at the expense of other filter parameters (such as absolute insertion loss) that might not be critical in some applications. These techniques are normally famous as lossy filter synthesis. In the open literature, the most promising approaches are predistortion [6]-[9] and lossy circuit techniques [12]-[18].

5.2.1 Application of lossy filters in communication systems

It is well known that the transmit filter must have low passband insertion loss in order to maximize the dc to RF efficiency of the power amplifier. However, for a

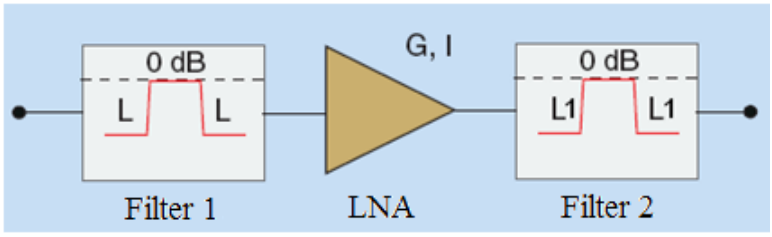

(a)

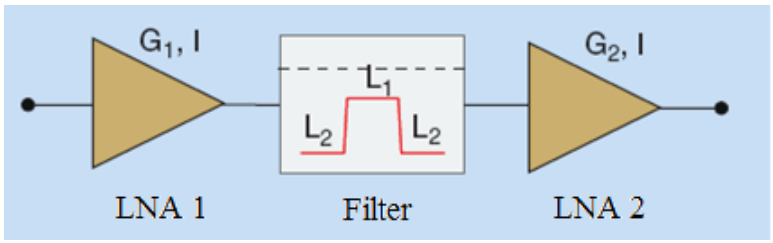

(b)

Figure 5.1: (a) Conventional receive-path architecture using two filters. (b) Alternative architecture with two LNAs [2].

receiver filter, the insertion loss and power handling performance are not crucial. Consider the two receiver architectures shown in Fig. 5.1. The first is a conventional filter/amplifer cascade architecure, as shown in Fig. 5.1 (a). In this case, a low-loss filter is often placed before the low nosie amplifier (LNA). Moving some selectivity requirements into the second filter is sometimes used to alleviate the design requirement of the first filter. In recent years, for some application, a new approach emerged to split the amplifier into two stages with a filter in between them, as indicated in Fig. 5.1 (b). In this case, the first amplifier has just enough gain to estabish a reasonable noise figure but not enough that it geneartes too many distortion products. The filter can now accpet additional passband insertion loss but a higher selecivity. The second stage of the amplifier is protected from interfering signals by the filter, so it can be designed with lower *Q* resonators than a conventional deisgn [2]. Overall, in this novel architecture, the most cirtial electrical parameters for the reciver filter are in band performance (such as loss variation) and selectivity that can ease the design requirements of LNAs . While the absolute passband insertion loss is secondary parameter that can be traded for size reduction. Further, in light of this concept, a potential application example of tunable lossy filter is illustrated in Fig. 5.2.

For a conventional channel-dropping input multiplexer (IMUX), different filter banks are used to channelize the input spectrum, which can be replaced by a tunable filter to reduce the size and complexity of the system. Likewise, in this tunable case, the absolute insertion loss value is no loger critical since the LNA can easily compensate the loss of the filter by setting the gain to a higer value. In contrast, in-band loss variation is also a more critical consideration for such application.

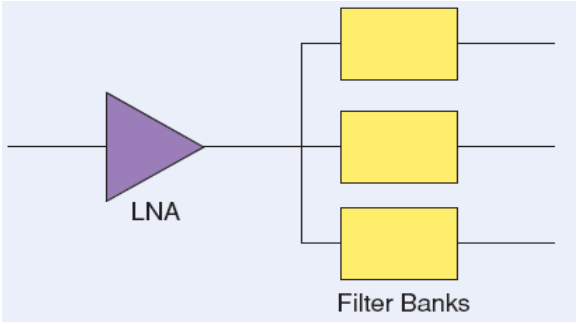

(a)

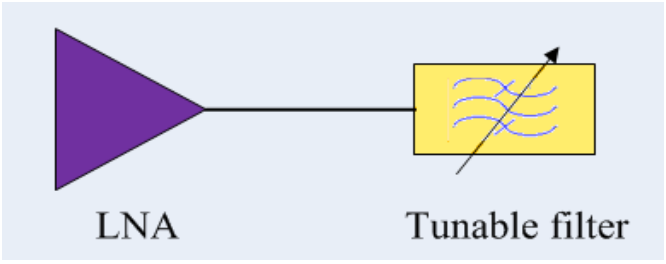

(b)

Figure 5.2: (a) Conventional multichannel receiver (IMUX) [1]. (b) Alternative architecture using tunable lossy filter.

5.2.2 Predistortion techniques

In the area of microwave filter design, the concept of predistortion was first proposed by Livingstone [6] and later described with more details by Williams [7] for cross-coupled microwave filters, that is a method of compensating for the rounding effect resulting from the finite unloaded *Q* of the resonators. As illustrated in Fig. 5.3, the principle of operation is to firstly deisgn a lowpass prototype filter that has a deliberately peaky response near the passband edges [2]. This means the band edges of the transmission response are considerablely high than the center. Then, the

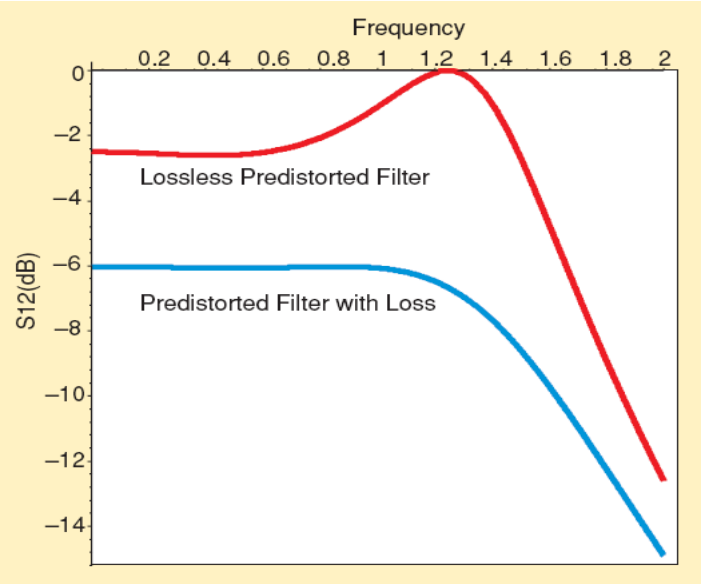

Figure 5.3: Typical lossless and lossy responses of predistortion technique [2].

introduction of loss can attenuate the band edges more than the center of the band leading to a flat passband, since the effect of loss become more significant at band edges where the group delay is larger. From different perspective, predistortion synthesis involves synthesizing an ideal transfer function initially as given as

$$S_{21} = \frac{\mathrm{D}(s)}{\mathrm{E}(s)} \qquad (5.1)$$

then shifting all the poles of the filter functuion (the zeros of E (*s*)) towards the right by the amount σ:

$$s \to s - \sigma \qquad (5.2)$$

where $\sigma = f_0/(Q_u \times \mathrm{BW})$ is derived from the anticipated unloaded Q_u of the filter, f_0 is the center frequency, and BW is the bandwidth. Sine the poles are pre-shifted to the right-half *s*-plane, they will be in the correct relative positions in relation to *s* for the lossless response to be recovered when taking into account the finite Q_u [10].

For the classical predistortion technique, a constant shift of σ (given in equation (5.2)) is adopted to combat the effect of dissipation factor in the transmission poles. However, the adaptive predistortion approach presented in [8] is realized by introducing adaptive correction terms α_i $(i = 1, 2, \cdots n)$ for each pole, so that the

equation (5.2) is modified to:

$$s \rightarrow s - \sigma + \alpha_i \qquad (5.3)$$

The correction terms α_i can be adjusted by an optimization algorithm to adapt the filter response into the required filter function. The detaied optimization process can be found in [8]. In contrast to the classical predistortion, the adaptive predistortion technique will result in much less insertion loss, despite using low *Q* resontaors, and the other parameters such as loss variation will also be better.

Neverthless, the biggest disadvantage associated with both types of predistortion techniques is that the passband equalizaiton is achieved by reflecting energy at frequencies in the middle of the passband and thus predistorted bandpass filters usually suffer from poor return loss and need to be compensated by nonreciprocal devices such as isolators and circulators [11].

5.2.3 Lossy circuit techniques

Lossy circuit techiques [12] [13] [14] usually use nonuniform *Q* distribution and modified topologies with exra resistrive coupling path to realize a low *Q* filter with high flatness and good return loss (*RL*). Generally, the synthesis process is composed of four steps as demonstrated in Fig. 5.4. Among these steps, two types of synthesis are necessary: polynomial synthesis (step 1) and circuit synthesis (step 3). In the literature [12], the direct synthesis of lossy polynomials is given as:

$$S_{11\_lossy} = K^2 S_{11\_\mathrm{lossless}} \qquad (5.4)$$

$$S_{21\_\mathrm{lossy}} = K^2 S_{21\_\mathrm{lossless}} \qquad (5.5)$$

where both reflection and transmission polynomilas of a lossless function are multiplied by a constant attenuation factor of K^2 ($K^2 < 1$). This is the simplest lossy scattering polynomial resutling in same-order admittance polynomials and thus is most commonly used. From the network perspective, this special case is equivalent to a model with two identical mathced attenuators placed at source and load of a lossless filter with attenuation factor of *K* (see in Fig. 5.5), and that can be used as an initial

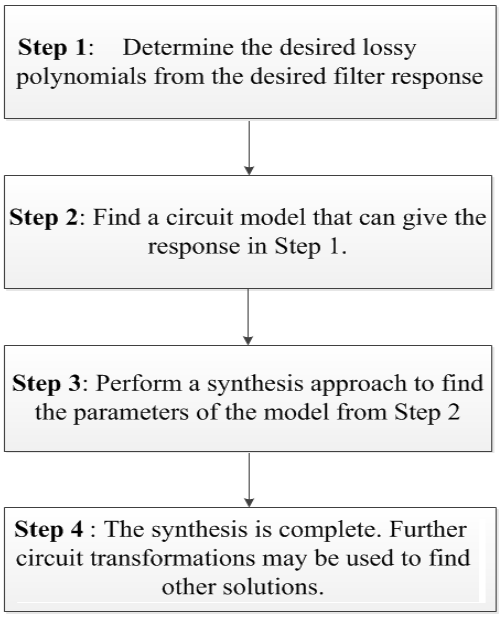

Figure 5.4: Generalized steps for direct synthesis of lossy filters [14].

Figure 5.5: An equivalent network of a lossy filter with *RL* and *IL* shifted down [1].

circuit model for the following synthesis steps. However, since this simple circuit model failed to introduce finite dissipation into the central resonators, additional use of resistive cross coupling and matrix hyperbolic rotation are required to re-distribute loss among resonators and improve the filter response [12]. The design method provided in [12] is based on even-odd mode analysis and is only applicable to symmetric networks. In addition, two other different approaches using coupling matrices with lossy filter characteristics (circuit model in step 2) are presented in [13] and [14]. The focus of the theoretical synthesis in [13] is presenting a general algorithm for lossy filters with finite resonaotr *Q* valus and aritrary complex coupling values. This method needs to rotate the coupling matrix with complex angles to arrive at a realizable configuration and the results usually contain resistive cross couplings.

While in [14], the authors put focus on the design of parallel connected lossy filters by employing nonuniform dissipations only at resonators, therefore, only the diagonal elements in the corresponding coupling matrixes are changed to complex entires. At this point, gradient-based optimization algorithm is utilized to obtain the desired nonuniform *Q* distribution.

In contrast to predistiortion techniques, lossy circuit techniques achieve inproved performance by power absorbtion in resonators rather than reflected, leading to a greater return loss in the passband.

5.3 Design of Microstrip Lossy Filter Using an Extended Doublet Topology

In the open literature, most of lossy filters were realized using coaxial resonators, dielectric resonators, cavity resonators or those ones mixed with microstrip resonators [13]-[17]. Only few works presented in [12] and [18] were done fully in microstrip technology. Nevertheless, these microstrip lossy filters normally required resistive cross couplings that were difficult to implement. In this section, a novel fixed-frequency third-order narrowband lossy filter is presented and discussed, which attempts to design a lossy filter using pure microstrip technology with easier fabrication, i.e. without any resistive coupling requirement. In order to achieve high performance of flat passband and high selectivity, the proposed filter mainly utilizes an extended doublet configuration as well as nonuniform *Q* distribution considered. The detailed discussion will be demonstrated below.

5.3.1 Filter design and analysis

As discussed in [14], for the pure transversal network shown in Fig. 5.6 (a), each resonator represents a pole (a global eigenmode) so that each resonator Q_u has an independent effect on the filter response shaping. That is to say, the resonators with smaller bandwidth and near bandedge resonant frequencies are more critical in determining filter characteristics and have to be designed with high-*Q*, while the others can be designed with low-*Q* to reduce the filter size and cost without deteriorating the performance. However, its practical implementation is somehow difficult as N input and output couplings are required. A more convenient topology

with an extended doublet, as seen in Fig. 5.6 (b), is considered and studied in this section. It is well known that such topology can be easily transformed from the pure transversal one with unchanged eigenmode [19], thus offering a possibility to achieve the same filter properties. A similar microstrip realization of this topology (Fig. 5.6 (b)) has been demonstrated in [20]. In this work, we take a step further to design a lossy filter with nonuniform *Q* distribution aiming to improve passband flatness and

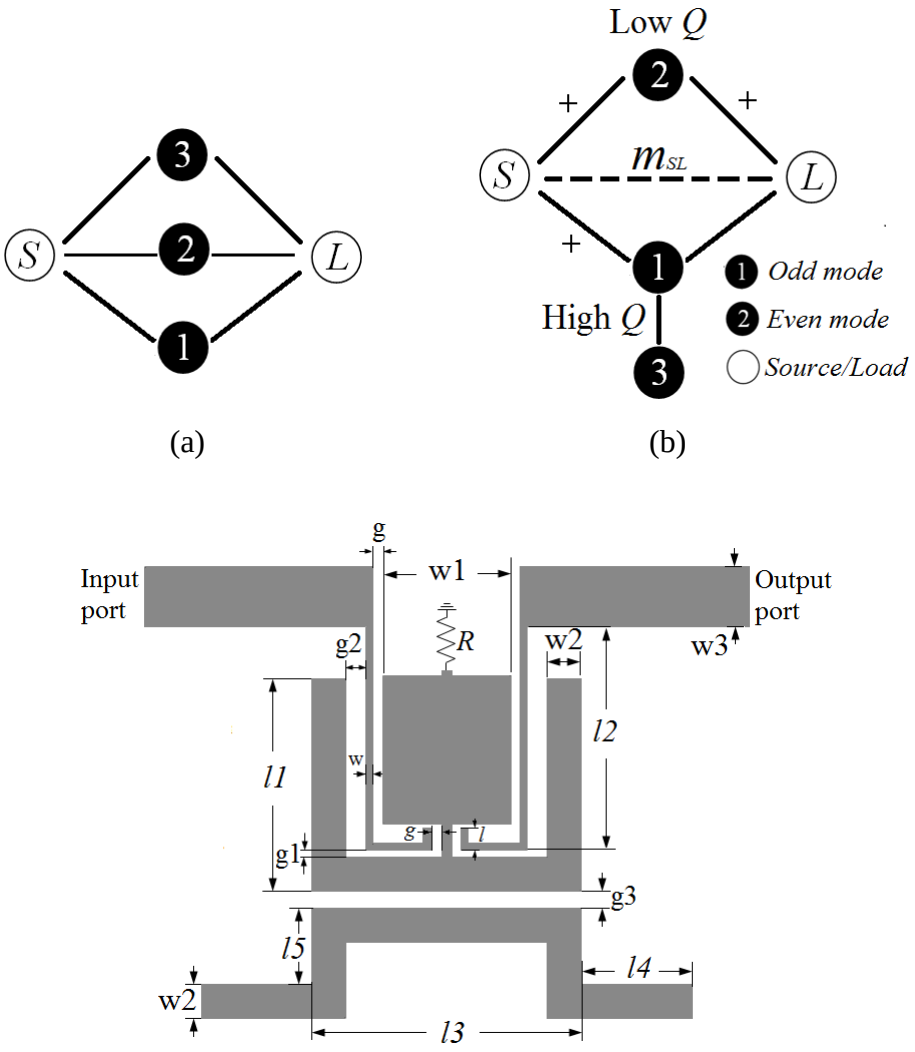

Figure 5.6: (a) Pure transversal network. (b) Proposed extended doublet with nonuniform *Q* distribution. (c) Proposed physical layout.

achieve high selectivity and wide stopband. To this end, a new compact microstrip realization is proposed in Fig. 5.6 (c), where the dual-mode resonator with two

degenerate modes (i.e. odd- and even-mode) correspond to resonator 1 and 2, and another half-wavelength resonator is associated with resonator 3. In addition, a resistor *R* is loaded in the open-circuited stub for getting a nonuniform *Q* distribution. A specific I/O feeding structure is implemented to facilitate some desired couplings.

The coupling matrix of the proposed lossy filter (see in Fig. 5.6) can be written as (5.6). Generally, the values of elements M_{Si}, M_{ii} and M_{Li} (i=1 to N, N=3) in the matrix are real and can be still obtained using lossless synthesis technique [10] according to the desired requirements. While after including the dissipative losses in the filter, the values of diagonal elements in the matrix become complex with imaginary parts $-j\delta_{ii}$ added, where $\delta_{ii} = f_0/(\mathrm{BW} \cdot Q_{ui})$, f_0 is the centre frequency of the passband, and BW is its design bandwidth. The value of M_{SL} represents a cross coupling between the source and load, which is used to create an additional transmission zero and will be demonstrated later.

$$M = \begin{bmatrix} 0 & M_{S1} & M_{S2} & 0 & M_{SL} \\ M_{S1} & M_{11} - j\delta_{11} & 0 & M_{13} & M_{L1} \\ M_{S2} & 0 & M_{22} - j\delta_{22} & 0 & M_{L2} \\ 0 & M_{31} & 0 & M_{33} - j\delta_{33} & 0 \\ M_{SL} & M_{1L} & M_{2L} & 0 & 0 \end{bmatrix} \qquad (5.6)$$

Based on the above discussion, a generalized Chebyshev filter with passband return loss of 20 dB and a pair of transmission zeros at $\Omega = \pm 2$ is taken as example. The impact of each resonator *Q* on passband insertion loss is examined in Fig. 5.7, where the lossless (ideal) transmission of each resonator is compared with the one of $Q_{ui} = 100$ ($\delta_{ii} = 0.1250, f_0 = 2.4$ GHz and $BW = 0.192$ GHz). It is notable that the dissipative loss of resonators 1 and 3 has a more significant effect on the insertion loss at the passband edge whereas the loss effect of resonator 2 is more critical at the middle band. Therefore, in order to avoid the rounded band edges and maintain a flat passband insertion loss, resonators 1 and 3 should be designed with higher *Q* than resonator 2. In the microstrip filter design, once the material and type of the resonator are chosen, there is no possibility to increase the *Q* of resonators 1 and 3. Instead, one could reduce the *Q* of resonator 2, which ensures the *Q* of resonators 1 and 3 are higher relative to that of resonator 2. Additionally, the unloaded *Q* of even-mode

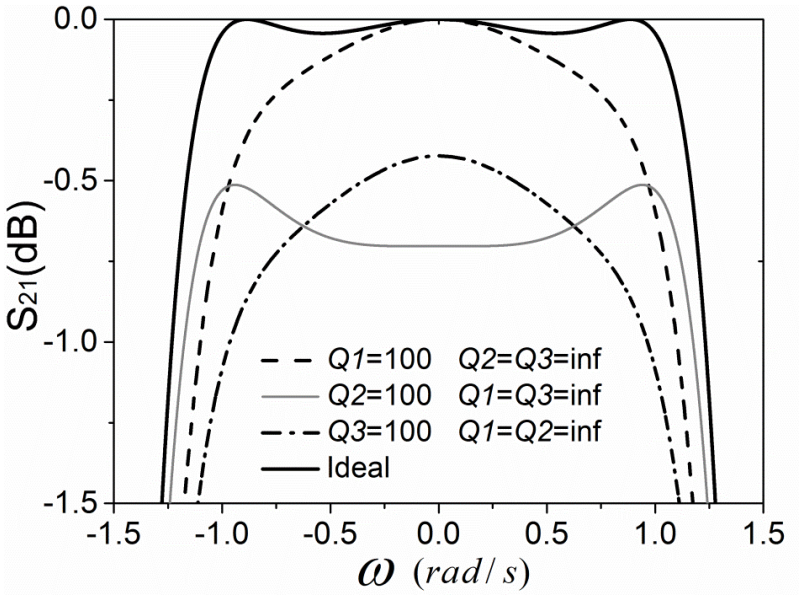

Figure 5.7: The impact of each resonator *Q* of 100 on passband insertion loss when comparing to the ideal one.

(resonator 2 in this case) is easier to adjust. As such, the optimized coupling matrix for the design is finally determined as (5.7) with a nonuniform *Q* distribution of 280, 84, 280. In Fig. 5.8, responses of coupling matrix (5.7) with different *Q* distribution and different M_{SL} are compared. It is shown that the source-load coupling successfully introduces an additional transmission zero TZ_3 below the passband with improved rejection level and indeed it can be moved to the upper stopband by adjusting the coupling nature of M_{SL}. However, the upper stopband attenuation and passband return loss is a bit degraded accordingly; hence, there is a trade-off for consideration. Also, it can be obviously noted that the insertion loss in the passband is less distorted by using nonuniform *Q* of 280, 84, 280 than the one with uniform *Q* of 280 (see in Fig. 5.8 (b)).

$$\mathrm{M} = \begin{bmatrix} 0 & -0.6202 & 0.8613 & 0 & -0.08 \\ -0.6202 & -0.0446\mathrm{j} & 0 & 1.3878 & 0.6202 \\ 0.8613 & 0 & -0.1488\mathrm{j} & 0 & 0.8613 \\ 0 & 1.3878 & 0 & -0.0446\mathrm{j} & 0 \\ -0.08 & 0.6202 & 0.8613 & 0 & 0 \end{bmatrix} \quad (5.7)$$

Observing the coupling matrix given in (5.7) and the physical layout shown in Fig. 5.6 (c), it can be seen that the lower *Q* of resonator 2 is obtained by loading a resistor

R at the end of open-stub. Note that the *R* only influences the *Q* of even-mode but has no effect on the odd-mode, which can be easily proved by using even- and odd-mode analyses [21] but not be repeated here.

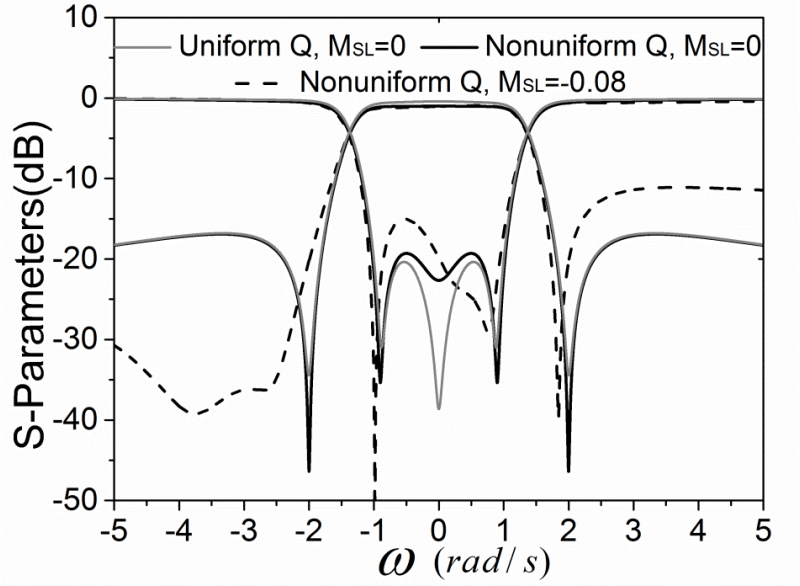

(a)

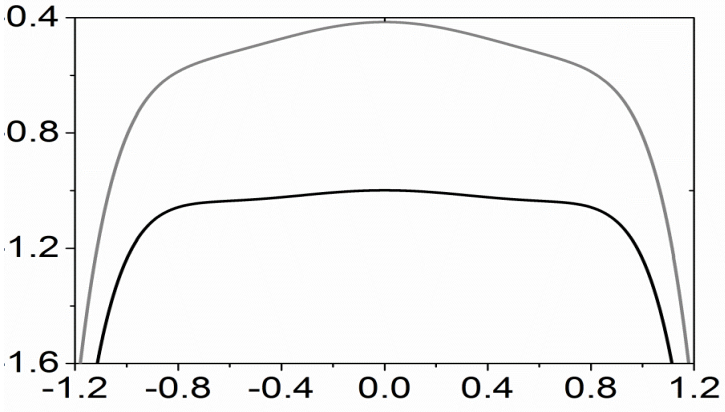

(b)

Figure 5.8: (a). Frequency responses of coupling matrix (5.7) with different *Q* distribution and different M_{SL}. (b). Detailed passband response comparison between uniform and nonuniform *Q* distribution.

Since the resonator 2 (even-mode) requires a stronger I/O coupling than the resonator 1 (odd-mode) does, a novel I/O feeding scheme as shown in Fig. 5.6 (c) is introduced. Typically, the desired and the extracted external quality factors Q_e can be

obtained by using equations (5.8) and (5.9), individually.

$$Q_{\text{e\_desired}} = \frac{1}{FBW \cdot {M_{si}}^2} \qquad (5.8)$$

$$Q_{\text{e\_extracted}} = \frac{2\pi f_{0\text{i}} \cdot \tau_{\text{s11}}(f_{0i})}{2} \qquad (5.9)$$

where i denotes resonator, FBW is the fractional bandwidth, $f_{0\text{i}}$ is the resonant frequency of i^{th} resonator, and $\tau_{\text{s11}}(f_{0\text{i}})$ is the group delay at resonance. Based on the geometrical parameters summarized in Table 5.1 and the simulated group delay given in Fig. 5.9, the extracted Q_e for even- and odd-mode are found as 18.8 and 49.8, respectively. In addition, due to the resonance of the feeding line, another transmission zero TZ_4 is created above the passband. As shown in Fig. 5.10, changing the length *l2* significantly shifts the transmission zero TZ_4.

Table 5.1: Dimensions of the Proposed Filter (Unit: mm)

l	***l1***	***l2***	***l3***	***l4***	***l5***	**w**
1.4	14	14.8	17.8	7.3	5	0.2
w1	**w2**	**w3**	**g**	**g1**	**g2**	**g3**
8.4	2.2	3.9	0.2	0.3	2.1	1.2

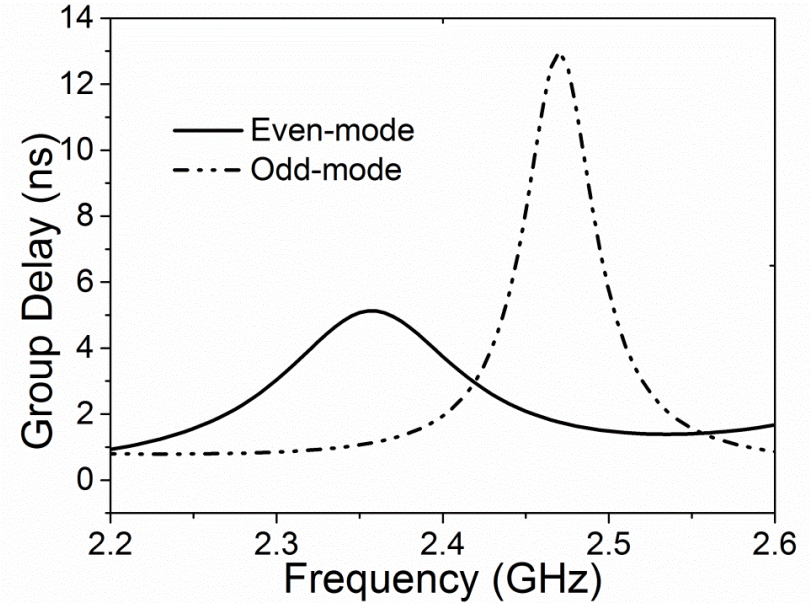

Figure 5.9: Group delay responses of odd-and even-mode for Q_e extraction.

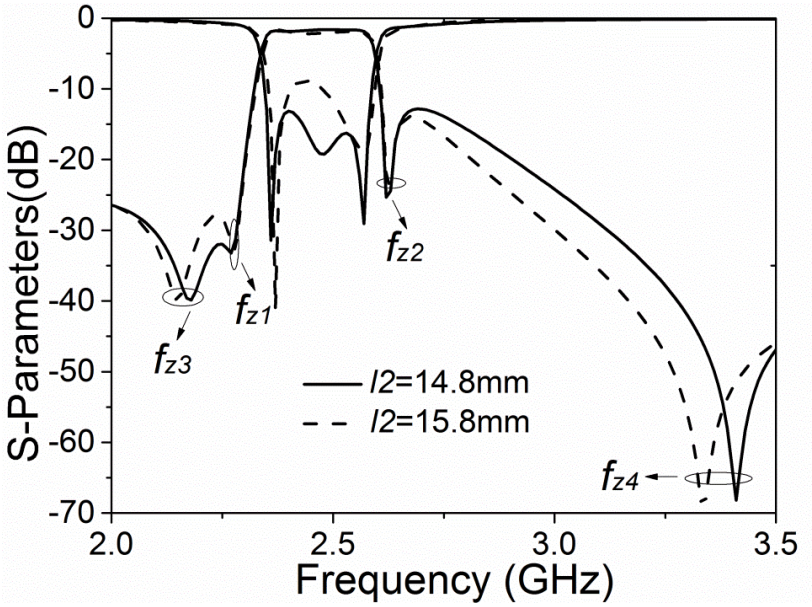

Figure 5.10: Simulated response of the filter versus different values of *l2*.

5.3.2 Fabrication and measurement

Shown in Fig. 5.11 (a) is the photo of the fabricated circuit with the relevant dimensions summarized in Table 5.1. Excluding the feed lines, the size of the filter is 32.4 mm × 29.8 mm. The substrate used is Rogers RO3003 with a thickness of 1.52 mm and dielectric constant of 3.0. In the full-wave simulation, dielectric losses ($\tan\delta = 0.0013$) and losses in the printed metallization ($\sigma = 5.8 \cdot 10^7$ S/m) are considered. A Panasonic metal film chip resistor $R = 2$ kΩ is attached to effectively reduce the unloaded *Q* of even-mode. The measured results in a wide frequency range with an enlarged view in a narrow range are shown in Fig. 5.11 (b), which are compared with the simulated results obtained in Sonnet [22]. As can be seen, the measured filter operates around 2.48 GHz with a 3-dB bandwidth of 250 MHz, giving a fractional bandwidth of 10%. The measured minimum passband insertion loss is 1.48 dB and the return loss is greater than 13 dB. As expected, four transmission zeros at 2.21, 2.30, 2.65 and 3.43 GHz result in an improved selectivity. In addition, it is noteworthy that the proposed filter achieves a wide stopband up to 6.4 GHz with 12 dB rejection. Such wide stopband is associated with the implemented feeding network that can effectively suppress the spurious response arising from the second harmonic

of the even-mode, which is expected at 5 GHz. In details, this is because the proposed feeding network provides a strong I/O coupling for even-mode at the fundamental frequency but it would be too weak at the second harmonic to support a passband due to the electromagnetic field distribution changed. Additionally, the reduced unloaded *Q* of even-mode is helpful for the suppression. In general, good agreement can be observed between the simulated and experimental results. A slight frequency shift in the passband results from some manufacturing tolerances.

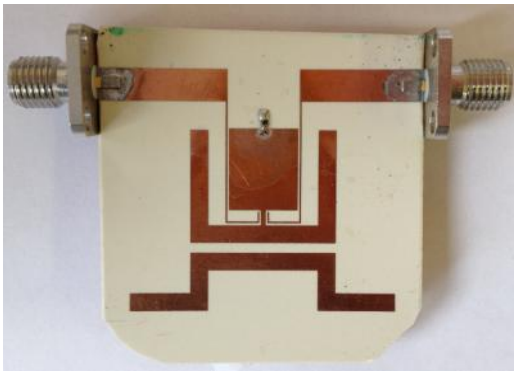

(a)

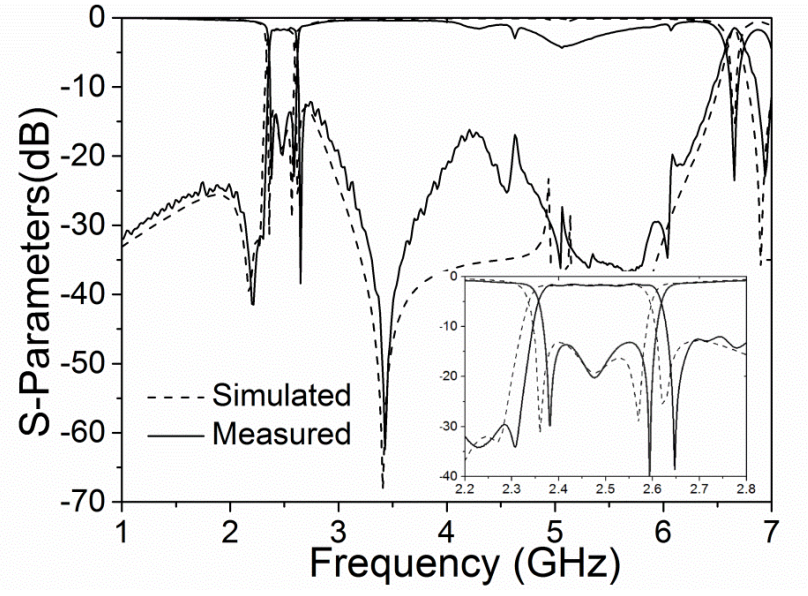

(b)

Figure 5.11: (a). Photograph of the fabricated filter. (b). Simulated and measured results of the proposed filter.

5.3.3 Performance comparison

A simple performance comparison of the presented filter with other ones that are similarly implemented in microstrip technology is summarized in Table 5.2. Equivalent Q is used here to define the filter transmission shape, except the absolute insertion loss. As can be seen, the proposed filter has greater advantages in passband insertion loss and equivalent Q. Additionally, expect without any resistive coupling requirement, the proposed lossy filter employs a shunt resistor to achieve a low-Q resonator instead of a small series resistor (0.3 Ω) used in [12], which is not only easier to be implemented but also makes the filter response is less sensitivity to the temperature characteristic of resistor used.

Table 5.2: Measured Performance Comparison with Other Related Works

Ref	**Order**	**f_0 (GHz)**	**FBW**	**In-band Insertion loss (dB)**	***Q* distribution**	**Equivalent *Q***	**Require Resistive cross couplings**
[12]	6	0.96	6.2%	7	250/250/80/ 80/80/80	750	Yes
[18]	4	1.0	11.5%	3	Uniform *Q* 200	1000	Yes
This work	**3**	**2.4**	**10%**	**1.5**	**280/84/280**	**1050**	**No**

5.4 An Investigation of Performance Enhancement for Tunable Microstrip Filter

As aforementioned, it is challenging to design a tunable bandpass filter with high performance, since the unloaded quality factors of the resonator structure and the quality factors of the tuning elements are quite limited. For instance, varactor diodes and BST varactors are commonly in use but their quality factors are less than 100 (see Table 1.1, Chapter 1), even if the quality factor of RF MEMS devices is also limited within 50 to 400. In this context, recently high Q_u evanescent-mode cavities have been proposed in [23]-[24] and a high Q_u suspended stripline resonator was presented in [25]. All these designs have achieved a Q of 400-1000; however, these structures are bulky and difficult to integrate with planar microwave circuits.

Based on the discussions in the above sections, it is noteworthy that lossy filter synthesis techniques have a promising advantage in designing a high-performance passive filter by using low Q resonators, which inspires us to solve the performance degradation existed in tunable microstrip filters in a similar fashion, aiming to obtain an equivalent high Q performance. The application background of tunable lossy filter has been simply demonstrated in Section 5.2.1, in this section, the detailed design technique with experimental examples will be described.

5.4.1 Tunable filtering structure

The configuration of the proposed third-order tunable combline filter with biasing scheme is shown in Fig. 5.12, which consists of three short-ended quarter-wavelength resonators with varactor diodes C_v for central frequency tuning, where r represents the varactor loss. C_d is the bypass or dc block capacitor. R_d is the dc bias resistor. The capacitor C placed at middle resonator is utilized for a desired detuning, and the resistor R added at each resonator is used to manipulate the resonator's unloaded Q factor. In addition, there are two shunt resistors (R_0) located at input and output (I/O) ports to improve the return loss and selectivity to some extent.

In order to characterize the selectivity, let us define it as:

$$selectivity = \frac{B}{\Delta B} \qquad (5.10)$$

where B is an equal ripple bandwidth and ΔB is a slope bandwidth that ranges from

the band edge frequency of the ripple bandwidth to the frequency at which the magnitude of S_{21} is dropped by 10 dB relatively.

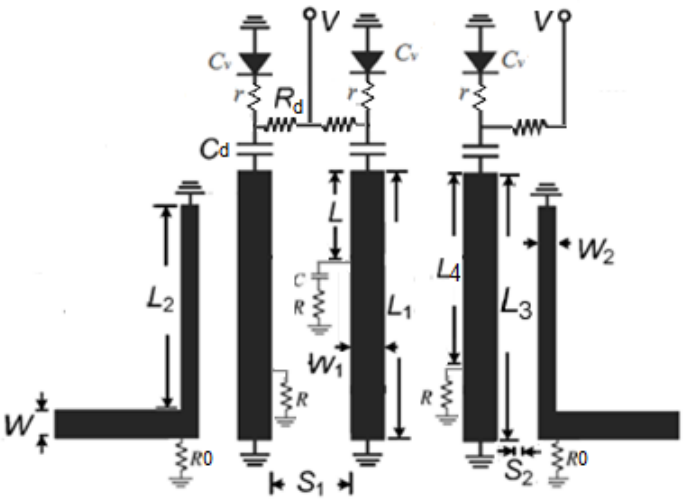

Figure 5.12: A three-pole tunable combline bandpass filter with enhanced performance.

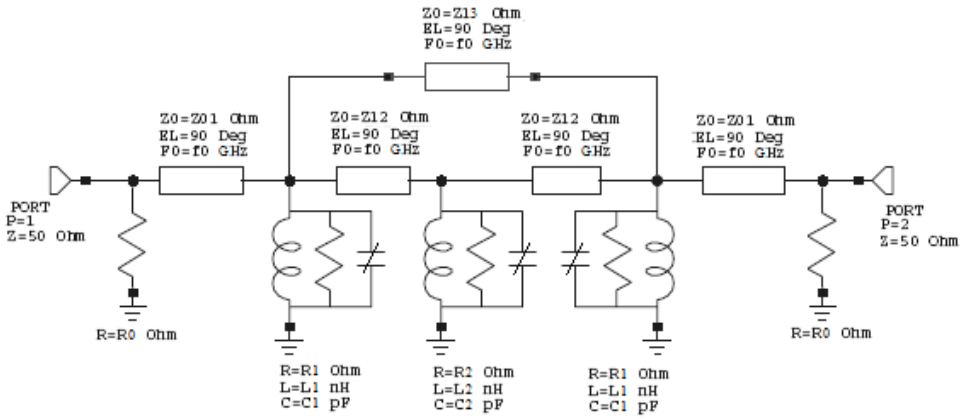

Figure 5.13: Equivalent circuit for the proposed tunable combline bandpass filter.

5.4.2 Theoretical synthesis of tunable lossy filter

For our investigation, an equivalent circuit model of the proposed tunable combline bandpass filter is presented in Fig. 5.13 for theoretical analysis. In this circuit, the lumped *RLC* elements represent finite-*Q* resonators whose resonant frequencies can be tuned by varying the capacitances, and the quarter-wavelength transmission lines, which have an electrical length $\mathrm{EL} = \pm 90^{\circ}$ at the centre

frequency f_0, are used to represent the inter-resonator couplings and the cross coupling to yield an inherent transmission zero of the combine filter. In addition, two shunt resistors R_0 are placed at input/output ports and their effects will be illustrated later on.

Using this circuit model, a third-order Chebyshev combline filter, which has a fractional bandwidth of 3% at the centre frequency f_0=1.5 GHz with 0.1-dB ripple, besides a transmission zero located around 1.62 GHz, is taken as an example to illustrate the design principles. The relevant circuit parameters can be derived from conventional filter theory [21] as follows: *L1*=*L2*=0.1543 nH, *C1*=72.97 pF, *C2*=72.45 pF, *Z12*=52.73 Ohm and *Z13*=280 Ohm. For the lossy resonator in the circuit, its unloaded quality factor is given by $Q_u = \omega_0 CR$. As the simulated responses illustrated in Fig. 5.14, it can be easily observed that, in the general lossy case, due to power dissipation (*R1*=*R2*=145 Ohm, Q_u=100) presented, the actual response will deviate somewhat from the lossless one, where it appears as an increased in the minimum insertion loss, a rounding of passband edges, and almost complete obliteration of the ripples.

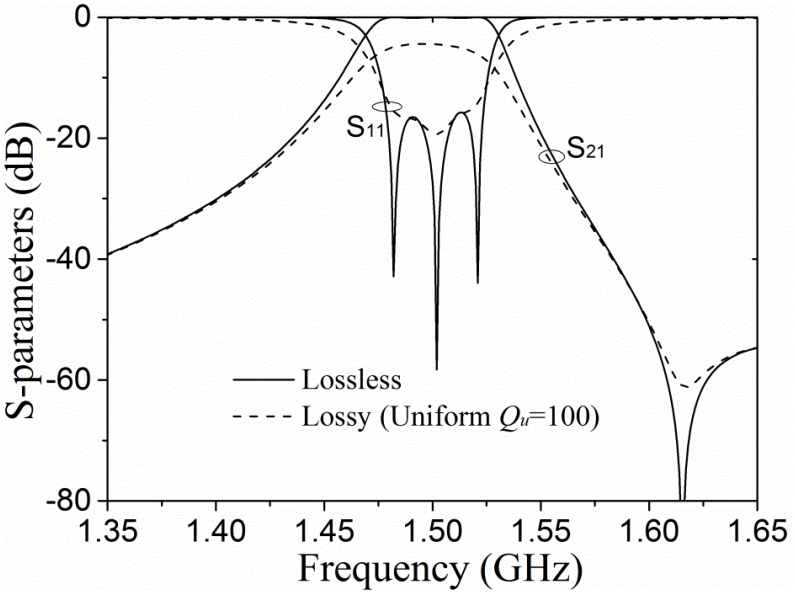

Figure 5.14: Lossless and lossy responses of the three-pole Chebyshev bandpass filter with 0.1-dB ripple.

A. Discussion on Detuning Conditions

As demonstrated in Section 5.2, in order to compensating for a rounding of passband edges with a poorer selectivity, the principle of predistortion technique is to design a prototype filter that has a peak transmission response near the passband edges by deliberately introducing mismatching in the midband, and then the dissipation loss flattens the filter passband response (see in Fig. 5.3). This type of predistortion is usually achieved by polynomial synthesis. Herein, it is simply done by direct detuning the resonators in the circuit model shown in Fig. 5.13 to realize such "peak" response. The results are illustrated in Fig. 5.15, where a simple Chebyshev lossless cases without transmission zeros are considered first. As can be seen, two typical transmission "peaks", denoted by p1 and p2, are obtained by varying the capacitance *C2* while the capacitance *C1* is kept fixed. For our discussion, the level of peak p2 is supposed to be higher than peak p1. It is shown that the peak p2 is mainly associated with the capacitance *C2* while p1 is more controllable by *C1*. Additionally, a dip with the largest insertion loss in the middle band, denoted by t0 in Fig. 5.15, is produced and determined by the detune degree among the resonators. This means two peaks are farther away from the passband that corresponds to a greater mismatch loss produced at band centre, which can be proved by the comparative results between the *C2*=75.0 pF and *C2*=69.0 pF given in Fig. 5.15. Indeed, the similar distorted response can also be observed by detuning the capacitance *C1* of outer resonators in Fig. 5.13.

Overall, detuning resonators is typically required and treated as the first step in the proposed technique to achieve performance enhancement in tunable filter design. An ideal detuned or distorted response should have a greater mismatch at the band center and two transmission peaks, namely p1 and p2 as defined above, placing near the desired band edges. To this end, the equivalent capacitances and inter-resonator couplings have to be adjusted. In addition, according to the relative location of peak p2 shown in Fig. 5.15, it is understood that there would be two optional solutions under different detuned conditions, i.e., either capacitance *C2* smaller or larger than capacitance *C1*. Herein the detuning condition of *C2* larger than *C1* will be mainly discussed in the following tunable combine filter design.

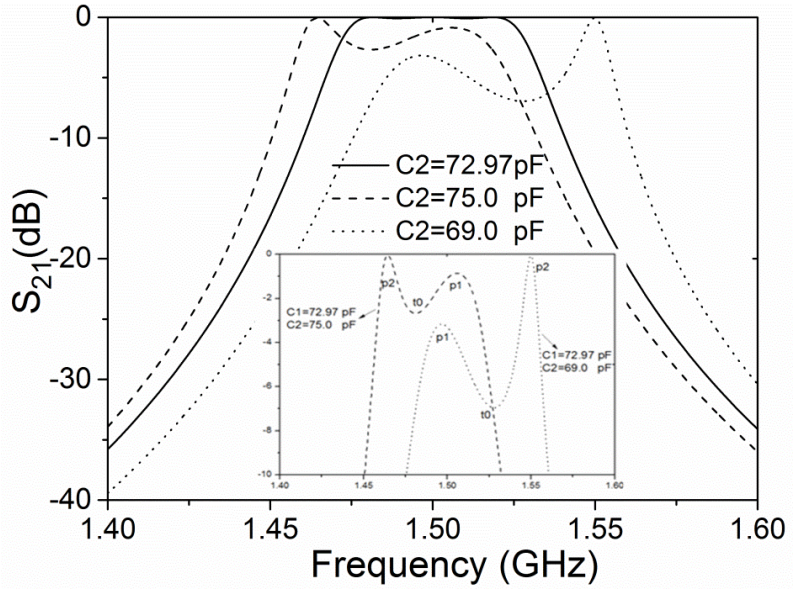

(a)

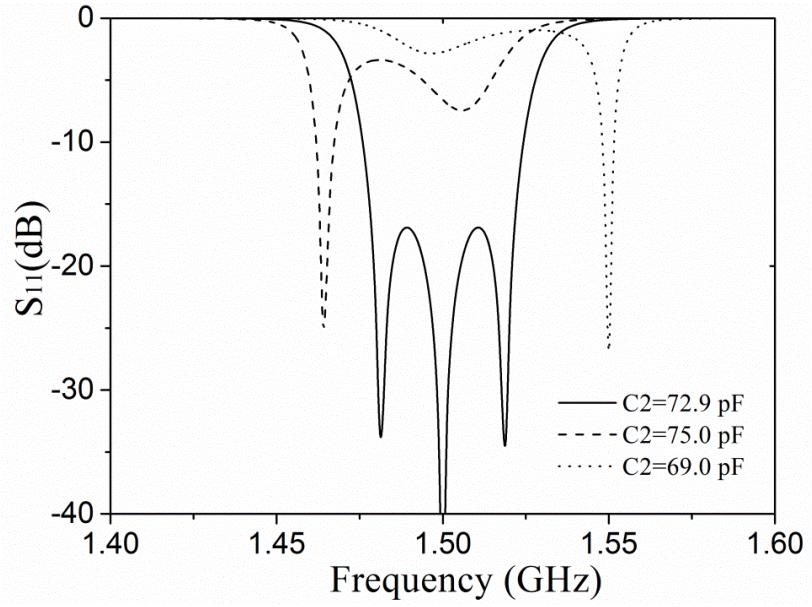

(b)

Figure 5.15: Frequency lossless "peak" responses by detuning the capacitor *C2*: (a) Insertion loss. (b) Return loss. (*L1*=*L2*=0.1543 nH, *C1*=*C2*=72.97 pF, *Z12*=52.73 Ohm).

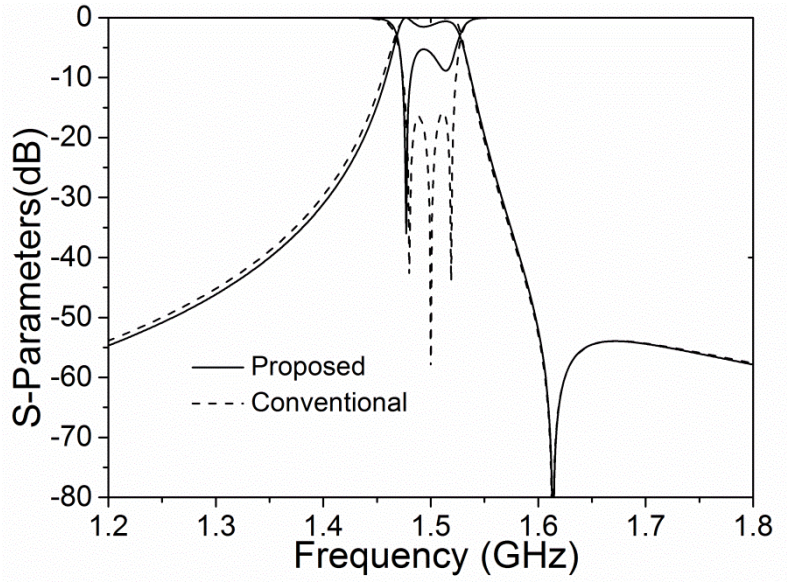

(a)

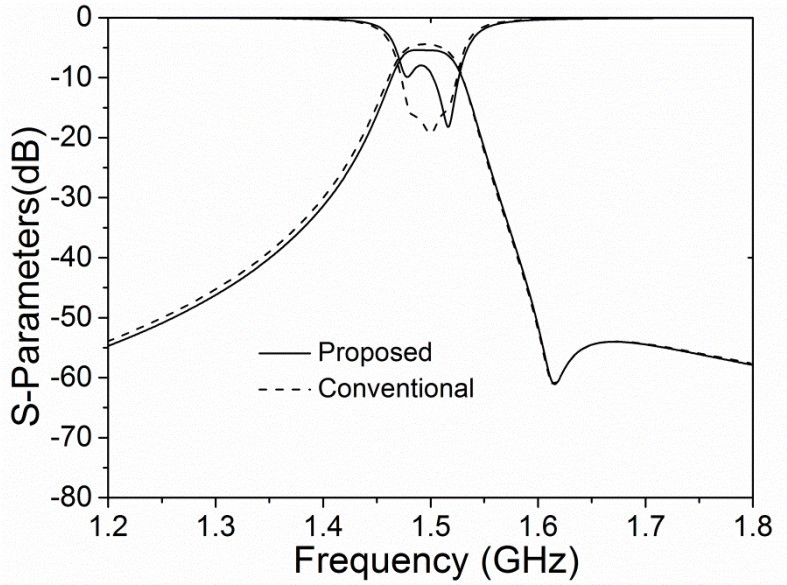

(b)

Figure 5.16: Frequency responses of the proposed filter as compared with the conventional design. (a) Lossless response. (b). Lossy response with uniform dissipative loss.

B. Optimizing Q Distribution in the Filter

Base on the above discussion, the initial lossless responses of the proposed design by detuning the resonators in the filter compared with the conventional response are obtained, as shown in the Fig. 5.16 (a). The corresponding lossless circuit parameters are given in Table 5.3, where, as expected, the equivalent capacitances *C2* and *C1* of the proposed designs are detuned from the conventional values. The place of transmission zero can be adjusted by changing the impedance of cross coupling stubs *Z13*. As implied in Fig. 5.16 (a) and Fig. 5.15, it should be highlighted that peak p2 locating near lower bandedge results in a higher selectivity at lower stopband in the detuned design, at the cost of slightly degrading the selectivity at the upper side. However, since there is an inherent transmission zero located in the upper stopband, such little degradation can be neglected. If we further consider a uniform *Q* distribution with *R1=R2*=145 Ohm for both cases, the in-band insertion loss variation of the proposed filter is relatively smaller than the conventional one as shown in Fig. 5.16 (b).

Nevertheless, there is still a room for improving the passband flatness by optimizing the *Q* distribution in the presented filter. To this aim, the impact of individual resonator's Q_u on the filter response under different detuned degree are studied and the results are illustrated in Fig. 5.17, where reducing *R1* or *R2* from the original value of 145 Ohms indicates a decrease of the unloaded *Q* of resonator 1 or 2, respectively. From these results, it is observed that decreasing the value of *R1*/*R2* in the proposed detuned filter leads to more insertion loss deviations around the upper/lower band edge, and which is more significant when the detune degree is increased. That is because in a larger detuned filter, the response at a band edge is mainly determined by that specific resonator, whose dissipation loss has an independent effect on the filter shape. In this manner, the dissipation loss of each resonator in the proposed detuned filter can be adjusted separately to further flatten the lossy passband response of Fig. 5.16 (b). For this proposed filter design, using nonuniform *Q* distribution instead of uniform one can further improve the passband flatness. The corresponding results will be demonstrated later.

Table 5.3: Circuit Parameters for Two Different Types of Filters

Filter Type	Lossless					Lossy terms		
	L1=L2 (nH)	*C1* (pF)	*C2* (pF)	*Z12* (Ω)	*Z13* (Ω)	*R1* (Ω)	*R2* (Ω)	R_0 (Ω)
Conventional	0.1543	72.97	72.45	52.73	280	145	145	none
Proposed	0.1543	72.3	73.4	52.73	300	125	145	300

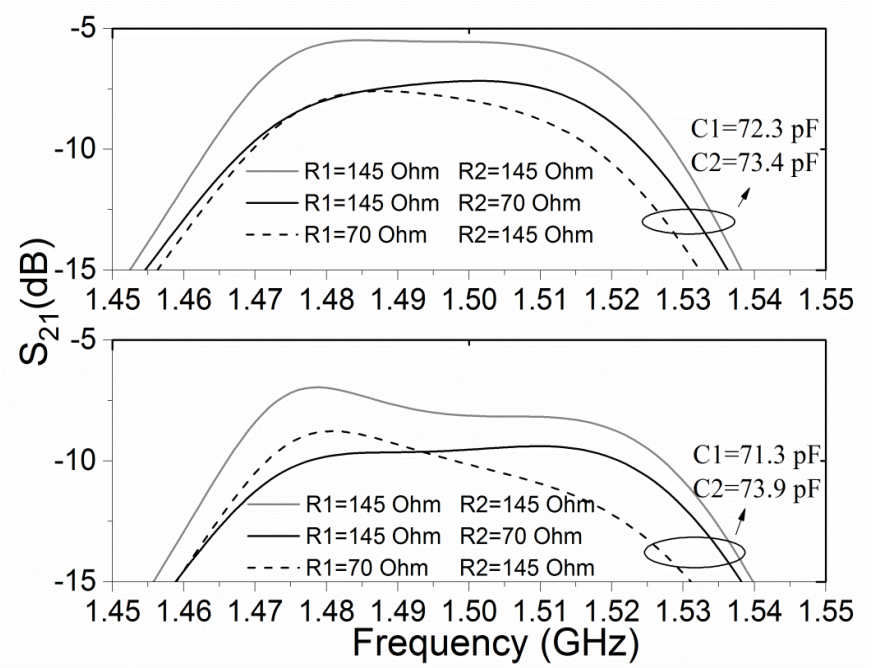

Figure 5.17: Impact of *Q* distributions on the passband response in proposed combine filter versus different detune degree.

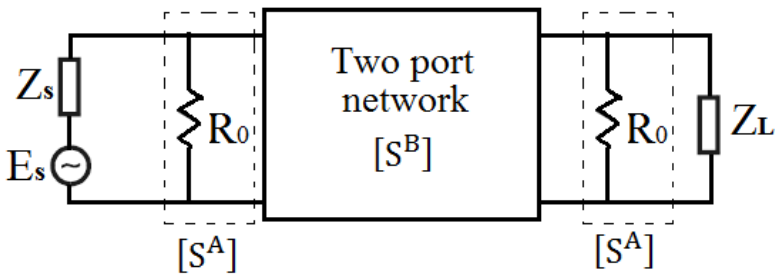

Figure 5.18: Equivalent filter network with two shunt resistor R_0 at source/load.

C. Impact of Two Shunt Resistors R_0 at Input and Output

In order to examine the effect of two shunt resistors placed at input/output ports shown in Fig. 5.13, a general equivalent circuit model is considered as in Fig. 5.18. From the network perspective, this special case can be treated as three independent networks connected in cascade, whose scattering matrixes are $[S^A], [S^B]$ and $[S^A]$ respectively. Here $[S^B]$ is an arbitrary filter and $[S^A]$ can be easily derived as:

$$[S^A] = \begin{bmatrix} \frac{-1}{2r+1} & \frac{2r}{2r+1} \\ \frac{2r}{2r+1} & \frac{-1}{2r+1} \end{bmatrix} \qquad (5.11)$$

where $r = R_0/Z_0$ is the normalized impedance, it is obvious to see the $[S^A]$ is a real matrix. For simplicity, let us only consider the impact of resistor R_0 presented at source on the filter's performance firstly, assuming no resistor R_0 at load. The scattering matrix of the whole cascaded network can be obtained using network analysis [10] as:

$$S_{21}{}^{\text{cascaded}}\,(\text{dB}) = -20\log\left|\frac{S_{21}{}^{\text{A}}}{1 - S_{22}{}^{\text{A}}S_{11}{}^{\text{B}}}\right| + S_{21}{}^{\text{B}}(\text{dB})$$

$$= \Delta S_{21}(\text{dB}) + S_{21}{}^{\text{B}}(\text{dB}) \qquad (5.12)$$

where $\Delta S_{21}(\text{dB})$ is the insertion loss deviation. It is evident that ΔS_{21} is not only associated with the values of resistor R_0, but also determined by the reflection coefficient $S_{11}{}^{\text{B}}$. Due to the $S_{22}{}^{\text{A}}$ in the formula (5.11) is negative constant, it will be obtained a larger deviation in the stopband ($S_{11}{}^{\text{B}} = 1$) than the passband ($S_{11}{}^{\text{B}} = 0$). This means presenting the resistor R_0 at source will improve the selectivity of the filter to some extent and such improvement would be more significant when adding a resistor R_0 at load. Furthermore, another important purpose of utilizing resistors R_0 at source/load is to improve in-band return loss by power absorption. An illustrative example for the impact of resistors R_0 is shown in Fig. 5.19, where the proposed filter with lossy components (i.e. *R1*=125 Ohm, *R2*=145 Ohm) is simulated with various R_0 at input/output ports. It is observed that that by virtue of resistors R_0 loading, the

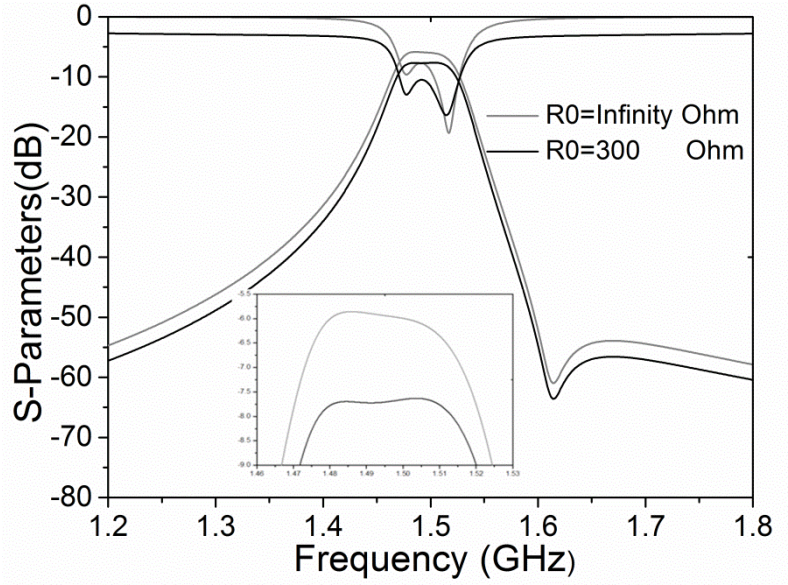

Figure 5.19: Frequency responses of the proposed filter with various shunt resistors R_0 at source/load.

return loss is significantly improved better than 10 dB, and the selectivity of the filter is also improved to some extent, although the absolute in-band insertion loss is increased by 1.6 dB. Furthermore, from the detailed passband response given in Fig. 5.19, it is noteworthy that the passband flatness of the filter with R_0 is better than the contrary one. That is because these two shunt resistors R_0 at I/O ports would bring about some deviations at band centre as well as detuning resonators. Such property can be understood based on the equations (5.11)-(5.12). In summary, two shunt resistors R_0 are mostly used to improve the in-band return loss and further improve the selectivity and passband flatness. However, obviously there is a trade-off between these improvements and additional absolute in-band insertion loss.

D. Coupling Matrix and Performance Demonstration

In light of the above discussions, the final circuit parameters are summarized in Table 5.3, where the proposed design has an optimized nonuniform *Q* distribution and two shunt resistors R_0 loaded at source/load. The corresponding coupling matrix is given in Fig. 5.20. As mentioned in section 5.3, the entries on the main diagonal $M_{i,i}$ are no longer real numbers after including dissipative loss in the lossy filter. Typically, the imaginary parts of source and load terminations $(Im(M_{s,s}), Im(M_{s,s}))$ are

associated with the shunt resistors R_0 placed at Input/output ports by normalizing to unity impedance, while all the other imaginary parts of diagonal elements relate to unloaded quality factor Q_u of resonators, where $Im(M_{i,i})\big|_{i=1,2,3} = -j \cdot f_0/(BW \cdot Q_{ui})$, f_0 is the centre frequency of the passband, and BW is the design bandwidth.

Once the coupling matrix [M] is determined, the scattering parameters are given by:

$$S_{11} = 1 + 2j[A]_{11}{}^{-1} \qquad (5.13)$$

$$S_{21} = -2j[A]_{(n+2)1}{}^{-1} \qquad (5.14)$$

with

$$[A] = p[U] - j[R] + [M] \qquad (5.15)$$

where n is the order of the filter, p is the complex lowpass prototype frequency variable, [U] is the identity matrix except $[U]_{11} = [U]_{(n+2)(n+2)}$=0, [$R$] is a matrix whose only nonzero entries are $[R]_{11} = [R]_{(n+2)(n+2)} = 1$, and [$M$] is a symmetric square coupling matrix.

	S	1	2	3	L
S	-0.1667j	0.9845	0	0	0
1	0.9845	-0.32064-0.3922j	0.92	0.16083	0
2	0	0.92	0.22909-0.3333j	0.92	0
3	0	0.16083	0.92	-0.32064-0.3922j	0.9845
L	0	0	0	0.9845	-0.1667j

Figure 5.20: Coupling matrix of the proposed lossy three-pole filter.

Fig. 5.21 plots the final responses of the proposed design obtained from the circuit simulation and coupling matrix, as compared with the conventional one. For the comparison, B in (5.10) is assumed to be the 0.2 dB equal ripple bandwidth. By comparison in Fig. 5.21 and Table 5.4, it is easily observed that the proposed design has a flatter passband performance up to 36 MHz equal ripple ($L_{Ar} = 0.2$ dB)

bandwidth. Under the selectivity defined in equation (5.10), it can be concluded that the selectivity performances of the proposed design illustrated in Fig. 5.21 are greatly enhanced at the expense of increased absolute insertion loss. In order to better show the performance improvement, Fig. 5.22 implies the normalized response of the proposed filter and it can be obtained that the proposed design can approximately achieve an equivalent *Q* of 330, while the actual *Q* distribution of the filter is 85, 100 and 85.

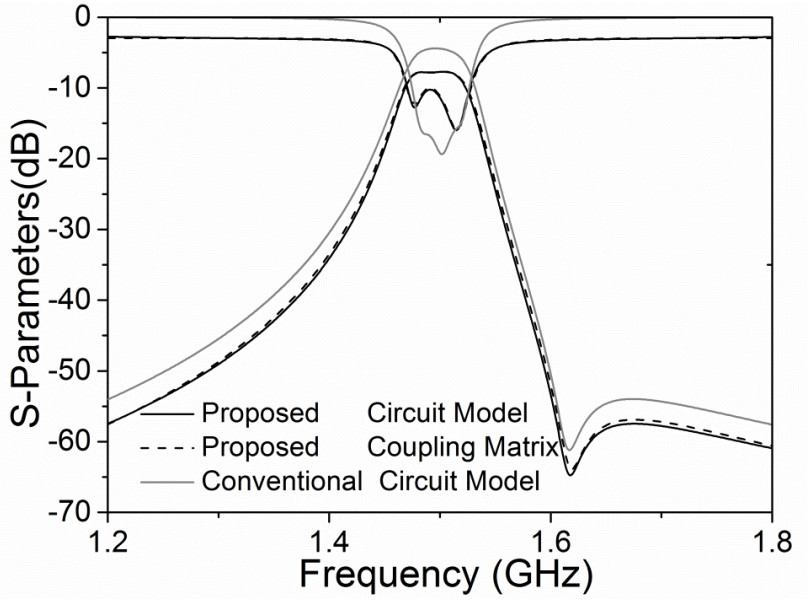

Figure 5.21: Frequency responses of the proposed design as compared with the convention design.

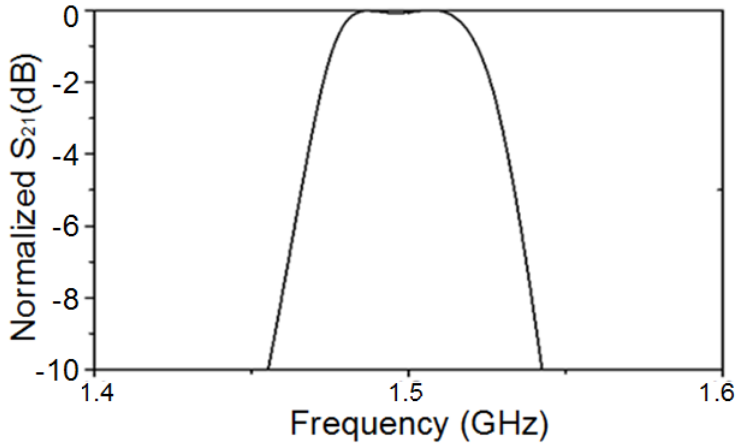

Figure 5.22: Normalized S_{21} response (simulated) of the proposed design to show the improved performance with an equivalent *Q* of 330.

Table 5.4: Passband Performance Comparison between the Proposed and the Conventional Designs

Filter Type	B Equal ripple bandwidth (LAr=0.2dB)	ΔB Slope bandwidth	Selectivity B/ΔB	IL/RL (dB) at f_0
Conventioanl	19 MHz	35MHz	0.542	4.4 /18.7dB
Proposed	36MHz	26MHz	1.385	7.8/10.3 dB

Table 5.5：Illustrative typical examples versus different *Q* distribution

Examples	*L1/L2* (nH) *C1/C2* (pF)	*Z12/Z13* (Ohm)	*R1/R2*(Ohm) *Q1/Q2*	R_0 (Ohm)	IL/RL At f_0 (dB)	Equivaent *Q*
Example I	0.1543/0.1543 72.45/72.7	51.5/278	173/476 Q: 120/328	500	4.1/11.8	700
Example II (**proposed**)	0.1543/0.1543 72.3/73.4	52.73/300	123/145 Q: 85/100	300	7.8/10.3	330
Example III	0.1543/0.1543 71.7/73.5	53.7/310	112/107 Q: 78/73	200	10.5/10.2	300

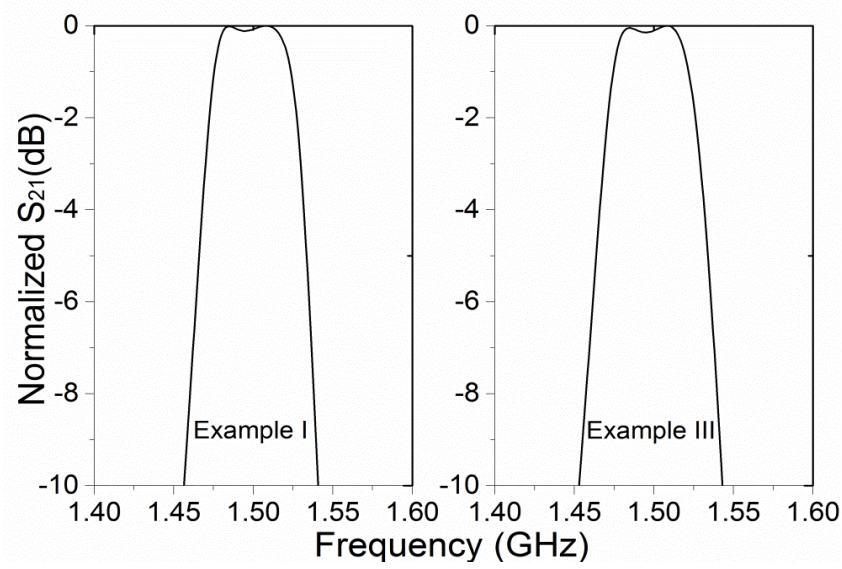

Figure 5.23: Normalized S_{21} response (simulated) of the illustrative examples given in Table 5.5 to show the improved performance.

E. Design Procedure

Step 1: Determine the detune degree among the resonators. This would depend on the given filter specifications and the types of resonator used in the design, where higher Q resonators are used, smaller detune degree would be required to avoid excessive mismatch loss produced in the passband.

Step 2: Optimizing the Q distribution of resonators and I/O shunt resistors R_0 in the filter to improve the passband return loss and flatness. It should be highlighted that nonuniform Q distribution is not necessarily required, which should be determined by the detune degree obtained in the step 1. Additionally, note that there is a trade-off between the improved return loss and increased absolute insertion loss.

To go through the design procedure, some illustrative examples are given in Table 5.5 and Fig. 5.23. It can be seen that Example I is composed of relatively higher Q resonators than Example III, so that its detune degree is smaller during the design accordingly. Moreover, all the given examples have good return loss below 10 dB with the help of different R_0, but suffer from different level of insertion loss deviation.

5.4.3 Discussion on filter realization

Ideally, in order to achieve a perfect tunable lossy filter design, it requires properly detuning the resonators and optimizing the Q distribution at each tuning state. However, it is well known that the unloaded Q_u of the resonator varies against frequency shifting and thus lead to a difficulty in obtaining an optimal Q distribution at each stage. When applying the proposed technique to tunable filter design, how to reduce the effect of Q variation on the filter response within a certain range is our first concern.

In terms of physical tunable filter implementation, we mainly utilize lumped elements (R and C) that are added at each resonator for controlling the detuned degree and Q distribution. In order to examine the corresponding effects, a single varactor-tuned resonator with different loading elements is simulated at illustrative tuning states, as shown in Fig. 5.24. Here, the substrate RT/Duriod 6010 with $\varepsilon_r = 10.2$ and h=1.27 mm is used. All the EM simulations are performed using a

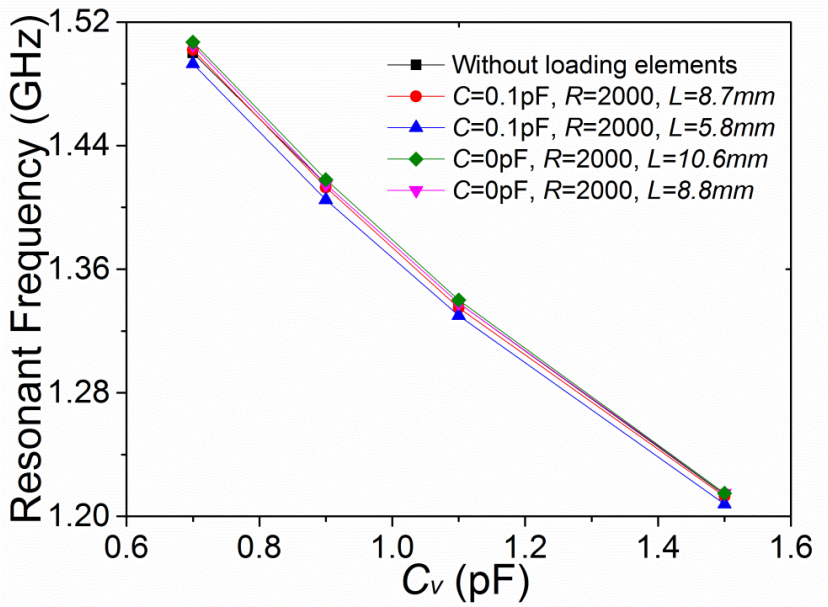

(a)

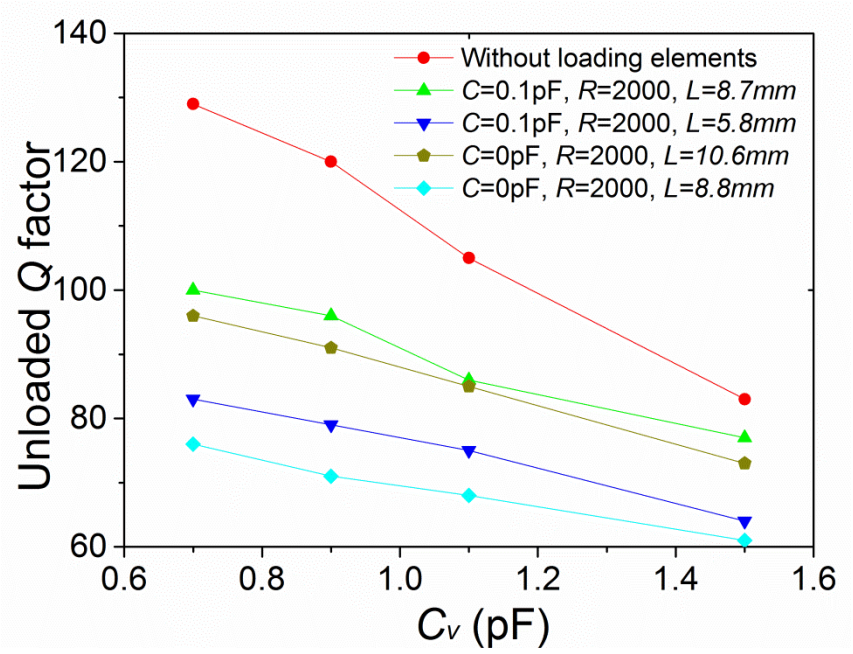

(b)

Figure 5.24: The impact of loading *RC* lumped elements. (a) Resonant frequency under various loading elements versus different tuning states. (b) Unloaded Q_u under various loading elements versus different tuning states.

commercially available tool SONNET [22]. Observing Fig. 5.24 (a), in comparison to the conventional case without any loading element, the resonant frequency of element-loaded resonator is somewhat changed at each tuning state, creating the desired detuning condition in design. In particular, capacitance *C* makes more contribution to the detuning degree than resistor *R*. On the other hand, in Fig. 5.24 (b), it is noted that by loading *RC* lumped elements, the unloaded Q_u of the resonator can be effectively controlled. Additionally, the rates of decline in unloaded Q_u against frequency shifting have slowed in comparison to the conventional case, which offers a possibility to remain the enhanced performance within a certain tuning range and that will be proved by the results in the next section. Apparently, from Fig. 5.24, except the the values of lumped elements (*R, C*), the locations (*L, L4*) of loading lumped elements are also quite important to control the unloaded quality factor of resonator and detuned degree, as a rule, when the loading location is nearer to the open end, the effect of loading elements on reducing the Q of resonator becomes significant. Normally, those two parameters of loading elements can be optimized with the help of computer-aided tuning techniques.

5.4.4 Simulated and measured results

To validate the proposed lossy circuit technique, a third-order narrowband tunable microstrip combline filter presented in Fig. 5.12 is demonstrated through both EM simulation and experimentally measured results. The final geometry parameters are summarized in Table 5.6. And the values of the added lumped element components are *C*=0.1 pF, *R*=2000 Ω and R_0=300 Ω, respectively. The GaAs diodes MA46H202 (0.7-6 pF, r=0.3 Ω at 1.5 GHz at C_v=0.7 pF [26]-[27]) are used for central frequency tuning. Also the AVX chip capacitors, Murata chip capacitors and the Panasonic resistors are used in the *RC* series section and dc-biasing circuit.

Fig. 5.25 depicts the simulated results of the proposed filter for varactors varying from 0.7 to 1.5 pF, which are also compared with the conventional tunable filter design. From the comparison, it is obvious to see by loading lumped elements, the proposed filter has a much flatter passband than the conventional design within the

Table 5.6：Filter Parameters for Two Different Types of Filters

Filter Type	*W*/*W1*/*W2* (mm)	*L*/*L1*/*L2*/*L3*/*L4* (mm)	*S1*/*S2* (mm)
Concentional	1.1/0.8/0.8	none/13.4/14.3/13.6/none	5.4/1.2
Proposed	1.1/0.8/0.8	8.7/13.4/14.3/13.5/10.6	5.3/1.2

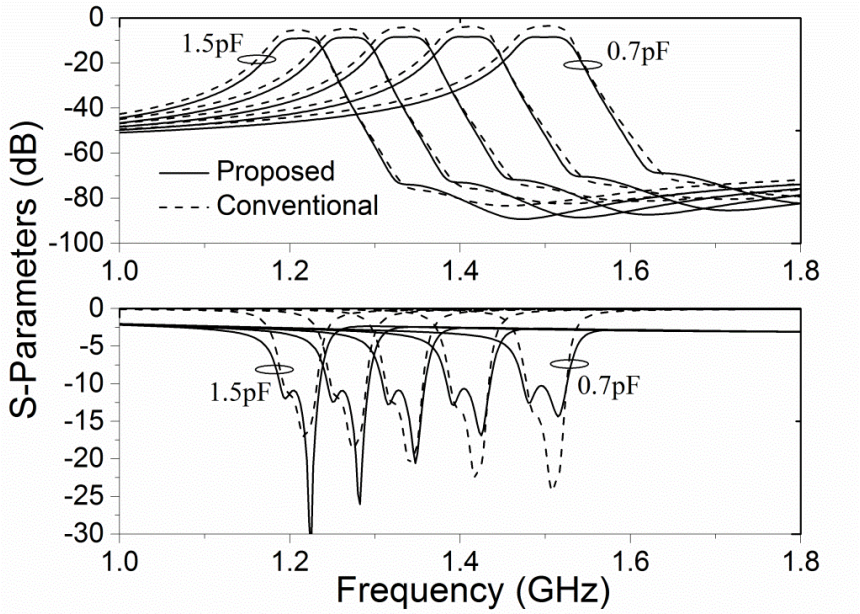

Figure 5.25: Comparison of the simulated results of the proposed and conventional tunable filter.

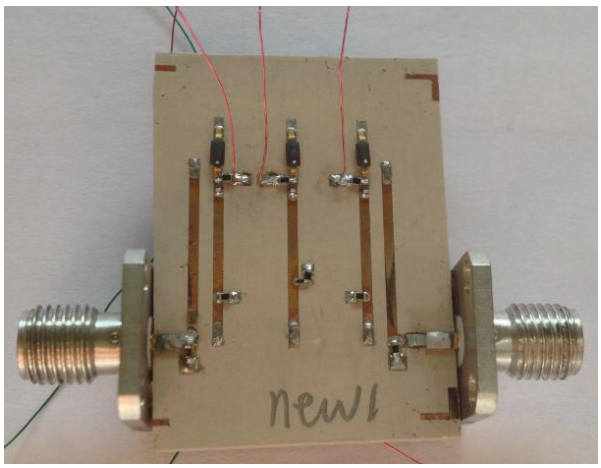

Figure 5.26: Fabricated tunable combline filter with enhanced performance.

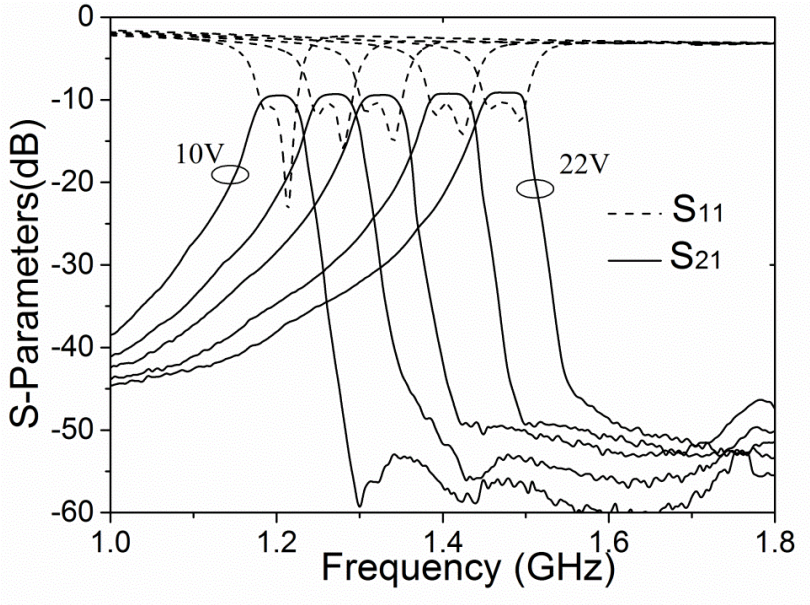

Figure 5.27: The measured responses of the proposed tunable combline filter with enhanced selectivity and passband.

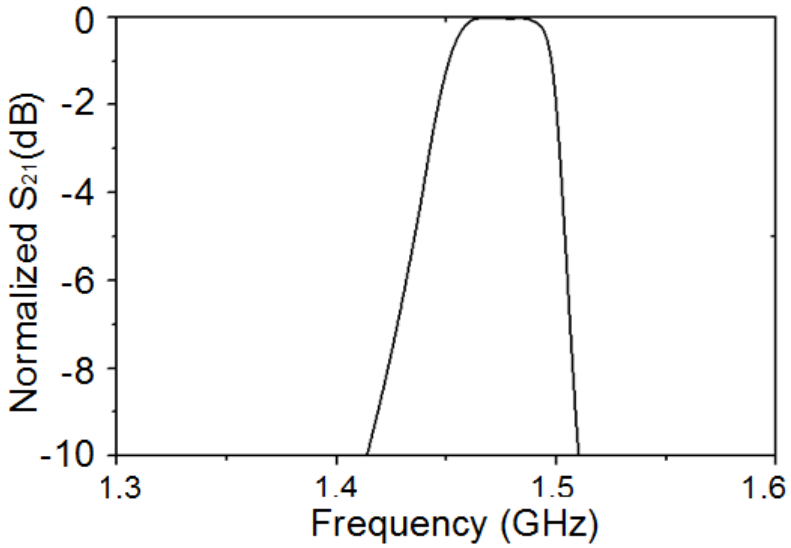

Figure 5.28: Normalized S_{21} response (measured) of the upper channel of the proposed tunable combline filter to show the improved selectivity with an equivalent Q of 340.

tuning range, and the rounding effects are compensated at the band edges, leading to a higher selectivity, although the absolute insertion losses are increased. The simulated insertion loss ranges from 8.6 to 9.1 dB with the passband return loss greater than 10 dB. Additionally, the loss variation in passband does not keep the same good level with the frequency tuning. This is because the varactor quality factor decreases as the frequency tunes down, while we get the optimal Q distribution at a varactor diode value C_v = 0.7 pF. And at the C_v = 0.7 pF (diode loss r = 0.3 Ω at 1.5 GHz), the simulated unloaded Q distribution of the filter is 92, 100, 92. Nevertheless, compared with conventional design, the performance of the proposed one (namely passband flatness and selectivity) at each tuning states is obviously enhanced at different degree.

For the experimental demonstration, Fig. 5.26 illustrates the photo of the fabricated tunable combline filter with enhanced performance. The measured results for the proposed filter are plotted together in Fig. 5.27. These results are obtained for DC bias voltage varying from 10.0 to 22.0 V. At 10.0 V bias, the centre frequency of the proposed filter is around 1.20 GHz, with insertion loss of 9.5 dB, equal-ripple ($L_{Ar} = 0.2$ dB) bandwidth of 16 MHz, effective 3 dB bandwidth of 52 MHz, respectively. At 22.0 V bias, the centre frequency of the proposed filter is around 1.48 GHz, with insertion loss of 9.1 dB, equal-ripple ($L_{Ar} = 0.2$ dB) bandwidth of 34 MHz, effective 3 dB bandwidth of 57 MHz, respectively. Also it is noted that the return loss of each state among the tuning range is greater than 10 dB. When compared with the simulated results shown in Fig. 5.25, the measured curves keep the same shape except the central frequency shifting down a bit, which results from manufacturing tolerances and effects of tuning elements.

Fig. 5.28 shows the normalized measured response of upper channel of the proposed tunable combline filter. In order to estimate the equivalent *Q*, the measured loss variation is compared to the computer-simulated performance of the filter with uniform *Q*. In this manner, the equivalent *Q* of the measured filter at upper channel is estimated to be 340. To our knowledge, a varactor-tuned microstrip filter with such high equivalent *Q* has not previously been reported.

Fig. 5.29 gives the measured third-order inter-nodulation intercept point (IIP3) of the proposed tunable combline filter for different bias voltages or center frequencies. As the bias voltage increases, the center frequency shifts upward and the bandwidth also increases, the operating point of the varactor moves toward the linear *C*-V curve region and IIP3 products become higher. The measured IIP3 of the proposed filter is around 15.7 dBm at 22 V and 12.3 dBm at 10 V.

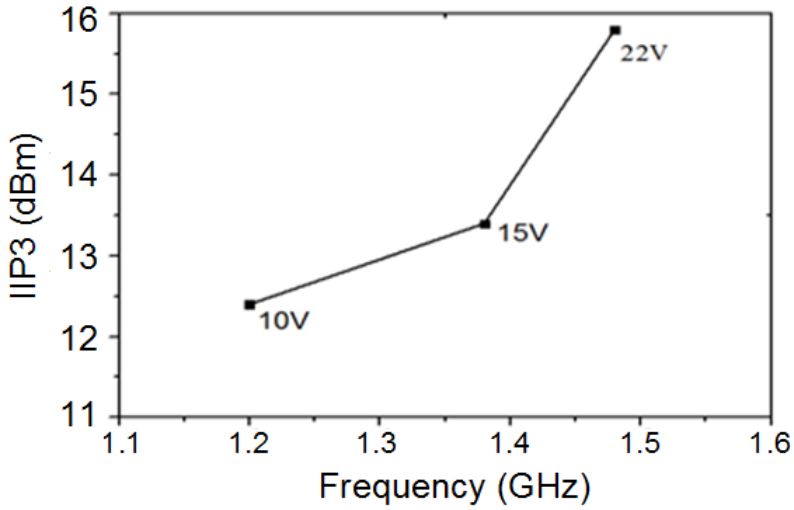

Figure 5.29: Measured IIP3 versus tunable center frequency.

5.5 Summary

In this chapter, two methodologies for the design of microstrip lossy filters were investigated, which aimed to construct a high-performance (passband flatness and selectivity) filter using lower *Q* resonators than conventional approaches. The first approach was to introduce a proper nonuniform *Q* distribution in an extended doublet filter topology, based on the independent effect of each resonator *Q* on the filter response shaping. Although the concept of nonuniform *Q* distribution was not firstly applied to design a lossy filter, our work still addressed diverse advantages in filter performance, including lower insertion loss, higher equivalent *Q*, wider stopband bandwidth and easier fabrication process in comparison to the other related works. After that, another method to improve the performance of tunable combline filter has been presented and analyzed, which was mainly realized by loading series-connected

RC elements and adding resistors at source/load in the structure. The equivalent circuit model of the proposed filter was utilized to demonstrate the mechanism of performance improvement. For theoretical verification, a three-pole tunable microstrip combine filter and its counterpart were investigated theoretically and experimentally. It has been shown that for very lossy tunable microstrip narrowband filter, the selectivity and passband flatness can be dramatically enhanced with different degree over the tuning range.

The main penalty in using presented techniques was in the increase of absolute insertion loss, particularly for the second approach. However, since the targeted application is for receiver filter such as IMUX, the increase in loss can be traded off for in-band flatness, size, volume, and overall system performance.

Reference

[1] M. Yu and V. Miraftab, “Shrinking microwave filters,” *IEEE Microw. Mag.*, vol. 9, no. 5, pp. 40–54, Oct. 2008.

[2] I. Hunter, A. Guyette, and R. D. Pollard, “Passive microwave receive filter networks using low- resonators,” *IEEE Microw. Mag.*, vol. 6, no. 3, pp. 46–53, Sep. 2005.

[3] S. B. Cohn, “Dissipation loss in multiple-coupled-resonator filters,” *IRE Trans. Trans. Microw. Theory Tech.*, vol. MTT-7, no. 8, pp.1342–1348, Jul. 1959.

[4] Yi-Chyun Chiou and Gabriel M. Rebeiz,” A Tunable Three-Pole 1.5–2.2-GHz Bandpass Filter With Bandwidth and Transmission Zero Control,*” IEEE Trans. Microw. Theory Tech.*, vol. 59, no. 11, pp. 2872–2878, Nov. 2011.

[5] Yi-Chyun Chiou and Gabriel M. Rebeiz,” A Quasi Elliptic Function 1.75–2.25 GHz 3-Pole Bandpass Filter with Bandwidth Control,*” IEEE Trans. Microw. Theory Tech.*, vol. 60, no. 2, pp. 244-249, Feb. 2012.

[6] R. M. Livingston, “Predistorted waveguide filters,” in *IEEE MTT-S Int. Microwave Symp. Dig.*, 1969, pp. 291–297.

[7] A. E. Williams, W. G. Bush, and R. R. Bonetti, “Predistortion technique for multicoupled resonator filters,” *IEEE Trans. Microw. Theory Tech*., vol. MTT-33, pp. 402–407, May 1985.

[8] M. Yu, W. C. Tang, A. Malarky, V. Dokas, R. Cameron, and Y. Wang, “Predistortion technique for cross-coupled filters and its application to satellite communication systems,” *IEEE Trans. Microw. Theory Tech*., vol. 51, no. 12, pp. 2505–2515, Dec. 2003.

[9] X.-P. Chen, L. Han, and K. Wu, “Synthesis and design of substrate integrated waveguide filter using predistortion technique,” in *Proc. APMC*, Dec. 2007, pp. 1–4.

[10] R. J. Cameron, C. M. Kudsia, and R. R. Mansour, *Microwave Filters for Communication Systems: Fundamentals, Design and Applications*. New York, NY, USA: Wiley, 2007.

[11] I. C. Hunter, *Theory and Design of Microwave Filters*. London, U.K.: IEE Press, 2001, pp. 41–43.

[12] A. Guyette, I. Hunter, and R. Pollard, “The design of microwave bandpass filters using resonators with nonuniform Q,” *IEEE Trans. Microw. Theory Tech*., vol. 54, no. 11, pp. 3914–3922, Nov. 2006.

[13] V. Miraftab and M. Yu, “Generalized lossy microwave filter coupling matrix synthesis and design using mixed technologies,” *IEEE Trans.Microw. Theory Tech.*, vol. 56, no. 12, pp. 3016–3027, Dec. 2008.

[14] M. Meng, I. C. Hunter and J. D. Rhodes, “The design of parallel connected filter networks with nonuniform Q resonators,” *IEEE Trans. Microw. Theory Tech.*, vol. 61, no. 1, pp. 372–381, Jan 2013.

[15] V. Miraftab and Ming Yu. "Advanced Coupling Matrix and Admittance Function Synthesis Techniques for Dissipative Microwave Filters," *IEEE Trans.Microw. Theory Tech.*, vol. 57, no. 10, pp. 2429-2438, Oct. 2009.

[16] L. Szydlowski, A. Lamecki, and M. Mrozowski, “Synthesis of coupled lossy resonator filters,” *IEEE Microw. Wireless Compon. Lett.*, vol. 20, no. 7, pp. 366–368, Jul. 2010.

[17] L. Szydlowski,A. Lamecki, andM.Mrozowski, “Design of microwave lossy filter based on substrate integrated waveguide (SIW),” *IEEE Microw. Wireless Compon. Lett.*, vol. 21, no. 5, pp. 249–251, May 2011.

[18] J. Mateu, A. Padilla, C. Colladol, M.-M Mendoza and E. Rocast. ect “Synthesis of 4^{th} order lossy filter with uniform Q distribution,” in *IEEE MTT-S Int. Microw. Symp. Dig.*, May. 23–28, 2010, pp. 568–571.

[19] R. J. Cameron, “Advanced coupling matrix synthesis techniques for microwave filters,” *IEEE Trans. Microw. Theory Techn.*, vol. 51, no. 1, pp. 1–10, Jan. 2003.

[20] C.-K. Liao, P.-L. Chi, and C.-Y. Chang, “Microstrip realization of generalized chebyshev filters with box-like coupling schemes,” *IEEE Trans. Microw. Theory Tech.*, vol. 55, no. 1, pp. 147–153, Jan. 2007.

[21] J.-S. Hong, Microstrip filter for RF/Microwave applications, 2^{nd} Edtion, New York: John Wiley & Sons, 2011.

[22] Sonnet *em*, Version 13.54, Sonnet Software Inc., New York, 2011.

[23] H. Joshi, H. H. Sigmarsson, S. Moon, D. Peroulis and W. J. Chappell, “High-*Q* fully reconfigurable tunable bandpass filter,” *IEEE Trans. Microw. Theory Tech.*, vol. 57 no. 12, pp. 3525-3533, Dec. 2009.

[24] H. Joshi, H. H. Sigmarsson, S. Moon, D. Peroulis, and W. J. Chappell,“High *Q* narrowband tunable filters with controllable bandwidth,” *IEEE/MTT-S Int. Microw. Symp. Dig.*, pp. 629–632, Jun. 2009.

[25] C. –C Cheng and G. M. Rebeiz, "High *Q* 4-6-GHz suspended stripline RF MEMS tunable filter with bandwidth control," *IEEE Trans. Microw. Theory Tech.*, vol. 59, no. 10, pp. 2469–2476, Oct. 2011.

[26] Sang-June Park and Gabriel M. Rebeiz, "Low-Loss Two-Pole Tunable Filters With Three Different Predefined Bandwidth Characteristics," *IEEE Trans. Microw. Theory Tech.*, vol. 56, no. 5, pp. 1137–1148, May. 2008.

[27] M/A-COM MA46H202 data sheet," M/A-COM Lowell, 2006.

CHAPTER 6

Introduction to Miniaturized Filter

6.1 Background

As discussed in Chapter 1, high level circuit integration is a major trend but presents a major challenge for today's wireless communication system design. In this context, Part I of this dissertation presents a solution by employing tunable filters to replace conventional switched filter-banks, which are promising to integrate multi-standards or multi-band functions in a single device to reduce the complexity and size of the system. Nevertheless, as specifications on system portability get more stringent, some applications, like smart phones, require continuing reductions in the size of discrete passive components to achieve the highest degree of integration density. Therefore, Part II of this dissertation is devoted to developing techniques to miniaturize microwave filters.

6.2 Overview of Miniaturization Techniques

In the open literature, diversity of miniaturized filters are addressed, among which contain the common uses of lumped-element filters, compact hairpin resonator filters, miniaturized dual-mode resonator filters, miniature fractal filters, slow-wave distributed resonator filters and multilayer filters, including those based on low-temperature co-fired ceramic (LTCC) and liquid crystal polymer (LCP) packaging materials.

Lumped-element filters exhibiting small physical size and broad spurious-free frequency bands result in popular uses at lower frequencies [1]-[5]. Basically, the key building blocks of lumped-element filters are inductors and capacitors, which can be designed in different layouts, such as the meander-line inductor and MIM capacitor employed in Chapter 3 (Fig. 3.10). The use of one or any other element layout mostly depends on the electrical performances that must be achieved as well as the ease of

the realization. The ability to accurately design and model these inductors and capacitors for accurate values is critical for designing lumped-element filters. However, at higher frequencies, the extremely small size of lumped-element filters may result in high insertion loss and possibly low power handling capacity.

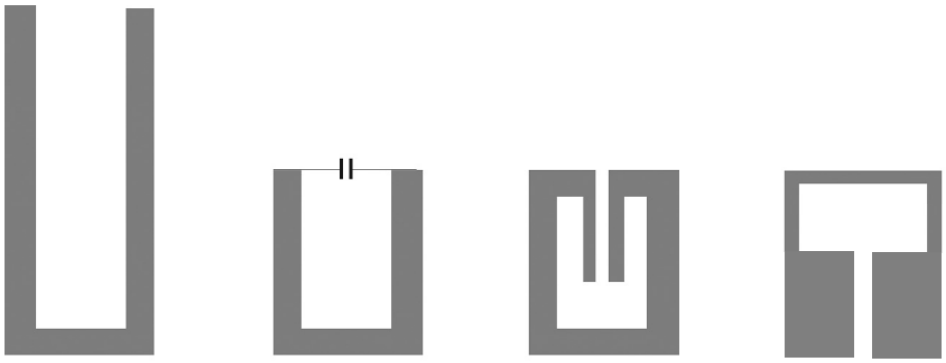

(a) (b) (c) (d)

Figure 6.1: Structural variations to miniaturize hairpin resonator. (a) Conventional hairpin resonator. (b) Miniaturized hairpin resonator with loaded lumped capacitor. (c) Miniaturized hairpin resonator with folded coupled lines. (d). Miniaturized stepped-impedance hairpin resonator.

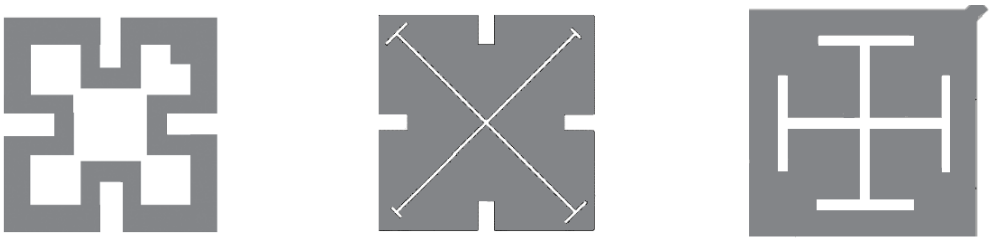

(a) (b) (c)

Figure 6.2: Various miniaturized microstrip dual-mode resonator. (a) Meander loop. (b) Inductively loaded cross-slotted patch. (c) Capacitively stepped-impedance resonator (CSIR).

In order to reach a compromise between size and performance, some compact topologies have been proposed. The size reduction of conventional microstrip line resonator implied in Fig. 6.1 (a), for example, may be miniaturized by adding a lumped-element capacitor between the both ends of the resonator, as indicated in Fig.

6.1 (b), or with a pair of coupled lines folded inside the resonator as shown in Fig. 6.1 (c) [6], or by shaping into stepped impedance hairpin resonators (SIR) as shown in Fig. 6.1 (d) with extra advantage of harmonic suppression [7]. Dual-mode resonators have been widely applied in many RF/microwave filters. A main feature and advantage of this type of resonator lies in the fact of each dual-mode resonator can be used as a doubly tuned resonant circuit, and thus the number of resonators required for a given degree of filter is reduced to half, leading to a compact filter configuration. Further, as illustrated in Fig. 6.2, by taking extra measures, reshaped dual-mode resonators, such as meander loop resonator [8], inductively loaded cross-slotted patch resonator [9] and capacitively stepped-impedance resonator (CSIR) [10], can accomplish a more compact size. Another approach for filter miniaturization, reported in the literature, is to use fractal geometries (Koch curve, Sierpinski gasket, Hilbert curve, etc.) for developing compact structures [11]-[12]. Generally, a fractal shape can be filled in a limited area as the order increases and occupies the same area regardless of the order, leading to reduced physical dimensions. Fractal filters are basically characterized by two factors: the iteration factor (fractal factor) and the iteration order. The iteration factor represents the construction law of fractal geometry generation and the iteration order depicts how many iteration processes are carried out. Indeed, such space-filling property is not only useful to miniaturize the size, but also can be used to control the higher harmonics, since it has a larger effect on the harmonic mode with a shorter electrical length than that of fundamental mode. Moreover, slow-wave resonator filters [13]-[16], frequently realized by alternatively loaded inductors and capacitors on a regular transmission line is also a common way to achieve highly integrated microwave circuit. In general, by using inductive or capacitive loadings, the transmission propagation $\beta = \omega\sqrt{LC}$ is increased. Conversely, the required physical length of the line for a given electrical length is smaller and thus results in miniaturization. Also, due to the effects of a slow wave, such filters are usually able to control spurious response leading to good stopbands.

In recent years, there has been a huge demand for multilayer filters to meet the

challenges of size, performance, and cost requirements. Additionally, multilayer filter technology provides three dimensions, leading to increased flexibility in filter design and integration of other microwave components, circuits and modules. With respect to the layouts of multilayer filter, for example, in [7], [17]-[19], they consisted of various coupled-line resonators or circuit elements that are located at different layers without any ground plane inserted between the adjacent layers. In contrast, another category of the multilayer filters employed aperture couplings on the common ground between adjacent layers. Patterning ground (s) to form slotted or so-called defect ground structures allows additional filtering functionality to be achieved [20]-[22]. Recent advances in packaging materials, such as the low-temperature co-fired ceramic (LTCC) and liquid crystal polymer (LCP), has also energized the development of multilayer filters. In the following section, these two multilayer technologies and the associated filters will be briefly introduced.

6.3 LTCC and LCP Multilayer Technologies

Recently, the development of multilayer filters has been stimulated by the emerging multilayer technologies using two advanced materials, namely, low-temperature co-fired ceramic (LTCC) and liquid crystal polymer (LCP). These technologies enable the innovation of monolithic, 3D, cost-effective microwave circuits/system package.

6.3.1 LTCC technology and filters

Low-temperature co-fired ceramic (LTCC) is most commonly used ceramic substrate material for compact RF designs and SoP (system-on-package) system. In general, LTCC-based device can be defined as a multilayer circuit fabricated by laminating single greensheet (terms for unfired tapes; Green Tape^{TM}, Dupont) with printed conductor lines etc. on the surface and then firing them all together in one step [23], as illustrated in Fig. 6.3. Compared with high-temperature co-fired ceramics (HTCC) technology, the big advantage of LTCC system is the possibility to use low resistivity conductors like silver, gold, copper instead of tungsten and molybdenum, since the firing temperature for LTCC is around 850℃ that is much lower than that of

HTCC in excess of 1000℃. Also, unlike thick-film process, where successive lamination and firing steps cause bowing and line degradation, the single-step lamination and firing of LTCC produces a circuit pattern at substrate with fine, high-quality line definition. The competitive advantages of LTCC technology can be found in Fig. 6.4.

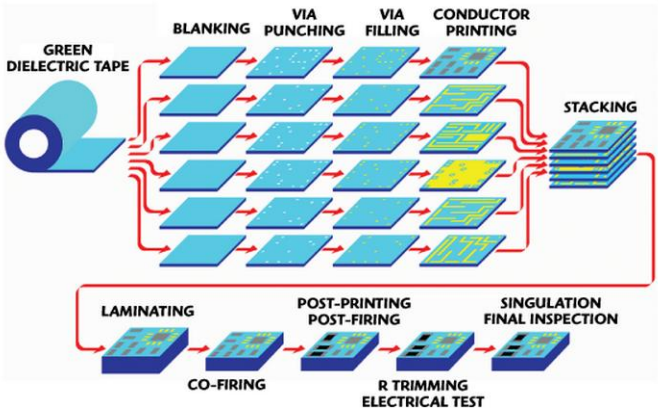

Figure 6.3: LTCC manufacturing process [23].

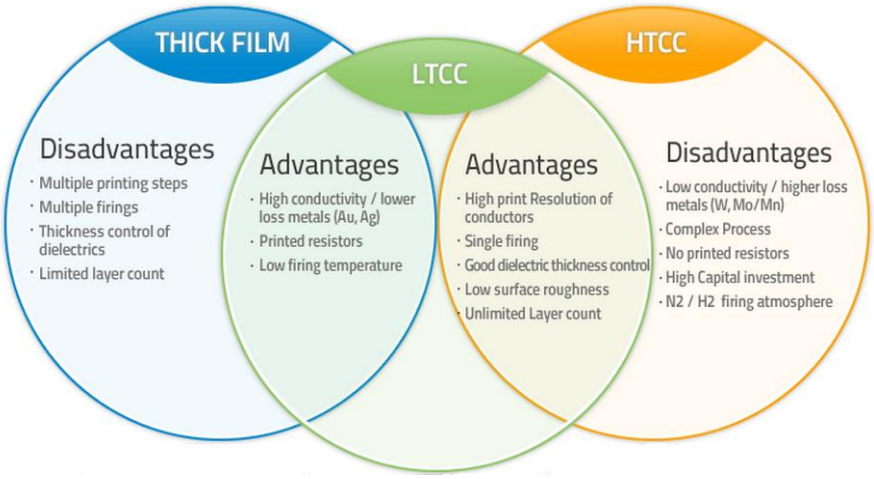

Figure 6.4: Advantages of LTCC technology [24].

LTCC has very low dielectric loss and can be used in multilayer laminated modules that have densely integrated passive and active devices stacked and connect vertically to save space and cost. For instance, Fig. 6.5 presents a compact module, where multiple circuitries are handled in a single self-contained, hermetic package by virtue of this technology. Besides, the multilayer characteristic of LTCC technology offers significant benefits in terms of 3D design flexibility and reliability for RF

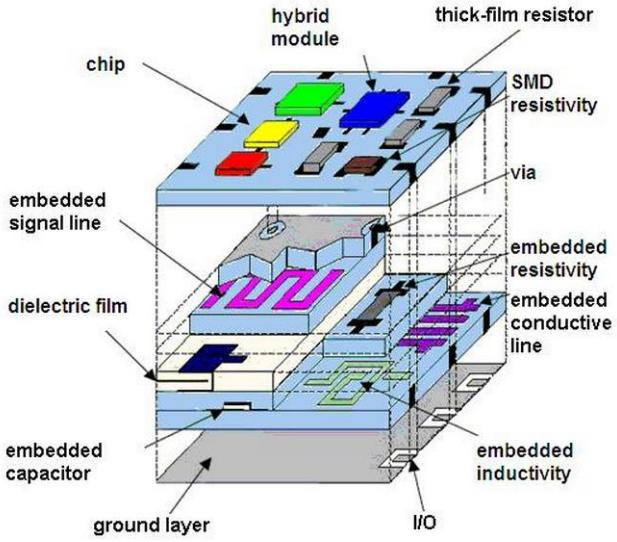

Figure 6.5: Complex LTCC circuit structure [24].

designs. In this aspect, many miniaturized LTCC filters, which were considered impossible to realize with traditional processes, have been proposed for various wireless applications such as mobile phones, Bluetooth, and/or wireless LAN (WLAN) equipped terminals [4]-[5], [25]-[29]. For example, with the added new design dimension in the *z*-direction provided by LTCC, a lumped-element two-pole bandpass filter for Bluetooth application was present in [28], where a mutual inductive coupling was achieved by overlapping the two inductor strips in the *z*-direction, resulting in a finite transmission zeros obtained to improve the selectivity at the image frequency. In [29], with the help of 3D design in LTCC technology, strong capacitive couplings between the strips at different layers were easily performed, leading to the associated multi-layer coupled strip-resonators filters achieve wide bandwidths up to 60% with reduced sizes of less than $\lambda/12 \times \lambda/12 \times h$ (λ is the wavelength at operating frequency and h is the substrate height).

However, as with any material, LTCC has application areas where it is not well suited. The first limitation stage of LTCC occurs at 850℃ that might not be acceptable for some fully integrated solutions. As a result of unpackaged chips containing active devices, they cannot survive the high temperature lamination process. Therefore, they have to be packaged separately, which will significantly increase the fabrication cost. Another limiting consideration for LTCC is that it may

not practical to use in applications that require large amounts of horizontal real estate. The maximum sizes of LTCC modules are $8" \times 8"$ even in the state-of-the-art LTCC manufacturing foundries [30]. Besides, LTCC may not be ideal for antenna applications because the relative high dielectric constant ($\varepsilon_r = 5.4 - 9.1$) is detrimental to the antenna radiation efficiency, where a dielectric constant close to the free space is desirable. Furthermore, LTCC is still expensive compared to some conventional laminate materials. To realize the full advantages of an integrated SoP system, alternative material technologies need to be explored.

6.3.2 LCP technology and filters

Liquid crystal polymer (LCP) is a new and promising organic thermoplastic material with unique structural and physical properties. Table 6.1 summarizes typical characteristics of commercially available LCP materials [31]. As can be seen, LCP has two different functional films: one is core film ULTRALAM 3850 with 315℃ melting temperature, which is mainly used to support metal circuits and has several available thicknesses, such as 100, 50 and 25 μm; the other one is bonding film ULTRALAM 3908 with 280℃ melting temperature, which is utilized as prepreg layer inserted between different core films for stack and has a typical thickness of 25 or 50 μm. Generally, LCP demonstrates simultaneous exceptional performance with respect to electrical, thermal, mechanical and chemical properties, thus, it is the perfect match for technically demanding high-frequency, harsh-environment and direct implantable applications. Being a polymer, the cost of LCP is comparable to that of conventional-print circuit-board material and is cheaper than LTCC. Active and passive devices can be integrated in compact, vertically integrated RF modules by using homogeneous multilayer LCP technology at low temperature (about 290℃), which would be more challenging for LTCC technology as stated earlier. Additionally, the low dielectric constant available in LCP can also be used for antenna applications. Moreover, LCP offers a unique combination of properties, such as low cost and excellent electrical and mechanical characteristics that make it a viable technology for SoP-based systems. Overall, LCP has great potential to act both as a substrate and a

Table 6.1: Typical Characteristics of Liquid Crystal Polymer (LCP) Films [31]

Property	Value		
	ULTRALAM 3850	ULTRALAM 3908	Unit
Mechanical Properties			
Dimensional MD	−0.06	< 0.1	%
Stability CMD	−0.03	< 0.1	
Tensile strength	200	216	MPa
Tensile modules	2255	2450	MPa
Density	1.4		gm/cm3
Thermal Properties			
Coefficient of mhermal expansion, CET (30◦C to 150◦C) X Y Z	17 17 150	17 17 150	ppm/◦C
Melting temperature	315	280	◦C
Relative thermal index, RTI Mechanical Electrical	190 240	190 240	◦C
Thermal conductivity	0.5		W/m/◦K
Electrical Properties			
Dielectric constant (10 GHz, 23◦C)	2.9	2.9	
Dissipation factor (10 GHz, 23◦C)	0.0025	0.0025	
Surface resistivity	1.0×10^{10}	1.0×10^{12}	MOhm
Volume resistivity	1.0×10^{12}	2.6×10^{14}	MOhm cm
Dielectric breakdown strength	1378	118	KV/cm
Environment Properties			
Chemical resistance	98.7	98.7	%
Water absorption (23◦C, 24-h)	0.04	0.04	%
Coefficient of hygroscopic expansion, CHE (60◦C)	4	4	ppm /%RH
Flammability	VTM-0	VTM-0	

package.

The numerous benefits of using LCP as an organic platform include [30]:

- Excellent electrical properties up to millimeter-wave frequencies (stable ε_r of 3.16 ± 0.05 and low loss tangent from 0.0028 to 0.0045 for $f < 110$ GHz)
- Low cost (\$5/ft^2 for a 2-mil single-clad low-melt LCP) [32]
- Quasi-hermetic (water absorption < 0.04%)
- Low *xy* coefficient of thermal expansion (CTE), which may be engineered to match metals or semiconductors
- Thermally stable electrical characteristics than many other substrates
- Lamination capabilities to generate homogenous multilayer RF architectures
- Relatively low temperature processing (~290℃)
- Flexible for conformal and/or flex-circuit applications
- Naturally non-flammable
- Recyclable

In the light of these advantageous characteristics, various miniaturized LCP filters have been developed for a wide range of applications. For example, based on LCP technology, Qian presented a miniature quasi-lumped-element wideband bandpass filter at 0.5-2GHz band by cascading lowpass and highpass filters [2]. UWB filters have been constructed [33]-[35], using multilayer LCP technology. With the multilayer capability, not only broadside coupling can easily be implemented for designing an ultra-wideband bandpass filter, but also more functionality can be integrated in a compact structure. For millimeter-wave applications, the development of integrated passive devices for V-band (50-75 GHz) transceiver applications using LCP technology was reported [36], where filter, matching networks, duplexers, and antenna arrays have been designed, implemented and characterized.

6.4 Text Organization

The second part (Part II) of this dissertation mainly focuses on the design and implementation of miniaturized filters with advanced characteristics. In more details, the outline of this part is as follows:

In Chapter 7, a novel compact second-order bandpass filter with two transmission zeros by utilizing transversal signal-interference technique is presented. Unlike other transversal filters reported, the proposed structure employs artificial right- and left-handed transmission lines instead of traditional distributed transmission lines in the signal-interference network, which is not only helpful in size reduction, but also promising for frequency-asymmetrical stopband performance achievement. Additionally, in order to further miniaturize the circuit footprint, all the artificial transmission lines are implemented in the form of multilayered structures by using liquid crystal polymer (LCP) multilayer technology. The associated LCP lamination process is briefly demonstrated and the proposed concept is eventually validated by the experimental results that are in good agreement with simulated ones.

In Chapter 8, the promising uses of stepped-impedance resonator (SIR) and tapped input/output coupling for the designs of wideband filter with compact sizes, harmonic suppressions and multiple transmission zeros are demonstrated. To this aim, two different classes of third-order wideband combline filters are presented: the first prototype is designed and implemented using LCP bonded multilayer PCB technology. In this manner, the proposed work not only can conveniently realize the required strong inter-couplings with the help of 3D-design of such fabrication technology, but also can achieve promisingly miniaturized size by taking advantages of available high dielectric constant of PCB substrate; the second filter consist of two $\lambda/4$ SIRs with an additional stepped impedance line in between them, which results in an increased inter-coupling as well as an extra resonance mode to realize a wideband performance. This present design is built on the standard PCB technology. But in comparison with most reported planar wideband filters, the demonstrated one does not require any small coupling gap and then relax the requirements for fabrication process. For theoretical verification, these two types of filters are fabricated and measured, showing the expected performances in terms of size, passband and stopband bandwidth, selectivity and simplicity.

After that, chapter 9 summarizes the contributions presented in this whole dissertation and submits recommendations for the future work.

Reference

[1] H. Joshi and W. J. Chappell, "Dual-band lumped-element bandpass filter," *IEEE Trans. Microw. Theory Tech.*, vol. 54, no. 12, pp. 4169–4177, Dec. 2006.

[2] S. Qian and J.-S. Hong, "Miniature quasi-lumped element wideband bandpass filter at 0.5–2 GHz band using multilayer liquid crystal polymer technology," *IEEE Trans. Microw. Theory Techn.*, vol. 60, no. 9, pp. 2799–2807, Sep. 2012.

[3] S. Qian, G. Brand, J.-S. Hong and P. Meyer, "The design of miniature multilayer bandpass filter with mixed couplings," *IEEE Trans. Microw. Theory Techn.*, vol. 61, no. 12, pp. 4072-4078, Dec. 2013.

[4] C.-W. Tang, C.-W. Shen, and P.-J. Hsieh, "Design of low-temperature co-fired ceramic bandpass filters with modified coupled inductors," *IEEE Trans. Microw. Theory Tech.*, vol. 57, no. 1, pp. 172–178, Jan. 2009.

[5] L. K. Yeung and K. L. Wu, "A compact second-order LTCC bandpass filter with two finite transmission zero," *IEEE Trans. Microw. Theory Tech.*, vol. 51, no. 2, pp. 337–341, Feb. 2003.

[6] M. Sagawa, K. Takahashi, and M. Makimoto, "Miniaturized hairpin resonator filters and their application receiver front-end MIC's," *IEEE Trans. Microw. Theory Tech.*, vol. 37, no. 12, pp. 1991–1997, Dec.1989.

[7] A. Djaiz and T. A. Denidni, "A new compact microstrip two-layer bandpass filter using aperture-coupled SIR-hairpin resonators with transmission zeros," *IEEE Trans. Microw. Theory Tech.*, vol. 54, no. 5, pp. 1929–1936, May 2006.

[8] J.-S. Hong and M. J. Lancaster, "Microstrip bandpass filter using degenerate modes of a novel meander loop resonator," *IEEE Microw. Guided Wave Lett.*, vol. 5, no. 11, pp. 371–372, Nov. 1995.

[9] L. Zhu, C. T. Boon and S. J. Quek, "Miniaturized dual-mode bandpass filter using inductively loaded cross-slotted patch resonator," *IEEE Microw. Wireless Compon. Lett.*, vol. 15, no. 1, pp. 22–24, Jan. 2005.

[10] S.-W. Fok, P. Cheong, K.-W. Tam and R. P. Martins, "A novel microstrip square-loop dual-mode bandpass filter with simultaneous size reduction and spurious response suppression," *IEEE Trans. Microw. Theory Tech.*, vol. 54, no. 5, pp. 2033–2041, May 2006.

[11] I. Kim, "Fractal-shaped microstrip coupled-line bandpass filters for suppression of second harmonic," *IEEE Microw.Wireless Compon. Lett.*, vol. 53, no. 9, pp. 2943–2948, Sep. 2005.

[12] W.-L. Chen and G.-M. Wang, "Effective design of novel compact fractal-shaped microstrip coupled-line bandpass filters for suppression of the second harmonic," *IEEE Microw.Wireless Compon. Lett.*, vol. 19, no. 2, pp. 74–76, Feb. 2009.

[13] Jia-Sheng Hong and Lancaster, M.J. "Theory and experiment of novel microstrip slow-wave open-loop resonator filters", *Microwave Theory and Techniques, IEEE Transactions on,* On page(s): 2358 - 2365 Volume: 45, Issue: 12, Dec 1997.

[14] J. P.Wang, B. Z.Wang, Y. X. Guo, L. C. Ong, and S. Q. Xiao, "A compact slow-wave microstrip branch-line coupler with high performance," *IEEE Microw.Wireless Compon. Lett.*, vol. 17, no. 7, pp. 501–503, Jul. 2007.

[15] J. Wang, J.-L. Li, J. Ni, S. Zhao, W. Wu, and D. Fang, "Design of miniaturized microstrip dual-mode filter with source-load coupling," *IEEE Microw.Wireless Compon. Lett.*, vol. 20, no. 6, pp. 319–321,Jun. 2010.

[16] L. H. Hsieh and K. Chang, "Slow-wave bandpass filters using ring or stepped-impedance hairpin resonators," *IEEE Microw.Wireless Compon. Lett.*, vol. 50, no. 7, pp. 1795–1800, Jul. 2002.

[17] J.-S. Hong and M. J. Lancaster, "Aperture-coupled microstrip open loop resonators and their applications to the design of novel microstrip bandpass filter," *IEEE Trans. Microw. Theory Tech.*, vol. 47, no. 9, pp. 1848–1855, Sep. 1999.

[18] Schwab, W and Menzel, W., "Compact Bandpass Filters with Improved Stop-Band Characteristics Using Planar Multilayer Structures," *IEEE Int. Microw. Symp. MTT-S.*, 1992, Albuquerque, pp. 1207-1209.

[19] C. Cho and K. C. Gupta, "Design methodology for multilayer coupled line filters," *IEEE Int. Microw. Symp. MTT-S.*, June 1997, pp. 785–788.

[20] D. Ahn, J. S. Park, C. S.Kim, J. N. Kin, Y.Qian, and T. Itoh, "Adesign of the low-pass filter using the novel microstrip defected ground structure," *IEEE Trans. Microw. Theory Tech.*, vol. 49, no. 1, pp. 86–93, Jan. 2001.

[21] N. Karmakar, S. M. Roy, and I. Balbin, "Quasi-static modeling of defected ground structure," *IEEE Trans. Microw. Theory Tech.*, vol. 54, no. 5, pp. 2160–2168, May 2006.

[22] C. Caloz, H. Okabe, T. Twai and T. Itoh, "A simple and accurate model for microstrip structures with slotted ground plane," *IEEE Microw. Wireless Compon. Lett.*, vol. 14, no. 4, pp. 133–135, Apr. 2004.

[23] LTCC technology, http://www.pilkorcnd.co.kr/sub/sub3_1.asp?mNum=3.

[24] LTCC consulting, http://www.ltcc-consulting.com/What_is_the_LTCC.

[25] W. Tung, Y. Chiang and J. Cheng, "A new compact LTCC bandpass filter using negative coupling," *IEEE Microw. Wireless Compon. Lett*., vol. 15, no. 10, pp. 641–643, Oct. 2005.

[26] G. Brzezina, L. Roy and L. MacEachern, “A miniature LTCC filter using novel resonators for GPS applications,” *in Eur. Microw. Conf.*, Oct. 2007, pp. 536–539.

[27] C. W. Tang, Y. C. Lin and C.Y. Chang, “Realization of transmission zeros in combine filters using an auxiliary inductively coupled ground plane,” *IEEE Trans. Microwave Theory Tech.*, vol. 51, no. 10, pp. 2112–2118, Oct. 2003.

[28] A. Sutono, J. Laskar, and W. R. Smith, “Development of three dimensional integrated Bluetooth image reject filter,” *IEEE Int. Microw. Symp. MTT-S.*, Boston, May, 2000, pp. 339–342.

[29] Y. C. Zhang and A. Kantar., “LTCC multi-layer coupled strip-resonator filters,” *IEEE Int. Microw. Symp. MTT-S.*, pp. 1039-1042, June 2007.

[30] Dane Thompson, “Characterization and design of liquid crystal polymer (LCP) based multilayer RF components and packages,” Doctor of Philosophy thesis, University of Georgia Institute of Technology, 2006.

[31] J.-S. Hong, "Microstrip Filters for RF/Microwave Application," *Second Edition, Wiley*, 2010.

[32] C. Murphy, Rogers Corporation, private communication. Jan. 2004.

[33] Z.-C. Hao and J.-S.Hong, “Ultra-wideband bandpass filter usingmultilayer liquid-crystal-polymer technology,” *IEEE Trans.Microw. Theory Tech.*, vol. 56, no. 9, pp. 2095–2100, Sep. 2008.

[34] Z.-C. Hao and J.-S. Hong, “UWB bandpass filter using cascaded miniature high-pass and low-pass filters with multilayer liquid crystal polymer technology,” *IEEE Trans. Microw. Theory Tech.*, vol. 58, no. 4, pp. 941–948, Apr. 2010.

[35] Z.-C. Hao and J.-S. Hong, “Ultra wideband bandpass filter using embedded stepped impedance resonators on multilayer liquid crystal polymer substrate,” IEEE Microw. Wireless Compon. Lett., vol. 18, no. 9, pp. 581–583, Sep. 2008.

[36] Z.-C. Hao and J.-S. Hong, “Compact wide stopband ultra wideband bandpass filter using multilayer liquid crystal polymer technology,” *IEEE Microw. Wireless Compon. Lett.*, vol. 19, no. 5, pp. 290–292, May 2009.

[37] Bairavasubramanian, R. et al, “Development of V-band Integrated Front-Ends on Liquid Crystal Polymer (LCP) Technology,” *IEEE Antenna and Wireless Propat. Lett.*, vol. 7, pp. 134-137, Jul. 2008.

CHAPTER 7

A Compact Bandpass Filter Based on Right- and Left-handed Transmission Line Sections

7.1 Introduction

Bandpass filters of high performance, low cost and miniaturized size are highly desirable in modern wireless communication systems. It is well known that having a good filter topology is a key step for the successful design of bandpass filter. Among various filter topologies and design techniques reported, signal interference technique is one of the popular solutions for microwave planar filter design. In comparison with coupled-resonator topologies, filtering functions with sharper cutoff slopes can be achieved in simpler networks. In addition, broader bandwidths are practicable as technological limits driven by the presence of coupled lines are avoided. The usefulness of signal-interference filters has been proven in past for moderate-to-broadband bandpass/bandstop specifications with both single- and multi-band characteristics [1]-[4]. However, as main drawbacks, these filter designs presented excessive circuit sizes and difficulties to carry out frequency-asymmetrical filtering actions, since they were exclusively composed of distributed transmission-line segments whose electrical lengths were selected as multiple of $\pi/2$ (e.g. $3\pi/2$ used in [2]) at the desired design frequency. Furthermore, in order to broaden stopband bandwidths, these filters usually required more than one transversal filtering section as well as extra matching lines, leading to increased circuit sizes as well. Even so, there were always some signals transmitted near the dc frequency, which degraded the out-of-band performance to some extent.

To overcome the aforementioned shortcomings, a novel signal-interference filter using artificial left-handed (LH) and right-handed (RH) transmission lines (TLs) is presented in this chapter. As demonstrated in the literatures [5]-[7], left-handed transmission line having simultaneously negative permittivity and permeability would

support backward-wave propagation and exhibit negative electrical length. Hence, replacing the conventional TL with long electrical length by artificial LH TL in the single-interference filter, the circuit size can be significantly reduced. Additionally, it is noteworthy that owning to the high-pass nature of LH TL, the proposed filter achieves an advanced characteristic of frequency-asymmetrical stopband. To further reduce the dimensions of the filter and make it comparable with the latest miniaturized filters used in mobile communication systems, all the artificial RH and LH TLs in this work are implemented in the form of multilayered structures by using liquid crystal polymer (LCP) technology.

This chapter is organized as follows: Section 7.2 describes the architectures of artificial RH TL and LH TL and their fundamental characteristics based on the equivalent circuit models. After that, a signal-interference bandpass filter design is demonstrated in Section 7.3, where analytical design equations and design guidelines are provided for easy reference. The measured results of the presented bandpass filter are shown to validate the proposed concept. Section 7.4 introduces a brief fabrication process of multilayer LCP technology that may be useful for practicing designers. Finally, this chapter is summarized in Section 7.5 with performance comparison between this work and the other related filters.

7.2 Fundamental Theory of Artificial Transmission Lines

7.2.1 Transmission line network approach [5] [7]

Over the last decade, artificial right and left handed transmission lines have drawn considerable interest in designing novel microwave components and devices [8]-[12]. The original concept of artificial transmission lines was introduced in [5]-[7] based on the mapping of filed component (i.e. *E* and *H*) in the medium to the voltages and currents of the equivalent *L*-*C* network. In other word, the dielectric properties like permittivity and permeability can be modeled using *L*-*C* circuits. As illustrated in Fig. 7.1 (a), a conventional transmission line (RH TL) of infinitesimal length Δz can be model as a lumped-element circuit [13], where the loss of the line is neglected (i.e. R=G=0), and L_s, C_p are defined as follows:

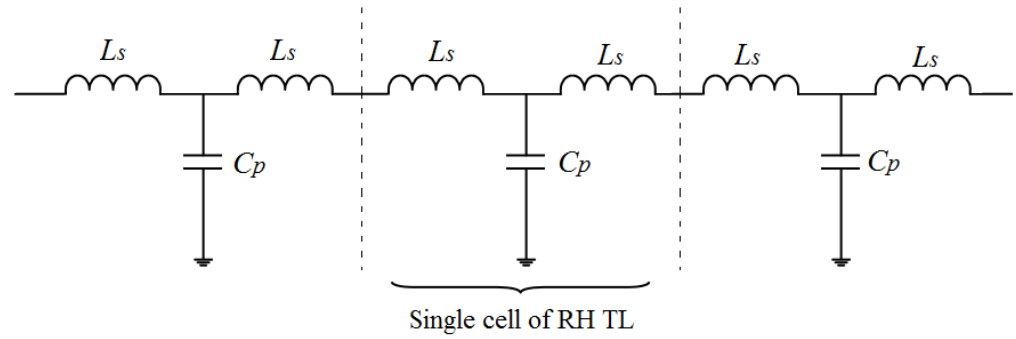

(a)

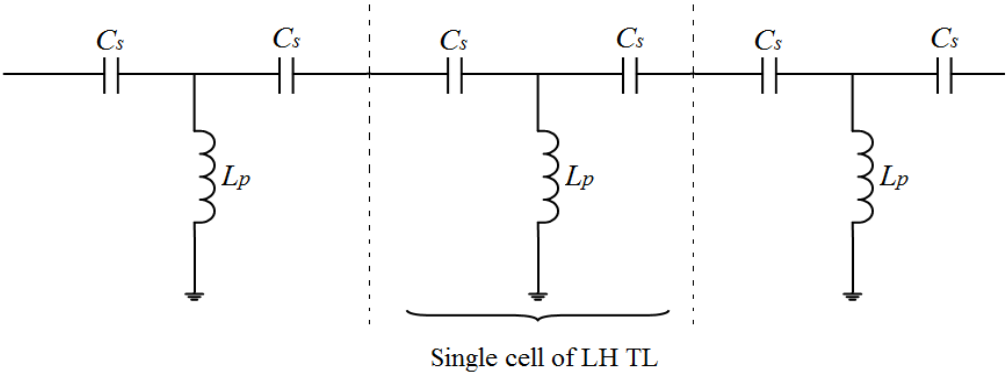

(b)

Figure 7.1: Equivalent circuit model of artificial (a) RH TL. (b) LH TL.

$L_s = L_1 \cdot \Delta z$, L_1 is series inductance per unit length, in H/m.

$C_p = C_1 \cdot \Delta z$, C_1 is shunt capacitance per unit length, in F/m.

In this case, the propagation constant is expressed as:

$$\gamma = \alpha + \beta = j\omega\sqrt{L_1 C_1} \qquad (7.1)$$

or

$$\beta = \omega\sqrt{L_1 C_1}\,; \qquad \alpha = 0 \qquad (7.2)$$

as expected for the lossless case, the attenuation constant α is zero. The characteristic impedance is given by

$$Z_0 = \sqrt{\frac{L_1}{C_1}} \qquad (7.3)$$

The wavelength is

$$\lambda = \frac{2\pi}{\beta} = \frac{2\pi}{\omega\sqrt{L_1 C_1}} \qquad (7.4)$$

and the phase velocity and group velocity are

$$v_p = \frac{\omega}{\beta} = \frac{1}{\sqrt{L_1 C_1}} \;; \qquad v_g = \frac{\partial\omega}{\partial\beta} = \frac{1}{\sqrt{L_1 C_1}} \qquad (7.5)$$

The TL approach of LH TL is based on the *dual* of the conventional TL, the equivalent circuit of which is shown in Fig. 7.1 (b). This circuit is obtained by interchanging the inductance/capacitance and inverting the series/parallel arrangements in the equivalent circuit of the conventional, right-handed (RH) TL shown in Fig. 7.1 (a), where L_p, C_s are defined as follows:

$L_p^{-1} = L_1^{-1} \cdot \Delta z$, L_1^{-1} is shunt inverse inductance per unit length, in H^{-1}/m^{-1}.

$C_s^{-1} = C_1^{-1} \cdot \Delta z$, L_1^{-1} is series inverse capacitance per unit length, in F^{-1}/m^{-1}.

The propagation factor γ of such line can be derived as

$$\gamma = \alpha + \beta = -\frac{1}{\omega}\sqrt{\frac{1}{L_1}\frac{1}{C_1}} \qquad (7.6)$$

or

$$\beta = \frac{1}{-\omega\sqrt{L_1 C_1}} \;; \quad \alpha = 0 \qquad (7.7)$$

where the negative sign in β indicates a negative phase velocity and its nonlinearity indicates frequency dispersion. In addition, the characteristic impedance of the line is given by

$$Z_0 = \sqrt{\frac{L_1}{C_1}} \qquad (7.8)$$

and is, therefore, identical to that of conventional RH TL given in (7.3). Also, the phase velocity and group velocity can be expressed as

$$v_p = \frac{\omega}{\beta} = -\omega^2\sqrt{L_1 C_1} \qquad (7.9)$$

$$v_g = \frac{\partial\omega}{\partial\beta} = \omega^2\sqrt{L_1 C_1} \qquad (7.10)$$

The different signs in the group velocity and phase velocity suggest the existence of a backward wave in the LH TL network. In light of above equations, Fig. 7.2 shows the dispersion diagram of a conventional RH TL and that of a LH TL. It is obvious to see the propagation β of LH TL is negative and inversely proportional to the frequency ω, which is in contrast to that of RH TL. Accordingly, compared with conventional RH TL, LH TL can provide a negative electrical length and a flatter phase response against frequency, which are very promising in size reduction and wide response achievement [11].

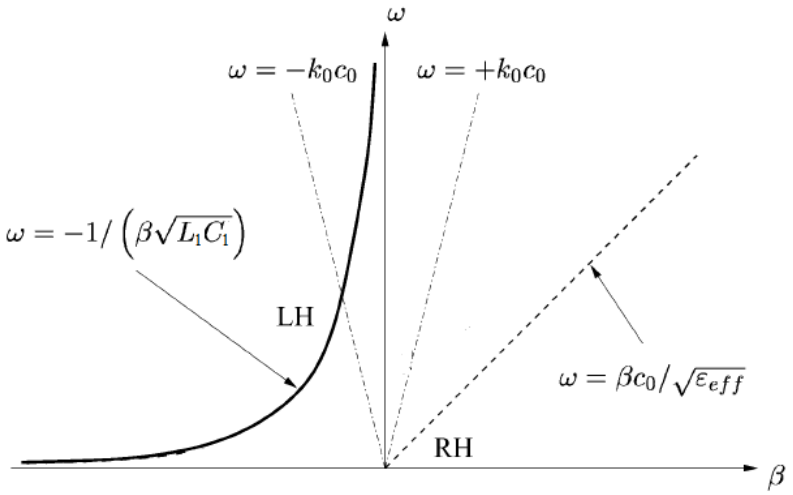

Figure 7.2: The dispersion curves of a RH-TL and that of a LH-TL in the lossless case [7].

7.2.2 Equivalent circuit parameters

Since a real LH TL does not exist in the nature, an artificial lumped-element implementation of the LH TL has to be used while the RH TL can be realized as either a lumped-element structure or the natural TL. As shown in Fig. 7.3, a lumped-element T or Π network can be considered as an equivalent circuit of an ideal TL section with either positive or negative dispersion. In order to derive the equivalent parameters, the

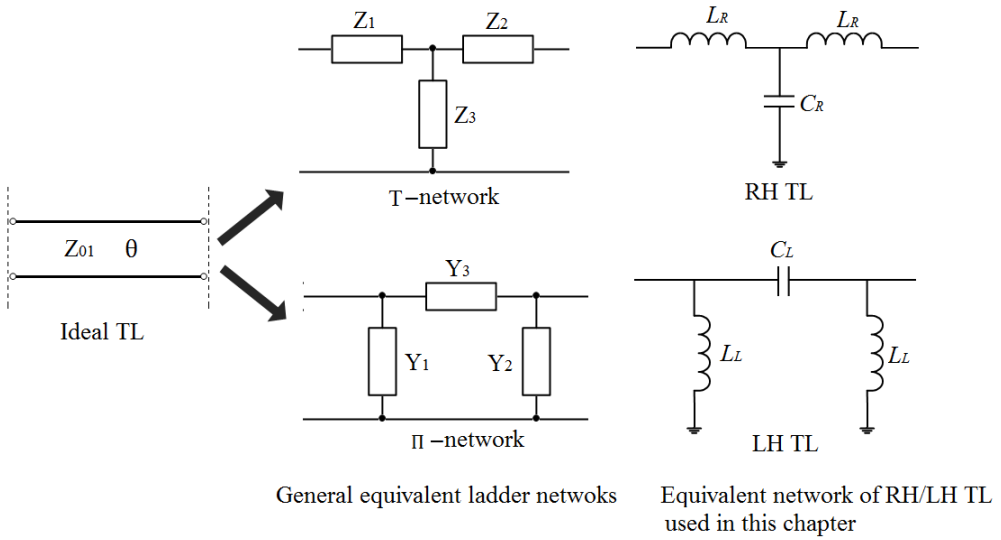

Figure 7.3: Realization of an ideal TL by using T or Π network along with the detailed lumped-element networks used latter in the chapter.

ABCD matrix method is applied.

As shown in Fig. 7.3, for an ideal transmission line with characteristics impedance Z_{01} and electrical length θ, its *ABCD* matrix can be written as:

$$\begin{bmatrix} A & B \\ C & D \end{bmatrix}_{\mathrm{TL}} = \begin{bmatrix} cos\theta & jZ_{01}sin\theta \\ jsin\theta/Z_{01} & cos\theta \end{bmatrix} \qquad (7.11)$$

While for the equivalent T and Π network, we can also get their *ABCD* matrixes as:

$$\begin{bmatrix} A & B \\ C & D \end{bmatrix}_{\mathrm{T}} = \begin{bmatrix} 1+\frac{Z_1}{Z_3} & Z_1+Z_2+\frac{Z_1Z_2}{Z_3} \\ \frac{1}{Z_3} & 1+\frac{Z_2}{Z_3} \end{bmatrix} \qquad (7.12)$$

$$\begin{bmatrix} A & B \\ C & D \end{bmatrix}_{\Pi} = \begin{bmatrix} 1+\frac{Y_2}{Y_3} & \frac{1}{Y_3} \\ Y_1+Y_2+\frac{Y_1Y_2}{Y_3} & 1+\frac{Y_1}{Y_3} \end{bmatrix} \qquad (7.13)$$

The relation between equivalent circuit elements and TL characteristic impedance and electrical length at the central frequency are determined by forcing the *ABCD* matrix of TL section given in (7.11) equal to that of T or Π network given in (7.12) or (7.13). In this manner, for the lumped element values L_R, C_R, L_L and C_L in the equivalent

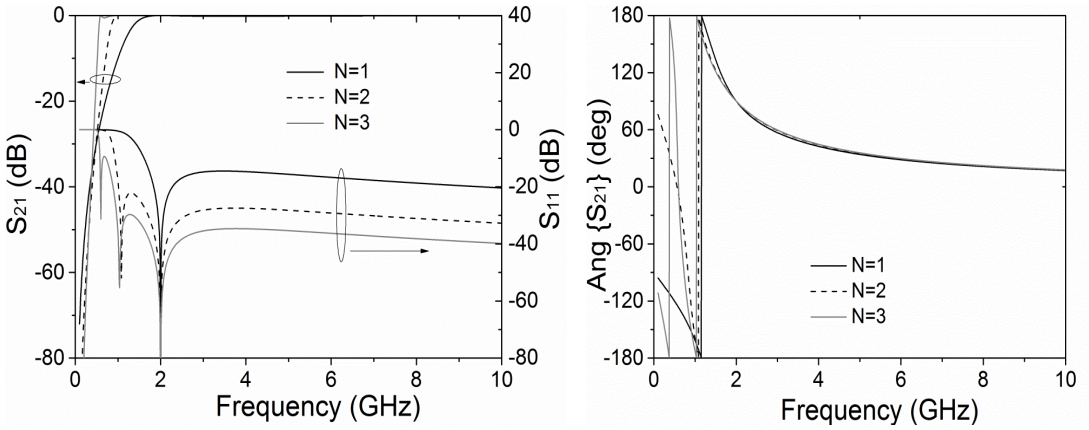

(a) (b)

Figure 7.4: Simulation results for the artificial ideal lumped LH TL with different number of unit-cell shown in Figure. 7.3. (a) Magnitude of the *S*-parameters. (b) Phase response of S_{21}.

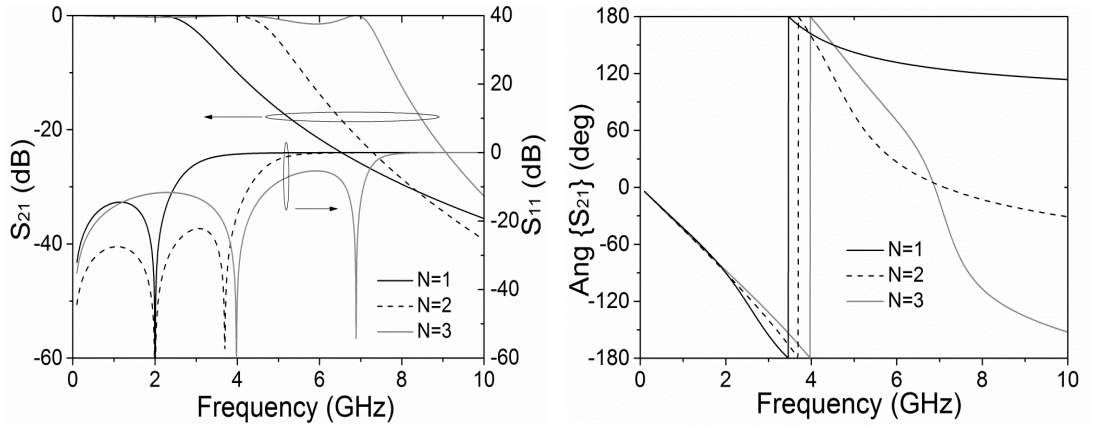

(a) (b)

Figure 7.5: Simulation results for the artificial ideal lumped RH TL with different number of unit-cell shown in Figure. 7.3. (a) Magnitude of the *S*-parameters. (b) Phase response of S_{21}.

Table 7.1: Design Parameters for the Artificial RH/LH TLs

versus Different Unit-cells

Number of unit-cells	LH-TL (Z_{01} = 50 Π-network) $\theta = 90^{\circ}$ at $f = 2$GHz		RH-TL (Z_{01} = 50 T-network) $\theta = 90^{\circ}$ at $f = 2$GHz	
	C_L (pF)	L_L (nH)	C_R (pF)	L_R (nH)
N=1	1.5915	3.9789	1.5915	3.9789
N=2	2.2508	9.6059	1.1254	1.6481
N=3	3.1831	14.8494	0.7958	1.0661

circuits of RH/LH TL used in the following section (refer to Fig.7.3) can be derived as:

$$L_R = \frac{Z_{01}\tan(\theta/2)}{\omega}; \quad C_R = \frac{\sin\theta}{\omega Z_{01}} \qquad (7.14)$$

$$L_L = \frac{Z_{01}}{\omega\sin\theta}; \quad C_L = \frac{1}{\omega Z_{01}\tan(\theta/2)} \qquad (7.15)$$

For our demonstration, Fig. 7.4 and Fig. 7.5 present the simulated results for the artificial ideal-lumped RH TL and LH TL, respectively. The corresponding circuit element values for different numbers of unit-cells are given in Table 7.1. Fig. 7.4 (a) shows *S*-parameters of LH TL for different number of cells. As can be seen, the resulting structure has a high-pass filter response to mimic the LH-TL in its passband. With the numbers of unit-cell *N* increased, the associated cutoff frequency f_c decreases, extending the validity range of the approximation to lower frequencies. Table 7.1 illustrates the tradeoff between the bandwidth and elements values: if bandwidth is to be increased (toward lower frequencies), larger values of capacitance/inductance are required owning to the larger number of unit-cells *N* to keep the characteristics of the line unchanged. The frequency dependence of $\lambda_g = 2\pi/|\beta| = 2\pi\omega\sqrt{L_1C_1} \propto \omega$ is clearly seen in the distribution of peaks of S_{11}, where the highest frequency peak corresponds to an electrical length $\theta = 90^\circ$ $(\lambda_g/4)$ and the other peaks are related with $N \cdot \lambda_g/4$ $(N = 2, 3\cdots)$. Fig. 7.4 (b) shows the phase of S_{21} in such ideal LH TL. As aforementioned, the phase incursion along an LH TL is positive, that leads to a negative electrical length obtained. Also the phase shift within the validity range is kind of flat due to the propagation constant is inversely proportional to the frequency. However, in the case of artificial RH TL described in Fig. 7.5 and Table 7.1, some different phenomena can be observed. The resulting structure is a low-pass filter emulating RH-TL in its passband. The associated cutoff frequency f_c increases when *N* increases, widening the validity range of the approximation to higher frequencies along with smaller values of capacitance/inductance required. Additionally, it is

expected that the phase incursion along an RH TL is negative and the phase shift within the validity range is almost linear to the frequency.

7.3 Bandpass Filter Design and Analysis

7.3.1 Description of the structure

A novel miniaturized bandpass filter topology having two transmission zeros placed near the both passband edges is presented in Fig. 7.6 (a). As shown, the new filter structure is based on the transversal signal-interference concept, but consists of a left-handed transmission line (LH TL) and a right-handed transmission line (RH TL) sections connected in-parallel. The RH and LH TLs have the characteristic impedances Z_R, Z_L and the electrical lengths θ_R, θ_L, respectively. In this work, it is assumed that $\theta_R = 90^\circ$ and $\theta_L = -90^\circ$ at the centre frequency f_0.

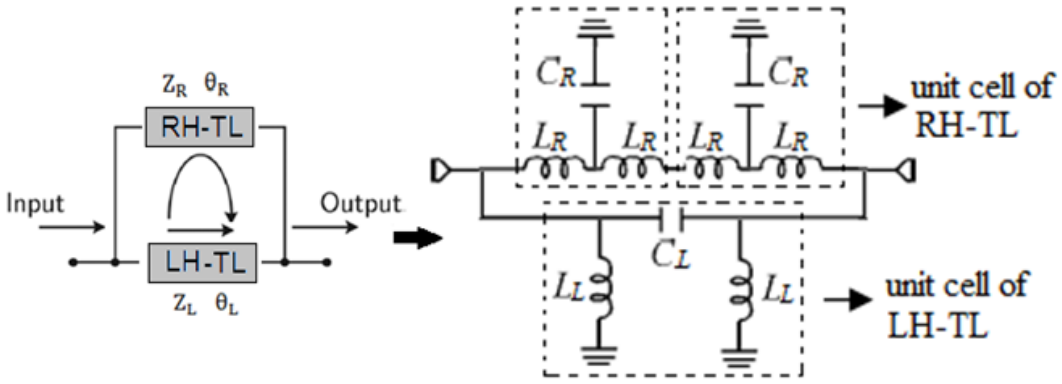

(a) (b)

Figure 7.6: (a) Proposed bandpass filter structure based on signal-interference concept. (b) Equivalent circuit of the proposed filter.

Based on the fundamental theory stated in Section 7.2, such transversal filtering topology can be realized artificially in form of the lumped-element network, as indicated in Fig. 7.6 (b). Considering the trade-off between the validity bandwidth and component's value, herein the RH TL section is implemented as a cascade of two identical T-networks consisting of the series inductances L_R and the shunt capacitance C_R. The LH TL section is realized as one unit-cell of Π-network with the shunt

inductances L_L and the series capacitance C_L. The relevant circuit parameters of each unit cell can be easily derived by using equations (7.14)-(7.15).

7.3.2 Basic guideline for filter design

It is well known that during the design process of the signal-interference filters, the electrical lengths and characteristic impedances of the transversal filter lines are the key parameters in achieving proper amplitude and phase responses. Specifically, the generation of perfect-constructive signal interference at the desired centre frequency is the main condition to be forced. For the structure shown in Fig. 7.6 (a), the normalized admittance matrix at the desired centre frequency f_0 can be written as:

$$[Y(f_0)] = [Y(f_0)]_{\mathrm{R}} + [Y(f_0)]_{\mathrm{L}} = \mathrm{j}\begin{bmatrix} 0 & -y_R + y_L \\ -y_R + y_L & 0 \end{bmatrix} \qquad (7.16)$$

where $y_R = Z_0/Z_R$ and $y_L = Z_0/Z_L$.

In turn, the power reflection coefficient of the proposed filter at the centre frequency can be readily obtained by the transformation:

$$S_{11}(f_0) = \frac{(1 + Y_{11})(1 + Y_{22}) + Y_{12}Y_{21}}{(1 + Y_{11})(1 + Y_{22}) - Y_{12}Y_{21}} = \frac{1 - (y_R - y_L)^2}{1 + (y_R - y_L)^2} \qquad (7.17)$$

To this end, if a desired value of the reflection coefficient at the centre frequency is given as $S_{11}(f_0) \leq \mathrm{k}$, the admittances y_R and y_L of the RH TL and LH TL should satisfy the following condition:

$$\frac{1-k}{1+k} \leq (y_R - y_L)^2 \leq \frac{1+k}{1-k} \qquad (7.18)$$

Note, there are two optional solutions obeying (7.18) when the admittance y_R is either smaller or larger than the admittance y_L. For better understanding, let us illustrate this fact by some typical examples summarized in Table 7.2 where we assume k = 0.316 corresponding to the desired reflection coefficient value $S_{11}(f_0) \leq$ 10 dB. As it can be seen, for the given passband specification, once the impedance Z_L is determined at the earlier step of the filter design, then a range of approximate values of the impedance Z_R can be obtained or vice versa. However, it is found that two transmission zeros appear around the passband allowing to improve the filter selectivity only when $Z_R > Z_L$ (see Fig. 7.7).

Table 7.2: Typical Examples of Filter RH TL and LH TL Characteristic Impedance Values

k = 0.316 (S_{11} <= -10dB)		
LH TL impedance	RH TL impedance	
	$Z_R > Z_L$ ($y_R < y_L$)	$Z_R < Z_L$ ($y_R > y_L$)
Z_L = 50 Ω (y_L = 1)	Z_R > 178 Ω	29 Ω > Z_R > 21 Ω
Z_L = 100 Ω (y_L = 0.5)	None	40 Ω > Z_R > 26.5 Ω
Z_L = 25 Ω (y_L = 2)	82 Ω > Z_R > 39 Ω	18 Ω > Z_R >14 Ω
Z_L = 10 Ω (y_L = 5)	14 Ω > Z_R > 11 Ω	9 Ω > Z_R > 8 Ω

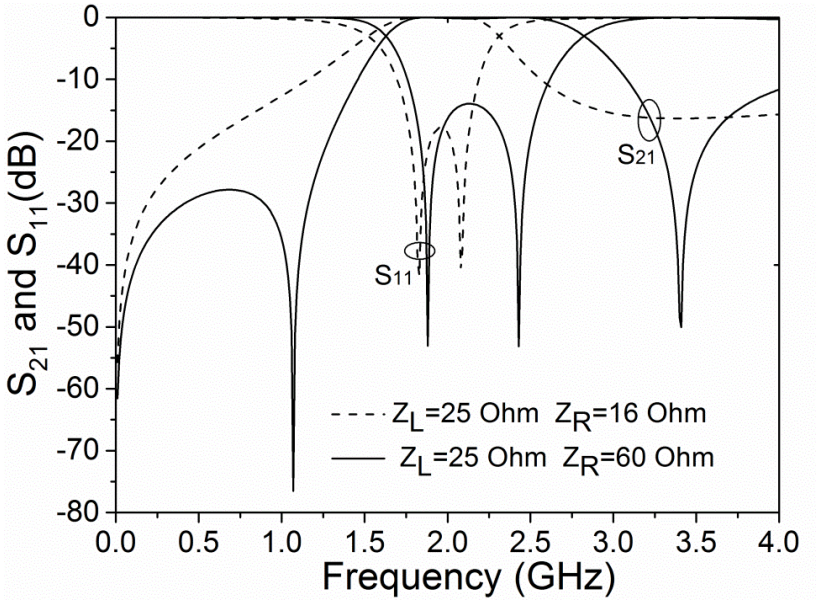

Figure 7.7: Typical frequency responses of the proposed filter when $Z_R > Z_L$ (solid lines) and $Z_R < Z_L$ (dashed lines).

In addition, the fractional bandwidth is mainly determined by the impedance ratio Z_R/Z_L i.e. the broader bandwidth is obtained as the higher impedance ratio is chosen. For example, as implied in Fig. 7.8, the fractional bandwidth of around 14% is provided for the filter with Z_R = 12 Ω and Z_L = 10 Ω, whereas the use of Z_R = 70 Ω and Z_L = 25 Ω allows achieving as wider fractional bandwidth as 61%. Though the two filter examples illustrated in Fig. 7.8 have the same impedance ratio (Z_R/Z_L = 70/25 = 126/45 = 2.8), they are alike in the frequency response. However,

when increasing the impedance ratio to achieve a wider passband, the rejection level in the stopband is getting worse accordingly (Fig. 7.8). Hence, there is a trade-off between the bandwidth and the stopband performance.

Fig. 7.9 demonstrates that the filter response can be adjusted and optimized by varying the capacitances C_L and C_R. In Fig. 7.9 (a), the transmission zero below the pass band is tuned by changing the values of C_L. Also the lower cut-off frequency and the location of the lower pole can be adjusted accordingly, while the upper ones remain almost unchanged. On the contrary, in Fig. 7.9 (b), by changing the values of C_R, the transmission zero above the pass band, as well as the upper cut-off frequency and a location of the upper pole are adjusted more significantly than the lower ones. Hence, the locations of two transmission zeros and the bandwidth can be adjusted independently by modifying the capacitances C_L and C_R, with the fixed values of L_L and L_R that results in an optimized frequency response obtained.

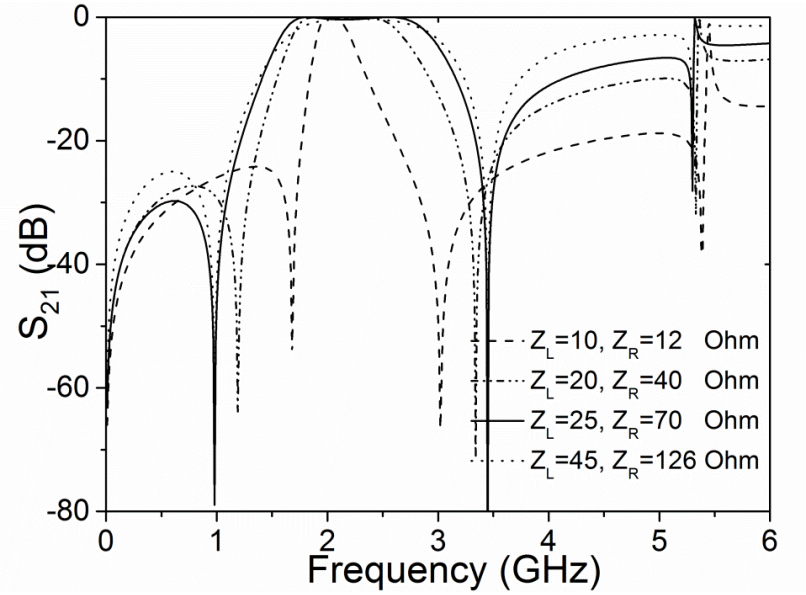

Figure 7.8: Transmission coefficient versus frequency for filters with different fractional bandwidths corresponding to different impedance ratio Z_R/Z_L.

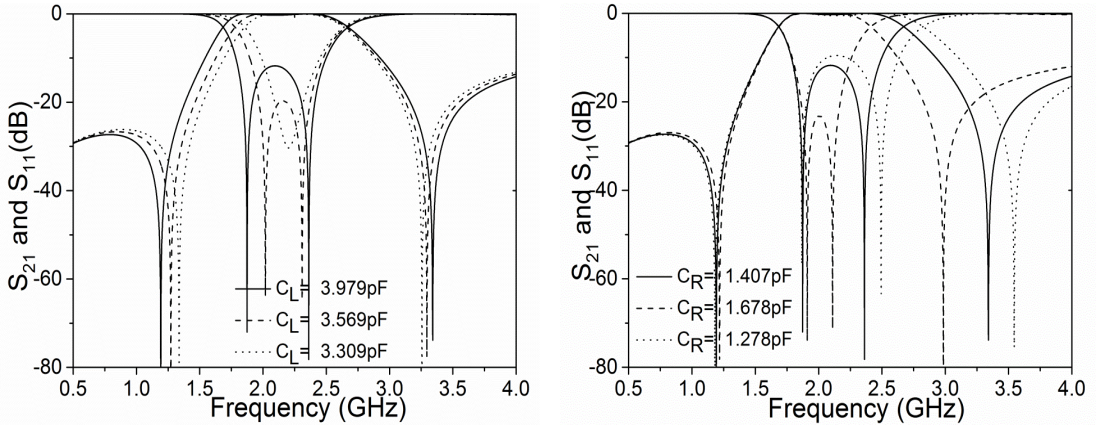

(a) (b)

Figure 7.9: Simulated frequency responses of the filter shown in Figure. 7.6 (b) by adjusting the capacitances C_L (a) and C_R (b).

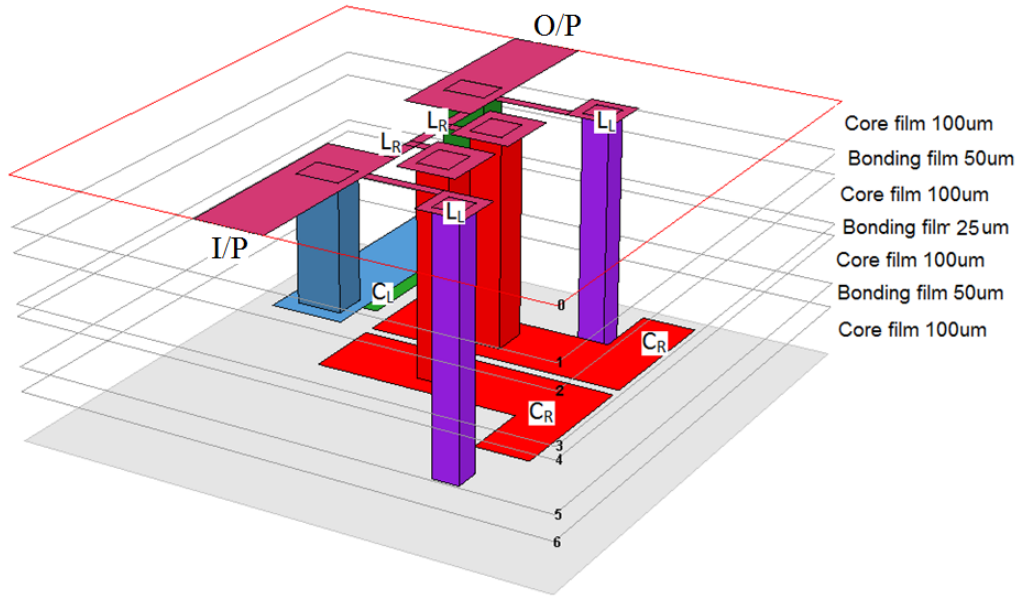

Figure 7.10: The multilayer LCP implementation of the proposed filter based on the structure shown in Fig. 7.6 (Z_L = 10 Ω Z_R = 13 Ω, L_L = 0.7958 nH, C_L = 7.9577 pF, L_R = 0.4285 nH, C_R = 4.3284 pF).

7.3.3 Implementation and experimental results

An experimental sample of the designed filter is fabricated using multilayer LCP lamination technology. The associated LCP laminiation process will be demonstrated in subsequent section. According to the above mentioned design guidelines and filter equivalent circuit, the filter layout shown in Fig. 7.10 is implemented as a five-metal-layer LCP structure using three types of LCP films (100 μm thick LCP core film as well as 50 μm and 25 μm thick LCP bonding films). Specifically, the form of parallel-plate capacitor is adopted to obtain the LH series capacitance C_L, which can be made extremely small by reducing the gap between two plates. The LH shunt inductance L_L is generated by the stub lines. The high-impedance line linking to two 50 Ω termination ports introduces a small RH series inductance L_R and the spacing between the conductive plate and the ground enclosure introduce a RH shunt capacitance C_R. An immediate benefit of such architecture for left-handed filters by using multilayer technology is the dramatically miniaturized circuit size, resulting in improved homogeneity in comparison with that achieved in planar configurations [12]. Regarding the procedure for determining the physical dimensions of each lumped component, the discussions in Section 3.32 (Chapter 3) and the flow chart given in Fig. 3.9 can be followed.

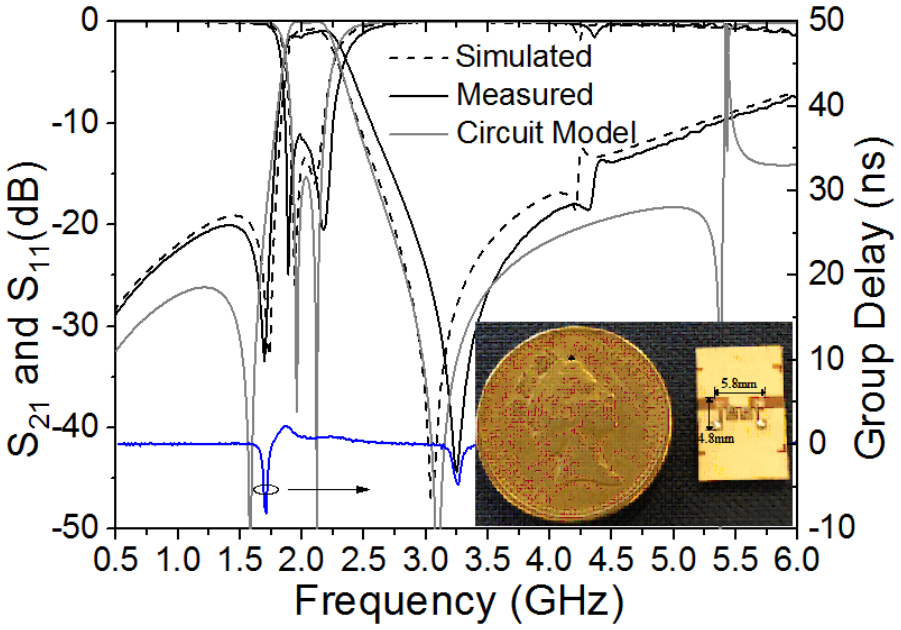

Figure 7.11: Measured filter *S*-parameters compared with the results of EM and circuit simulations and measured group delay.

Frequency characteristics of the fabricated filter are measured using an HP8510 vector network analyzer and an Anritsu Test Fixture (TRL calibration, Ref. Plane: I/O ports plane). The measured *S*-parameters, the simulated filter performance obtained by Sonnet software [14] and the theoretical frequency response of the filter equivalent circuit are shown in comparison in Fig. 7.11. All the results are generally in a good agreement. A high performance is achieved for the filter with two transmission zeros designed for the centre frequency of 2.06 GHz and 3-dB bandwidth of 24%. The measured insertion loss in the pass band is about 1.5 dB, and the measured group delay is fairly small and flat, which is 0.73 ns at centre frequency with a variation within 0.4 ns from 1.94 GHz to 2.51 GHz. The transmission zeros are located at 1.69 GHz and 3.26 GHz, respectively. Compared with the simulated results, the upper cut-off frequency and the location of the transmission zero above the pass band are slightly shifted due to the fabrication errors, including line-width variation and via connection. The photograph of the fabricated filter prototype is shown in the inset to Fig. 7.11. The size of the filter is 5.8 mm × 4.8 mm (0.06 λ_g × 0.05 λ_g), excluding the input and output microstrip lines.

7.4 LCP Circuit Processing and Fabrication

In the past few years, the industry has made great efforts on multilayer LCP process development. More recently Rogers Corporation has defined LCP circuit fabrication guidelines that greatly enhance the reliability of a LCP circuit as well as making the circuit fabrication more robust [15]. In general, four main processes have to be developed to create multilayer laminated LCP modules:

1. Preliminary preparation for LCP lamination.
2. A multilayer alignment procedure.
3. Precision hole and cavity drilling.
4. A reliable bonding recipe/procedure.

In this section, based on our group's LCP fabrication experiences accumulated as well as the process indicated in [17], the above four processes will be briefly introduced for better understanding.

- *Preliminary Preparation for LCP Lamination*

As demonstrated in Table 7.3, the preparation of the inner layer or single sided

materials for LCP lamination is for reference. Normally, two points are critical to yield good results if the latter lamination cycle is done properly: the first one is all the LCP films should be cleaned to get rid of contaminants that include impair adhesion, including dust, grease, oil, fingerprints, non-adherent oxides, or other process chemical residues; the second one is hot air oven baking films should be used to assure removal of all solvent residues and moisture. Incomplete removal of such absorbed solvent or water may swell the circuit surface with some bubbles to a small degree or create corrosion problems later in assembly since solvents in contact with moisture may form corrosive hydrochloric acid by hydrolysis.

Table 7.3: Preparation of Inner Layer or Single Sided Materials for LCP High Temperature Lamination [16].

Image pre-clean	Conveyorized chem. clean and microetch. Mechanical scrub not recommended.
Resist lamination and image	Standard process for flex layers
Develop	Standard aqueous or semi-aqueous
Etch	Ammonical or cupric chloride If leaders needed, use small pieces of tape, not one long strip
Resist Strip	Standard aqueous strippers If leaders are used -must double pass, changing tape locations, to insure complete resist removal
Microetch and acid wash (no oxide at this time)	40μ" to 60 μ"–micro-roughening (persulfate microetch) to promote adhesion, followed by 4 to 5 minute soak in acetic or 10% sulfuric acid. Triple rinse in cascading DI water rinse
Bake layers and bondplies	Strip2 to 4 hours at 250F –suspending or supporting etched layers vertically in stainless steel racks is preferred. Bondplies can be stacked but slipsheeted to allow proper venting.

- *Multilayer Alignment Procedure*

Bonding fixture with alignment pins is required that enabled multilayer aligned

LCP laminations. Special considerations are made to achieve the required temperature inaccuracy and tolerance across the lamination surface for an LCP bond as small as possible. Firstly, the total vertical dimension of the stacked plates plus the inserted sample cannot be more than 6 mm [17]. Next, the suggested thickness of the inserted LCP circuit is less than 1 mm; otherwise it is better to do more than one lamination.

Fig. 7.12 shows the photograph of an alignment fixture with horizontal dimensions of 8 cm by 10 cm. The alignment pins are press fit into the bottom press plate. The top press plate slides on/off. In this way, the alignment procedure requires pre-cutting holes through the LCP substrates before laminating to make the locations of these alignment pins match in the press plates. After that, all LCP substrates can be stacked on the alignment fixture and run through a bonding process to create a laminated multilayer LCP circuit.

Figure 7.12: Alignment fixture with horizontal dimensions of 8 cm by 10 cm.

Figure 7.13: CO_2 laser (10.6 μm wavelength).

- *Laser Processing*

To create precise alignment hole and package cavities, laser processing is performed rather than mechanical drilling. Since laser processing of LCP does not require de-burring and the laser precision is far superior to satisfy the job having stringent requirements. For instance, infrared laser system has stage positioning accuracy of 1 μm or better and precise alignment procedures using video microscopes [17].

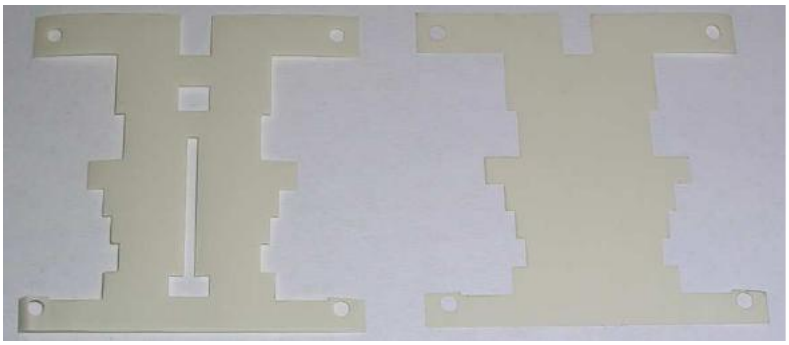

Figure 7.14: LCP layers cut into the desired shapes with the CO_2 laser, including the sample perimeter, alignment holes, and cavities in the left sample [17].

In our lab, the CO_2 laser (10.6 μm wavelength) is commonly used, as shown in Fig. 7.13. In general, this CO_2 laser has great advantage of fast and continuously for cutting alignment holes, outer sample boundaries and other arbitrary shapes such as square holes through bare LCP. Additionally, this laser cannot cut through metal, which is ideal for cutting holes (e.g. plated through hole) surrounded by metals, thus reducing the errors generated from miss-focusing during the cutting process. However, the precision of CO_2 laser is relatively lower than the infrared and excimer lasers, though it is still good enough to make cavities, alignment holes. Generally, the laser spot size is too large to make features below a few hundred microns. Moreover, this laser usually leaves the worst burn reside of carbon ash along the cutting edges which can smudge and dirty the sample. So after cutting, it requires to clean the sample. Fig. 7.14 shows an example of the CO_2 laser cutting capabilities with different shapes.

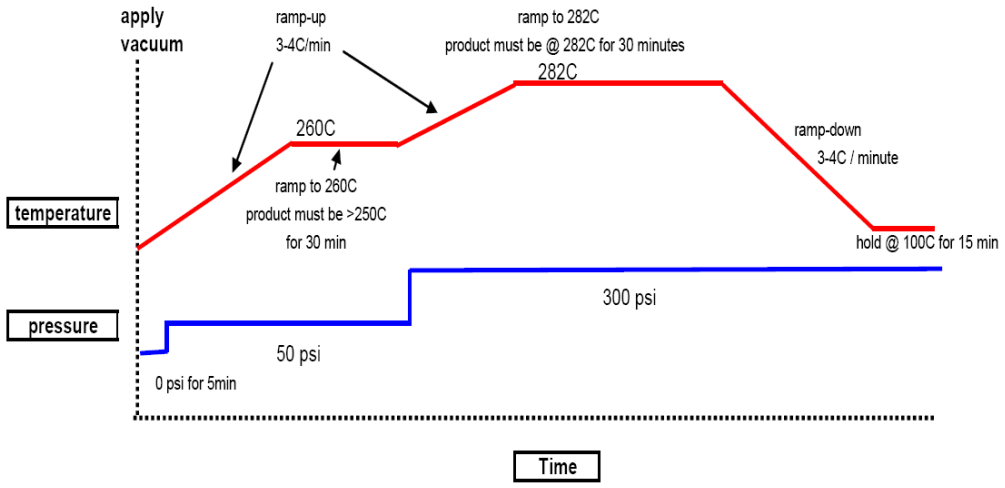

Figure 7.15: Recommended LCP lamination cycle.

- *Bonding Process*

The bonding/lamination process of LCP is something that required the iterative testing of several different hot presses and many recipes of varying time, pressure, temperature, and vacuum settings. Fig. 7.15 shows a graphic representation of the desirable LCP bond parameters that are recommended by Rogers Corporation [15]. These recipe parameters are those deemed reliable for commercial bonding. Observing Fig. 7.15, the high temperature lamination cycle uses a dwell at 260℃ with low pressure and vacuum assist in order to help remove the outgassing prior to raising the pressure and temperature for the fusion bond cycle. The trick to a successful LCP bond is to reach an extremely uniform 282℃ temperature distribution across press plates with a bit deviation. Obviously, this temperature 282℃ is related with the melting temperature of LCP bonding film. Only when the temperature is high enough, LCP bonding films can be properly melted as "glue" layers to hold all the core layers stacked. At this highest-temperature stage, the pressure and time also should be controlled properly. If the pressure is too tight and/or the time is too long, it would cause circuit misalignments (or shift) among stacked LCP layers and mechanical deformation, such as the surface metallization on the core layer would be embedded into the substrate. Conversely, the layers would be easily pulled apart or

sometimes with bubbles as well. In addition, LCP bondling films are thermoplastic adhesive materials so pressure drop during the cooling process can cause large registration error. Therefore, the lamination pressure should be kept until the cooling is finished. As briefly mentioned already, all the layers, i.e. bonding films and core films, stacked over a fixture for bonding process should have laser cut alignment holes to ensure precise alignment. Overall, this successful LCP lamination process is probably the most critical enabling step to continue research in multilayer LCP RF constructions.

7.5 Summary

In this chapter, a novel structure of miniaturized bandpass transversal filter was presented by utilizing specific dispersion properties of the artificial RH and LH TLs. Design equations, curves and guidelines have been provided for such signal-interference filter design. The proposed filtering configuration has been experimentally validated through the design and implementation by using multilayer LCP technology. The associated LCP circuit processing and fabrication have also been demonstrated for reference. In the light of the measured results, the proposed filter addressed a good performance, including an excellent selectivity due to transmission zeros located near the both passband edges and a very compact size, which seem to be a valuable candidate for applications in modern communication systems. Furthermore, a simple performance comparison with other left-handed bandpass filters in the literature is summarized in the Table 7.4 to highlight the merits of the proposed filter.

Table 7.4: Comparison with Other Reported Left-handed Bandpass Filters

Ref.	Fabrication technology	f_0 (GHz)	Size (mm)	Number of *Tzs*
[9]	PCB (ε_r = 2.2)	4.35	6.07 × 5.14	1
[10]	PCB (ε_r = 10.2)	3.5	4.29 × 5.09	1
This work	**LCP (ε_r = 3.0)**	**2.06**	**5.80 × 4.80**	**2**

Reference

[1] R. Gómez-García and J. I. Alonso, “Design of Sharp-rejection and Low-loss Wide-band Planar Filters Using Signal-interference Techniques,” *IEEE Microw. Wireless Compon. Lett.*, vol. 15, no. 8, pp.530–532, Aug. 2005.

[2] R. Gómez-García and M. Sánchez-Renedo, “A Class of Microwave Transversal Signal-Interference Dual-Passband Planar Filters,” *IEEE Microw. Wireless Compon. Lett.*, vol. 19, no. 3, pp.158–160, Mar. 2009.

[3] M. Á. Sánchez-Soriano and E. Bronchalo, “Compact UWB Bandpass Filter Based on Signal Interference Techniques,” *IEEE Microw. Wireless Compon. Lett.*, vol. 19, no. 11, pp.692–694, Nov. 2009.

[4] R. Gómez-García, J. Muñoz-Ferreras, and M. Sánchez-Renedo, “Signal-interference Stepped-impedance-line Microstrip FIlters and Application to Duplexers,” *IEEE Microw. Wireless Compon. Lett.*, vol. 21, no. 8, pp. 421–423, Aug. 2011.

[5] G. V. Eleftheriades, A. K. Iyer, and P. C. Kremer. “Planar Negative Refractive Index Media Using Periodically L–C Loaded Transmission Lines”, *IEEE Trans. Microwave Theory & Tech.*, vol. 50, no. 12, pp. 2702-2712, Dec. 2002.

[6] G.V. Eleftheriades, O. Siddiqui and A.K. Iyer, “Transmission line models for negative refractive index media and associated implementations without excess resonators.” *IEEE Microw. Wireless Compon. Lett.*, vol. 13, no. 2, pp. 51-53, Feb. 2003.

[7] C. Caloz and T. Itoh, “Transmission Line Approach of Left-Handed (LH) Materials and Microstrip Implementation of an Artificial LH Transmission Line,” *IEEE Trans. Microw. Theory Tech.*, vol. 52, no. 3, pp. 980–992, May. 2004.

[8] I. B. Vendik, O. G. Vendik, D. V. Kholodnyak, E. V. Serebryakova, and P. V. Kapitanova, “Digital Phase Shifters Based on Right- and Left-Handed Transmission Lines”, *Proc. of the European Microwave Association*, vol. 2, no. 2, pp. 30-37, March 2006.

[9] S. Karimian and Z. Hu, "Miniaturized Composite Right/Left-Handed Stepped-Impedance Resonator Bandpass Filter, " *IEEE Microw. Wireless Compon. Lett.*, vol. 22, no. 8, pp.421-423, Aug. 2012.

[10] H. Wen, L. Jin and H. Chen, "Improved composite right/left handed transmission line metamaterials and its application in bandpass filters," *Int. Workshop on Microwave and Millimeter Wave Circuits and System Technology*, pp. 1-3, April 2012.

[11] Dmitry Kholodnyak and Irina Vendik, “Broadband Digital Phase Shifter Based on Switchable Right- and Left-Handed Transmission Line Sections,” *IEEE Microw. Wireless Compon. Lett.*, vol. 16, no.5, pp.258–260, May. 2006.

[12] Y. Horii, C. Caloz, and T. Itoh, “Super-compact multilayered left-handed transmission line and diplexer application,” *IEEE Trans. Microw. Theory Tech.*, vol. 53, no. 4, pp. 1527–1534, Apr. 2005.

[13] D. Pozar, *Microwave Engineering*, 3rd ed. New York: Wiley, 2005.

[14] Sonnet *em*, Version 13.54, Sonnet Software Inc., New York, 2011.

[15] ULTRALAM ®3850 Laminates, Rogers Corporation advanced circuit materials. https://www.rogerscorp.com/acm/products/63/ULTRALAM-3850-Laminates.aspx

[16] Various LCP based circuit construction and fabrication techniques, Rogers Corporation advanced circuit materials.

[17] Dane Thompson**, “**Characterization and design of liquid crystal polymer (LCP) based multilayer RF components and packages**,”** Doctor of Philosophy thesis, The University of Georgia Institute of Technology, 2006.

CHAPTER 8

Compact Wideband Combline Bandpass Filters Utilizing Different Fabrication Technologies

8.1 Introduction

Recently, there has been an increased interest in wideband bandpass filters for use in modern wireless communication systems for applications such as wideband radar and high data-rate communication system. In general, this type of bandpass filter not only needs a wide bandwidth to meet the required large data rate but also demands low loss, compact size, good selectivity and stopband suppression to improve the performance of wideband systems. Various wideband bandpass filters have been developed [1]-[7]. In this context, distributed element approaches, such as half-wavelength parallel coupled-line structure, exhibiting a far superior performance with regard to the insertion loss and power handling capabilities in comparison to lumped-element filters, are the most commonly used. However, these parallel coupled-line structures usually suffer from some shortcomings when realizing a wideband response. Firstly, very small gaps between coupled strips are required to achieve tight couplings [4]-[6], which may cause some difficulties in the fabrication processes. Secondly, the size is a drawback as half-wavelength resonators normally occupy a large area, particularly at a low frequency. For this reason, folded resonators were developed in [7] to reduce the filter's size but resulted in a degraded return loss. Moreover, it is known that the traditional parallel-coupled filters usually suffer from poor stopband performance with the spurious responses locating at $2f_0$. In order to achieve good selectivity and wide stopband, common methods are to increase the number of coupled-line stage or add extra short-circuited/open stubs, at the expense of additional circuit size and insertion loss of the designed filter.

To cope with the above issues, two different classes of 3^{rd} –order wideband combline bandpass filters are presented in this chapter. Firstly, the adoption of

quarter-wavelength stepped-impedance resonators ($\lambda/4$ SIRs) instead of half-wavelength ones is a key to broaden the stopband and also to compact the circuit size in both filters: the span between adjacent spurious resonance frequencies of $\lambda/4$ SIR is greater than that of $\lambda/2$ SIR and the size can be reduced half accordingly. Additionally, both of these filters utilize tapped-line input/output and don't require small coupling gaps (e.g. 50 μm in [4] and 100 μm in [5]) to achieve tight external couplings for a wideband response, and then relax the requirements for fabrication processes. In the meanwhile, the tapped feeding line will produce extra transmission zeros in the stopband, enhancing the filters' out-of-band performance. The two types of filters presented here are realized using two separate design methods, and implemented using two types of topologies. One type of combline filters is implemented by using liquid crystal polymer (LCP) bonded multilayer printed circuit board (PCB) technology, while the other one utilizes a standard planar PCB technology. The associated discussions will be detailed in the following sections.

8.2 Resonant Properties of SIR [8] [9]

The structure of quarter-wavelength stepped-impedance resonator ($\lambda/4$ SIR) that is frequently used in this chapter is shown in Fig. 8.1. This resonator is composed of two transmission-line sections of different characteristic impedances. The wider line section of characteristic impedance Z_1 and electrical length θ_1 is open at one end and connected to the narrower section at the other end. The narrower line section of characteristic impedance Z_2 and electrical length θ_2 is connected to the ground through a via-hole.

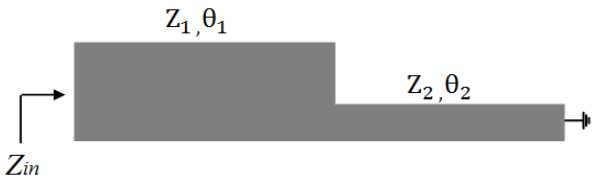

Figure 8.1: Quarter-wavelength stepped-impedance resonator with one end short circuited to ground.

By neglecting the effects of discontinuities and open end, one may express the

input impedance seen from the open end as:

$$Z_{in} = jZ_1 \frac{Z_1 \tan\theta_1 + Z_2 \tan\theta_2}{Z_1 - Z_2 \tan\theta_1 \tan\theta_2} \qquad (8.1)$$

The parallel resonance occurs when $Y_{in} = 1/Z_{in} = 0$, from which the fundamental resonance condition can be given as:

$$R_z = \tan\theta_1 \tan\theta_2 \qquad (8.2)$$

where $R_z = Z_1/Z_2$ is the impedance ratio of the SIR. To simplify the calculation, we choose the electrical length $\theta_1 = \theta_2$, and then the solution of corresponding length θ_1 at fundamental frequency f_0 can be found as

$$\theta_1 = \tan^{-1}\left(\sqrt{R_z}\right) \qquad (8.3)$$

Taking the spurious resonance frequency to be f_{sn} (n=1, 2, 3⋯) and corresponding θ with θ_{sn}, we obtain:

$$\frac{f_{s1}}{f_0} = \frac{\theta_{s1}}{\theta_1} = \frac{\pi - \theta_1}{\theta_1} = \frac{\pi - \tan^{-1}\left(\sqrt{R_z}\right)}{\tan^{-1}\left(\sqrt{R_z}\right)} \qquad (8.4)$$

$$\frac{f_{s2}}{f_0} = \frac{\theta_{s2}}{\theta_1} = \frac{\pi + \theta_1}{\theta_1} = \frac{\pi + \tan^{-1}\left(\sqrt{R_z}\right)}{\tan^{-1}\left(\sqrt{R_z}\right)} \qquad (8.5)$$

$$\frac{f_{s3}}{f_0} = \frac{\theta_{s1}}{\theta_1} = \frac{2\pi - \theta_1}{\theta_1} = \frac{2\pi - \tan^{-1}\left(\sqrt{R_z}\right)}{\tan^{-1}\left(\sqrt{R_z}\right)} \qquad (8.6)$$

One set of illustrative results are shown in Fig. 8.2 as a function of R_z. It becomes evident the spurious response can be controlled by the impedance ration R_z, and that is one of the special features of the SIR. Also, compared with the $\lambda/2$ UIR, the spurious frequencies of $\lambda/4$ UIR (R_z=1) with one end short circuited are located at odd multiples of the fundamental frequency, i.e., (2n+1)f_0 (n=1, 2, 3⋯), and the frequency span of adjacent higher order resonances is approximately 2f_0. Taking advantage of the stepped-impedance technique, the range of spurious span can further be made apart (see in Fig. 8.2). This feature facilitates the wide stopband bandwidth

achieved in the filter design. In addition to the merit of separating spurious frequencies, the utilization of $\lambda/4$ resonators also reduces the filter size when compared to $\lambda/2$ resonators. These properties make $\lambda/4$ SIRs good candidates for building compact wideband bandpass filters with multiple spurious suppressions.

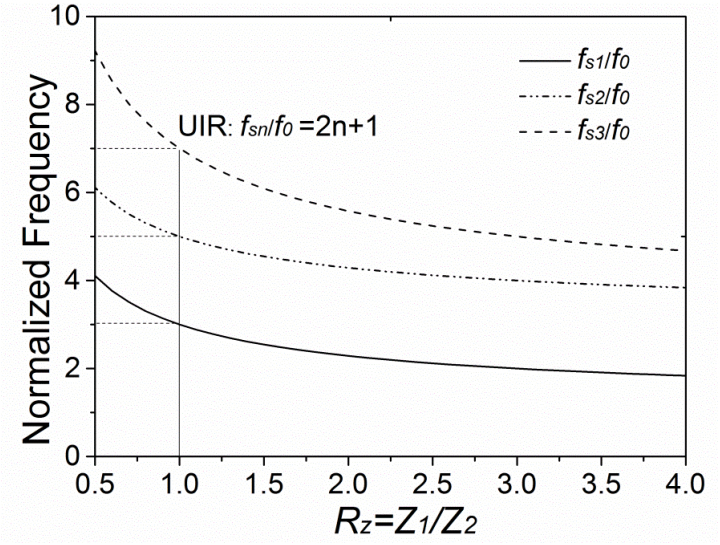

Figure 8.2: Spurious frequencies of $\lambda/4$ SIRs normalized with respect to their fundamental resonance frequency f_0 versus impedance ratio R_z.

8.3 Compact Wideband Combline Filter Using LCP Bonded Multilayer PCB Technology

8.3.1 *Advantage of the proposed filter in size reduction*

Fig. 8.3 shows the construction of the proposed wideband three-pole combline filter based on the LCP bonded multilayer PCB technology, which is composed of three metal layers including a solid ground plane at the bottom. The proposed filter consists of three $\lambda/4$ SIRs. Shown in Fig. 8.3 (a) are the two SIRs with input/output (I/O) tapped lines on the top layer; while Fig. 8.3 (b) displays a dissimilar $\lambda/4$ SIR in the middle layer. As can be seen, the resonator in the middle layer is just underneath the two resonators on the top layer; hence it requires no additional filter footprint. Also, tight inter-resonator couplings required for wideband design are achievable using such a broadside coupled structure, which would not be possible for those reported single-layer coupled SIR filters [10]-[12] that, hence, are all of narrowband

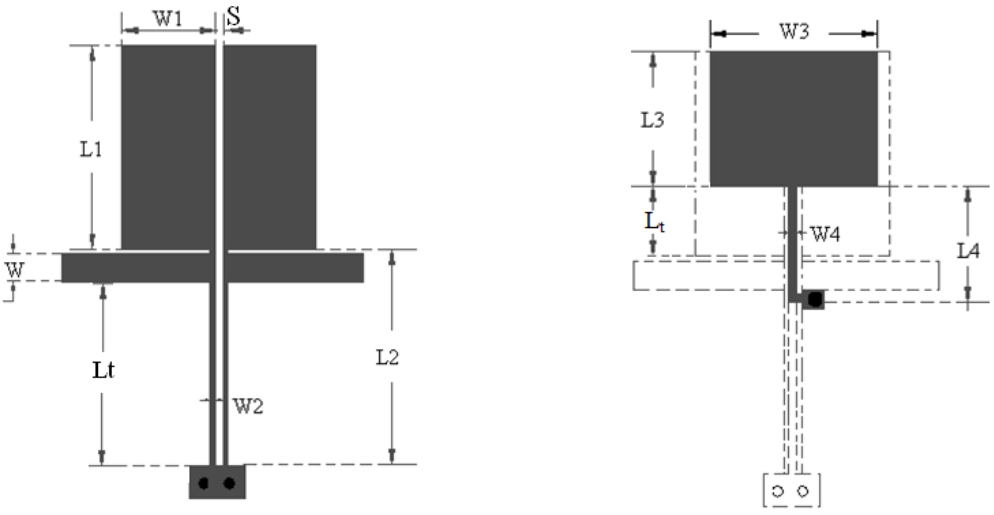

(a) (b)

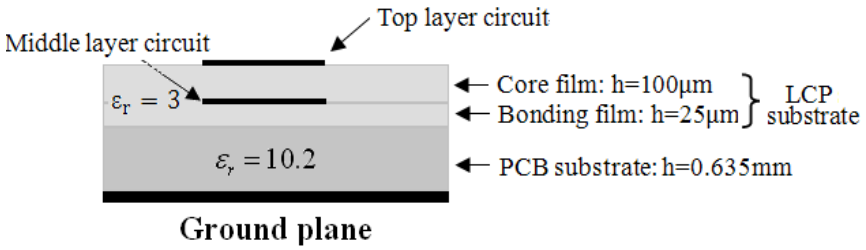

(c)

Figure 8.3: Proposed wideband combline filter (a) Top layer layout. (b) Middle layer layout. (c) Views of the multilayer technology.

Table 8.1: Comparison in Size of Various Resonators Based on Different Technologies

Filter topology and fabrication technology	f_0 (GHz)	SIR Impedance ration R_z	Occupied area (mm^2)	Size reduction (%)
SIR I designed on Multilayer LCP	1.04GHz	R_z≈5	6.4×21.4 mm^2	0%
SIR I designed on LCP bonded multilayer PCB			3.7×16.7 mm^2	**54.88%**
SIR II designed on Multilayer LCP	1.23GHz	R_z≈7	11.8×15 mm^2	0%
SIR II designed on LCP bonded multilayer PCB			6.6×9.9 mm^2	**63.08%**

with 3 dB fractional bandwidths less than 15% or even smaller. Referring to Fig. 8.3 (c), LCP films, which have a dielectric constant of 3.0 and loss tangent of 0.0025, are used to support the metal circuits. The thickness between the top and middle layers is 100 μm. The metal circuits on LCP are then bonded directly on to a high dielectric constant PCB substrate with a 25-μm-thick LCP bonding film without any adhesive. The PCB used here is RT/Duroid 6010 with a dielectric constant of 10.2, loss tangent of 0.0023 and a thickness of 0.635 mm. If an entire LCP multilayer technology is deployed, namely the PCB is replaced with the LCP substrate; the size of the filter would be significantly large. This can be seen from the comparison results in Table 8.1.

In Table 8.1, we compared the occupied circuit sizes of SIRs shown in Fig. 8.3 (i.e. the type of SIR I on the top layer and the type of SIR II in the middle layer) when they are designed on (i) the multilayer LCP and (ii) the LCP bonded multilayer PCB, respectively, where the total thickness of substrates, fundamental frequency of SIRs and SIR impedance ratio R_z are kept the same. From the compared results, it is obvious that the design utilizing the proposed multilayer technology can achieve a size reduction of more than 50%, meaning a less half size, which is a significant miniaturization.

8.3.2 *Filter design and analysis*

Since the bandwidth of the proposed combline filter is up to 80%, the conventional analytical equation approach [13] can't be employed anymore, which are best for bandwidths narrow than 50%. Thus, an optimization procedure based on parameters analysis is used. In general, the filter is designed in three stages: the first stage is to determine the length and line impedance of each SIR according to the desired central frequency and stopband bandwidth. The fundamentals of $\lambda/4$ SIR stated in Section 8.2 can be for reference. The second stage is to allocate the resonant mode of each resonator inside the desired passband by optimizing the couplings between each other. The last stage is to obtain proper tapped-line couplings to support a wide passband by tuning the tapped positions. For our investigation, full-wave

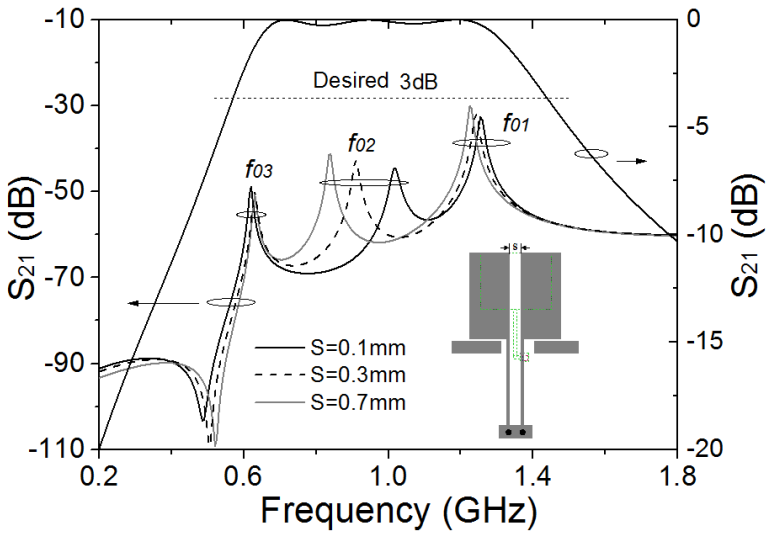

(a)

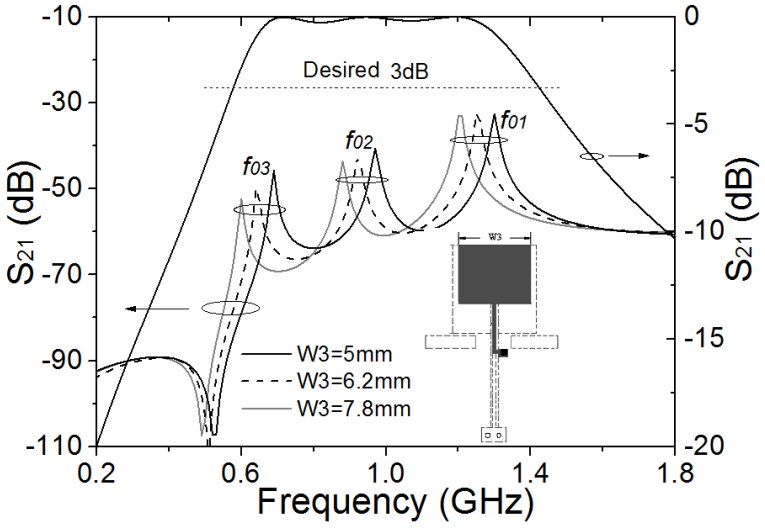

(b)

Figure 8.4: Simulated insertion loss of the proposed wideband bandpass filter under weak coupling with varied (a) Parameter *S*. (b) Parameter *W3*.

electromagnetic (EM) simulator Sonnet [14] is employed. Fig. 8.4 demonstrates the EM-simulated insertion loss of the proposed structure under weak coupling versus varied parameters of *S* and *W3*, where f_{01} and f_{02} represent the resonant frequencies of two resonators (SIR I) on the top layer and f_{03} corresponds to that of resonator SIR II in the middle layer. As can be noted in Fig. 8.4 (a), by increasing the space *S* between two SIRs I, the resonant frequencies f_{01} and f_{02} can be controlled since the associated coupling is changed, while the resonant mode f_{03} and the separation between f_{01} and

f_{03} almost maintain unchanged. Fig. 8.4 (b) indicates the simulated responses of insertion loss by varying the width *W3*. From theory it is known that increasing the width *W3* results in the resonant frequency of SIR II shifting downwards. Additionally, it is noteworthy that the resonant modes f_{01} and f_{02} also shift accordingly. This is because SIR II works not only as a resonator, but also as a floating plate having effect on the resonant frequencies and the coupling coefficient of two resonators SIR I. Furthermore, it is easy to understand by reducing the thickness of the core film used in the circuit to 50/25 μm, the couplings between the SIR I and SIR II would be increased to obtain wider bandwidth.

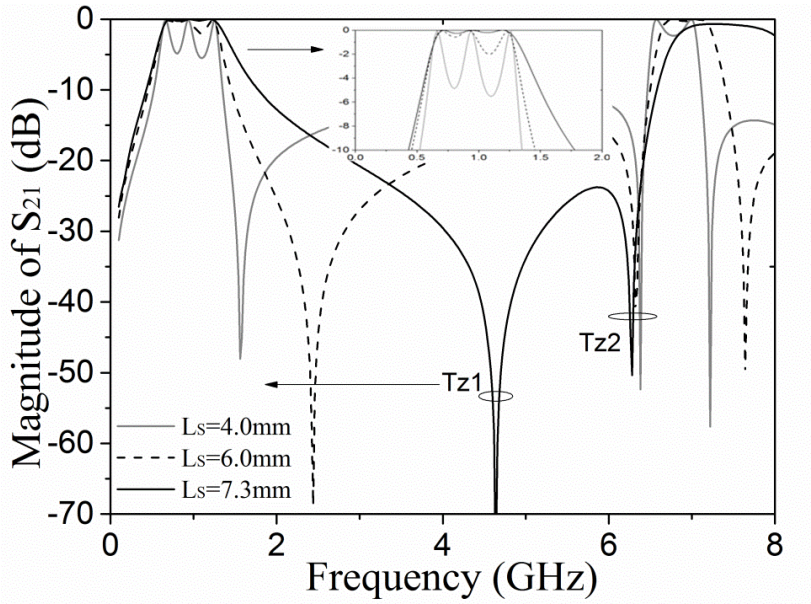

Figure 8.5: Simulated insertion loss of the proposed wideband bandpass filter with varied tapping position *Ls*.

Fig. 8.5 indicates the frequency responses of S_{21} magnitude under different tapped-line couplings by varying the tapping position *Ls*. The smaller the *Ls*, the closer the tapped line is to the grounding of the resonator, which results in a weaker coupling or a larger external quality factor. Therefore, after allocating the resonant modes inside the desired passband properly based on the above discussions, we need to adjust the *Ls* to obtain a matched passband. In addition, it is interesting to note that in Fig. 8.5 the filter has a wide stopband range with two transmission zeros, i.e. Tz1

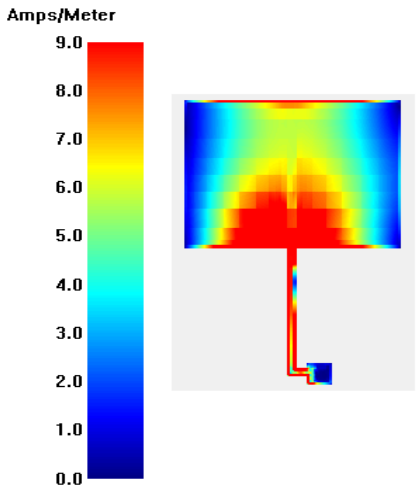

(a)

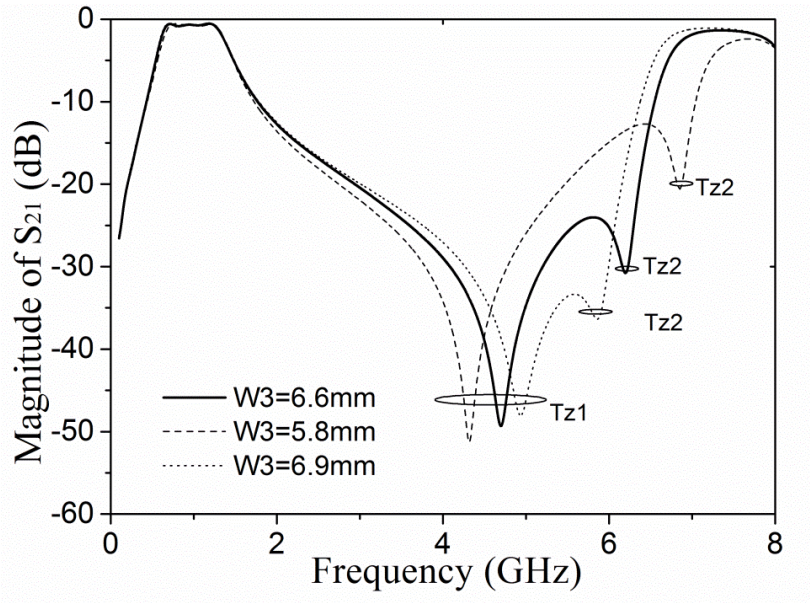

(b)

Figure 8.6: (a) The current distribution at Tz2 in Figure. 8.5. (b) Simulated responses for the proposed filter with various *W3* defined in Figure 8.3.

and Tz2, enhancing the selectivity or upper stopband performance. From these curves, it can be seen that the Tz1 is effectively affected by the I/O tapped line position (*Ls*) defined in Fig. 8.3; while the Tz2 remains nearly unchanged. This implies that the first transmission zero Tz1 is generated by the nonuniform line section from the open end of the resonator to the tapped point, which can be treated as a quarter-wave open stub [12]. As for the second transmission zero Tz2, EM simulations are carried out to study this phenomenon, as shown in Fig. 8.6. From the current distribution given in

Fig. 8.6 (a), it is interesting to note that at approximately 6 GHz in Fig. 8.5, the middle layer resonator exhibits a transverse resonance, which can account for Tz2. Therefore, in principal, Tz2 can be adjusted by a transverse dimension of the width *W3*. Fig. 8.6 (b) plots the simulation responses showing the Tz2 shifts against *W3*. Note that Tz1 is also affected. This is because, as aforementioned, in this multilayer structure, changing *W3* can affect the top layer resonators as well.

8.3.3 *Fabrication process and experiment results*

LCP bonded multilayer PCB technology has been investigated for packaging in the open literature [15], but not often discussed in microwave component designs. However, based on this design and other filters previously demonstrated in Chapter 3 and Chapter 4, we can understand LCP bonded multilayer PCB technology is very promising in a simple multilayer circuit (e.g. three-metal layer circuit including ground metal) realization, which not only makes best use of the available high dielectric constant of PCB to realize more miniaturized size, but also obtain the same features of LCP, like the flexibility in multilayer construction and low cost.

In order to characterize the signal transmission through the inhomogeneous medium (i.e. LCP and PCB), a 50 Ω microstrip transmission line (TL) based on this multilayer technology is examined. Fig. 8.7 shows simulated responses with different thickness combinations of LCP core film and bonding film mounted onto a 0.635mm-thick Rogers RO6010 PCB. As can be seen, within the frequency range 0 to 10 GHz, no matter what types of LCP films used, we can achieve a simulated return loss of greater than 30dB and a simulated insertion loss of better than 0.17 dB. Therefore, it can be concluded even though LCP bonded multilayer PCB technology brings about substrate discontinuities, a well-matched signal transmission can be obtained to enable the microwave components performance designed based on this technology. Regarding the lamination process of LCP bonded multilayer PCB, it is quite similar to that of pure LCP multilayer technology discussed in Chapter 7. Most of basic lamination rules stated in Section 7.4 can also be applied here except the lamination cycle is slightly different. According to the author's experimental

experiences, the bonding cycle suitable for LCP bonded multilayer PCB technology is recommended in Fig. 8.8, where the temperature setting is kept the same while the pressure setting can be reduced.

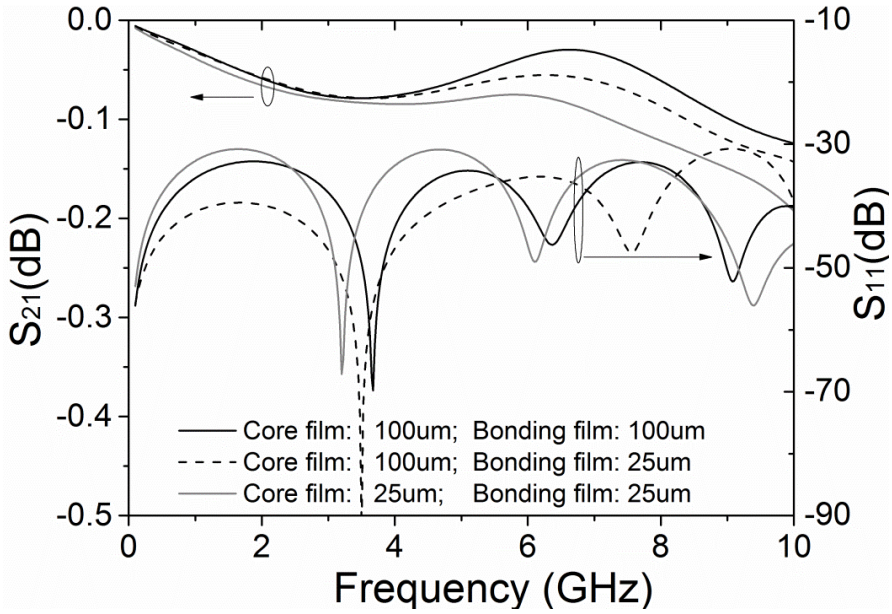

Figure 8.7: Simulated *S*-parameters of a 50 Ω microstrip TL based on different thickness combinations of LCP core film and bonding film mounted onto a PCB (ε_r=10.2 and h=0.635mm).

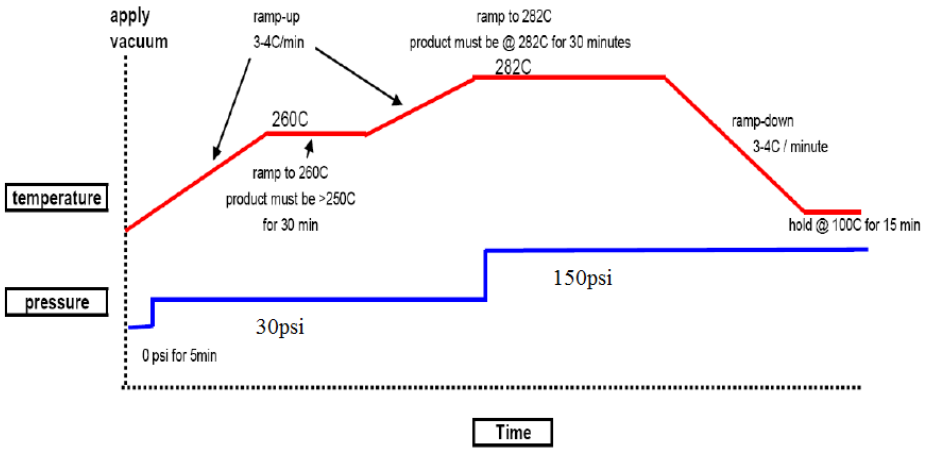

Figure 8.8: Recommended bonding cycle of LCP bonded multilayer PCB technology.

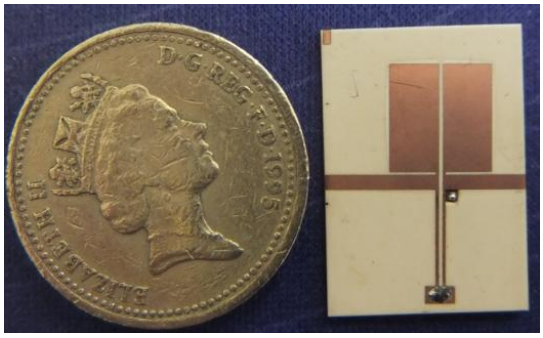

(a)

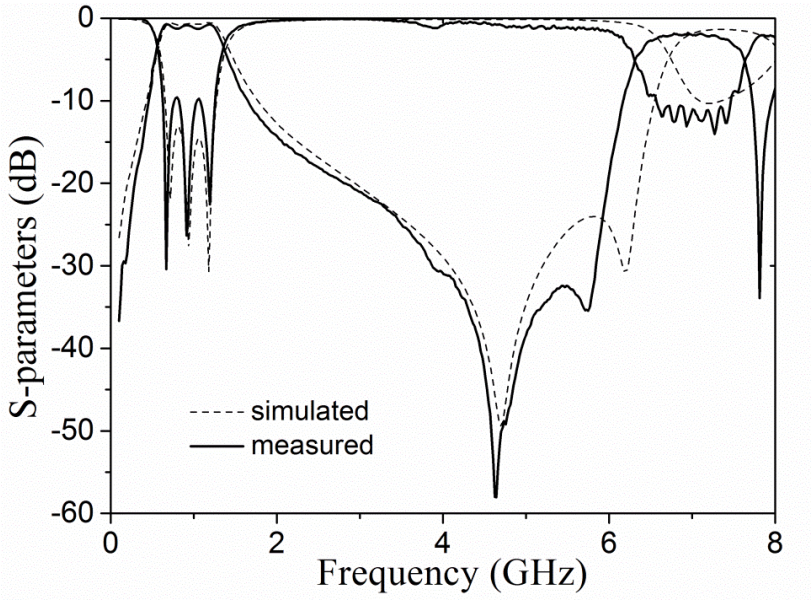

(b)

Figure 8.9: (a) Photograph of the fabricated filter. (b) The measured and simulated results for the fabricated filter (*W*=1.1 mm *W1*=3.7 mm *W2*=0.2 mm *W3*=6.6 mm *W4*=0.3 mm *L1*=8.1 mm *L2*=8.6 mm *L3*=5.3 mm *L4*=4.6 mm *Ls*=7.3 mm *Lt*=2.8 mm and *S*=0.3 mm).

Shown in Fig. 8.9 (a) is the photograph of the fabricated circuit, which has a size of 16.7mm by 7.7mm excluding the input and output microstrip lines. This is very compact filter only occupying a circuit area about $0.153\,\lambda_g * 0.06\,\lambda_g$, where λ_g is the guided wavelength at the center frequency. A vector network analyzer HP 8510B is used to measure the fabricated prototype. The measured results are plotted in Fig. 8.9 (b), where a good agreement between the simulation and measurement can be observed. The measured filter is operated at central frequency 0.95 GHz, which has a

3 dB bandwidth from 0.57 GHz to 1.34 GHz or a fractional bandwidth 81%. The measured insertion loss of the third-order combline filter in the passband is around 0.7 dB. And the proposed filter has 6th harmonic suppression up to 6 GHz with better than 15 dB rejection level. Two transmission zeros, located at 4.6 GHz and 5.7 GHz respectively, improve the rejection over that frequency range. The measured Tz2 is somehow shifted from the simulated one, which would attribute to fabrication tolerance.

8.4 Compact Wideband Combline Filter Using Standard PCB Technology

The subject of this section is to present and implement another new class of wideband combline bandpass filter with miniaturized size and excellent out-of-band performance based on the standard PCB fabrication process.

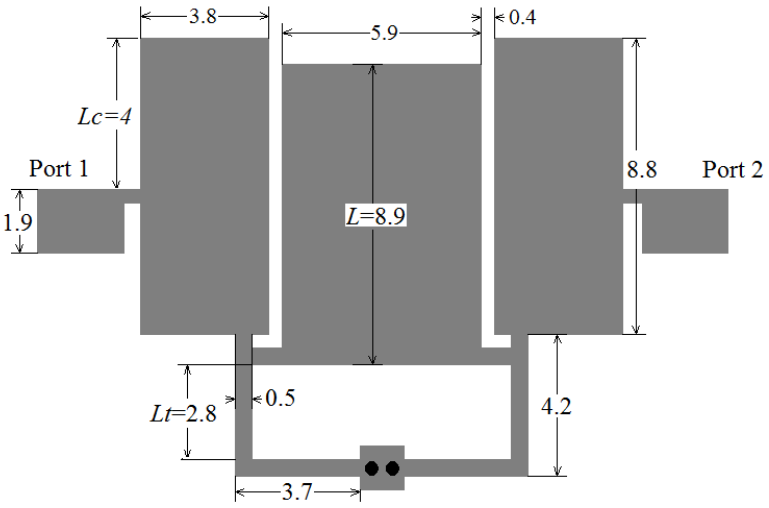

Figure 8.10: Configuration proposed combline filter using standard PCB fabrication technology (all dimensions in millimeter).

8.4.1 *Filter design and analysis*

Fig. 8.10 depicts the schematic of the proposed microstrip wideband combline filter. As can be seen, this structure is composed of two quarter-wavelength ($\lambda/4$) stepped-impedance resonators (SIRs), which are directly connected with an additional stepped-impedance transmission line in between. From the coupled-resonator point of view, such connecting line between two resonators may be considered as providing a

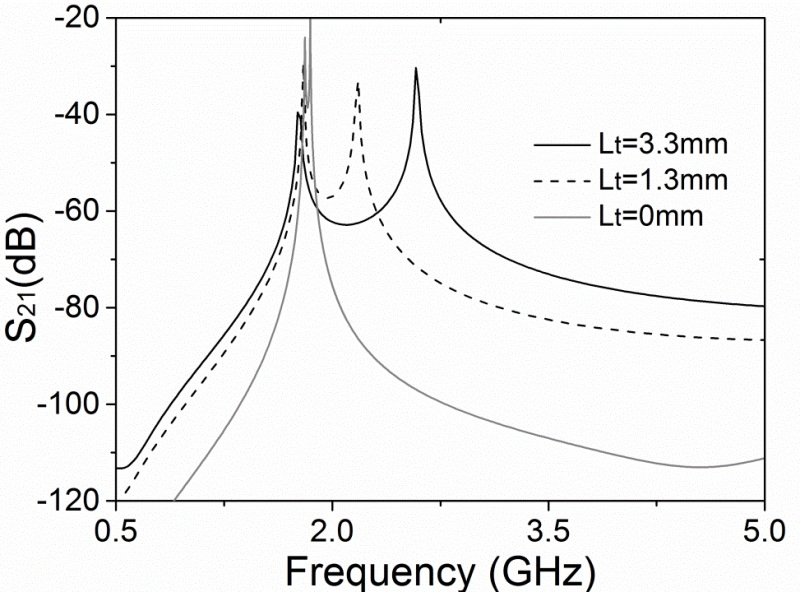

Figure 8.11: Full-wave simulated resonance-splitting phenomenon for different *Lt*.

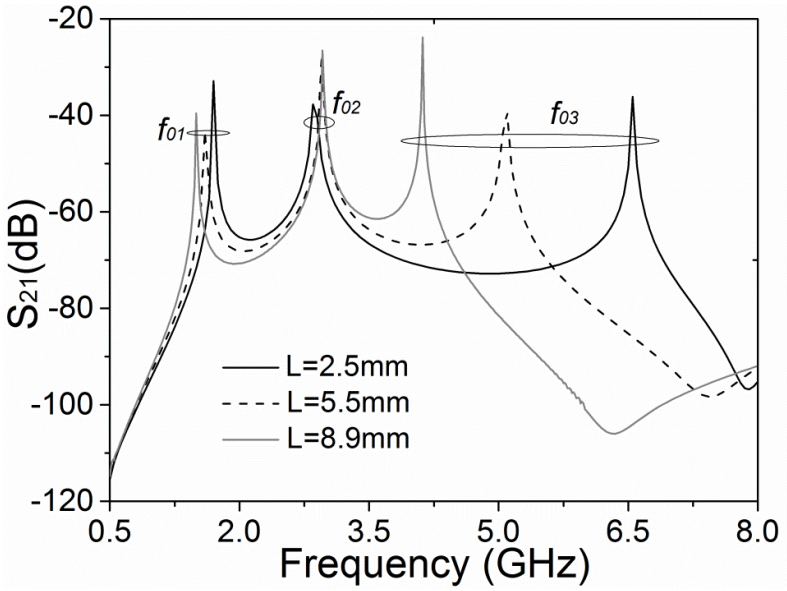

Figure 8.12: Full-wave simulated resonant responses under weak coupling versus different *L*.

direct signal transmission path to result in a stronger coupling than that of the conventional form [16]. Furthermore, the connecting line structure can be made non-redundant to contribute an additional pole to the filter. For demonstration, Fig. 8.11 plots the simulated resonance splitting phenomenon for different *Lt*, where the geometry parameter *L* shown in Fig. 8.10 is assumed to zero (i.e. uniform line).

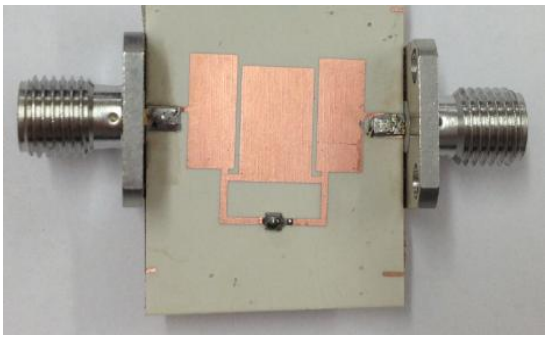

(a)

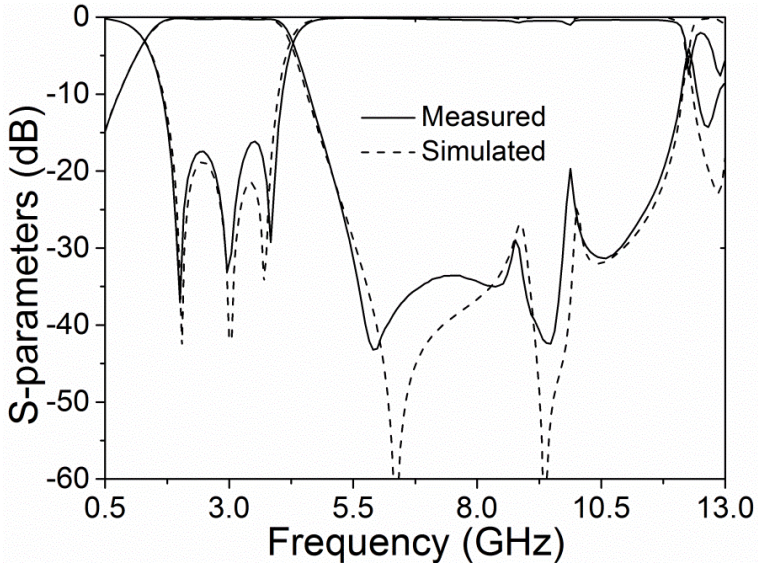

(b)

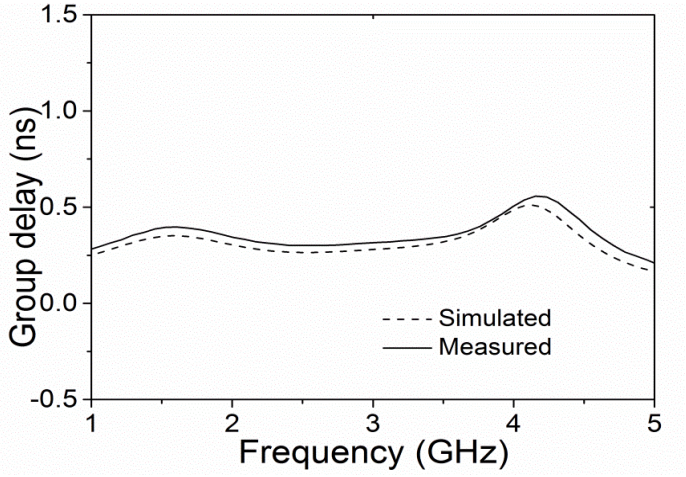

(c)

Figure 8.13: (a) Photograph of the fabricated filter. (b) The measured and simulated results for the fabricated filter. (c) Group delay.

Compared with the case of *Lt*=0 (without connecting line), the separations between two split resonance frequencies for other two cases are obviously wider to represent increased couplings. Normally the larger the *Lt*, the remoter to the via ground, the larger the coupling. However, in order to realize an ultra-wide bandwidth up to 100%, it is necessary to introduce an extra resonant mode based on such two widely split frequencies. Fig. 8.12 demonstrates the simulated resonant responses versus different *L* (refer to Fig. 8.10) with a fixed connecting position *Lt*=3.3mm. It can be noted that by increasing the length, i.e. *L* of low-impedance section of the connecting line, the resonant mode f_{03} is getting closer to the resonant frequencies f_{01}, f_{02} of two $\lambda/4$ SIRs, which offers a possibility to make up a wide passband by using three resonant modes. Overall, by adjusting the parameters (*Lt*, *L*) of stepped-impedance connecting line, the resonant modes can be allocated properly to realize a desired wide passband.

8.4.2 *Experimental results*

The final physical dimensions are given in Fig. 8.10. Using standard PCB technique, the filter is fabricated on a Rogers RO3003 with a relative dielectric constant of 3.0 and thickness of 0.75mm. Shown in Fig. 8.13 (a) is the photograph of the fabricated circuit, which has a size of 14.3 mm by 13 mm excluding the input and output microstrip lines. This is very compact filter only occupying a circuit area about $0.224\,\lambda_g * 0.2040\,\lambda_g$, where λ_g is the guided wavelength at the center frequency. A vector network analyzer HP 8510B is used to measure the fabricated prototype. The measured results are plotted in Fig. 8.13 (b), where a good agreement between the simulation and measurement can be observed. The measured filter roughly operates at central frequency 2.78 GHz, which has a 3 dB bandwidth from 1.29 GHz to 4.27 GHz (FBW=107%). The measured maximum insertion loss of the third-order combline filter in the passband is around 0.27 dB. And the proposed filter has 4th harmonic suppression up to 11.8 GHz with better than 19 dB rejection level. Two transmission zeros, located at 5.96 and 9.45 GHz respectively, improve the rejection over that frequency range. The first transmission zero is associated with the parameter *L*, while the second one is generated by the low-impedance line section from the open end of

the resonator to the tapped point (controlled by the length *Lc*), which can be treated as a quarter-wave open stub. The measured group-delay response is shown in Fig. 8.13 (c), where a flat group-delay can be observed in the passband.

8.5 Summary

In this chapter, two classes of wideband combline filters using different fabrication technologies have been introduced. Owning to adopting $\lambda/4$ stepped-impedance resonators (SIRs) in these designs, both combline filters achieved wideband stopband with harmonic suppressions and also compact circuit size. Specifically, the first filter was fabricated based on LCP bonded multilayer PCB technology, which not only obtained promisingly miniaturized size by taking advantages of available high dielectric constant of PCB substrate, but also easily realized tight couplings with the help of 3D-design of such fabrication technology. A multilayer lamination process has been developed to implement the designed prototype. The demonstrated measured results, has verified that the LCP bonded multilayer PCB technology is very attractive for the development of compact wideband microwave filters, in particular at low frequency bands. The second filter is built on single PCB technology. By introducing a stepped impedance line between two $\lambda/4$ SIRs for direct connection, the associated coupling was dramatically increased as well as an extra resonance mode was produced in the desired passband, which offered a possibility to realize a wideband performance. Guidelines and design rules have been given in this chapter for ease of reference. Overall, both two combline filters have addressed advantages in size reduction, wide passband bandwidths and stopband improvements. The most important is all of these promising features can be implemented using ease fabrication process without small coupling gaps required.

Reference

[1] Z.-C. Hao and J.-S. Hong, "Ultra-wideband bandpass filter using multilayer liquid-crystal-polymer technology," *IEEE Trans. Microwave Theory Tech.*, vol. 56, no. 9, pp. 2095–2100, Sept. 2008.

[2] C. Nguyen, "New compact wideband bandpass filter using three parallel-coupled lines," *Electron. Lett.*, vol. 30, no. 25, pp. 2149–2150, Dec. 1994.

[3] C.-H. Chi and C.-Y. Chang, "A wideband bandpass filter with wide upper stopband using stepped-impedance cascadable 180 hybrid rings," *IEEE Microw. Wireless Compon. Lett.*, vol. 17, no. 8, pp. 589-591, Aug. 2007.

[4] L. Zhu, S. Sun, and W. Menzel, "Ultra-wideband (UWB) bandpass filters using multiple-mode resonator," *IEEE Microw. Wireless Compon. Lett.*, vol. 15, no. 11, pp. 796–798, Nov. 2005.

[5] S. Sun and L. Zhu, "Wideband microstrip ring resonator bandpass filters under multiple resonances," *IEEE Trans. Microw. Theory Tech.*, vol. 55, no. 10, pp. 2176–2182, Oct. 2007.

[6] H. N. Shaman, "New -band bandpass filter (BPF) with wideband passband for wireless communication systems," *IEEE Microw. Wireless Compon. Lett.*, vol. 22, no. 5, pp. 242–244, May 2012.

[7] M. Mokhtaari, J. Bornemann and S. Amari, "Folded compact ultrawideband stepped-impedance resonator filters," in *IEEE MTT-S Int. Dig.*, Jun. 2007, pp. 747–750.

[8] M. Makimoto and S. Yamashita, "Bandpass filters using parallel coupled stripline stepped impedance resonators," *IEEE Trans. Microw. Theory Tech.*, vol. MTT-28, no. 12, pp. 1413–1417, Dec. 1980.

[9] S. C. Lin, P.-H. Deng, Y.-S. Lin, C.-H. Wang and C. H. Chen, "Wide-stopband microstrip bandpass filters using dissimilar quarter-wavelength stepped-impedance resonators," *IEEE Trans. Microw. Theory Tech.*, vol. 54, no. 3, pp. 1011–1018, Mar. 2006.

[10] Y. M. Chen, S. F. Chang, C. C. Chang and T. J. Hung, "Design of Stepped-Impedance Combline Bandpass Filters With Symmetric Insertion-Loss Response and Wide Stopband Range." *IEEE Trans. Microw. Theory Tech*., Vol.55, pp.2191– 2199, Oct. 2007.

[11] S. C Lin, P. H. Deng, Y. S. Lin, C. H. Wang and C. H. Chen, "Wide-Stopband Microstrip Bandpass Filters Using Dissimilar Quarter-Wavelength

Stepped-Impedance Resonators." *IEEE Trans. Microw. Theory Tech*., Vol.54, pp.1011– 1018, Mar. 2006.

[12] J. T. Kuo and E. Shih, "Microstrip Stepped Impedance Resonator Bandpass Filter with an Extended Optimal Rejection Bandwidth." *IEEE Trans. Microw. Theory Tech.*, Vol.51, no.5, pp.1554– 1559 May. 2003.

[13] J.-S. Hong, Microstrip filter for RF/Microwave applications, 2nd Edition, New York: John Wiley & Sons, 2011.

[14] Sonnet *em*, Version 13.54, Sonnet Software Inc., New York, 2011.

[15] K. Aihara, M. J. Chen and A. Pham, "Development of thin-film liquid crystal polymer surface mount packages for Ka-band applications," *IEEE Trans. Microw. Theory Tech.*, Vol.56, no.9, pp.2111– 2117 Sep. 2009.

[16] T.-N. Kuo, S.-C. Lin, C.-H. Wang and C.-H. Chen, "New coupling scheme for microstrip bandpass filters with quarter-wavelength resonators," *IEEE Trans. Microw. Theory Tech.*, vol. 56, no. 12, pp. 2930–2935, Dec. 2008.

CHAPTER 9

Conclusions and Future Work

9.1 Conclusions and Contributions

The core of the work presented in this dissertation is directly applicable to the design of reconfigurable and miniaturized microwave filters for modern wireless communication systems. Generally, in Part I, different novel classes of tunable filtering topologies and tunable design methods have been proposed, and applied to the implementations of varactor-diode-based microwave filters with advanced characteristics. These presented designs can help in improving the efficiency use of available spectrum, in addition to decreasing the size, complexity and cost of the system. Part II of this dissertation have mainly discussed the designs and implementations of compact passive filters using two different available multilayer technologies, i.e. LCP multilayer technology and LCP bonded multilayer PCB technology, for achieving the highest degree of integration density in systems.

In detail, the major contributions of the research presented in this dissertation are summarized as below:

In Chapter 2 and Chapter 3, new topologies for designing continuously tunable microstrip lowpass and highpass filters with the merits of compact size, wide tuning range, high selectivity and broad stopband were fully demonstrated and validated by experimental results. Analytical equations, design rules and element-value synthesis procedure have been provided for revealing the performance controlling mechanisms of all the suggested topologies and also guiding the associated microstrip realizations. As illustrative fabricated examples, the presented tunable lowpass and highpass filters can achieve a frequency tuning range of 46% (1600 to 2940 MHz) and 52.1% (1030 to 2150 MHz), respectively. To the author's knowledge, in the associated aspects, such high-performance tunable filters have never been reported in the literature. In practical applications, the proposed tunable lowpass/highpass filter can be used alone

in a functional way or can be used partly in a cascaded topology to offer a possibility to obtain tunable bandpass/bandstop performance.

In Chapter 4, novel realizations of tunable bandpass filters with different passband characteristics were presented to address the advantages in flexible control of bandwidth and centre frequency. Based on varactor-loaded parallel-coupled microstrip line structure coupled to short-circuited stubs, the first design obtained a reconfigurable lower passband edge with a wide tuning range up to 42.5% (1160 to 2019 MHz) as well as four transmission zeros that helped with improving selectivity. Furthermore, the second tunable bandpass filter was constructed with a tunable bandpass filter (the first design) cascaded to a tunable lowpass filter, which provided an additional degree of freedom of bandwidth adjustment at each tunable center-frequency state. The illustrative measured bandwidth tuning of 685% efficiently demonstrated the proposed tunable cascaded topology would be promising for reconfigurable applications.

Chapter 5 proposed a novel concept of tunable microstrip lossy filter with enhanced in-band loss variation and selectivity. Unlike the other reported tunable bandpass filter, the presented one put focus on investigating a design method to achieve an equivalent high-Q filter performance by using low Q resonators. The associated operating principles have been demonstrated by virtue of equivalent circuit model and coupling matrix model. For theoretical verification, a three-pole varactor-tuned microstrip combline filter was designed and measured, which obtained different degrees of performance improvement at various tuning states, at cost of increased absolute insertion loss. As illustrated, an equivalent Q of 340 was achieved at highest-frequency state, by utilizing the resonators with average Q of 95 in the design. Moreover, another type of microstrip lossy filter using extended doublet topology with nonuniform Q distribution was discussed. Compared with the other related passive lossy filters in the literature, the presented one attained a higher equivalent Q with a simpler structure and easier design methodology, avoiding complex topologies or difficult implementations.

In Chapter 7 and Chapter 8, different novel classes of miniaturized microwave bandpass filters have been demonstrated. The first design mostly utilized the artificial right-handed and left-hand transmission lines in a simple single-interference filtering topology instead of distributed transmission lines adopted in conventional approaches, which helped in reducing the circuit size and improving the out-of-band performance. Particularly, this filter was implemented in forms of quasi-lumped elements by means of liquid crystal polymer (LCP) multilayer technology leading to a further miniaturization. The other two types of filter achieved compact sizes due to the use of stepped-impedance resonators. Both of them have shown a sharp response with wide passband, low insertion loss and wide stopband bandwidth with transmission zeros, demonstrating the proposed filters to be very competitive for the emerging wideband wireless communication systems. However, expect the difference at design theory, one of two filters was mainly realized by using liquid crystal polymer (LCP) bonded multilayer printed circuit board (PCB) technology, which took advantage of high dielectric constant of PCB substrate resulting in more compact size; while the other one utilized a standard planar PCB technology with easier fabrication process. Moreover, the fabrication processes of multilayer technologies, i.e. LCP multilayer technology and LCP bonded multilayer PCB technology, have been fully demonstrated.

9.2 Future Work

The following are suggestions to expand upon the research presented in this dissertation:

- The tunable lowpass and highpass filter topologies introduced in Chapter 2 and Chapter 3 can be realized and implemented using high *Q* tuning elements, such as RF MEMS, resulting in lower insertion loss, higher roll-off rate, deeper stopband rejection and higher linearity for some stringent applications.

- The concept of using cascaded topology (tunable bandpass cascaded tunable lowpass) to realize a tunable bandpass filter presented in Chapter 4 can be applied to design a tunable bandstop filter, to obtain the similarly advanced characteristic

in controlling the centre frequency and bandwidth. Additionally, an alternative cascaded topology for designing tunable bandpass or bandstop filter can be constructed by the combination of tunable lowpass filter and tunable highpass filter individually introduced in Chapter 2 and Chapter 3.

- The concept of tunable lossy filter proposed in Chapter 5 showed interesting characteristics for applications in receiver filters. This philosophy provided one approach for designing a tunable combline filter with enhanced performance within a certain tuning range by using low *Q* resonators. However, there are still some interesting and challenging issues worthy of further consideration. For instance, how to obtain the optimal *Q* distribution at each tuning state to further improve the tunable performance of the filter. Additionally, the other fixed-frequency microstrip lossy filter presented in Chapter 5 has demonstrated the dual-mode resonator has great advantages of compact size and flexible *Q*-control in even- and odd-modes, which is promising for realizing microstrip lossy filters with other topologies, such as four-order microstrip transversal lossy filter.

- The signal-interference filter using artificial RH and LH TLs demonstrated in Chapter 7 can be further exploited to obtain better out-of-band rejections in stopband by cascading additional filtering sections. Furthermore, such design concept could be applied to the design of miniaturized dual-band bandpass filter by modifying the signal-interference topology.

- The recommended bonding cycle of LCP bonded multilayer PCB technology introduced in Chapter 8 can be further explored to enhance the reliability and repeatability of the associated multilayered circuit. Additionally, this multilayer technology can be used for designing various simple multilayered filters (e.g. three-metal layer circuit) to achieve size reduction.

- Tolerance analysis on the presented multilayer technologies/circuits can be carried out, specifically geometric tolerance analysis. Managing such tolerance

can make us well understand the acceptable range of variation in geometry from a nominal or reference one, leading to efficiently achieving the desired performance of engineered systems.

Appendix A

Synthesis of Physical Dimensions of Stepped-Impedance Hairpin Resonator

This appendix describes how to calculate the physical dimensions of the stepped-impedance hairpin resonator filter, as shown in Fig. A.1, based on *ABCD* matrix. This study mainly complements the synthesis process introduced in Chapter 2.

The schematic of the stepped-impedance hairpin resonator filter is shown in Fig. A.1, which consists of the single transmission line with high characteristic impedance Z_s, in addition to the coupled lines with characteristic even- and odd-mode impedance Z_{oo} and Z_{oo}, where $Z_s > \sqrt{Z_{oe}Z_{oo}}$ is selected for size reduction and harmonic suppression.

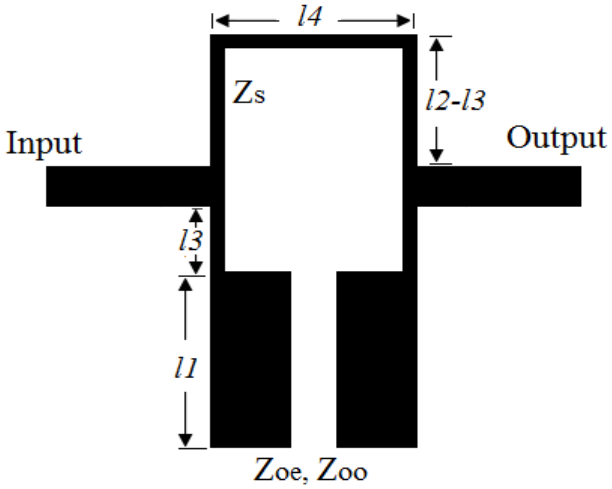

Figure A.1: The stepped-impedance hairpin resonator filter introduced in Chapter 2.

In theory, the single transmission line can be modeled as an equivalent *L-C* π-network, as indicated in Fig. A.2 (a). For the distributed transmission line, the *ABCD* matrix is given by:

$$\begin{bmatrix} A & B \\ C & D \end{bmatrix} = \begin{bmatrix} \cos(\beta l) & jZ_s \sin(\beta l) \\ jY_s \sin(\beta l) & \cos(\beta l) \end{bmatrix} \qquad \text{(A. 1)}$$

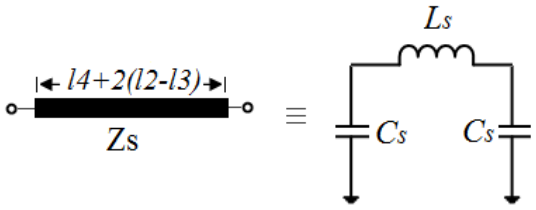

(a)

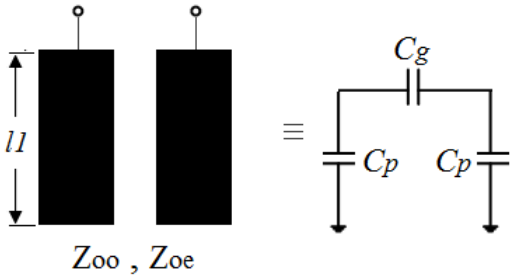

(b)

Figure A.2: Equivalent circuit of: (a) Single transmission line. (b) Symmetric coupled lines.

where *l=l4+2(l2-l3)*, β and $Y_s = 1/Z_s$ are the phase propagation constant and characteristic admittance of this single transmission line, respectively. While the *ABCD* matrix of the equivalent *L-C* π-network is

$$\begin{bmatrix} A & B \\ C & D \end{bmatrix} = \begin{bmatrix} 1-\omega^2 L_s C_s & j\omega L_s \\ 2j\omega C_s - j\omega^3 {C_s}^2 L_s & 1-\omega^2 L_s C_s \end{bmatrix} \qquad (A.2)$$

where ω is the angular frequency, and L_s and C_s are the equivalent inductance and capacitance. Comparing (A.1) and (A.2), the length of the single transmission line can be obtained as:

$$l = \frac{sin^{-1}(\omega_c L_s / Z_s)}{\beta} \quad (\text{unit: mm}) \qquad (A.3)$$

where ω_c is the 3-dB cutoff angular frequency.

Likewise, as seen in Fig. A.2 (b), the symmetric parallel coupled lines are equivalent to a capacitive π-network. The associated *ABCD* matrix can be expressed as:

$$\begin{bmatrix} A & B \\ C & D \end{bmatrix} = \begin{bmatrix} \dfrac{Z_{oe}+Z_{oo}}{Z_{oe}-Z_{oo}} & \dfrac{-2jZ_{oe}Z_{oo}\cot(\beta l_1)}{Z_{oe}-Z_{oo}} \\ \dfrac{2j}{Z_{oe}Z_{oo}\cot(\beta l_1)} & \dfrac{Z_{oe}+Z_{oo}}{Z_{oe}-Z_{oo}} \end{bmatrix} \quad \text{(A. 4)}$$

where β is the phase propagation constant of the coupled lines. Also, the *ABCD* matrix of the equivalent capacitive π-network is

$$\begin{bmatrix} A & B \\ C & D \end{bmatrix} = \begin{bmatrix} 1+C_p/C_g & 1/j\omega C_g \\ 2j\omega C_p + j\omega {C_p}^2/C_g & 1+C_p/C_g \end{bmatrix} \quad \text{(A. 5)}$$

Comparing (A.3) and (A.4), the length of the coupled lines can be derived as:

$$l_1 = \frac{tan^{-1}(2\omega_c C_g Z_{oe} Z_{oo}/(Z_{oe}-Z_{oo}))}{\beta} \quad \text{(unit: mm)} \qquad \text{(A. 6)}$$

Appendix B

Impedance Matrix of Varactor-loaded Parallel Coupled-line Filter

The following are the detailed process of deriving the impedance matrix of varactor-loaded parallel coupled-line filter demonstrated in Chapter 4.

Shown in Fig. B.1 is a simple quarter-wave coupled-line structure with a varactor diode loaded. For simplify, we assume that the even- and odd-mode phase velocities are equal. In order to obtain the electrical characterization of such filter, an alternative parallel coupled-line section with four ports is studied firstly, as implied in Fig. B.2.

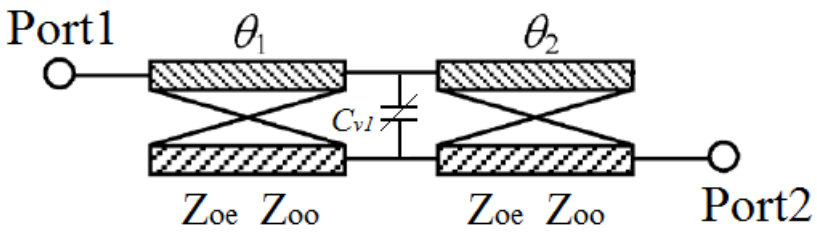

Figure B.1: A simple varactor-loaded parallel coupled-line filter adopted in Chapter 4.

Since the network is symmetrical, even- and odd-mode excitations can be further applied to the structure as indicated in Fig. B.3 (a), where the current sources i_1 and i_3 drive the line in the even mode, while i_2 and i_4 drive the line in odd mode. By comparing the voltage and current sources defined in Fig. B.2, the total port currents, I_i can be expressed in terms of even- and odd-mode current as:

$$I_1 = i_1 + i_2 \qquad \text{(B. 1)}$$

$$I_2 = i_1 - i_2 \qquad \text{(B. 2)}$$

$$I_3 = i_3 - i_4 \qquad \text{(B. 3)}$$

$$I_4 = i_3 + i_4 \qquad \text{(B. 4)}$$

First consider the even-mode circuit driven by the i_1 current sources in Fig. B.3 (b).

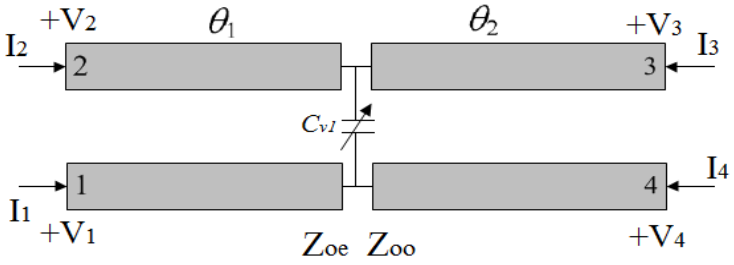

Figure B.2: A varactor-loaded parallel coupled-line section with four ports under voltages and current definitions.

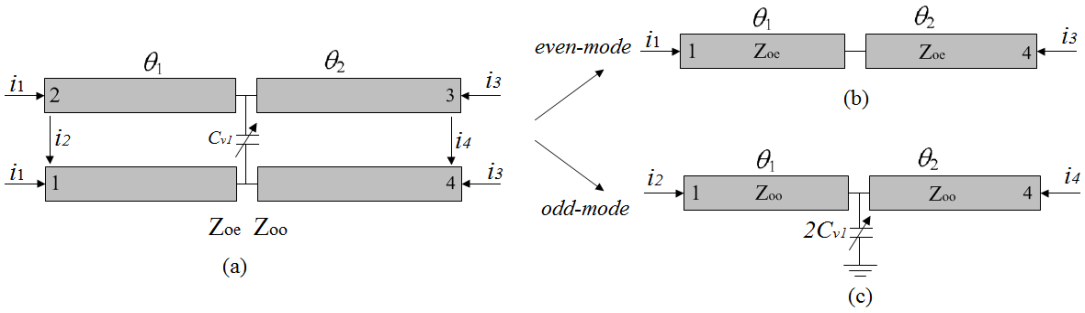

Figure B.3: (a) A varactor-loaded parallel coupled-line section with even- and mode current sources. (b) Equivalent even-mode circuit. (c) Equivalent odd-mode circuit.

If the other port is open-circuited, the even-mode input impedance seen at port 1 is

$$Z_{ine} = -jZ_{oe}\cot(\theta_1 + \theta_2) \qquad \text{(B. 5)}$$

The corresponding voltage at port 1 is given by

$$v_{1\_1} = i_1 Z_{ine} \qquad \text{(B. 6)}$$

Similarly, the voltage due to current source i_3 driving the collinear port 4 of the line in the even mode is expressed as

$$v_{4\_3} = i_3 Z_{ine} \qquad \text{(B. 7)}$$

In this case, measuring the open-circuit voltage at port 1 by virtue of *ABCD* matrix, it can be derived as

$$v_{1\_3} = v_{4_3}/A_e \qquad \text{(B. 8)}$$

$$A_e = \cos(\theta_1 + \theta_2) \qquad \text{(B. 9)}$$

where v_{1_3} represents the transfer voltage measured at port 1 excited by the current source i_3.

In a similar fashion, consider the odd-mode circuit driven by the i_2 current sources in Fig. B.3 (c). If the other port is open-circuited, the odd-mode input impedance at port 1 is

$$Z_{ino} = -j\frac{Z_{oo} - Z_{oo}\tan\theta_1(2Z_{oo}\omega C_{v1} + \tan\theta_2)}{2Z_{oo}\omega C_{v1} + \tan\theta_1 + \tan\theta_2} \qquad (B.10)$$

The corresponding voltage at port 1 is given by

$$v_{1\_2} = i_2 Z_{ino} \qquad (B.11)$$

Similarly, the voltage due to current source i_4 driving the collinear port 4 of the line in the odd mode can be expressed as

$$v_{4\_4} = i_4 Z_{ino\_1} \qquad (A.12)$$

$$Z_{ino\_1} = -j\frac{Z_{oo} - Z_{oo}\tan\theta_2(2Z_{oo}\omega C_{v1} + \tan\theta_1)}{2Z_{oo}\omega C_{v1} + \tan\theta_1 + \tan\theta_2} \qquad (A.13)$$

where Z_{ino_1} is the odd-mode input impedance obtained from port 4 when the counterpart is open-circuited. Only when the electrical length $\theta_1 = \theta_2$, Z_{ino_1} is equal to Z_{ino} given in (B.10).

Likewise, measuring the open-circuit voltage at port 1 by virtue of *ABCD* matrix, it can be expressed as

$$v_{1\_4} = v_{4_4}/\mathrm{A_o} \qquad (B.14)$$

$$\mathrm{A_o} = \cos(\theta_1 + \theta_2) - 2Z_{oo}\omega C_{v1}\cos\theta_1\sin\theta_2 \qquad (B.15)$$

where v_{1_4} represents the transfer voltage measured at port 1 excited by the current source i_4.

Based on the above discussions, the total voltage at port 1 can be finally demonstrated as

$$V_1 = v_{1\_1} + v_{1\_2} + v_{1\_3} + v_{1\_4}$$

$$= i_1 Z_{ine} + i_2 Z_{ino} + \frac{i_3 Z_{ine}}{A_e} + \frac{i_4 Z_{ino\_1}}{A_o} \qquad (B.16)$$

Now considering i_j in the above equation as being replaced by the I_j based on the expressions given in (B.1)-(B.4), the voltage V_1 can be further written as

$$V_1 = \frac{I_1}{2}(Z_{ine}+Z_{ino}) + \frac{I_2}{2}(Z_{ine}-Z_{ino}) + \frac{I_3}{2}\left(\frac{Z_{ine}}{A_e} - \frac{Z_{ino\_1}}{A_o}\right) + \frac{I_4}{2}\left(\frac{Z_{ine}}{A_e} + \frac{Z_{ino\_1}}{A_o}\right) \quad \text{(B. 17)}$$

This result yields the top row of the open-circuit impedance matrix [Z] that describes the varactor-loaded coupled line section. From symmetry, all other matrix elements can be found once the first row is known. The matrix elements are then

$$Z_{11} = Z_{22} = \frac{1}{2}(Z_{ine}+Z_{ino}); \quad Z_{33} = Z_{44} = \frac{1}{2}\left(Z_{ine}+Z_{ino\_1}\right) \quad \text{(B. 18)}$$

$$Z_{12} = Z_{21} = Z_{34} = Z_{43} = \frac{1}{2}(Z_{ine}-Z_{ino}) \quad \text{(B. 19)}$$

$$Z_{13} = Z_{31} = Z_{24} = Z_{42} = \frac{1}{2}\left(\frac{Z_{ine}}{A_e} - \frac{Z_{ino\_1}}{A_o}\right) \quad \text{(B. 20)}$$

$$Z_{14} = Z_{41} = Z_{23} = Z_{32} = \frac{1}{2}\left(\frac{Z_{ine}}{A_e} + \frac{Z_{ino\_1}}{A_o}\right) \quad \text{(B. 21)}$$

A two-port network can be formed from the coupled line section by terminating two of four ports in desired boundary conditions, such as open or short circuits. For the case given in Fig. B.1, port 2 and port 4 are imposed by open circuits, thus $I_2 = I_4 = 0$ and then four-port impedance matrix equations can be reduced to

$$Z_{11} = \frac{1}{2}(Z_{ine}+Z_{ino}) \quad \text{(B. 22)}$$

$$Z_{22} = \frac{1}{2}\left(Z_{ine}+Z_{ino\_1}\right) \quad \text{(B. 23)}$$

$$Z_{12} = Z_{21} = \frac{1}{2}\left(\frac{Z_{ine}}{A_e} - \frac{Z_{ino\_1}}{A_o}\right) \quad \text{(B. 24)}$$